*Eur*JIC

European Journal of Inorganic Chemistry

= Bulky Ligand
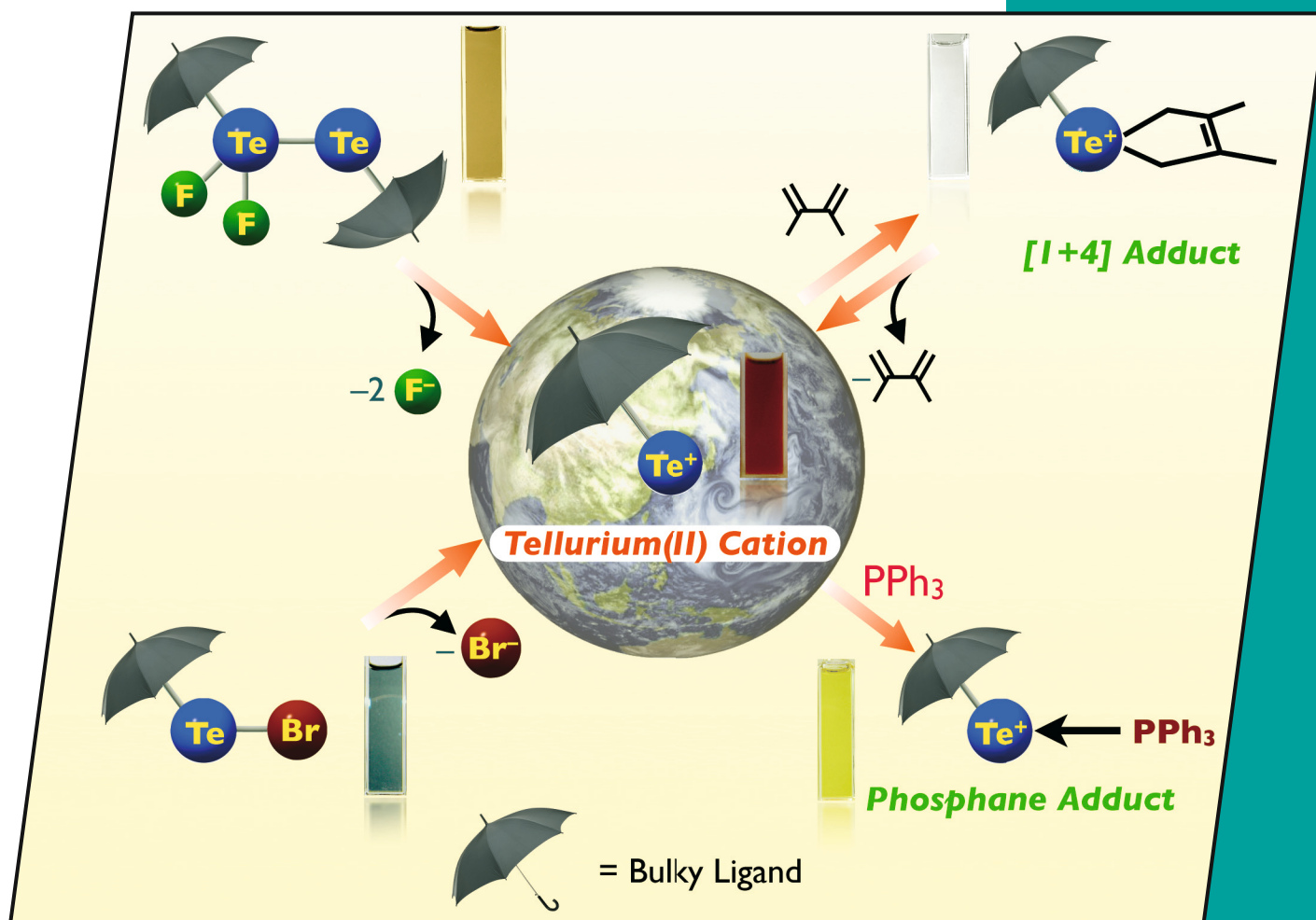
Cover Picture

Koh Sugamata, Takahiro Sasamori, and Norihiro Tokitoh
Generation of an Organotellurium(II) Cation

Microreview

Ines dos Santos Vieira and Sonja Herres-Pawlis
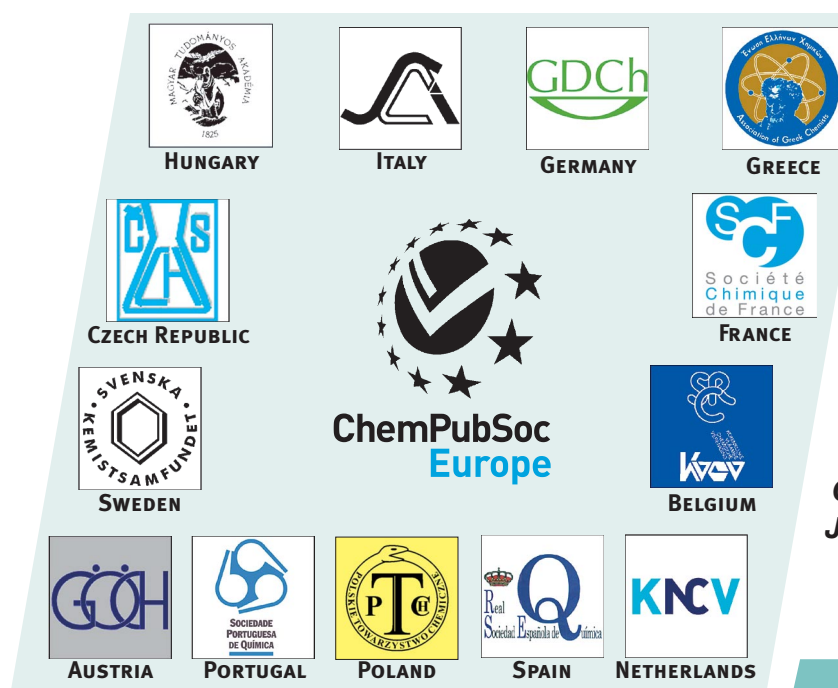*Lactide Polymerisation with Complexes of Neutral N-Donors*

HUNGARY	ITALY	GERMANY	GREECE

CZECH REPUBLIC

ChemPubSoc
Europe

FRANCE

SWEDEN

BELGIUM

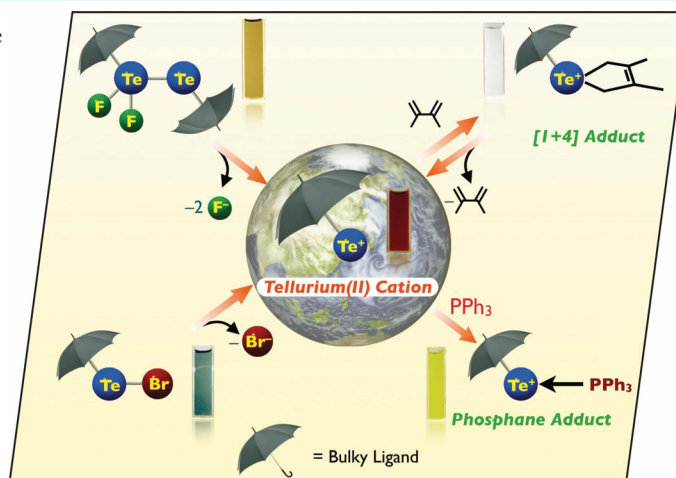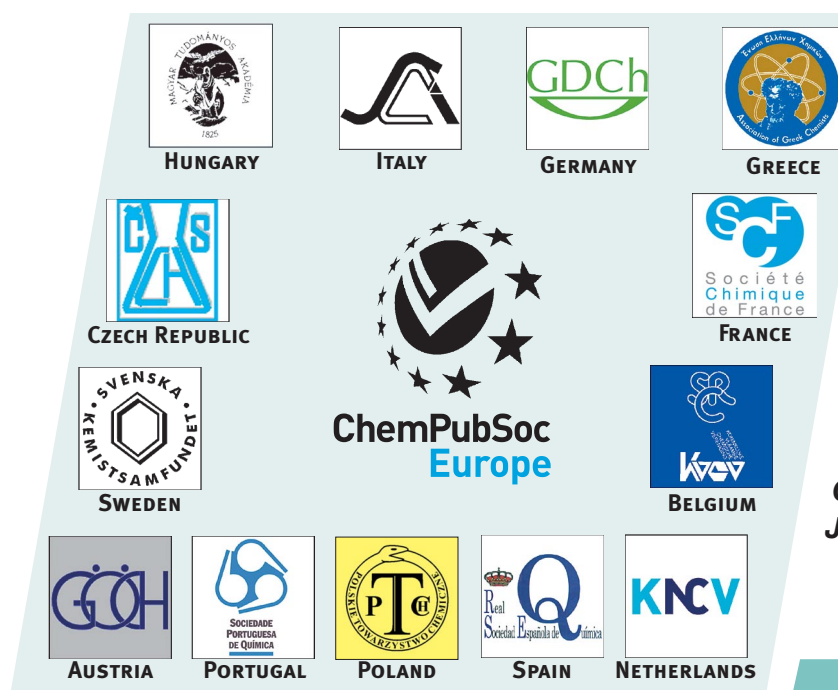|				
AUSTRIA	PORTUGAL	POLAND	SPAIN	NETHERLANDS

EurJIC is a journal of ChemPubSoc Europe, a union of 16 European chemical societies formed for the purpose of publishing high-quality science. All owners merged their national journals to form two leading chemistry journals, the *European Journal of Inorganic Chemistry* and the *European Journal of Organic Chemistry*.

Other ChemPubSoc Europe journals are *Chemistry – A European Journal*, *ChemBioChem*, *ChemPhysChem*, *ChemMedChem*, *ChemSusChem*, *ChemCatChem*, *ChemPlusChem* and *ChemistryOpen*.

COVER PICTURE

The cover picture shows the generation of the tellurium(II) cationic species bearing a sterically demanding ligand, exhibiting a deep red color. It was generated from the corresponding tellurium halides and trapped by diene and phosphane to give the corresponding adducts. The tellurium(II) cationic species was found to be regenerated by the thermolysis of the diene adduct. Details are discussed in the Short Communication by T. Sasamori, N. Tokitoh et al. on p. 775ff. The origin of "tellurium" is "tellus" in Latin meaning "earth".

Other ChemPubSoc Europe journals are *Chemistry – A European Journal*, *ChemBioChem*, *ChemPhysChem*, *ChemMedChem*, *ChemSusChem*, *ChemCatChem*, *ChemPlusChem* and *ChemistryOpen*.

COVER PICTURE

The cover picture shows the generation of the tellurium(II) cationic species bearing a sterically demanding ligand, exhibiting a deep red color. It was generated from the corresponding tellurium halides and trapped by diene and phosphane to give the corresponding adducts. The tellurium(II) cationic species was found to be regenerated by the thermolysis of the diene adduct. Details are discussed in the Short Communication by T. Sasamori, N. Tokitoh et al. on p. 775ff. The origin of "tellurium" is "tellus" in Latin meaning "earth".
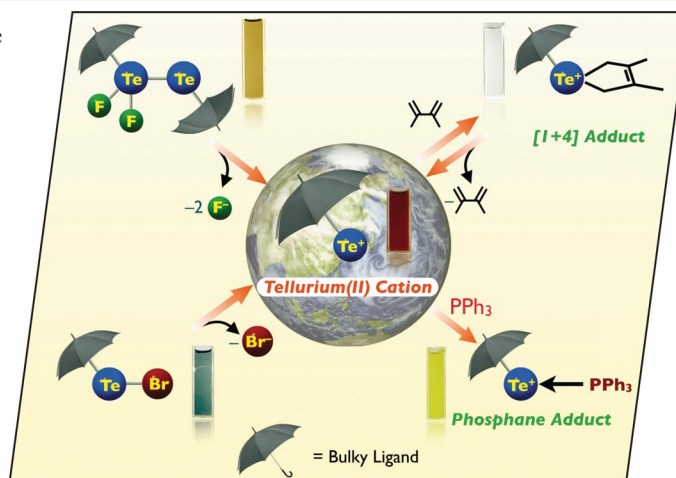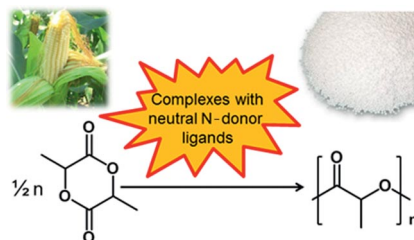
CONTENTS

MICROREVIEW

Sustainable Chemistry

Lactide Polymerisation with Complexes of
Neutral N-Donors − New Strategies for
Robust Catalysts

Keywords: Biodegradable polymers / N-donor ligands / Zinc / Ring-opening polymerization / Density functional calculations / Substainable chemistry

Recent developments in the area of lactide ring-opening polymerisation catalysed by complexes with neutral N-donor ligands are summarised. The applicability of these complexes is highlighted with special emphasis on the polymerisation conditions. Robustness and tolerance of the catalyst towards moisture and monomer impurities are identified as crucial features for the polymerisation activity.

SHORT COMMUNICATIONS

Organotellurium(II) Cations

Generation of an Organotellurium(II) Cation

Keywords: Tellurium / Cations / Steric protection / Structure elucidation

Organotellurium(II) cation species bearing a bulky aryl group were generated by dehalogenation from the corresponding tellurium(II) halides with silver salts or trimethylsilyl cations. In the presence of a diene or a phosphane as a trapping reagent, the tellurium(II) cations readily undergo [1+4] addition or phosphane coordination to form the diene and phosphane adducts, respectively.

Lanthanide Complexes

A New Type of Lanthanide Complex − Two Divalent Ytterbium Species Assembled from Cation−π Interactions

Keywords: Ytterbium / Cation−π interactions / Amides / Dimers / Synthesis design
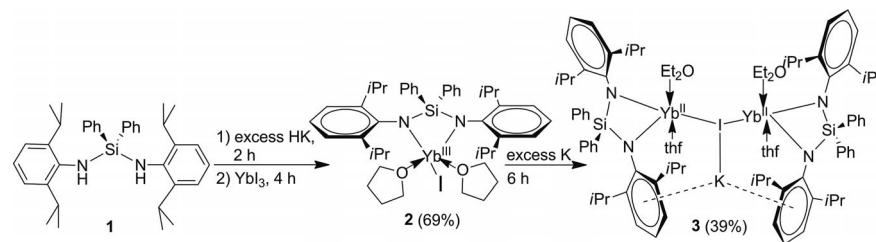
A new divalent ytterbium complex, [{(L^{Ph})Yb^{II}(Et$_2$O)(thf)}$_2$(μ-KI)] {L^{Ph} = Ph$_2$Si-(NAr)$_2$, Ar = 2,6-iPr$_2$C$_6$H$_3$} (**3**), was synthesized by the reaction of [(L^{Ph})Yb^{III}I-(thf)$_2$] (**2**) and an excess of potassium. The bimetallic ytterbium(II) species with bulky diamido ligands are bridged by a KI molecule with cation−π interactions.

FULL PAPERS

Nanomaterials

In Situ X-ray Absorption Spectroscopy/Energy-Dispersive X-ray Diffraction Studies on the Hydrothermal Formation of Bi$_2$W$_{1−x}$ Nanomaterials

Keywords: Bismuth / Tungsten / Molybdenum / Hydrothermal synthesis / Nanostructures
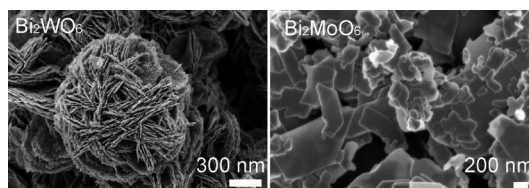
Hierarchical Bi$_2$W$_{1−x}$Mo$_x$O$_6$ nanostructures and nanosheets have been selectively obtained by adjusting the W/Mo ratio. The hydrothermal formation process of these solid solutions was monitored by complementary in situ X-ray absorption spectroscopy/energy-dispersive X-ray diffraction. Their different morphology types correlate with the observed reaction kinetics.

Porous Coordination Polymers

A new Zr porous coordination polymer with azobenzenedicarboxylate linkers was prepared by using a modulated synthetic approach. Without a modulator (benzoic acid), no crystalline products were formed. The material is thermally stable in air up to 400 °C and exhibits a large specific surface area (3000 $m^2 g^{-1}$).
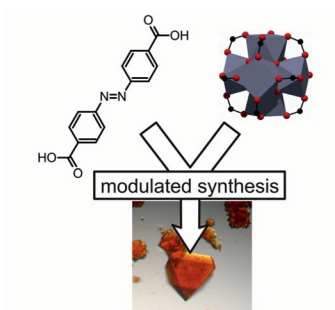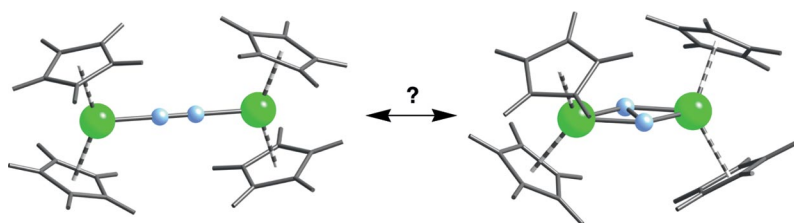
A. Schaate, S. Dühnen, G. Platz, S. Lilienthal, A. M. Schneider, P. Behrens* .... 790−796

A Novel Zr-Based Porous Coordination Polymer Containing Azobenzenedicarboxylate as a Linker

Keywords: Adsorption / Azo compounds / Coordination polymers / Metal−organic frameworks / Zirconium

Dinitrogen Coordination Modes

B. Peigné, J. Cano, G. Aullón* .... 797−806

On the Coordination of Dinitrogen to Group 4 Metallocenes

Keywords: Density functional calculations / Dinitrogen / Isomers / Coordination modes / Metallocenes

A theoretical study of $[M_2Cp_4N_2]$ complexes shows the preference of the metal for two isomeric forms. The analysis of electronic and molecular structures for the M_2N_2 unit provides information on the coordination modes of dinitrogen to metallocenes.

Pd−Zn Coordination Polymers

Four new Pd−Zn coordination polymers have been synthesized by slow concentration or solvothermal methods, and structurally characterized. Two of the four Pd−Zn coordination polymers showed selective H_2 gas adsorption over N_2 gas adsorption at 77.35 K and 760 Torr.
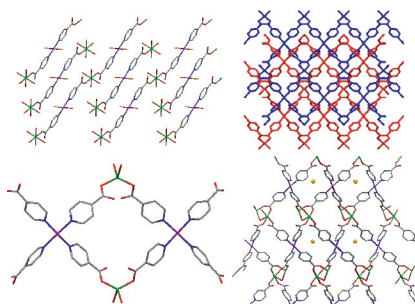
Y. Miyazaki, Y. Kataoka, T. Kawamoto,* W. Mori .... 807−812

Synthesis, Crystal Structure and Gas Adsorption Properties of Four Pd−Zn Coordination Polymers Containing Potential Catalytic Active Sites

Keywords: Polymers / Selective gas adsorption / Crystal engineers / Palladium / Zinc

Metal-Based Enzyme Inhibitors

Inert octahedral rhodium(III) complexes were used as structural templates for the design of highly potent inhibitors of the protein kinase Pim1.
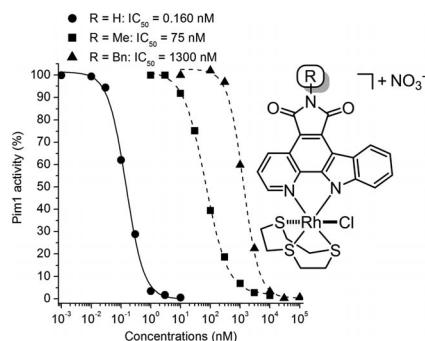
S. Dieckmann, R. Riedel, K. Harms, E. Meggers* .... 813−821

Pyridocarbazole-Rhodium(III) Complexes as Protein Kinase Inhibitors

Keywords: Enzymes / Inhibitors / Protein kinases / Biotransformations / Rhodium

CONTENTS
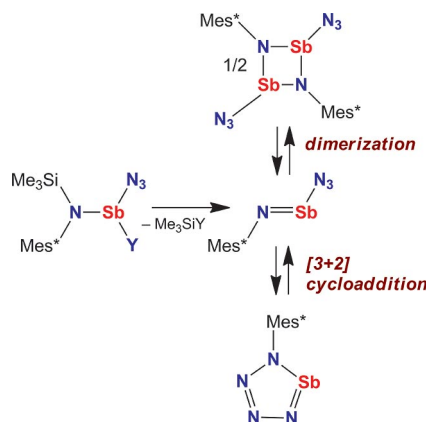
Amino(azido)stibanes Mes*N(SiMe₃)Sb-(N₃)X (X = N₃, Cl, OTf) were synthesized and characterized. Their thermal stability with respect to Me₃Si−X elimination was studied.
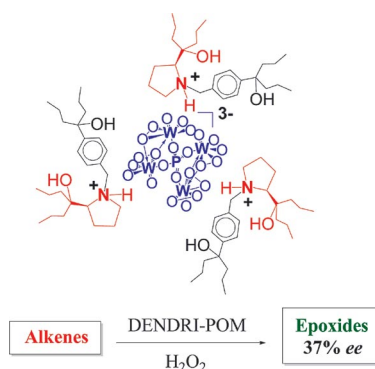
ʟ-Proline-derived dendritic tetrakis(diperoxotungsto)phosphate was prepared by assembling enantiopure ʟ-proline-derived ligands with the anionic polyoxometalate (POM) unit. This DENDRI-POM catalyzes the oxidation of alkenes to the corresponding epoxides with 37% *ee*. This *ee* value is the best enantioselectivity reported to date in the oxidation of organic substrates with chiral POM hybrids.
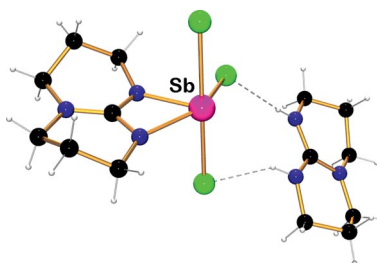
Bicyclic guanidinate [hpp]⁻ (hppH = 1,3,4,6,7,8-hexahydro-2*H*-pyrimido[1,2-*a*]-pyrimidine) chelates to antimony in Sb(hpp)Cl₂ and Sb(hpp)₂Cl. Attempted preparation of the neutral adduct with hppH afforded the salt [hppH₂][Sb(hpp)-Cl₃], in which a net proton transfer between guanidine molecules had taken place.
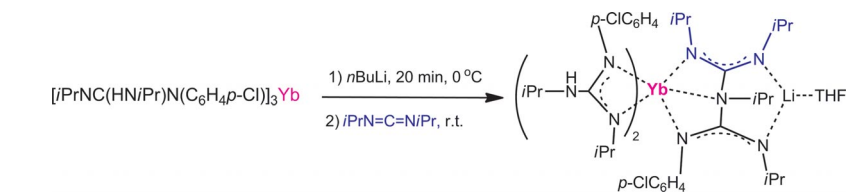
Triguanidinate lanthanide complex [{*i*PrNHC(N*i*Pr)(NC₆H₄*p*-Cl)}₃Yb(THF)] was treated with *n*BuLi and then *i*PrN=C=N*i*Pr to afford heterometallic Yb−Li complex [{*i*PrNHC(N*i*Pr)N(C₆H₄*p*-Cl)}₂Yb{(*i*PrNC(N*i*Pr)₂)N(C₆H₄*p*-Cl)C-(*i*PrN)}Li(THF)]·THF, which represents the first example of the insertion of a carbodiimide molecule into a guanidinate−metal bond to give a biguanidinate ligand.

Benzothiazole Coordination

The facile synthesis of a new 6-chloro-aminobenzothiazole-functionalised phosphane and its O, S and Se analogues is described. This anionic phosphorus(V) ligand coordinates to a potassium metal centre in two unusual modes: a κ^3-N_2E tridentate (E = O) or κ^2-N_2 bridging (E = S) mode leading to unique 1D polymeric chain motifs. In contrast, the deprotonated phosphane sulfide or selenide κ^2-NE chelates to a range of late transition metal fragments.
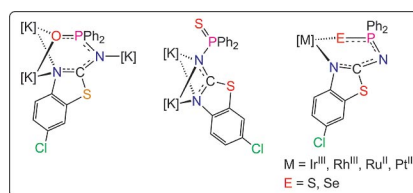
S. J. Coles, S. H. Dale, M. R. J. Elsegood, K. G. Gaw, T. Gelbrich, M. B. Hursthouse, M. E. Light, T. A. Noble, M. B. Smith* .... 859−865

Diverse Coordination Behaviour of Phosphorus(V)-Functionalised 6-Chloroaminobenzothiazole Anions at Various Metal Centres

Keywords: Benzothiazole / Chalcogenides / Phosphanes / Potassium / Structure elucidation

Energetic Hydrazine Derivatives

Salts of the $[MeNH_2−NH_2Me]^{2+}$ cation with energetic anions form extensive hydrogen bonds in the solid state, which stabilize the materials. The low sensitivity of the compounds in combination with moderate to high performances and low vapor pressures make these materials interesting candidates for future energetic applications.
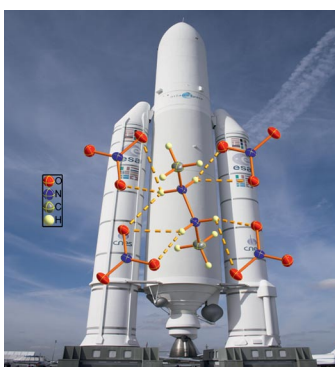
C. M. Sabaté,* H. Delalu .... 866−877

Energetic Salts of Symmetrical Dimethylhydrazine (SDMH)

Keywords: Hydrogen bonds / Hydrazines / Nitrogen compounds / Thermodynamics / Structure elucidation

Thin Films

We present an easily obtainable silver-based precursor suitable for printing applications. The simple reaction of silver nitrate and 2-pyrrolidone (Pyl) yields a stable $[Ag(Pyl)_2]NO_3$ complex, the crystal structure of which was solved. Highly concentrated solutions can be obtained in ethanol/water, thereby allowing for manufacture of thin films through coating or printing techniques.

$$AgNO_3 + 2 \text{ } Pyl \xrightarrow{H_2O} [Ag(Pyl)_2]NO_3$$
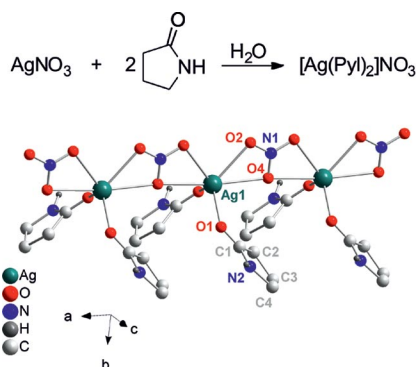
J. Fritsch, B. Schumm, R. Biedermann, J. Grothe,* S. Kaskel .... 878−883

A New Silver-Based Precursor as Ink for Soft Printing Techniques

Keywords: Silver / Pyrrolidone / Photoreduction / Thin films / Patterning

---

* Author to whom correspondence should be addressed.

📃 Supporting information on the WWW (see article for access details).

This article is available online free of charge (Open Access).

If not otherwise indicated in the article, papers in issue 4 were published online on January 24, 2012

SPOTLIGHTS …

On these pages, we feature a selection of the excellent work that has recently been published in our sister journals. If you are reading these pages on a computer, click on any of the items to read the full article. Otherwise please see the DOIs for easy online access through Wiley Online Library.

Biocoordination Polymers

Y. Liu, Z. Tang*

Nanoscale Biocoordination Polymers: Novel Materials from an Old Topic

Nature bestows many gifts upon us, among which countless biomolecules have the ability to bridge metal ions and exert important functions in biology. By taking advantage of specific interactions between metal ions and biomolecules, this article highlights a novel concept for the construction of nanoscale biocoordination polymers through replacement of synthetic organic molecules with natural biomolecules as building blocks. The most recent advances are summarized and future challenges are discussed.
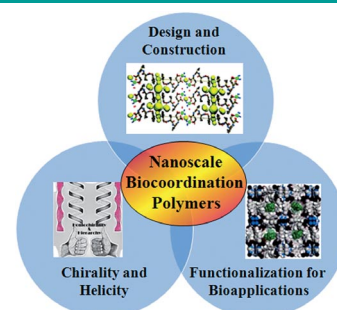
Chem. Eur. J.
DOI: **10.1002/chem.201101520**

Antibiotics

A. Sliwa, G. Dive,* J. Marchand-Brynaert*

12- to 22-Membered Bridged β-Lactams as Potential Penicillin-Binding Protein Inhibitors

Bridging inhibition: A series of 12- to 22-membered bicyclic bridged β-lactams were synthesized with the aim of developing new inhibitors of penicillin-binding proteins and feature a planar amide function and no carboxy group (see picture; Boc = *tert*-butyloxycarbonyl).
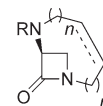
R = Boc, *n* = 3, 4, 5, 6, 8
R = PhOCH$_2$CO, *n* = 3, 4, 5

Chem. Asian J.
DOI: **10.1002/asia.201100732**
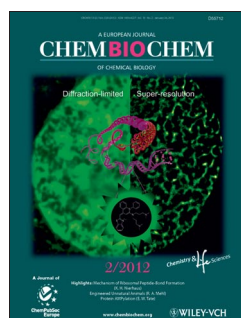
Glycosylation

V. Siitonen, M. Claesson, P. Patrikainen, M. Aromaa, P. Mäntsälä, G. Schneider, M. Metsä-Ketelä*

Identification of Late-Stage Glycosylation Steps in the Biosynthetic Pathway of the Anthracycline Nogalamycin

Topoisomerase inhibition: Nogalamycin is an anthracycline antibiotic with an unusual structure and significant cytotoxicity. In this work the nogalamycin biosynthetic gene cluster has been expressed in a heterologous host, late-stage tailoring steps of nogalamycin biosynthesis have been investigated and new compounds have been isolated.
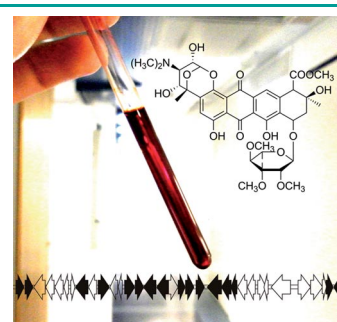
ChemBioChem
DOI: **10.1002/cbic.201100637**

Hydrogen Storage

B. Pathak, K. Pradhan, T. Hussain, R. Ahuja, P. Jena*

Functionalized Boranes for Hydrogen Storage

Li- and Mg-functionalized boranes (see picture) are promising materials for hydrogen storage. They can store up to 12 wt % hydrogen with a desorption energy of 0.07 eV–0.27 eV per H_2 molecule.
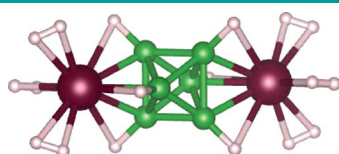
ChemPhysChem
DOI: **10.1002/cphc.201100585**

Protein–Protein Interactions

Y. Huang, S. Wolf, D. Koes, G. M. Popowicz, C. J. Camacho, T. A. Holak, A. Dömling*

Exhaustive Fluorine Scanning toward Potent p53–Mdm2 Antagonists

Fluorine dance: We discovered potent p53–Mdm2 antagonists by systematically varying the fluorine substitution pattern around a benzyl group that undergoes stacking interactions with His 96 of Mdm2. The potency of the optimized enantiomer (**S**)-**7e** is > 50-fold better than the worst compound of the series. All compounds were efficiently synthesized by Ugi multicomponent reaction chemistry.

ChemMedChem
DOI: **10.1002/cmdc.201100428**

Fuel Cells

W. Zhang, P. N. Pintauro*

High-Performance Nanofiber Fuel Cell Electrodes

A nanofiber electrode is fabricated by electrospinning an ink composed of ;Pt/C catalyst particles in a solution of Nafion and poly(acrylic acid). Exceptionally high power densities and platinum mass activity are achieved when using the mat as cathode in H_2/air and H_2/O_2 fuel cell membrane–electrode assemblies. The nanofiber cathode also exhibits outstanding stability in accelerated durability tests.

ChemSusChem
DOI: **10.1002/cssc.201100245**

Hydrogenation

E. Castillejos, M. Jahjah, I. Favier, A. Orejón, C. Pradel, E. Teuma, A. M. Masdeu-Bultó, P. Serp,* M. Gómez*

Synthesis of Platinum–Ruthenium Nanoparticles under Supercritical CO_2 and their Confinement in Carbon Nanotubes: Hydrogenation Applications

Into the nanotube: Platinum–ruthenium nanoparticles confined into functionalized multiwalled carbon nanotubes were found to be efficient catalysts for the hydrogenation of cinnamaldehyde in contrast to the unsupported catalytic systems. Although bimetallic nanoparticles synthesized in supercritical CO_2 led to more agglomerated materials than those in THF, no important differences were observed in catalysis.

ChemCatChem
DOI: **10.1002/cctc.201100244**
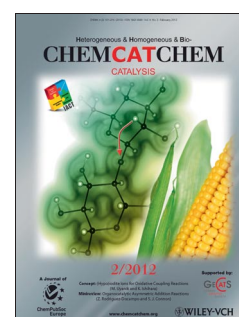
Nanoctystals

X.-H. Guan, B.-T. Zheng, M. Lu, X. Guan, G.-S. Wang,*
L. Guo*

Highly Water-Dispersible Fe_3O_4 Single Nanocrystals: Gram-Scale Preparation by a Solution-Phase Route and Application for the Absorption of Cd^{2+} in Water

It's all under control: High-yield production of Fe_3O_4 (10–15 nm) was realized by using a simple solution-phase method at room temperature. The Fe_3O_4 nanocrystals were continually synthesized by controlling the pH value of the reaction solution. The SEM, TEM, and XRD studies reveal the particles to be single nanocrystals. New adsorbents of FNBC prepared by a simple blending method exhibit significantly higher property in removing the heavy metal Cd^{2+} than BC and Fe_3O_4 nanocrystals, and show excellent properties in removing Cd^{2+}.
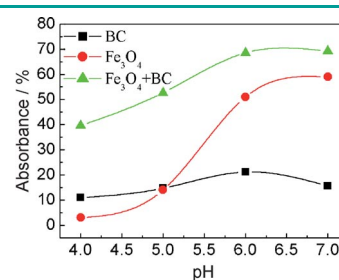
Virus Host Recognition

B. Fiege, C. Rademacher, J. Cartmell, P. I. Kitov, F. Parra,
T. Peters*

Molecular Details of the Recognition of Blood Group Antigens by a Human Norovirus as Determined by STD NMR Spectroscopy

Tracing the infection: The binding of human norovirus particles to blood group antigens was investigated using NMR spectroscopy. Binding epitopes were determined at atomic resolution, information on the binding specificity was obtained, and the bioactive conformation of various sugars was revealed. This provides valuable information for the design of entry inhibitors against this important class of human pathogenic viruses.
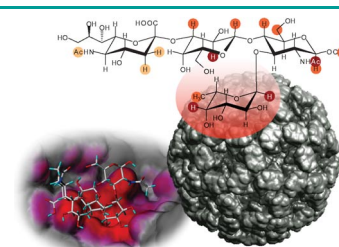
Orthogonal Protecting Groups

P. Ruiz-Sanchis, S. A. Savina, G. A. Acosta, F. Albericio,*
M. Álvarez*

Orthogonal Protecting Groups in the Synthesis of Tryptophanyl-Hexahydropyrroloindoles

Several tryptophanyl-hexahydropyrroloindoles (Trp-HPI) with four or five orthogonal protecting groups have been synthesized. This polyheterocyclic system constitutes a scaffold for many natural products that have recently been isolated.
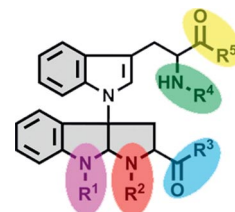
Food Chemistry

Klaus Roth

Pesto - Mediterranean Biochemistry

When we take pesto prepared from fresh basil, fold it into steaming pasta, and allow the inimitable fragrance to rise up, we ask ourselves: with what aromatic molecules is this plant blessing us? By uncovering the nature of this culinary-chemical marvel, we come to enjoy it all the more.
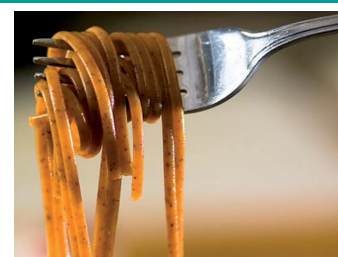
Lactide Polymerisation with Complexes of Neutral N-Donors – New Strategies for Robust Catalysts

Ines dos Santos Vieira[a] and Sonja Herres-Pawlis*[a][‡]

Dedicated to Professor Bernhard Lippert on the occasion of his retirement

Ring-opening polymerisation of cyclic esters represents a growing field of research, because the resulting polymers are biodegradable and mostly based on renewable raw materials, which ensures increasing interest in this process within the context of green chemistry. Up to now, neutral N-donor ligands have been overlooked in their potential to stabilise catalytically active systems. This contribution summarises recent developments in this area as well as their applicability in lactide polymerisation with special regard to the reaction conditions. When a use on the industrial scale is targeted, tolerance towards moisture, air, lactide impurities and high temperatures is an important issue to be considered during catalyst design. A multitude of sodium, calcium and zinc complexes with amines, carbenes, guanidines, phosphinimines, pyridines and tris(pyrazolyl)methanes is discussed and their activity in lactide polymerisation is highlighted.

Introduction

In the new century, two severe problems have to be solved: the society's dependence on petrochemical resources and the growing amounts of non-compostable and some-times poisonous waste spread in the environment. Due to the growing ecological awareness, sustainable development leads to an increasing demand for biodegradable plastics based on renewable raw materials.[1] In an effort to solve these problems, numerous studies have been undertaken on the synthesis of biodegradable polymers. Over the last 30 years, great advances in the synthesis, manufacture and processing of these materials have enabled a broad range of practical applications from short-term packaging to highly sophisticated biomedical devices.

Among the variety of biodegradable plastics, aliphatic polyesters have conquered the bioplastics market, because hydrolytic and/or enzymatic chain cleavage yields ω-hy-

[a] Fakultät Chemie, Anorganische Chemie, Technische Universität Dortmund,
44221 Dortmund, Germany
Fax: +49-231-7555048
E-mail: sonja.herres-pawlis@tu-dortmund.de
[‡] Present address: Fakultät für Chemie und Pharmazie, Department Chemie, Ludwig-Maximilians-Universität München, Butenandtstr. 5–13, 81377 München, Germany
Fax: +49-89-218077867
E-mail: sonja.herres-pawlis@cup.uni-muenchen.de

Ines dos Santos Vieira (1981) studied Chemistry at the universities of Bielefeld and Paderborn and finished her Master's degree in 2009. She then started her graduate studies at the Technische Universität Dortmund under the supervision of Prof. Dr. S. Herres-Pawlis. She is currently working on experimental and theoretical investigations in the field of lactide polymerisation with zinc guanidine complexes.

Sonja Herres-Pawlis (1979) finished her Diplom in Chemistry in 2002 and received her Ph.D. degree (2005) at the Universität Paderborn, under the supervision of Prof. Gerald Henkel. She continued her scientific education as postdoctoral fellow with Prof. T. Daniel P. Stack at Stanford University (2006). In 2007, she started her own research group and moved in 2009 with a Liebig fellowship to the Technische Universität Dortmund, where she is currently finishing her Habilitation. In November 2011, she has been appointed to an associate professorship in coordination chemistry at the Ludwig-Maximilians-Universität München. Her research interests focus on the activation of small molecules for oxidation and polymerisation with N-donor transition metal complexes. Recently, she has been awarded the Innovation Prize of the state Northrhine-Westfalia in the category for young researchers for her studies on lactide polymerisation.

droxyacids, which in most cases are completely metabolised.[2,3] Within the intensive research in the field of aliphatic polyesters, polylactide or poly(lactic acid) (PLA) has gained the greatest attention due to its favourable chemical and mechanical properties. PLA shows mechanical similarities to poly(ethylene terephthalate) (PET) but also to poly-(propylene) (PP). It can be processed in most polymer processing equipment, which is a critical factor for industrial use. But even more important: It appears to be the polymer with the broadest range of applications, because of its ability to be stressed or thermally crystallised, filled and copolymerised.[4] Until now, PLA has found many fields of application, for example in biomedical implants and sutures (owing to its biocompatibility) or for packaging, films and fibres.[4]

As it is biodegradable, it makes a contribution to minimise the problem of waste disposal.[2] With regard to rising oil prices and emerging ecoplastics markets, PLA will become a viable alternative to PET with a better cost/performance balance. Moreover, this material offers transparency and a refractive index similar to that of poly-(methyl methacrylate) (PMMA), a polymer widely used for optical applications. The feasibility of using PLA as an eco-sustainable PMMA alternative in luminescent solar concentrators has been recently reported.[5]

PLA can be produced from inexpensive, annually renewable raw materials. Corn or sugar beets are the most significant source of lactic acid, but agricultural waste and non-food-quality carbohydrates may be used as well.[4] After bacterial fermentation of the carbohydrate feed, lactic acid is readily available and converted to lactide. PLA can be produced by ring-opening polymerisation (ROP) of lactide (LA), the cyclic diester of lactic acid, or by direct polycondensation of lactic acid. The polylactide can be either recycled or composted after use, and therefore its CO_2 emission is neutral. Hence, PLA is less environmentally costly than common recyclable polymers, which can only be recycled a limited number of times before losing the desired material properties. Among the numerous polyesters studied to date, PLAs have proven to be the most attractive and useful class of biodegradable polyesters.[2–4]

Coordination–Insertion Polymerisation

In comparison to polyesterification, the ROP of lactide uses mild reaction conditions and avoids the formation of small molecule byproducts.[6] Within the last decade, several ROP processes have been developed, including anionic, cationic, organocatalytic and coordination–insertion methods.[3] The coordination–insertion process is now commonly regarded as the most efficient method for the well-controlled synthesis of polyesters with regard to composition, molecular weight and microstructure.[3,4] The coordination–insertion mechanism of lactide polymerisation (Scheme 1) involves the coordination of the monomer to the metal centre, followed by a nucleophilic attack of the alkoxide on the acyl carbon atom and the insertion of lact-

ide into the metal–alkoxide species with retention of configuration.[6] A new metal–alkoxide species is formed, which is capable of further insertion reactions.
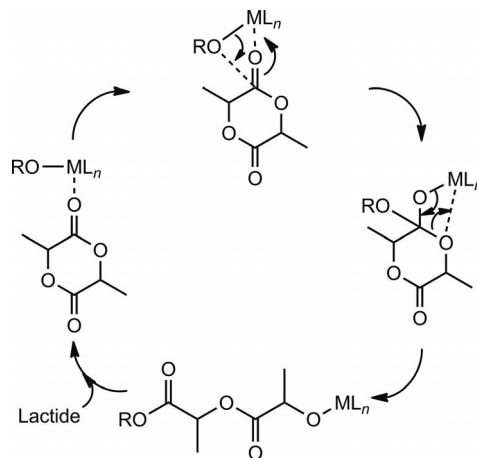
Scheme 1. Coordination–insertion mechanism for lactide ROP.

Under industrial conditions, mostly homoleptic catalysts are used, such as tin(II) ethylhexanoate, zinc(II) lactate and aluminium isopropoxide, in combination with alcohols as initiators.[7] Already in 1971, Dittrich and Schulz defined a three-step coordination–insertion mechanism for the ROP of cyclic esters.[8] Later, Kricheldorf et al. and Teyssié et al. showed that such a mechanism was involved in the ROP of different lactones initiated by Al(OiPr)3.[9,10]

These catalyst systems can be conveniently synthesised and utilised in the polymerisation of cyclic esters, but complicated equilibrium phenomena and multiple nuclearities of the active species result in limited polymerisation control. Detrimental side reactions like transesterifications and epimerisations may occur, which lead to a broadening of the molar mass distribution.

Consequently, the development of new single-site metal catalysts for the ring-opening polymerisation of lactide has seen tremendous growth over the past decade.[1–4,6] As an amelioration, these catalysts shall enable a better control, activity and selectivity during the polymerisation by optimal adaptation of the coordinating ligands. The ideal catalyst is tolerant towards the lactide melt and acidic impurities in the monomer, low-priced, odourless, colourless and nontoxic.[3]

A vast multitude of well-defined Lewis acid catalysts following a coordination–insertion mechanism has been developed for this reaction mainly based on tin,[11] zinc,[12–15] aluminium[16–18] and rare earth metals.[19–23] Moreover, organocatalysts have been successfully used in ROP.[24–26] However, PLA is still more expensive than petrochemical-based plastics, and therefore it is merely used in biomedical applications and packaging of organic products. To change this polymer from a specialty material to a large-volume commodity plastic, the development of new polymerisation catalysts is required. Most large-scale processes are based on the use of stannous compounds as initiators.[1–3] For use in food packaging or similar applications, heavy metals are undesirable because of accumulation effects.[2,3g]

Despite the enormous efforts, the new single-site catalysts have not become accepted in industrial context.[4] To date, the design of new single-site catalysts mostly follows the paradigm that an efficient lactide ROP initiating system needs an anionic ligand, for example, alkoxides, amides, ketiminates or an alcohol as co-initiator that forms the truly active species as alkoxide. The high polymerisation activity of all these systems is often combined with high sensitivity towards air and moisture. For industrial purposes and especially the breakthrough of PLA in the competition with petrochemical based plastics, there is an exigent need for active catalysts that tolerate air, moisture and small impurities in
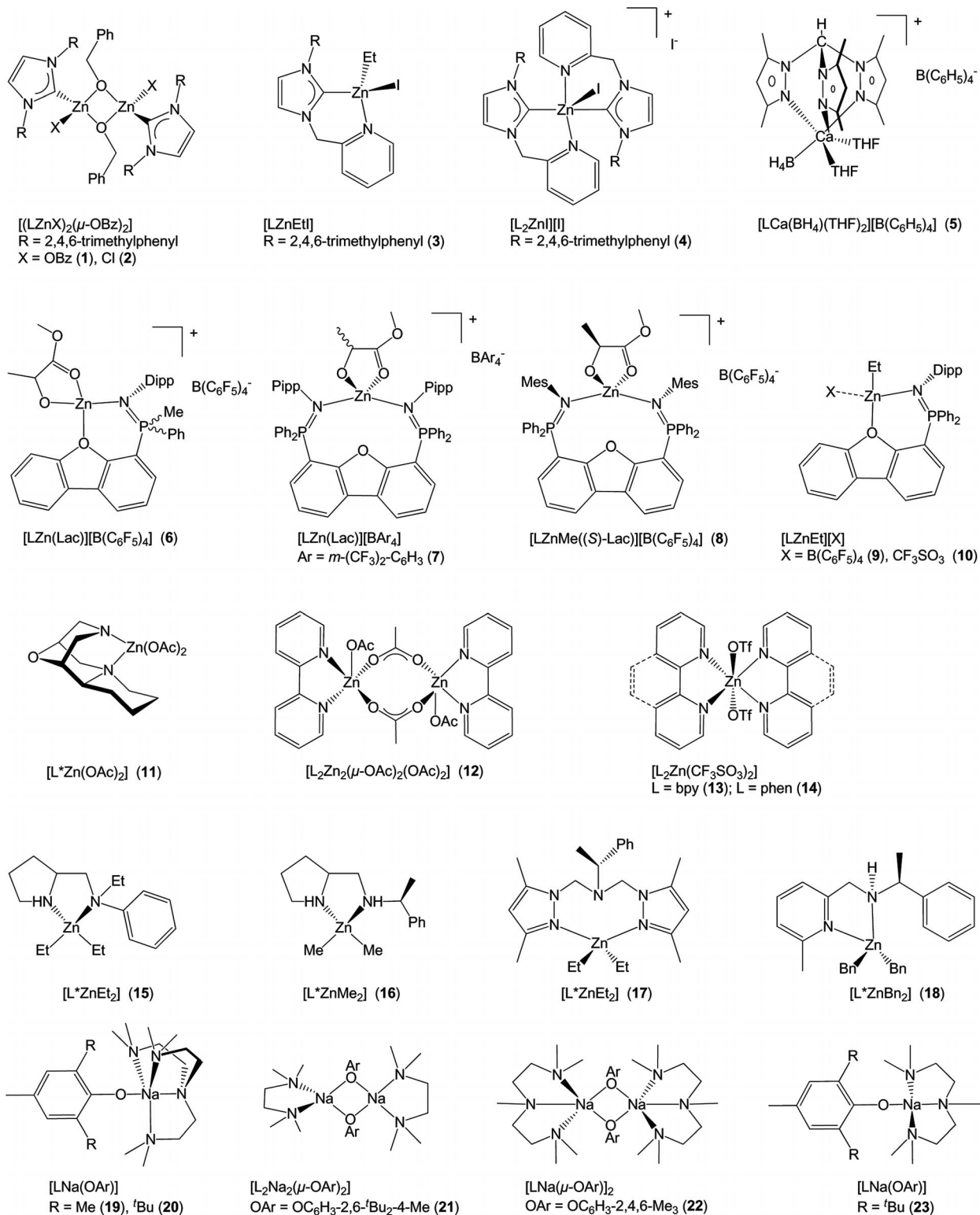
Scheme 2. ROP-active systems stabilised by neutral donor ligands.

the monomer.[1–3] The disadvantageous sensitivity can be ascribed to the anionic nature of the ligand systems stabilising almost all of these complexes.

In this contribution, the role of neutral donor ligands for the stabilisation of ROP-active systems will be highlighted, because this niche has been overlooked for years.

Neutral Donor Systems

Up to now, only few ROP-active systems using neutral ligands in single-site metal catalysts have been described (Scheme 2). They make use of strong donors such as carbenes[27,28] and phosphinimines[29–32] but also moderate donors like amines[33–38] and pyridines[39] for the ROP of lactide and ε-caprolactone (Scheme 2). In case of carbenes, Tolman et al. have reported that the activity of the pure carbene as organocatalyst is higher than that in its zinc complexes 1–4.[27,28] However, Tolman's carbene zinc complexes 1 and 2 polymerise lactide under glove-box conditions at room temperature within minutes in high yields and with low polydispersity (PD = M_w/M_n, Table 1).[27] Pyridine–

carbene systems 3 and 4 polymerise lactide at 140 °C within minutes but with higher PDs.[28]

Tris(pyrazolyl)methanes have been introduced into ROP chemistry as tripodal N-donor ligand systems by Mountford et al.[40] In the cationic calcium complex 5, the tetrahydroborate serves as initiator and lactide is polymerised in a few hours at 25 °C in THF with high agreement between calculated and measured molecular weights and a low polydispersity.

Phosphinimine ligands represent a versatile ligand class that stabilises magnesium and zinc complexes with high ROP activity, as exemplified in Scheme 2 with complexes 6–10.[29–32] The bis(phosphinimine) pincer ligand within cationic lactate complex 7 enables living lactide polymerisation.[30] Hayes and Wheaton report controlled reaction kinetics between 37 and –7 °C with slight deviation from theoretical molar weights at higher conversion. The good reactivity is very remarkable for these low temperatures. The polydispersities range between 1.1 and 1.3, which is indicative for a controlled coordination–insertion polymerisation process.[30] In further studies, this group synthesised

Table 1. Summary of lactide ROP activity of complex systems with neutral ligands.

Catalyst	Solvent	[M]/[I]	T [°C]	t	Conversion [%]	M_n [g mol^{-1}]	PD	P_r[a]	Ref.
1	CH$_2$Cl$_2$	130	25	20 min	96	17000	1.25	0.60	[27]
1	CH$_2$Cl$_2$	260	25	20 min	97	17000	1.25	0.60	[28]
2	CH$_2$Cl$_2$	130	25	4 min	99	20000	1.52	0.60	[28]
3	—[b]	100	140	5 min	96	12000	2.45	0.60	[28]
3	—[b]	200	140	5 min	86	20000	2.04	0.60	[28]
4	—[b]	50	140	5 min	91	6000	2.51	0.60	[28]
4	—[b]	200	140	5 min	73	12000	1.78	0.60	[28]
5	THF	250	25	2 h	99	43000	1.2–1.4	0.50	[40]
6	C$_6$H$_5$Br	200	100	9 h	74	17000	1.98	0.49	[29]
6	C$_6$H$_5$Br	300	100	9 h	69	21000	1.89	n.d.	[29]
6	C$_6$H$_5$Br	400	100	9 h	69	27000	1.81	n.d.	[29]
7	CD$_2$Cl$_2$	200	25	50 min	90	29000	1.05	0.63	[30]
8	C$_6$H$_5$Br	50	60	3.5 h	90	18000	1.2–1.3	n.d.	[31]
9	C$_6$D$_6$/C$_6$D$_5$Br	100	100	6 h	90	2500–5000	n.a.	n.d.	[32]
10	C$_6$D$_6$/C$_6$D$_5$Br	100	100	6 h	85	2500–5000	n.a.	n.d.	[32]
11	—[b]	500	150	48 h	29	11000	1.93	0.50	[33]
12	—[b]	500	150	48 h	57	76000	1.90	0.59	[39]
13	—[b]	500	150	24 h	94	33000	1.70	0.50	[39]
13	—[b]	500	150	48 h	89	24000	1.90	n.d.	[39]
14	—[b]	500	150	48 h	21	44000	2.00	0.61	[39]
15	CH$_2$Cl$_2$	67	25	1 h	90	14000	1.35	n.d.	[34]
15	CH$_2$Cl$_2$	122	25	1 h	99	26000	1.64	n.d.	[34]
15	THF	100	25	1 h	95	34000	1.34	n.d.	[34]
15	Toluene	100	25	7 h	99	47000	2.40	n.d.	[34]
16	CH$_2$Cl$_2$/THF	110	25	12 h	97	15000	1.23	0.71	[35]
16	CH$_2$Cl$_2$/THF	110	–25	12 h	96	15000	1.21	0.75	[35]
17	THF/toluene	200	25	2 h	84	16000	1.52	0.56	[37]
17	THF/toluene	200	–20	12 h	36	8000	1.16	0.58	[37]
18	THF	100	25	2 h	67	13000	1.05	n.d.	[36]
18	THF	200	25	2 h	61	23000	1.18	n.d.	[36]
19	CH$_2$Cl$_2$	100	25	5 min	99	37000	1.54	0.47	[38]
19	CH$_2$Cl$_2$	300	25	5 min	82	14000	1.59	0.47	[38]
20	CH$_2$Cl$_2$	100	25	5 min	57	7000	1.30	0.47	[38]
21	CH$_2$Cl$_2$	100	25	30 min	97	28000	2.61	0.47	[38]
22	CH$_2$Cl$_2$	100	25	30 min	99	26000	1.69	0.43	[38]
23	CH$_2$Cl$_2$	100	25	30 min	90	106000	1.51	0.45	[38]

[a] P_r: probability of racemic enchainment calculated by analysis of the homonuclear decoupled ^{1}H NMR spectra.[41] [b] Bulk polymerisation of lactide.

a variety of mono- and bis(phosphinimine) zinc complexes **7–10** with high to excellent ROP activity.[31,32] In all cases, the phosphinimine ligand serves as stabilising ligand and does not participate in the initiation. This function is adopted by the lactate or alkyl groups incorporated in the complex. It has to be noted that all these studies were performed under strict inert gas conditions in the NMR tube.

When an industrial large-scale applicability is targeted, more robust initiators are needed. In this context, the robust zinc acetate complex **11**, which comprises an elaborate chiral tricyclic 9-oxabispidine, has been reported as ROP-active system in the lactide melt.[33]

As rather simple neutral ligand systems, the classic N-donor ligands 2,2′-bipyridine and 1,10-phenanthroline were proven to stabilise zinc complexes (**12–14**) with surprising ROP activity under challenging conditions in melt.[39] The polydispersities of approximately 2 account for the presence of transesterification reactions. The tolerance of the catalysts towards air and moisture is a key issue for general applicability. With regard to industrial usefulness, most single-site catalysts are restricted by their sensitivity towards moisture and air. In many cases, the monomer has to be recrystallised or sublimated in order to remove residual lactic acid, water and other impurities which affect the catalyst or even start new chains. Additionally, the role of polymerisation temperature has to be regarded as a critical factor: On the one hand, good ROP behaviour at low temperatures testifies the high catalyst reactivity, but on the other hand, industrial application requires the catalyst's survival at temperatures up to 200 °C. Hence, the activity of complexes **3**, **4**, **6** and **9–14** in ROP at temperatures higher than 100 °C approves their potential as catalysts for large-scale production.

More sophisticated amine systems have also been used: for example, Novak et al. introduced *N*-ethyl-*N*-phenyl-2-pyrrolidinemethanamine in lactide chemistry, but a lactide ROP activity is only reported for the corresponding sensitive diethylzinc complex **15**.[34] Here, the ethyl group is the true initiator. Jeong et al. reported a related pyrrolidine–amine zinc complex, which initiates, as ZnMe₂ species **16**, the ROP of lactide with high yields.[35] In this case, a significant enrichment of heterotactic enchainments has been observed. With bis(pyrazol)amine diethylzinc complex **17**, Lee et al. observed good ROP activity even at –20 °C.[37] The use of diethylzinc is essential for the ROP of lactide. With the pyridylamine zinc benzylate complex **18**, polylactides with very small polydispersities could be obtained.[36]

With simpler peralkylated diamines, Davidson et al. have shown that polyamine-stabilised sodium aryloxides **19–23** exhibit good activity in room-temperature lactide ROP with moderate control.[38] Dinuclear complexes **21** and **22** give polylactide with broader molecular weight distributions, whereas Me₆tren derivatives **19** and **20** lead to material with a PD of 1.3–1.6. When benzyl alcohol is added as co-initiator, the reaction proceeds faster and with higher control, although transesterifications can still be observed.[38] It has to be remarked that for polyamine-stabilised sodium aryloxides **19–23**, the probability of heterotactic enchainment indicates an isotactic bias with values smaller than 0.5. This is ascribed to stereorandom transesterification processes, as epimerisation was excluded in stereopure polymerisations. When using lower catalyst loadings (300:1), the authors observed polymer yields of 80%, whereas the residual monomer was converted into cyclic oligomers by an intrachain esterification process.

Guanidine Systems

In order to overcome the limitations of anionic and other sensitive ligand systems, the potential of a neutral but highly Lewis-basic ligand system was evaluated. Guanidines seem very suitable because of their good donor properties and strong nucleophilicity.[42,43] Within the last decade, they have been used for numerous applications in transition metal chemistry.[44] In 2007, the first cationic complex, [Zn(DMEG₂e)₂][OTf]₂ (**24**), has been reported as active ROP catalyst for lactide polymerisation in melt (Table 2, Scheme 3).[45] At 150 °C, molecular weights of 24000 g mol⁻¹ could be obtained within 24 h. Besides bis(chelate) complex **24**, mono(chelate) complexes **25** and **26** and their lactide ROP activity were reported.[45] At that point in time, the active mechanism was not clear. In following studies of complexes **27** and **28** with the closely related but more basic imino–imidazoline ligand 8MeBL,[44f,44g] it

Table 2. Polymerisation results with zinc guanidine complexes.[a]

Catalyst	t [h]	Conversion [%]	M_n [g mol⁻¹]	PD	P_r[b]	Ref.
24	24	83	24000	1.6	n.d.	[45]
25	24	79	22000	1.7	0.50	[45]
26	24	69	15000	1.6	0.50	[45]
27	24	85	25000	2.0	0.53	[46]
28	24	88	12000	2.0	0.50	[46]
29	48	0	–	–	–	[47]
30	48	0	–	–	–	[47]
31	48	0	–	–	–	[48]
32	48	17	16000	2.0	0.55	[48]
33	24	51	30000	1.6	0.57	[48]
34	24	72	31000	1.8	0.56	[48]
35	48	41	9000	2.1	n.d.	[47]
36	48	58	9000	2.0	n.d.	[48]
37	48	60	19000	1.8	n.d.	[48]
38	48	51	15000	1.7	0.49	[48]
39	48	29	13000	1.7	0.49	[48]
40	48	0	–	–	–	[49]
41	48	33	18000	1.6	n.d.	[49]
42	24	93	70000	2.2	n.d.	[47,52]
43	24	92	77000	2.1	n.d.	[47,52]
44	24	81	19000	1.9	0.54	[50a]
45	24	71	12000	1.9	0.52	[50a]
46	24	72	12000	1.8	0.53	[50a]

[a] Conditions for *rac*-LA polymerisation with zinc guanidine complexes **24**–**46**: solvent-free melt polymerisation at 150 °C, monomer/initiator ratio 500:1. [b] P_r: probability of racemic enchainment calculated by analysis of the homonuclear decoupled ¹H NMR spectra.[41]

appeared that the partial charge on the zinc atom, as well as that on the donating N_{imine} atom, is crucial for the lactide activity.[46] Using mono(chelate) zinc imino–imidazoline complexes **27** and **28**, similar molecular weights (25000 and 12000 gmol^{-1}, respectively) and conversions (85 and 88%, respectively) were observed. With the use of the sterically less demanding guanidine–pyridine ligands, a multitude of zinc complexes **29–43** could be isolated, and trends for their ROP activity were derived.[47,48] In case of the quinoline–guanidine complexes, mono(chelate) chlorido complexes **29–32** exhibit a lower activity than mono(chelate) acetato complexes **35–39**.[47,48] Especially quinoline–guanidine bis-(chelate) triflato complexes **42** and **43** exhibited very high activity and robustness towards monomer impurities at the same time. By using **42** and **43** for the ROP of technical quality lactide, molecular weights of 70000 and 77000 gmol^{-1} could be obtained with conversions of > 90%. These molecular weights are highly desired for industrial use.

Comparative studies with mono(chelate) mesylato complex **40** and bis(chelate) mesylato complex **41**[49] revealed that – within bis(chelate) complexes **42** and **43** – the zinc atom possesses a high positive partial charge and the guanidine a pronounced negative charge. The corresponding mono(chelate) chlorido (**29**, **30**) and acetato complexes (**35**, **36**) with a smaller positive charge on the zinc displayed lower activity. Besides this correlation of partial charges and activity, the zinc–oxygen distance in the solid-state structures correlated with the ROP activity as well: short Zn–O distances [2.103(1) Å] in mesylato complex **41** resulted in lower ROP activity due to strong anion binding. In the triflato complexes with Zn–O distances of 2.684(3) Å in **42** and 2.452(7) Å in **43**, the anionic component can be regarded as placeholder for the lactide molecules, whereas in the mesylato complexes, the zinc–oxygen bond is stronger. In further studies, the influence of denticity and ligand bite has been evaluated. As example for poly(guanidines), dinuclear tetra(guanidine) zinc complex **44** and the

[Zn(DMEG₂e)₂][OTf]₂ (**24**)

[Zn(DMEG₂e)X₂] X = Cl (**25**)
                X = OAc (**26**)

[Zn(8MeBL)X₂] X = Cl (**27**)
               X = OAc (**28**)

[Zn(TMGqu)X₂] $R^1 = R^2 = R^3 = R^4 = CH_3$, X = Cl (**29**), OAc (**35**)
[Zn(DMEGqu)X₂] $R^1 = R^4 = CH_3$, $R^2 = R^3 = -(CH_2)_2-$,
                   X = Cl (**30**), OAc (**36**), OMes (**40**)
[Zn(DMPGqu)X₂] $R^1 = R^4 = CH_3$, $R^2 = R^3 = -(CH_2)_3-$,
                   X = Cl (**31**), OAc (**37**)
[Zn(TEGqu)X₂] $R^1 = R^2 = R^3 = R^4 = CH_2CH_3$, X = Cl (**32**)
[Zn(DMorphGqu)X₂] $R^1 = R^2 = R^3 = R^4 = -(CH_2)_2O(CH_2)_2-$,
                   X = Cl (**33**), OAc (**38**)
[Zn(MorphDMGqu)X₂] $R^1 = R^2 = CH_3$, $R^3 = R^4 = -(CH_2)_2O(CH_2)_2-$
                   X = Cl (**34**), OAc (**39**)

[Zn(TMGqu)₂(X)][X] $R^1 = R^2 = CH_3$
                     X = OMes (**41**), OTf (**42**)
[Zn(DMEGqu)₂(X)][X] $R^1 = CH_3$, $R^2 = -(CH_2)_2-$
                     X = OTf (**43**)

[(TMG₄(baem)₂b)(ZnCl₂)₂] (**44**)

[Zn(TMG₃tren)(Cl)][Cl]   R = CH₃ (**45**)
[Zn(DMEG₃tren)(Cl)][Cl] R = -(CH₂)₂- (**46**)

Scheme 3. Zinc guanidine complexes for the ROP of lactide.

tris(guanidine) complexes **45** and **46** were tested with modest activities.[50a]

In all these polymerisation experiments with commercial grade PLA, no external initiator had been added. The lactide impurities might act as chain starter, but it could be shown that the polymerisation proceeds with sublimated lactide as well.[50b] The donor strength of guanidines is comparable to that of ketimitines, such that guanidines might act as ring-opening nucleophiles. This idea served as working hypothesis for the subsequent spectroscopic and kinetic studies.

The fluorescence activity of the guanidine–quinoline ligands[51] gave the next mechanistic hint because the quinoline-related emission can be traced in the zinc complexes and the resulting polylactide. Moreover, the UV absorption of the guanidine-quinoline ligands was found in the corresponding lactide as well.[52] Together with polymerisation kinetics and computational studies, the active mechanism for zinc guanidine complexes **42** and **43** was investigated. Up to 165 °C, the polymerisation follows first-order kinetics with activation parameters of $\Delta H^{\ddagger} = 79(4)$ kJ mol^{-1} and $\Delta S^{\ddagger} = -33(4)$ J K^{-1} mol^{-1}. These values are in good accordance with those of other single-site catalysts,[53] but they indicate that the polymerisation is energetically too difficult to run at room temperature with these complexes. The polydispersities of 2 show that transesterification reactions occur at these high temperatures in melt. However, the molecular weights increase proportionally with the conversion, which indicates, once more, a controlled reaction progress.[32] As all polymerisations were carried out without additional initiator, the question for the actual mechanism arose. As guanidines are strong neutral donors, their nucleophilicity was proposed to help the ring-opening reaction. Hence, the working hypothesis implied the coordination of the lactide to the zinc centre followed by a nucleophilic attack of the guanidine on the carbonyl C atom of the lactide molecule. Guided by this idea, extensive density functional studies were accomplished for ROP with **42**, which yielded the reaction coordinate presented in Figure 1.[52] In fact, this computational study is the first DFT study for ROP with neutral ligands without additional co-initiators. The pre-coordination of the lactide molecule is

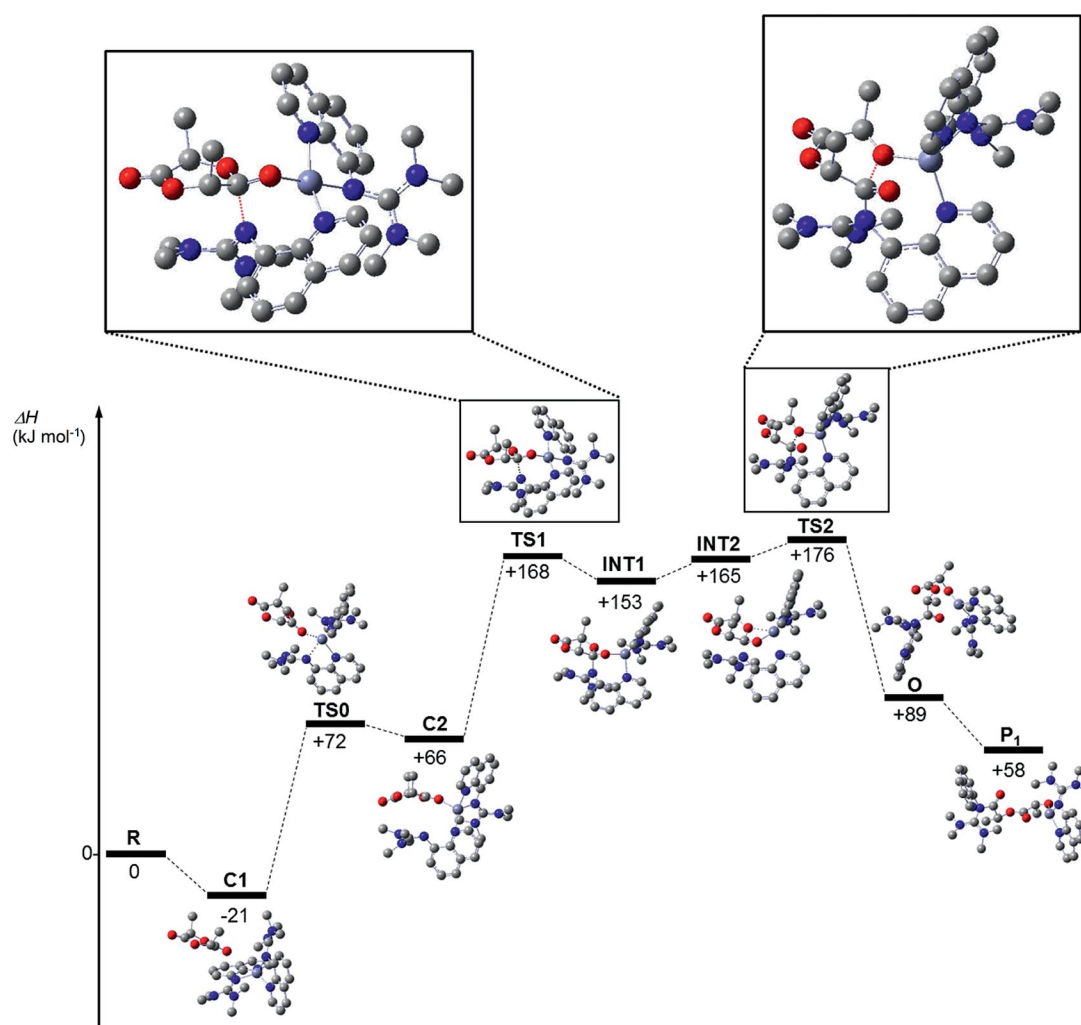Figure 1. Complete reaction coordinate diagram for the insertion of the first lactide molecule (**R**: reactants, **C**: zinc coordinated lactide, **TS**: transition state, **INT**: tetrahedral intermediate, **O**: opened species, **P**: propagating species).
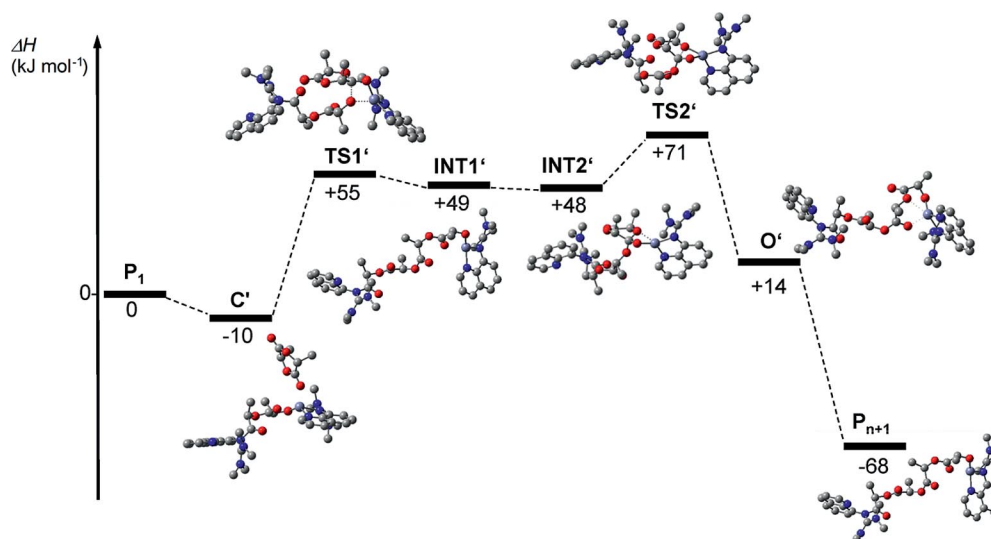
Figure 2. Complete reaction coordinate diagram for the insertion of the second lactide molecule as model for the propagation step (**C′**: zinc coordinated lactide, **TS**: transition state, **INT**: tetrahedral intermediate, **O′**: opened species, **P**: propagating species).

slightly exothermic, but the coordination sphere around the zinc atom undergoes rearrangement via transition state **TS0**, which results in a stronger lactide binding (2.05 vs. 3.74 Å prior to **TS0**). With this close substrate coordination, the guanidine attacks the carbonyl C atom nucleophilically (**TS1**) with formation of a tetrahedral intermediate (**INT1**). Going from **INT1** to **INT2**, the coordination sphere of the zinc rearranges once more such that both oxygen atoms of the lactide bind to the zinc. This enables the subsequent C–O bond breaking in **TS2** with an energy cost of 102 kJ mol⁻¹. After this crucial step, the ring-opened lactide unfolds, going from **O** to **P1**. This reaction coordinate is in good accordance with those reported for other single-site coordination–insertion mechanisms.[54] The typical two-step procedure consisting of nucleophilic attack and ring-opening is reproduced very well here. The complete analysis shows that the guanidine N_{imine} donor function is nucleophilic enough to conduct the ring-opening of the lactide as the first step of the polymerisation. Hence, the ROP of lactide is possible with cationic complexes in the absence of anionic ligands or co-ligands if the incorporated neutral ligands are nucleophilic enough.

In fact, this step represents the ring-opening of the first lactide and is not representative for the majority of polymerisation steps, because the coordination sphere changes after the first step. After ring-opening of the first lactide, a lactate group is bound to the zinc atom, which now performs the nucleophilic attack and thus the ring-opening step of the second lactide. This complete reaction sequence is a representative step for all following polymerisation steps. The reaction coordinate diagram for the ring-opening of the second lactide is detailed in Figure 2. The DFT analysis reveals a similar reaction progression with the characteristic transition states for nucleophilic attack (**TS1′**) and ring-opening event (**TS2′**) but without the pre-transition state (**TS0**, coordination rearrangement of guanidine). More importantly, the **TS2′** is lower in energy with

65 kJ mol⁻¹. This compares very well with the experimentally observed value of 79 kJ mol⁻¹.[52] With regard to the whole combined study, the special variant of the coordination–insertion mechanism that is active for zinc guanidine complexes could be clarified.

The great advantage of guanidine systems is their extraordinary robustness towards moisture and monomer impurities. Until now, comparable robust systems have only been reported by Davidson et al.,[55] who used tris(phenolate) titanium complexes. However, zinc guanidine systems combine in a unique manner many crucial features for efficient large-scale lactide ROP. In detail, the robustness of zinc guanidine complexes in lactide ROP supersedes monomer recrystallisation or sublimation and saves cost-extensive processing steps. Moreover, the polymerisation can be accomplished under melt conditions at high temperatures up to 200 °C without racemisation effects.[52] This is important for further applications in reactive polymer extrusion.

With regard to the biodegradability and sustainability of PLA and its final fate in landfill or composting, the use of zinc is especially advantageous, when the metal toxicity is considered, because the catalyst can remain in the polymer, and time-consuming purification procedures can be omitted. Hence, the studies on zinc guanidine complexes represent an important step towards the ultimate breakthrough of PLA in competition with petrochemical-based plastics. Together with the complete study on the active mechanism, the efficient use of these neutral donors in the development of ROP-active systems has shed more light on a hitherto overlooked ligand category.

Conclusions and Outlook

In this review, the utility of the overlooked category of neutral donors for the stabilisation of complex systems for the ring-opening polymerisation of cyclic esters has been

highlighted. Until 2004, only anionic ligands had been used, but with regard to the industrial demand novel systems that support the use of commercial lactide and elevated reaction temperatures were urgently needed. Within the last years, the introduction of neutral donor ligands to ROP led to numerous studies with calcium, sodium and zinc complexes with remarkable ROP activities. Many ligand classes like amines, carbenes, guanidines, phosphinimines, pyridines and tris(pyrazolyl)methanes have been investigated in this young but flourishing field. In some cases, the neutral ligands are accompanied by anionic co-ligands such as alkoxide, phenoxide or alkyl. Here, the anionic co-ligands perform the nucleophilic attack that initiates the ring-opening reaction. Concomitantly, the anionic nature of these co-ligands does not enable increased robustness towards air, moisture and lactide impurities, as was originally targeted. The pyridine- and guanidine-stabilised complexes are active in the absence of anionic co-ligands. Chloride, acetate and triflate serve here as charge-compensating unit. Screening of a multitude of these zinc guanidine complexes allowed to evaluate a structure–reactivity relationship. The variety within this ligand class encompasses aliphatic and aromatic frameworks as well as polydentate systems and combinations with other donors. In fact, quinoline–guanidine zinc triflate complexes show the best performance with high molecular weights and controlled polymerisation behaviour. A combined spectroscopic, kinetic and theoretical study revealed that the coordination–insertion mechanism is valid for these complexes.

The comprehensive concept of robust zinc guanidine systems has been proven to yield efficient and versatile ROP-active catalysts. The great impact of the guanidine ligand is expressed in two central traits: its excellent donor capacity stabilises very robust zinc complexes and its high nucleophilicity enables the ring-opening of cyclic esters by the N_{imine} donor functionality.

In general, the importance of neutral ligands for the ring-opening polymerisation of lactide cannot be underestimated. With regard to the major breakthrough of bioplastics for the substitution of petrochemical plastics in the commodity market, every robust catalyst system represents a huge step towards greater sustainability of our society. In the near future, this will improve the economic situation for biodegradable polymers from renewable resources and establish polylactide in many fields of polymer applications.

Acknowledgments

[1] a) L. S. Nair, C. T. Laurencin, *Prog. Polym. Sci.* **2007**, *32*, 762–798; b) K. Sudesh, T. Iwata, *Clean* **2008**, *36*, 433–442.

[2] a) A. P. Gupta, V. Kumar, *Eur. Polym. J.* **2007**, *43*, 4053–4074; b) D. Garlotta, *J. Polym. Environ.* **2001**, *9*, 63–84; c) S. Inkinen, M. Hakkarainen, A.-C. Albertsson, A. Södergard, *Biomacromolecules* **2011**, *12*, 523–532; d) J. Ahmed, S. K. Varshney, *Int. J. Food Prop.* **2011**, *14*, 37–58.

[3] a) R. H. Platel, L. M. Hodgson, C. K. Williams, *Polym. Rev.* **2008**, *48*, 11–63; b) O. Dechy-Cabaret, B. Martin-Vaca, D. Bourissou, *Chem. Rev.* **2004**, *104*, 6147–6176; c) C. A. Wheaton, P. G. Hayes, B. J. Ireland, *Dalton Trans.* **2009**, 4832–4846; d) J. Wu, T.-L. Yu, C.-T. Chen, C.-C. Lin, *Coord. Chem. Rev.* **2006**, *250*, 602–626; e) R. Drumwright, P. Gruber, D. Henton, *Adv. Mater.* **2000**, *12*, 1841–1846; f) R. Mehta, V. Kumar, H. Bhunia, S. N. Upadhyay, *J. Macromol. Sci. C: Polym. Rev.* **2005**, *45*, 325–349; g) H. R. Kricheldorf, *Chemosphere* **2001**, *43*, 49–54; h) P. J. Dijkstra, H. Dum, J. Feijen, *Polym. Chem.* **2011**, *2*, 520–527; i) M. J. Stanford, A. P. Dove, *Chem. Soc. Rev.* **2010**, *39*, 486–494.

[4] a) R. Auras, L.-T. Lim, S. E. M. Selke, H. Tsuji in *Poly(lactic acid) – Synthesis Structures, Properties, Processing, and Applications*, John Wiley & Sons, Inc, Hoboken, New Jersey **2010**; b) S. Inkinen, M. Hakkarainen, A.-C. Albertsson, A. Södergard, *Biomacromolecules* **2011**, *12*, 523–532.

[5] V. Fattori, M. Melucci, L. Ferrante, M. Zambianchi, I. Manet, W. Oberhauser, G. Giambastiani, M. Frediani, G. Giachic, N. Camaioni, *Energy Environ. Sci.* **2011**, *4*, 2849–2853.

[6] C. M. Thomas, *Chem. Soc. Rev.* **2010**, *39*, 165–173.

[7] a) H. R. Kricheldorf, J. Meier-Haak, *Macromol. Chem.* **1993**, *194*, 715–725; b) M. Yuan, D. Liu, C. Xiong, X. Deng, *Eur. Polym. J.* **1999**, *35*, 2139–2145; c) H. R. Kricheldorf, D.-O. Damrau, *Macromol. Chem. Phys.* **1997**, *198*, 1753–1766.

[8] W. Dittrich, R. C. Schulz, *Angew. Makromol. Chem.* **1971**, *15*, 109–126.

[9] H. R. Kricheldorf, M. Berl, N. Scharnagl, *Macromolecules* **1988**, *21*, 286–293.

[10] P. Dubois, R. Jérôme, P. Teyssié, *Makromol. Chem. Macromol. Symp.* **1991**, *42/43*, 103–116.

[11] A. P. Dove, V. C. Gibson, E. L. Marshall, H. S. Rzepa, A. J. P. White, D. J. Williams, *J. Am. Chem. Soc.* **2006**, *128*, 9834–9843.

[12] C. K. Williams, L. E. Breyfogle, S. K. Choi, W. Nam, V. G. Young, M. A. Hillmyer, W. B. Tolman, *J. Am. Chem. Soc.* **2003**, *125*, 11350–11359.

[13] B. M. Chamberlain, M. Cheng, D. R. Moore, T. M. Ovitt, E. B. Lobkovsky, G. W. Coates, *J. Am. Chem. Soc.* **2001**, *123*, 3229–3238.

[14] J. Ejfler, S. Szafert, K. Mierzwicki, L. B. Jerzykiewicz, P. Sobota, *Dalton Trans.* **2008**, 6556–6562.

[15] J.-C. Wu, B.-H. Huang, M.-L. Hsueh, S.-L. Lai, C.-C. Lin, *Polymer* **2005**, *46*, 9784–9792.

[16] M. D. Jones, M. G. Davidson, C. G. Keir, L. M. Hughes, M. F. Mahon, D. C. Apperley, *Eur. J. Inorg. Chem.* **2009**, 635–642.

[17] Z. Y. Zhong, P. J. Dijkstra, J. Feijen, *Angew. Chem.* **2002**, *114*, 4692–4695; *Angew. Chem. Int. Ed.* **2002**, *41*, 4510–4513.

[18] Z. Y. Zhong, P. J. Dijkstra, J. Feijen, *J. Am. Chem. Soc.* **2003**, *125*, 11291–11298.

[19] H. Ma, T. P. Spaniol, J. Okuda, *Inorg. Chem.* **2008**, *47*, 3328–3339.

[20] H. Ma, T. P. Spaniol, J. Okuda, *Angew. Chem.* **2006**, *118*, 7982–7985; *Angew. Chem. Int. Ed.* **2006**, *45*, 7818–7821.

[21] I. Peckermann, A. Kapelski, T. P. Spaniol, J. Okuda, *Inorg. Chem.* **2009**, *48*, 5526–5534.

[22] B. Lian, H. Ma, T. P. Spaniol, J. Okuda, *Dalton Trans.* **2009**, 9033–9042.

[23] A. Amgoune, C. M. Thomas, S. Ilinca, T. Roisnel, J. F. Carpentier, *Angew. Chem.* **2006**, *118*, 2848–2850; *Angew. Chem. Int. Ed.* **2006**, *45*, 2782–2784.

[24] a) R. C. Pratt, B. G. G. Lohmeijer, D. A. Long, R. M. Waymouth, J. L. Hedrick, *J. Am. Chem. Soc.* **2006**, *128*, 4556–4557; b) A. Chuma, H. W. Horn, W. C. Swope, R. C. Pratt, L. Zhang, B. G. G. Lohmeijer, C. G. Wade, R. M. Waymouth, J. L. Hedrick, J. E. Rice, *J. Am. Chem. Soc.* **2008**, *130*, 6749–6754.

[25] N. E. Kamber, W. Jeong, R. M. Waymouth, R. C. Pratt, B. G. G. Lohmeijer, J. L. Hedrick, *Chem. Rev.* **2007**, *107*, 5813–5840.

[26] J. M. Becker, S. Tempelaar, M. J. Stanford, R. J. Pounder, J. A. Covington, A. P. Dove, *Chem. Eur. J.* **2010**, *16*, 6099–6105.

[27] T. R. Jensen, L. E. Breyfogle, M. A. Hillmyer, W. B. Tolman, *Chem. Commun.* **2004**, 2504–2505.

[28] T. R. Jensen, C. P. Schaller, M. A. Hillmyer, W. B. Tolman, *J. Organomet. Chem.* **2005**, *690*, 5881–5891.

[29] H. Sun, J. S. Ritch, P. G. Hayes, *Inorg. Chem.* **2011**, *50*, 8063–8072.

[30] C. A. Wheaton, P. G. Hayes, *Chem. Commun.* **2010**, *46*, 8404–8406.

[31] C. A. Wheaton, P. G. Hayes, *Dalton Trans.* **2010**, *39*, 3861–3869.

[32] a) B. J. Ireland, C. A. Wheaton, P. G. Hayes, *Organometallics* **2010**, *29*, 1079–1084; b) C. A. Wheaton, B. J. Ireland, P. G. Hayes, *Organometallics* **2009**, *28*, 1282–1285.

[33] J. Börner, U. Flörke, A. Döring, D. Kuckling, M. D. Jones, M. Steiner, M. Breuning, S. Herres-Pawlis, *Inorg. Chem. Commun.* **2010**, *13*, 369–371.

[34] J. H. Jeong, Y. H. An, Y. K. Kang, Q. T. Nguyen, H. Lee, B. M. Novak, *Polyhedron* **2008**, *27*, 319–324.

[35] S. Nayab, H. Lee, J. H. Jeong, *Polyhedron* **2011**, *30*, 405–409.

[36] Y. K. Kang, Q. T. Nguyen, R.-E. Lee, H. Lee, J. H. Jeong, *Bull. Korean Chem. Soc.* **2009**, *30*, 257–260.

[37] Y. K. Kang, J. H. Jeong, N. Y. Lee, Y. T. Lee, H. Lee, *Polyhedron* **2010**, *29*, 2404–2408.

[38] B. Calvo, M. G. Davidson, D. García-Vivó, *Inorg. Chem.* **2011**, *50*, 3589–3595.

[39] J. Börner, U. Flörke, A. Döring, D. Kuckling, M. D. Jones, S. Herres-Pawlis, *Sustainability* **2009**, *1*, 1226–1239.

[40] M. G. Cushion, P. Mountford, *Chem. Commun.* **2011**, *47*, 2276–2278.

[41] B. M. Chamberlain, M. Cheng, D. R. Moore, T. M. Ovitt, E. B. Lobkovsky, G. W. Coates, *J. Am. Chem. Soc.* **2001**, *123*, 3229–3238.

[42] a) A. Neuba, S. Herres-Pawlis, O. Seewald, J. Börner, A. J. Heuwing, U. Flörke, G. Henkel, *Z. Anorg. Allg. Chem.* **2010**, *636*, 2641–2649; b) S. Herres-Pawlis, U. Flörke, G. Henkel, *Eur. J. Inorg. Chem.* **2005**, 3815–3824.

[43] a) N. Schulenberg, S. Litters, E. Kaifer, H.-J. Himmel, *Eur. J. Inorg. Chem.* **2011**, 2657–2661; b) D. Domide, C. Neuhäuser, E. Kaifer, H. Wadepohl, H.-J. Himmel, *Eur. J. Inorg. Chem.* **2009**, 2170–2178; c) A. Maronna, E. Bindewald, E. Kaifer, H. Wadepohl, H.-J. Himmel, *Eur. J. Inorg. Chem.* **2011**, 1302–1314; d) P. Roquette, A. Maronna, M. Reinmuth, E. Kaifer, M. Enders, H.-J. Himmel, *Inorg. Chem.* **2011**, *50*, 1942–1955; e) M. Reinmuth, U. Wild, D. Rudolf, E. Kaifer, M. Enders, H. Wadepohl, H.-J. Himmel, *Eur. J. Inorg. Chem.* **2009**, 4795–4808; f) B. Oelkers, J. Sundermeyer, *Green Chem.* **2011**, *13*, 608–618; g) H. Wittmann, V. Raab, V. Schorm, J. Plackmeyer, J. Sundermeyer, *Eur. J. Inorg. Chem.* **2001**, 1937–1948; h) V. Raab, K. Harms, J. Sundermeyer, B. Kovacevic, Z. B. Maksic, *J. Org. Chem.* **2003**, *68*, 8790–8797; i) A. G. Trambitas, J. Yang, D. Melcher, C. G. Daniliuc, P. G. Jones, Z. Xie, M. Tamm, *Organometallics* **2011**, *30*, 1122–1129; j) A. G. Trambitas, T. K. Panda, J. Jenter, P. W. Roesky, C. Daniliuc, C. G. Hrib, P. G. Jones, M. Tamm, *Inorg. Chem.* **2010**, *49*, 2435–2446; k) T. Glöge, D. Petrovic, C. Hrib, P. G. Jones, M. Tamm, *Eur. J. Inorg. Chem.* **2009**, 4538–4546.

[44] a) P. J. Bailey, S. Pace, *Coord. Chem. Rev.* **2001**, *214*, 91–141; b) M. P. Coles, *Dalton Trans.* **2006**, 985–1001; c) J. Sundermeyer, V. Raab, E. Gaoutchenova, U. Garrelts, N. Abicilar, K. Harms in *The Chemistry of Superbasic Guanidines in Activating Unreactive Substrates: The Role of Secondary Interactions* (Eds.: C. Bolm, E. F. Hahn), Wiley-VCH, Weinheim **2009**; d) T. Ishikawa in *Superbases for Organic Synthesis: Guanidines, Amidines, Phosphazenes and Related Organocatalysts*, Wiley, Wiltshire, **2009**; e) O. Bienemann, A. Hoffmann, S. Herres-Pawlis, *Rev. Inorg. Chem.* **2011**, *31*, 83–108; f) D. Petrovic, L. M. R. Hill, P. G. Jones, W. B. Tolman, M. Tamm, *Dalton Trans.* **2008**, 887–894; g) M. Tamm, D. Petrovic, S. Randoll, S. Beer, T. Bannenberg, P. G. Jones, J. Grunenberg, *Org. Biomol. Chem.* **2007**, *5*, 523–530; h) D. Petrovic, T. Bannenberg, S. Randoll, P. G. Jones, M. Tamm, *Dalton Trans.* **2007**, 2812–2822; i) T. Glöge, D. Petrovic, C. G. Hrib, C. Daniliuc, E. Herdtweck, P. G. Jones, M. Tamm, *Z. Anorg. Allg. Chem.* **2010**, *636*, 2303–2308; j) S.-A. Filimon, C. G. Hrib, S. Randoll, I. Neda, P. G. Jones, M. Tamm, *Z. Anorg. Allg. Chem.* **2010**, *636*, 691–699; k) V. Raab, J. Kipke, O. Burghaus, J. Sundermeyer, *Inorg. Chem.* **2001**, *40*, 6964–6971; l) M. Schatz, V. Raab, S. P. Foxon, G. Brehm, S. Schneider, M. Reiher, M. C. Holthausen, J. Sundermeyer, S. Schindler, *Angew. Chem.* **2004**, *116*, 4460–4464; *Angew. Chem. Int. Ed.* **2004**, *43*, 4360–4363; m) C. Würtele, E. Gaoutchenova, K. Harms, M. C. Holthausen, J. Sundermeyer, S. Schindler, *Angew. Chem.* **2006**, *118*, 3951–3954; *Angew. Chem. Int. Ed.* **2006**, *45*, 3867–3869; n) D. Maiti, D.-H. Lee, K. Gaoutchenova, C. Würtele, M. C. Holthausen, A. A. Narducci Sarjeant, J. Sundermeyer, S. Schindler, K. D. Karlin, *Angew. Chem.* **2008**, *120*, 88–91; *Angew. Chem. Int. Ed.* **2008**, *47*, 82–85.

[45] J. Börner, S. Herres-Pawlis, U. Flörke, K. Huber, *Eur. J. Inorg. Chem.* **2007**, 5645–5651.

[46] J. Börner, U. Flörke, T. Glöge, T. Bannenberg, M. Tamm, M. D. Jones, A. Döring, D. Kuckling, S. Herres-Pawlis, *J. Mol. Catal. A* **2010**, *316*, 139–145.

[47] J. Börner, U. Flörke, K. Huber, A. Döring, D. Kuckling, S. Herres-Pawlis, *Chem. Eur. J.* **2009**, *15*, 2362–2376.

[48] J. Börner, I. dos Santos Vieira, M. D. Jones, A. Döring, D. Kuckling, U. Flörke, S. Herres-Pawlis, *Eur. J. Inorg. Chem.* **2011**, 4441–4456.

[49] J. Börner, U. Flörke, A. Döring, D. Kuckling, S. Herres-Pawlis, *Macromol. Symp.* **2010**, *296*, 354–365.

[50] a) J. Börner, I. dos Santos Vieira, U. Flörke, A. Döring, D. Kuckling, S. Herres-Pawlis in *Renewable and Sustainable Polymers*, American Chemical Society, Division of Polymer Chemistry (Eds.: G. F. Payne, P. B. Smith), Oxford University Press, Washington, DC, **2011**, pp. 169–200; b) J. Börner, I. dos Santos Vieira, U. Flörke, A. Döring, D. Kuckling, S. Herres-Pawlis, *Polym. Prepr.* **2010**, *51*, 743–744.

[51] A. Hoffmann, J. Börner, U. Flörke, S. Herres-Pawlis, *Inorg. Chim. Acta* **2009**, *362*, 1185–1193.

[52] J. Börner, I. dos Santos Vieira, A. Pawlis, A. Döring, D. Kuckling, S. Herres-Pawlis, *Chem. Eur. J.* **2011**, *17*, 4507–4512.

[53] A. F. Douglas, B. O. Patrick, P. Mehrkhodavandi, *Angew. Chem.* **2008**, *120*, 2322–2325; *Angew. Chem. Int. Ed.* **2008**, *47*, 2290–2293.

[54] a) M. Ryner, K. Stridsberg, A.-C. Albertsson, M. von Schenck, M. Svensson, *Macromolecules* **2001**, *34*, 3877–3881; b) H. von Schenck, M. Ryner, A.-C. Albertsson, M. Svensson, *Macromolecules* **2002**, *35*, 1556–1562; c) E. L. Marshall, V. C. Gibson, H. S. Rzepa, *J. Am. Chem. Soc.* **2005**, *127*, 6048–6051; d) A. P. Dove, V. C. Gibson, E. L. Marshall, H. S. Rzepa, A. J. P. White, D. J. Williams, *J. Am. Chem. Soc.* **2006**, *128*, 9834–9843; e) J. Ling, J. Shen, T. E. Hogen-Esch, *Polymer* **2009**, *50*, 3575–3581.

[55] a) S. D. Bull, M. G. Davidson, A. L. Johnson, D. E. J. E. Robinson, M. F. Mahon, *Chem. Commun.* **2003**, 1750–1751; b) M. G. Davidson, C. T. O'Hara, M. D. Jones, C. G. Keir, M. F. Mahon, G. Kociok-Köhn, *Inorg. Chem.* **2007**, *46*, 7686–7688; c) A. J. Chmura, D. M. Cousins, M. G. Davidson, M. D. Jones, M. D. Lunn, M. F. Mahon, *Dalton Trans.* **2008**, 1437–1443; d) M. D. Jones, M. G. Davidson, G. Kociok-Köhn, *Polyhedron* **2010**, *29*, 697–700.

Generation of an Organotellurium(II) Cation

Koh Sugamata,[a] Takahiro Sasamori,*[a] and Norihiro Tokitoh*[a]

We expected that the chemical trapping products of low-coordinated tellurenyl cation species can also be kinetically stabilized by the Tbt or Bbt group. Recently, we have reported the halogenation reactions of Bbt-substituted ditelluride, BbtTeTeBbt, leading to the formation of the Te^{II}–Te^{IV} mixed-valent tellurenyl fluoride, BbtTeTe(F)$_2$Bbt, and tellurenyl halides, BbtTeX (X = Cl, Br, I). During the dehalogen-

ation reactions of these tellurium halides, it is rational to postulate the formation of a tellurenyl cation species as an intermediate. In this paper, we report the successful trapping of tellurenyl cation species with butadienes or triphenylphosphane, and the regeneration of the tellurenyl cation species by thermal retro [1+4] cycloaddition of the diene adducts.

Introduction

A number of studies on sulfur(II) cations, RS$^+$, have been reported, and they have raised interest in many research fields.[1] Although analogous species of selenium(II) and tellurium(II) cations have also attracted much attention, only a few examples are known, because they are difficult to isolate as a result of their intrinsic high reactivity.[2] Thus, only a few chalcogen(II) cationic species have been structurally characterized to date.[3] The tellurium(II) cation, [2,6-(Me$_2$NCH$_2$)$_2$C$_6$H$_3$Te]$^+$ PF$_6^-$, was stabilized by intramolecular coordination of the N atom, though no structural details were disclosed.[4] Recently, by applying the (N,C,N) "pincer" ligand, Silvestru and co-workers have succeeded in the first isolation of tellurium(II) cation species as stable crystals.[5]

On the other hand, methyl or 4-fluorophenyl-substituted ditelluride was reported to be oxidized by nitrosonium salts, giving the corresponding transient tellurium(II) cation species.[6] The generation of the tellurium(II) cationic species was confirmed only by the isolation of the corresponding phosphane adduct. In recent studies, there are two remarkable reports on the trapping reaction of tellurium(II) cation species, where synthesis of aryltellurium(II) cations stabilized by the coordination of NHC (Scheme 4)[7] and the [1+2] adducts of tellurium(II) cations with alkynes[8] were reported by the Beckmann and Seppelt groups, respectively. Meanwhile, we have succeeded in the first chemical trapping of a stibinidene (R–Sb:), which exhibits a structure that is isoelectronic to that of a tellurium(II) cation, by tak-

ing advantage of a bulky aryl substituent, Tbt, or Bbt group.[9,10] Accordingly, we expected that the chemical trapping products of low-coordinated tellurium(II) cation species can be kinetically stabilized by the Tbt or Bbt group. Recently, we have reported the halogenation reactions of Bbt-substituted ditelluride, BbtTeTeBbt, leading to the formation of the mixed-valent ditelluride difluoride, BbtTeTe(F)$_2$Bbt (**2**) and tellurium(II) halides, BbtTeX (**3**, X = Br, **4**, X = I).[11] It is rational to postulate the formation of tellurium(II) cation species **1** as an intermediate during the dehalogenation reactions of **2**–**4**. In this paper, we present the successful trapping of tellurium(II) cation species **1**$^+$ with butadienes or triphenylphosphane and the regeneration of **1**$^+$ by thermal retro [1+4] cycloaddition of the diene adducts.

Results and Discussion

BbtTeTe(F)$_2$Bbt (**2**) was treated with 2 equiv. of TMSOTf or TMSNTf$_2$ in the presence of isoprene or 2,3-dimethyl-1,3-butadiene in hexane at –40 °C for 1 h. The color changed from dark-red to colorless, and then a colorless solid precipitated. The crude product was recrystallized from CH$_2$Cl$_2$/hexane. As a result, the corresponding diene adducts **5**, **6**, and **8** were obtained in yields of 70, 88, and 77%, respectively. On the other hand, the reaction of BbtTeI (**4**) with AgBF$_4$ in the presence of 2,3-dimethyl-1,3-butadiene afforded diene adduct **7** (71%, Scheme 1). The debromination reaction of **3** with AgOTf in the presence of 2,3-dimethyl-1,3-butadiene (Scheme 2) also afforded cycloadduct **6** (66%), which is identical with the product obtained from **2**. Thus, the formation of [1+4] adducts **5**–**8** is most likely to have proceeded through an intermediate tellurium(II) cation species generated by the dehalogenation reactions of **2** and **3**.

[a] Institute for Chemical Research, Kyoto University
Gokasho, Uji, Kyoto 611-0011, Japan
Fax: +81-774-38-3209
E-mail: sasamori@boc.kuicr.kyoto-u.ac.jp
tokitoh@boc.kuicr.kyoto-u.ac.jp
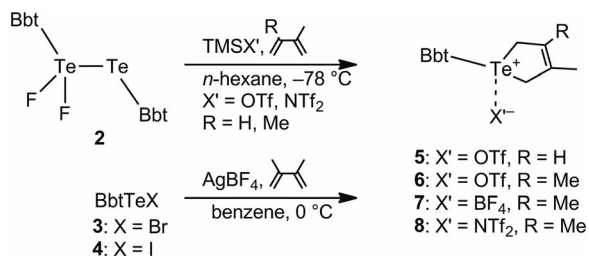
Scheme 1. Synthesis of diene adducts **5**–**8**.
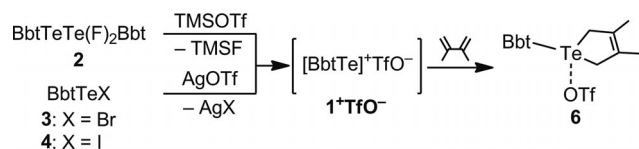
Scheme 2.

On the other hand, the reaction of **2** with TMSOTf or TMSNTf$_2$ in the presence of triphenylphosphane gave the corresponding phosphane adducts **9** and **11** as yellow solids in yields of 67% and 54%, respectively. The reaction of BbtTeBr (**3**) with AgBF$_4$ in the presence of triphenylphosphane afforded phosphane adduct **10** (67%, Scheme 3). Since the blank experiments of the treatment of tellurium(II) halides **2** and **3** with dienes and phosphanes in the absence of TMSOTf or Ag$^+$ salt resulted in no reactions, the formation of phosphane adducts **9**, **10**, and **11** from **2** mentioned above strongly suggest the generation of **1**$^+$ species.
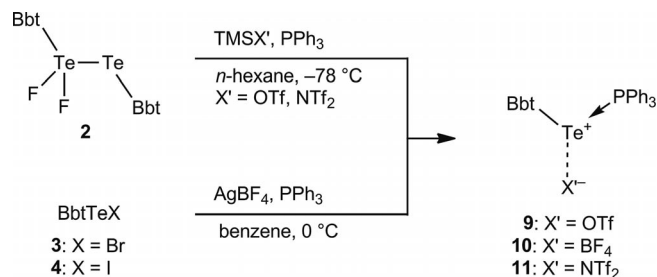
Scheme 3. Synthesis of phosphane adducts **9**–**11**.

The molecular structures of **5**–**11** were unambiguously determined by X-ray crystallographic analysis.[12] The molecular structures of **6** and **9** are shown in Figures 1 and 2. All cycloadducts exhibit pseudo-trigonal-bipyramidal geometry as hypervalent species.[13] The phosphane adducts **9**–**11** exhibit T-shaped structures, slightly distorted for steric reasons [as can be seen in compound **9**; C–Te–P 103.25(8)°, Te–P–O 76.91(5)°]. The P–Te–O angle in **9** is almost linear [174.95(9)°]. These remarkable structural parameters are

similar to those of PPh$_3$Te(Ph)I.[14] There are weak interactions between Te$^+$ and counterion. It was found that the interactions increase in the order TfO$^-$ > BF$_4^-$ > NTf$_2^-$ on the basis of the observed Te$^+$···counterion distances (Table 1), and there seems to be almost negligible interaction between NTf$^-$ and Te$^+$ in **11**. The Te$^+$···anion distances of carbene adducts **12** and **13** (Scheme 4) are 3.270(4) (Te···Cl) and 3.651(6) Å (Te···I), which are shorter than the sums of the van der Waals radii, 3.81 and 4.04 Å, respectively. In contrast, the Te···O distance in **11** is 3.605(3) Å, which is longer than the sum of the van der Waals radii (3.60 Å). However, the phosphane adduct PhTe(PPh$_3$)I contains a rather covalent Te–I bond [3.0930(9) Å].
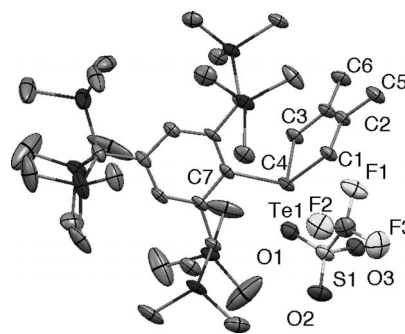
Figure 1. Molecular structure of **6** with thermal ellipsoids set at 50% probability. Hydrogen atoms are omitted for clarity.
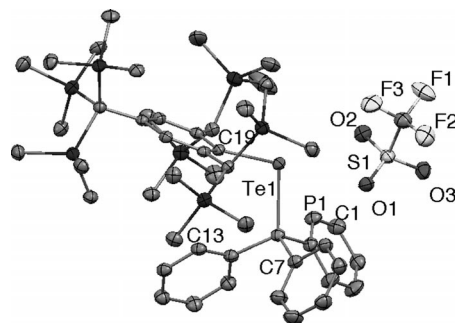
Figure 2. Molecular structure of **9** with thermal ellipsoids set at 50% probability. Hydrogen atoms are omitted for clarity.

The ^{125}Te NMR chemical shifts of telluronium compounds **5**–**11** in CDCl$_3$ are shown in Table 1. The signals for the diene adducts, excluding compound **5**, appeared at around 600 ppm, while those of the phosphane adducts were observed at around 465 ppm.[15] No reason can be offered for the observed signal of compound **5** at 713 ppm. These results indicate that the central Te^{IV} moieties of diene adducts **6**–**8** would be slightly affected by the counteranion depending on the distance, and the electronic effects of the

Table 1. Some structural parameters and ^{125}Te NMR chemical shifts for compounds **5**–**11**.

|	5	6	7	8	9	10	11
Te–anion distance [Å]	2.916(9)	2.894(5)	2.955(8)	2.988(5)	3.072(2)	3.189(3)	3.605(3)
Sum of the van der Waals radii[16] [Å]	Te–O: 3.60	Te–O: 3.60	Te–F: 3.24	Te–O: 3.60	Te–O: 3.60	Te–F: 3.24	Te–O: 3.60
^{125}Te NMR chemical shifts [ppm]	713	613	607	593	464	463	465
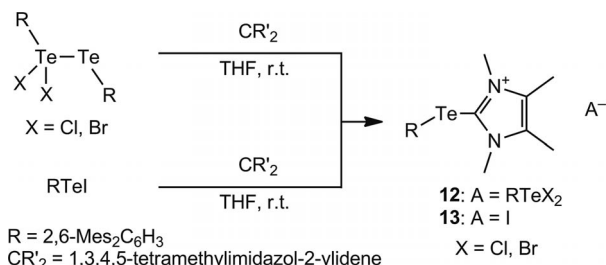
Scheme 4. Reported carbene adducts of aryltellurium(II) cations **12** and **13**.

counteranion toward those of phosphane adducts **9**–**11** would be negligible.

Thermolysis of **5** in [D$_6$]benzene in the presence of an excess amount of 2,3-dimethyl-1,3-butadiene (120 °C for 1 h in a sealed tube) afforded the corresponding diene-exchanged product **6** quantitatively. Moreover, **6** was heated in the presence of 10 equiv. of triphenylphosphane in [D$_6$]-benzene to give phosphane adduct **9** quantitatively. These results can be most likely interpreted in terms of the intermediacy of the tellurium(II) cations (**1$^+$** [TfO]$^-$) in the thermal retrocycloaddition of the diene adduct **6** (Scheme 5). Thermolysis of **6** in the absence of a trapping reagent under the same conditions resulted in the formation of a red solution containing a sole product, compound X. Although compound X would be the expected species **1$^+$**[OTf]$^-$, it has not been identified yet because it was difficult to perform detailed spectroscopic analysis of the product due to its extreme instability even in an inert atmosphere, giving BbtTe-TeBbt.
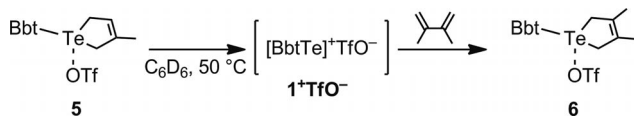
Scheme 5. Thermolysis of diene adduct **5**.

Further investigation on the synthesis and isolation of tellurium(II) cations with a new bulky ligand is currently in progress.

Experimental Section

Compounds 5, 6, and 8: To a hexane solution (10 mL for **5**, 5 mL for **6**, **8**) of BbtTeTe(F)$_2$Bbt (**2**) (100 mg, 64.8 µmol for **5**, 50.0 mg, 32.4 µmol for **6**, **8**) in the presence of an excess amount of 2,3-dimethyl-1,3-butadiene (0.5 mL) was added trimethylsilyl trifluoromethansulfonate (23.4 mL, 12.3 µmol for **5** 11.7 µL, 64.8 µmol for **6**) or N-trimethylsilyl bis(trifluoromethanesufonyl)imide (14.9 µL, 64.8 µmol for **8**), and the reaction mixture was stirred for 1 h at –78 °C. The mixture was then warmed up to room temperature. The colorless precipitates were washed with hexane and dried in vacuo. Analytically pure samples were obtained by crystallization from CH$_2$Cl$_2$/hexane. Yields: 70% (87.7 mg, 90.5 µmol) for **5**, 88% (56.0 mg, 57.0 µmol) for **6**, and 77% (55.7 mg, 50.0 µmol) for **8**.

Compound 7: To a benzene (10 mL) solution of BbtTeI (100 mg, 11.4 µmol) in the presence of an excess amount of 2,3-dimethyl-1,3-buadiene (0.5 mL) was added AgBF$_4$ (22.1 mg, 11.4 µmol) in

benzene (5 mL), and the mixture was stirred for 1 h at 0 °C. The mixture was then warmed up to room temperature. The resulting white precipitate was filtered and recrystallized from toluene at –40 C to afford a colorless solid. Yield: 71% (74.5 mg, 80.9 µmol).

Compounds 9 and 11: To a hexane (10 mL) solution of BbtTeTe-(F$_2$)Bbt (**2**) (50 mg, 32.4 µmol) in the presence of triphenylphosphane (15.0 mg, 48.6 µmol, 1.5 equiv.) was added trimethylsilyl trifluoromethansulfonate (11.7 µL, 64.8 µmol for **9**) or N-trimethylsilyl bis(trifluoromethanesufonyl)imide (14.9 µL, 64.8 µmol for **11**), and the mixture was stirred for 1 h at –78 °C. The mixture was then warmed up to room temperature. Filtration of the reaction mixture followed by purification with gel permeation liquid chromatography afforded the phosphane adducts. Analytically pure samples were obtained by crystallization from CH$_2$Cl$_2$/hexane for **9**, toluene for **11**. Yields: 67% (50.5 mg, 43.4 µmol) for **9** and 54% (45.5 mg, 0.0351 mmol) for **11**.

Compound 10: To a benzene (10 mL) solution of BbtTeBr (50 mg, 60.0 µmol) in the presence of PPh$_3$ (23.6 mg, 90.0 µmol) was added AgBF$_4$ (11.7 mg, 60.0 µmol) in benzene (5 mL), and the mixture was stirred for 1 h at 0 °C. The mixture was then warmed up to room temperature. Filtration of the reaction mixture followed by purification with gel permeation liquid chromatography afforded the crude product. An analytically pure sample of **10** was obtained by crystallization from CH$_2$Cl$_2$/hexane. Yield: 67% (44.2 mg, 40.1 µmol).

Supporting Information (see footnote on the first page of this article): General procedures, analytical data, and X-ray diffraction studies for compounds **5**–**11**.

Acknowledgments

[1] a) R. E. Benesch, R. Benesch, *J. Am. Chem. Soc.* **1958**, *80*, 1666; b) J. M. Bolster, H. Hogeveen, R. M. Kellogg, L. Zwart, *J. Am. Chem. Soc.* **1981**, *103*, 3955–3956; c) Q. T. Do, D. El-othmani, G. Le Guillanton, *Tetrahedron Lett.* **1998**, *39*, 4657–4658; d) E. D. Edstrom, T. Livinghouse, *J. Am. Chem. Soc.* **1986**, *108*, 1334–1336; e) J. L. Ginsburg, R. F. Langler, *Can. J. Chem.* **1983**, *61*, 589; f) M. Gressenbuch, B. Kersting, *Z. Anorg. Allg. Chem.* **2010**, *636*, 1435; g) S. R. Harring, T. Livinghouse, *Tetrahedron Lett.* **1989**, *30*, 1499; h) O. Neunhoeffer, A. Nowak, *Naturwissenschaften* **1958**, *45*, 491.

[2] a) S. E. Denmark, W. R. Collins, M. D. Cullen, *J. Am. Chem. Soc.* **2009**, *131*, 3490; b) G. H. Schmid, D. G. Garratt, *Tetrahedron Lett.* **1975**, *16*, 3991; c) S. Tamagaki, I. Hatanaka, *Chem. Lett.* **1976**, 301; d) T. Yamada, E. Mishima, K. Ueki, S. Yamago, *Chem. Lett.* **2008**, *37*, 650; e) C. G. Hrib, J. Jeske, P. G. Jones, W.-W. du Mont, *Dalton Trans.* **2007**, 3483; f) J. Jeske, W.-W. du Mont, F. Ruthe, P. G. Jones, L. M. Mercuri, P. Deplano, *Eur. J. Inorg. Chem.* **2000**, 1591.

[3] a) K. Kobayashi, S. Sato, E. Horn, N. Furukawa, *Tetrahedron Lett.* **1998**, *39*, 2593; b) V. P. Singh, H. B. Singh, R. J. Butcher, *Eur. J. Inorg. Chem.* **2010**, 637.

[4] H. Fujihara, H. Mima, N. Furukawa, *J. Am. Chem. Soc.* **1995**, *117*, 10153.

[5] A. Beleaga, V. R. Bojan, A. Pollnitz, C. I. Rat, C. Silvestru, *Dalton Trans.* **2011**, *40*, 8830.

[6] C. Kollemann, F. Sladky, *J. Organomet. Chem.* **1990**, *396*, C1.

[7] J. Beckmann, P. Finke, S. Heitz, M. Hesse, *Eur. J. Inorg. Chem.* **2008**, 1921.

[8] H. Poleschner, K. Seppelt, *Angew. Chem.* **2008**, *120*, 6561; *Angew. Chem. Int. Ed.* **2008**, *47*, 6461.

[9] a) T. Sasamori, Y. Arai, N. Takeda, R. Okazaki, Y. Furukawa, M. Kimura, S. Nagase, N. Tokitoh, *Bull. Chem. Soc. Jpn.* **2002**, *75*, 661; b) T. Sasamori, Y. Arai, N. Takeda, R. Okazaki, N. Tokitoh, *Chem. Lett.* **2001**, 42.

[10] Tbt = 2,4,6-tris[bis(trimethylsilyl)methyl]phenyl, Bbt = 2,6-bis[bis(trimethylsilyl)methyl]-4-[tris(trimethylsilyl)methyl]-phenyl.

[11] a) T. Sasamori, K. Sugamata, N. Tokitoh, *Heteroat. Chem.* **2011**, *22*, 405; b) K. Sugamata, T. Sasamori, N. Tokitoh, *Chem. Asian J.* **2011**, *6*, 2301.

[12] CCDC-851389 (for **5**), -851390 (for **6**), -851391 (for **7**), -851392 (for **8**), -851393 (for **9**), -851394 (for **10**), and -851395 (for **11**) contain the supplementary crystallographic data for this paper. These data can be obtained free of charge from The Cambridge Crystallographic Data Centre via www.ccdc.cam.ac.uk/data_request/cif.

[13] K.-y. Akiba (Ed.), *Chemistry of Hypervalent Compounds*, Wiley-VCH, Weinheim, **1999**.

[14] P. D. Boyle, W. I. Cross, S. M. Godfrey, C. A. McAuliffe, R. G. Pritchard, S. Sarwar, J. M. Sheffield, *Angew. Chem.* **2000**, *112*, 1866; *Angew. Chem. Int. Ed.* **2000**, *39*, 1796.

[15] In general, ^{125}Te NMR chemical shifts of telluronium salts, R_3Te^+, span a range from 400 to 700 ppm with respect to Me_2Te. Z. L. Zhou, Y. Z. Huang, Y. Tang, Z. H. Chen, L. P. Shi, X. L. Jin, Q. C. Yang, *Organometallics* **1994**, *13*, 1575.

[16] S. S. Batsanov, *Inorg. Mater.* **2001**, *37*, 871.

A New Type of Lanthanide Complex – Two Divalent Ytterbium Species Assembled from Cation–π Interactions

Cheng-Ling Pan,*[a,b] Shao-Ding Sheng,[a] Chang-Min Hou,[b] Yu-Song Pan,[a] Jing Wang,[a] and Yong Fan*[b]

A new divalent ytterbium complex, [{(L^{Ph})Yb^{II}(Et$_2$O)(thf)}$_2$(μ-KI)] {L^{Ph} = Ph$_2$Si(NAr)$_2$, Ar = 2,6-iPr$_2$C$_6$H$_3$} (**3**), was synthesized by the reaction of [(L^{Ph})Yb^{III}I(thf)$_2$] (**2**) and an excess of potassium. The bimetallic ytterbium(II) species with bulky diamido ligands are bridged by a KI molecule with cation–π interactions. These two complexes have been fully characterized, particularly by X-ray crystallography.

Introduction

Ever since Kagan's report on SmI$_2$, the chemistry of lanthanide complexes has been increasingly attractive. However, the chemistry of divalent lanthanide complexes is largely limited, because of destabilizing factors.[1] For a long time, the coordination chemistry of divalent lanthanide ions has been limited to that of the classical three elements Eu^{2+}, Yb^{2+}, and Sm^{2+}.[2] These Ln^{2+} ions have the configuration of 6s^{0}5d^{0}4f^n, with n = 6 (Sm), 7 (Eu), and 14 (Yb). The reduction potentials for the trivalent ions Ln^{3+} + e$^-$ = Ln^{2+} are Eu^{3+}/Eu^{2+} (–0.35 V), Yb^{3+}/Yb^{2+} (–1.15 V), and Sm^{3+}/Sm^{2+} (–1.55 V), similar to those of one-electron reducing agents in organic and inorganic synthesis.[3] In contrast, the reduction potential for potassium is much more negative [K/K$^+$ (–2.92 V)].[4] Therefore, with a properly useful ligand, we should be able to stabilize these ions with oxidation state +2 in solution by alkali metal reduction of their trivalent precursors. However, the synthesis of a wide variety of low-valent lanthanide complexes with N,N'-ligands remains sparsely studied.[5]

The accessibility and applications of divalent lanthanide complexes can potentially be significantly broadened if they can be readily prepared.[6–9] In addition to the success in their synthesis, it is still important to explore alternative ligands that are able to satisfy the coordination requirements of relatively large lanthanide cations.[10,11] In contrast to the popular cyclopentadienyl (Cp) ligands, relatively little effort has been devoted to Cp-free ligands.[12] The lanthanide chemistry of complexes with simple amido ligands is limited primarily to an amido ligand, namely N(SiMe$_3$)$_2$.[13,14] In this respect, it is noteworthy that the stabilizing properties of L^{Ph} [L^{Ph} = Ph$_2$Si(NAr)$_2$, Ar = 2,6-iPr$_2$C$_6$H$_3$] appear to be similar to those of bulky, N,N'-chelating β-diketiminates [{(R^1)NC(R^2)}$_2$C(R^3)]$^-$ (nacnac$^-$)[15,16] and guanidinate ligands [(ArN)$_2$CN(C$_6$H$_{11}$)$_2$]$^-$ (Giso$^-$),[17] which have been utilized in the preparation and characterization of homoleptic four-coordinate Ln^{2+} complexes.

In our previous work, we obtained planar four-coordinate Ln^{II} diamido complexes [(L^{Ph})$_2$Ln{K(solv.)$_x$}$_2$] (Ln = Sm, Yb, and Eu), which represent the first example of lanthanides bearing heteroleptic sandwich structures.[18–19] These results inspired us to extend the coordination chemistry of bulky diamido ligands to ytterbium(II) by taking advantage of related synthetic routes and cation–π interactions. We have explored the coordination of amido ligand H$_2$(L^{Ph})[20] [L^{Ph} = Ph$_2$Si(NAr)$_2$, Ar = 2,6-iPr$_2$C$_6$H$_3$] (**1**) to stabilize the ytterbium(II) complex, [{(L^{Ph})Yb^{II}(thf)(Et$_2$O)}$_2$(μ-KI)] (**3**), by the reaction of [(L^{Ph})Yb^{III}I(thf)$_2$] (**2**)
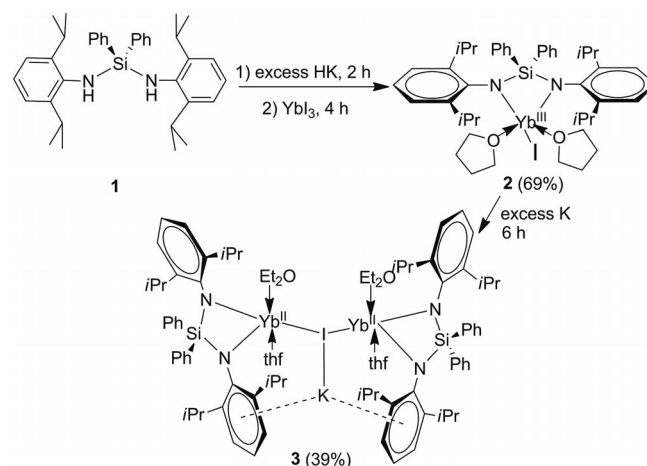
Scheme 1.

[a] School of Materials Science and Engineering, Anhui University of Science and Technology,
Huainan 232001, Anhui, P. R. China
E-mail: chengling_pan@126.com
[b] State Key Laboratory of Inorganic Synthesis and Preparative Chemistry, College of Chemistry, Jilin University,
Changchun 130012, P. R. China
E-mail: mrfy@jlu.edu.cn

and an excess of potassium, as illustrated in Scheme 1. Herein, we report the synthesis and structural studies of these complexes. To the best of our knowledge, ytterbium(II) dimer complexes of amido ligands assembled from cation–π interactions are rare in lanthanide chemistry.

Results and Discussion

The use of a dry-box and access to single crystals for X-ray diffraction techniques made it possible to safely handle and characterize these complexes. The crystal structure of **2** shows that the five-coordinate ytterbium center is coordinated by a chelating diamido ligand, two thf molecules, and an iodine atom, forming a distorted square-pyramidal geometry. The N1, N2, O1, and O2 atoms form the basal plane, whilst the I1 occupies the apical position, as shown in Figure 1. The Yb1–N1, Yb1–N2, Yb1–O1, and Yb1–O2 bond lengths are 2.165(2), 2.179(2), 2.319(2), and 2.339(2) Å, respectively. The Yb1–I1 bond length is 2.9151 Å. However, the Yb^{II}–N bond lengths of similar complex $[(L^{Ph})Yb^{II}(thf)_3]$ in our previous work fall within the range 2.346(4)–2.394(4) Å.[18] The observed Yb^{III}–N bond lengths of **2** are obviously shorter than the corresponding bond lengths of the ytterbium(II) complex, probably because of the smaller ionic radius of Yb^{III} as compared to Yb^{II}. As a result of the paramagnetic nature of **2**, well-resolved NMR spectra could not be obtained for the trivalent ytterbium(III) complex.

bly influence the structure of the usually formed mononuclear or X-bridged dinuclear complexes "[Cp_2Ln-$(\mu$-X)$]_2$".[22] However, there is a growing interest in synthetic applications of σ-bonded organolanthanide complexes of composition R_2LnX (Ln = Sm, Eu, Yb; X = Cl, Br, I).[23]

X-ray crystallographic results indicated that complex **3** contains two ytterbium(II) units bridged by a KI molecule, as shown in Figure 2. The L^{Ph} ligands coordinate in a chelating fashion [Yb1–N1 2.322(6) Å, Yb1–N2 2.345(5) Å, Yb2–N3 2.346(6) Å, and Yb2–N4 2.323(6) Å], these Yb–N distances are apparently longer than those observed in related trivalent ytterbium species {e.g., five-coordinate $[Yb(NHC_6H_3iPr_2-2,6)_3(thf)_2]$ 2.17(2)–2.20(2) Å[12] and complex **2**}. The Yb–O (Et_2O or thf) bond lengths are Yb1–O1 2.411(7) Å, Yb1–O2 2.375(7) Å, Yb2–O3 2.373(8) Å, and Yb2–O4 2.450(9) Å. The KI is just at the center of two ytterbium(II) groups with bond lengths Yb1–I1 3.235(1) Å, Yb2–I1 3.156(1) Å, and K1–I1 3.329(2) Å, and K···C bond lengths range from 2.957(7) to 3.484(10) Å. To the best of our knowledge, there are no previously reported examples of complexes containing a ytterbium(II) dimer assembled from cation–π interactions.
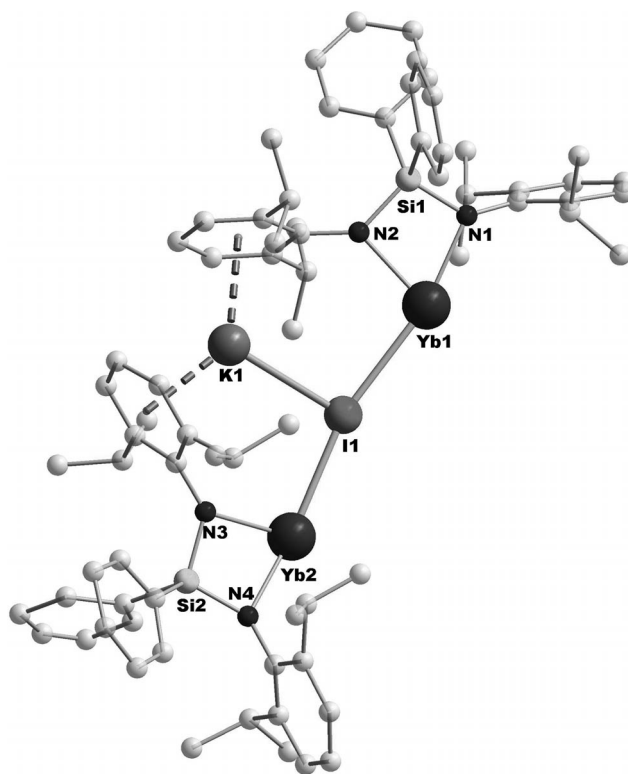
Figure 2. Molecular structure of **3**, hydrogen atoms, Et_2O, and thf molecules, omitted for clarity. Selected bond lengths [Å] and angles [°]: Yb1–N1 2.322(6), Yb1–N2 2.345(5), Yb2–N3 2.346(6), Yb2–N4 2.323(6), Yb1–O1 2.411(7), Yb1–O2 2.375(7), Yb2–O3 2.373(8), Yb2–O4 2.450(9), Yb1–Si1 2.997(2), Yb2–Si2 2.972(2), Yb1–I1 3.235(1), Yb2–I1 3.156(1), I1–K1 3.329(2); N1–Yb1–N2 68.36(19); N4–Yb2–N3 69.2(2).
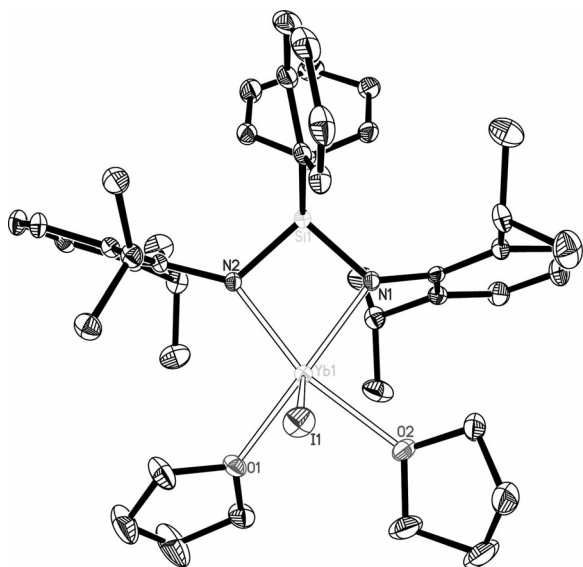

Figure 1. Molecular structure of **2**. POV-RAY illustration, 30% thermal ellipsoids, all hydrogen atoms omitted for clarity. Selected bond lengths [Å] and angles [°]: Yb1–N1 2.165(2), Yb1–N2 2.179(2), Yb1–O1 2.319(2), Yb1–O2 2.339(2), Yb1–I1 2.915(1), Si1–N1 1.722(2), Si1–N2 1.738(2); N1–Yb1–N2 72.65(8).

Bis(cyclopentadienyl) complexes of type "Cp_2LnX", similar to complex **2**, have attracted increased attention, and derivatives of the latter are meanwhile established homogeneous catalysts.[21] Heteroligands X (e.g., H⁻, X⁻) and the presence of neutral donor ligands (e.g., thf, OEt_2) remarka-

The ligand $[Ph_2Si(2,6-iPr_2C_6H_3N)_2]^{2-}$ (L^{Ph}) seems an excellent candidate for the stabilization of divalent lanthanide complexes by means of cation–π interactions.[18,19] Most

Cp-free divalent ytterbium complexes are mononuclear. Gambarotta et al. discovered an octameric macrocyclic structure consisting of eight [Ph$_2$C(C$_4$H$_3$N)$_2$Yb^{II}] units with σ and π bonds and a flat tetrametallic unit with mixed-valent ytterbium.[24] A few years ago, a binuclear ytterbium(II) hydrido complex of a bulky hydrotris(pyrazolyl)-borate ligand was reported.[25] Monoamide and guanidinate ligands with ytterbium(II) atoms were bridged by halogen atoms to form bimetallic complexes.[17,26] Therefore, the use of divalent lanthanide ions for the construction of oligomers is more difficult than the use of d-block metal analogues.[22,27] In complex **3**, the interaction between the alkali metal cation and the π-face of neutral aromatic system is an important binding force, which helps to stabilize the divalent ytterbium metal center. The construction of lanthanide–alkali chains,[28] layers,[29] and wheels[30] with π interactions has been a field of rapid growth, because of the formation of fascinating structures and their potential applications.[31]

Conclusions

We have successfully synthesized the diamido complex of Yb^{II} by the potassium reduction of a new Yb^{III} starting material. This method proved to be efficient in the synthesis of some divalent ytterbium complexes in lanthanide chemistry. Our studies revealed that diamido ligand can be used as a ditopic linker to generate polymetallic complexes by taking advantage of the cation–π interaction. The structural versatility and the novelty of these ytterbium complexes are a starting point for further investigations. The method might be extended to the synthesis of other lanthanide elements. The work is in progress in our laboratory.

Experimental Section

General Procedures: All operations were performed under an inert atmosphere (<5 ppm oxygen or water) in a nitrogen-filled dry-box or by using standard Schlenk techniques. Solvents thf and *n*-hexane were freshly distilled from sodium benzophenone ketyl prior to use. All other chemicals were purchased from either Aldrich or Acros Chemical Co. and were used as received unless otherwise indicated. ^{1}H and ^{13}C NMR spectra were recorded with a Bruker DPX300 spectrometer at 300.13 and 75.47 MHz, respectively.

Syntheses

[(L^{Ph})Yb^{III}I(thf)$_2$] (2): A solution of [Ph$_2$Si(2,6-*i*Pr$_2$C$_6$H$_3$NH)$_2$][20] (0.77 g, 1.5 mmol) in thf (15 mL) was slowly added to a stirred suspension of KH (0.16 g, 4 mmol), and the resulting mixture was stirred for 2 h at room temperature. The yellow solution was then filtered to remove the excess of KH, and then a yellow solution of the potassium amido compound (1.5 mmol) in thf (15 mL) was treated with YbI$_3$ (0.83 g, 1.5 mmol) at room temperature for 4 h. The solvent was removed under reduced pressure, followed by addition of Et$_2$O (40 mL). The Et$_2$O extract of the solid was filtered, reduced to approximately 5 mL, and kept for several days at room temperature, after which single crystals of **2** suitable for X-ray crystallographic studies were obtained to give the title compound **2** as red crystals (69%). C$_{44}$H$_{60}$IN$_2$O$_2$SiYb (977.00): calcd. C 54.09, H 6.19, N 2.87; found C 53.78, H 5.94, N 2.49.

[{(L^{Ph})Yb^{II}(thf)(Et$_2$O)}$_2$(μ-KI)] (3). A thf solution of complex **2** [(L^{Ph})YbI(thf)$_2$] (1.01 g, 1.0 mmol) was stirred with an excess of K (0.06 g, 1.5 mmol) for 6 h at room temperature. The solvent was removed under reduced pressure, followed by addition of Et$_2$O (40 mL). The Et$_2$O extract of the solid was filtered, reduced to approximately 3 mL, and kept for several days at room temperature, after which single crystals of **3** suitable for X-ray crystallographic studies were obtained to give the title compound **3** as deep red crystals (39%). ^{1}H NMR (C$_6$D$_6$, 300 MHz): δ = 7.82 (d, *J* = 4.8 Hz, 4 H, Ar*H*), 7.24–7.05 (m, 10 H, Ar*H*), 6.99 (t, *J* = 7.2 Hz, 2 H, Ar*H*), 3.26–3.54 (m, 8 H, *thf*), 4.33 (sept., *J* = 6.9 Hz, 4 H,

Table 1. Crystal data and structure refinements for complexes **2** and **3**.

Empirical formula	C$_{44}$H$_{60}$IN$_2$O$_2$SiYb	C$_{88}$H$_{124}$IKN$_4$O$_4$Si$_2$Yb$_2$
Formula weight	976.97	1870.17
Temperature [K]	173(2)	173(2)
Crystal system	orthorhombic	orthorhombic
Space group	*Pbca*	*Pbca*
a [Å]	19.9934(6)	23.6218(9)
b [Å]	18.4582(5)	21.3970(7)
c [Å]	23.4780(7)	34.5017(12)
Volume [Å^3]	8664.4(4)	17438.4(11)
Z	8	8
Density (calculated) [Mg m^{-3}]	1.498	1.425
Absorption coefficient [mm^{-1}]	2.935	2.610
F(000)	3928	7616
Crystal size [mm]	0.30 × 0.20 × 0.20	0.28 × 0.23 × 0.19
θ range for data collection	1.73 to 26.07°	1.18 to 26.04°
Reflection collected	46356	94252
Independent reflections	8572 [*R*(int) = 0.0304]	17202 [*R*(int) = 0.0619]
Completeness to θ	θ = 26.07°, 100.0%	θ = 26.04°, 100.0%
Max. and min. transmission	0.5914 and 0.4730	0.6369 and 0.5285
Refinement method	Full-matrix least-squares on *F*^{2}	Full-matrix least-squares on *F*^{2}
Data/restraints/parameters	8572/0/460	17202/47/827
Goodness-of-fit on *F*^{2}	1.044	1.037
Final *R* indices [*I* > 2σ(*I*)]	*R1* = 0.0235, *wR2* = 0.0565	*R1* = 0.0582, *wR2* = 0.1341
R indices (all data)	*R1* = 0.0330, *wR2* = 0.0616	*R1* = 0.0995, *wR2* = 0.1869
Largest diff. peak and hole [e Å^{-3}]	0.733 and –0.496	2.360 and –2.307

CHMe$_2$), 1.25–1.44 (br., 8 H, thf), 1.11 (d, J = 6.9 Hz, 24 H, CHMe_2) ppm. ^{13}C NMR (C$_6$D$_6$, 75.47 MHz): δ = 161.3, 158.2, 149.4, 143.4, 135.8, 126.8, 124.9, 116.4, 69.1, 28.2 [OCH$_2$CH$_2$ (thf)], 25.7, 23.9 (CHMe$_2$) ppm. C$_{80}$H$_{104}$IKN$_4$O$_2$Si$_2$Yb$_2$ (1722.0) (**3** – 2OEt$_2$): calcd. C 55.80, H 6.09, N 3.25; found C 55.59, H 6.14, N 2.99.

X-ray Structure Determination: All single crystals were immersed in Paratone-N oil and sealed under N$_2$ in thin-walled glass capillaries. Data were collected at 173 K with a Bruker SMART II CCD diffractometer by using Mo-K_α radiation. An empirical absorption correction was applied with the SADABS program.[32] All structures were solved by direct methods and subsequent Fourier difference techniques and refined anisotropically for all non-hydrogen atoms by full-matrix least-squares calculations on F^2 by using the SHELXTL program package.[33] Most of the carbon hydrogen atoms were located from difference Fourier syntheses. All other hydrogen atoms were geometrically fixed by using the riding model. Crystal data and details of data collection and structure refinements are given in Table 1.

CCDC-722477 and -722478 contain the supplementary crystallographic data for this paper. These data can be obtained free of charge from The Cambridge Crystallographic Data Centre via www.ccdc.cam.ac.uk/data_request/cif.

Acknowledgments

[1] a) J. L. Namy, H. B. Kagan, *Nouv. J. Chim.* **1977**, *1*, 5–8; b) P. Girard, J. L. Namy, H. B. Kagan, *J. Am. Chem. Soc.* **1980**, *102*, 2693–2698.

[2] W. J. Evans, *J. Organomet. Chem.* **2002**, *647*, 2–11.

[3] a) W. J. Evans, B. L. Davis, *Chem. Rev.* **2002**, *102*, 2119–2136; b) K. C. Nicolaou, S. P. Ellery, J. S. Chen, *Angew. Chem.* **2009**, *121*, 7276; *Angew. Chem. Int. Ed.* **2009**, *48*, 7140–7165.

[4] a) W. J. Evans, D. S. Lee, D. B. Rego, J. M. Perotti, S. A. Kozimor, E. K. Moore, J. W. Ziller, *J. Am. Chem. Soc.* **2004**, *126*, 14574–14582; b) References therein: G. Meyer, *Angew. Chem.* **2008**, *120*, 5040; *Angew. Chem. Int. Ed.* **2008**, *47*, 4962–4964.

[5] a) F. T. Edelmann, *Chem. Soc. Rev.* **2009**, *38*, 2253–2268; b) S. Yao, H.-S. Chen, C.-K. Lam, H.-K. Lee, *Inorg. Chem.* **2009**, *48*, 9936–9946; c) S. Yao, H.-S. Chen, C.-K. Lam, H.-K. Lee, *Inorg. Chem.* **2009**, *48*, 9936; M. L. Cole, P. C. Junk, *Chem. Commun.* **2005**, 2695–2696; d) C.-L. Pan, W. Chen, S. Song, H. Zhang, X. Li, *Inorg. Chem.* **2009**, *48*, 6344–6346.

[6] W. J. Evans, D. K. Drummond, H. Zhang, J. L. Atwood, *Inorg. Chem.* **1988**, *27*, 575–579.

[7] I. Nagl, W. Scherer, M. Tafipolsky, R. Anwander, *Eur. J. Inorg. Chem.* **1999**, 1405–1407.

[8] K. Izod, *Angew. Chem.* **2002**, *114*, 769; *Angew. Chem. Int. Ed.* **2002**, *41*, 743–744.

[9] T. Dubé, M. Ganesan, S. Conoci, S. Gambarotta, G. P. A. Yap, *Organometallics* **2000**, *19*, 3716–3721.

[10] W. J. Evans, *Inorg. Chem.* **2007**, *46*, 3435–3449.

[11] Review: F. T. Edelmann, *Chem. Soc. Rev.* **2009**, *38*, 2253–2268.

[12] References therein: W. J. Evans, M. A. Ansari, J. W. Ziller, *Inorg. Chem.* **1996**, *35*, 5435–5444.

[13] D. C. Bradley, J. S. Ghotra, F. A. Hart, *J. Chem. Soc., Dalton Trans.* **1973**, 1021–1023.

[14] J. S. Ghotra, M. B. Hurthouse, A. J. Welch, *J. Chem. Soc., Chem. Commun.* **1973**, 669–670.

[15] a) S. Harder, *Angew. Chem.* **2004**, *116*, 2768; *Angew. Chem. Int. Ed.* **2004**, *43*, 2714–2718; b) A. G. Avent, P. B. Hitchcock, A. V. Khostov, M. F. Lappert, A. V. Protchenko, *Dalton Trans.* **2003**, 1070–1075.

[16] A related homoleptic ytterbium(II) amidopyridine complex has also been reported; a) S. Qayyum, K. Haberland, C. M. Forsyth, P. C. Junk, G. B. Deacon, R. Kempe, *Eur. J. Inorg. Chem.* **2008**, 557–562; b) N. M. Scott, R. Kempe, *Eur. J. Inorg. Chem.* **2005**, 1319–1324.

[17] a) D. Heitmann, C. Jones, P. C. Junk, K. A. Lippert, A. Stasch, *Dalton Trans.* **2007**, 187–189; b) D. Heitmann, C. Jones, D. P. Mills, A. Stasch, *Dalton Trans.* **2010**, *39*, 1877–1882.

[18] C.-L. Pan, Ph. D. Thesis, The Chinese University of Hong Kong, **2008**.

[19] a) C.-L. Pan, W. Chen, J. Song, *Organometallics* **2011**, *30*, 2252–2260; b) C.-L. Pan, Y.-S. Pan, J. Wang, J. Song, *Dalton Trans.* **2011**, *40*, 6361–6363.

[20] a) M. S. Hill, P. B. Hitchcock, *Organometallics* **2002**, *21*, 3258–3262; b) R. Murugavel, N. Palanismi, R. J. Butcher, *J. Organomet. Chem.* **2003**, *675*, 65–71.

[21] G. M. Sheldrick, *SADABS*: Program for Empirical Absorption Correction of Area Detector Data; University of Göttingen, Göttingen, Germany, **1996**.

[22] G. M. Sheldrick, *SHELXTL 5.10 for Windows NT: Structure Determination Software Programs*; Bruker Analytical X-ray Systems,Inc., Madison, WI, **1997**.

[23] H. Schumann, M. R. Keitsch, J. Winterfield, J. Demtschuk, *J. Organomet. Chem.* **1996**, *525*, 279–281.

[24] References therein: R. Anwander, *Angew. Chem.* **1998**, *110*, 619; *Angew. Chem. Int. Ed.* **1998**, *37*, 599–602.

[25] G. Heckmann, M. Niemeyer, *J. Am. Chem. Soc.* **2000**, *122*, 4227–4228.

[26] D. M. M. Freckmann, T. Dubé, C. D. Bérubé, S. Gambarotta, G. P. A. Yap, *Organometallics* **2002**, *21*, 1240–1246.

[27] G. M. Ferrence, R. McDonald, J. Takats, *Angew. Chem.* **1999**, *111*, 2372; *Angew. Chem. Int. Ed.* **1999**, *38*, 2233–2237.

[28] L. Zhou, J. Wang, Y. Zhong, Y. Yao, Q. Shen, *Inorg. Chem.* **2007**, *46*, 5763–5772.

[29] X.-H. Bu, W. Weng, W. Chen, R.-H. Zhang, *Inorg. Chem.* **2002**, *41*, 413–415.

[30] a) D. L. Clark, G. B. Deacon, T. Feng, R. V. Hollis, B. L. Scott, B. W. Skelton, J. G. Watkin, A. H. White, *Chem. Commun.* **1996**, 1729–1730; b) D. L. Clark, J. G. Watkin, J. C. Huffman, *Inorg. Chem.* **1992**, *31*, 1556–1558; c) D. L. Clark, J. C. Gordon, J. C. Huffman, R. L. Vincent-Hollis, J. G. Watkin, B. D. Zwick, *Inorg. Chem.* **1994**, *33*, 5903–5911; d) D. L. Clark, R. V. Hollis, B. L. Scott, J. G. Watkin, *Inorg. Chem.* **1996**, *35*, 667–674; e) M. R. Bürgstein, P. W. Roesky, *Angew. Chem.* **2000**, *112*, 559; *Angew. Chem. Int. Ed.* **2000**, *39*, 549–551; f) G. B. Deacon, E. E. Delbridge, D. J. Evans, R. Harika, P. C. Junk, B. W. Skelton, A. H. White, *Chem. Eur. J.* **2004**, *10*, 1193–1204.

[31] a) M. R. Bürgstein, M. T. Gamer, P. W. Roesky, *J. Am. Chem. Soc.* **2004**, *126*, 5213–5218; b) J. Wang, M. G. Gardiner, *Chem. Commun.* **2005**, 1589–1591.

[32] a) M. T. Gamer, P. W. Roesky, *Inorg. Chem.* **2005**, *44*, 5963–5965; b) T. Dubé, S. Conoci, S. Gambarotta, G. P. Yap, *Organometallics* **2000**, *19*, 209–211; c) S. Gambarotta, J. Scott, *Angew. Chem.* **2004**, *116*, 5412; *Angew. Chem. Int. Ed.* **2004**, *43*, 5298–5308.

[33] a) O. M. Yaghi, H. Li, C. Davis, D. Richardson, T. L. Groy, *Acc. Chem. Res.* **1998**, *31*, 474–484; b) B. Moulton, M. J. Zaworotko, *Chem. Rev.* **2001**, *101*, 1629–1658.

In Situ X-ray Absorption Spectroscopy/Energy-Dispersive X-ray Diffraction Studies on the Hydrothermal Formation of $Bi_2W_{1-x}Mo_xO_6$ Nanomaterials

Ying Zhou,[a,b] Elena Antonova,[c] Yuanhua Lin,[d] Jan-Dierk Grunwaldt,[e] Wolfgang Bensch,[c] and Greta R. Patzke*[b]

Bi_2WO_6 has attracted considerable interest as a visible-light-driven photocatalyst with a layered Aurivillius structure. The catalytic performance of bismuth tungstate is notably enhanced through the partial substitution of tungsten with molybdenum. Whereas hydrothermally obtained $Bi_2W_{1-x}Mo_xO_6$ solid solutions maintain the Bi_2WO_6 structure, their morphologies vary with the molybdenum content. Lower Mo contents ($x < 0.5$) favor the formation of hierarchically nanostructured microspheres that consist of sheet-like building blocks. Their disintegration is observed for greater extents of W/Mo substitution, hand in hand with a decrease in the surface area. Raman spectra furthermore indicate changes in

the local structure of the octahedral W/Mo moieties upon variation of the Mo content. As little is known about the growth kinetics and hydrothermal formation processes of nanostructured $Bi_2W_{1-x}Mo_xO_6$ catalysts, in situ XAS investigations were performed to determine the onset of their hydrothermal formation from $Bi(NO_3)_3 \cdot 5H_2O$, K_2WO_4 and Na_2MoO_4. In situ energy-dispersive X-ray diffraction (EDXRD) experiments revealed a correlation between particle shape, Mo content and formation pathway of the $Bi_2W_{1-x}Mo_xO_6$ nanomaterials. The results are compared to related in situ studies on hierarchically structured W/Mo oxides.

Introduction

Functional nanostructured oxides are essential building blocks for tomorrow's technological challenges, such as sustainable energy sources and constant access to clean water resources.[1] Photocatalytic nano-oxides play a major role in these developments,[2] and their morphology is a crucial parameter for catalytic efficiency. Therefore, tunable solution syntheses of oxide materials, such as hydro- and solvothermal techniques, attract increasing research interest.[3] Despite constant progress in shaping nanoscale oxides for tailor-made applications, only a small fraction of these systems are understood and accessible on a sound mechanistic basis.[4] The lack of direct insight into hydrothermal and related formation processes renders morphology control in oxide synthesis an ongoing challenge that hinders informed

design. Although an increasing repertoire of combined in situ techniques for monitoring growth processes in solution or various catalytic reactions has been established,[5] only a few of these studies have been devoted to the important materials class of visible-light-driven oxide photocatalysts as alternatives to TiO_2.[6] Bismuth oxide based materials are currently a focus of worldwide photocatalyst research with special emphasis on $BiVO_4$[7] and Aurivillius-type Bi_2WO_6 with a layered structure.[8] Over the past years, we have developed a new way to access hierarchically nanostructured Bi_2WO_6 spheres,[9] and we have monitored their formation pathway with in situ energy-dispersive X-ray diffraction (EDXRD) techniques for the first time.[10] Hierarchical morphologies have been found to be favorable for other bismuth-containing photocatalysts as well, such as for Bi_2O_3,[11] bismuth titanate[12] or BiOCOOH,[13] but their growth mechanisms have all been proposed on the basis of ex situ data and quenched intermediates. Due to the lack of in situ studies, the particle shaping of oxide materials often remains an empirical question of trial and error. Given that doping of binary oxides with additional metal ions is a frequently used performance optimization strategy, achieving morphology control in multi-component systems has become a considerable challenge that needs to be resolved.

Although Bi_2MoO_6 and Bi_2WO_6 have the same Aurivillius structure in common, we have discovered notable differences in the humidity-sensing behaviors of both compounds that are linked to their surface properties.[14] Mo

[a] State Key Laboratory of Oil and Gas Reservoir Geology and Exploitation, Southwest Petroleum University, Chengdu 610500, China
[b] Institute of Inorganic Chemistry, University of Zurich, 8057 Zurich, Switzerland
Fax: +41-44-63-56802,
E-mail: greta.patzke@aci.uzh.ch
[c] Institute of Inorganic Chemistry, University of Kiel, 24098 Kiel, Germany
[d] School of Materials Science and Engineering, Southwest Petroleum University, Chengdu 610500, China
[e] Institute for Chemical Technology and Polymer Chemistry, Karlsruhe Institute of Technology (KIT), 76131 Karlsruhe, Germany

WILEY ONLINE LIBRARY

G. R. Patzke et al.

incorporation into nanostructured bismuth tungstate hosts has furthermore been identified as a new strategy to enhance their photocatalytic activity by means of the emerging $Bi_2W_{1-x}Mo_xO_6$ phases.[15] However, not only electronic and structural effects play a role in photocatalyst design, but crystallinity, specific surface area and morphology are equally important parameters.[16] As outlined above, they can only be efficiently steered through detailed knowledge about the underlying materials formation processes. Whereas advanced in situ studies have been performed on the solution growth of Bi_2MoO_6 catalysts[4a,17,18] and Bi_2WO_6 has been investigated in our previous recent work,[10] no such information is available for the growth kinetics and processes of the catalytically more efficient mixed $Bi_2(W,Mo)O_6$ phases.

The present study now closes this gap, given that our extensive studies on the formation mechanisms of molybdenum[19] and tungsten oxide nanomaterials[20] and their combination into hierarchically structured (W/Mo) oxides[21] have encouraged us to transfer this knowledge to the exploration of morphology–mechanism relationships to $Bi_2W_{1-x}Mo_xO_6$ materials. Therefore, we present the first complementary in situ X-ray absorption spectroscopy (XAS) and EDXRD studies on the hydrothermal incorporation of Mo into hierarchical Bi_2WO_6 architectures. Whereas in situ XAS can both monitor the liquid and the solid phase, in situ EDXRD techniques were used to cover the entire $Bi_2W_{1-x}Mo_xO_6$ (x = 0, 0.25, 0.50, 0.75 and 1.0) series. The results are correlated to our in situ investigations on the formation of related hierarchical particle arrangements in tungstate and (W/Mo) oxide based hydrothermal systems.[20,21]

Results and Discussion

Hydrothermal Synthesis of $Bi_2W_{1-x}Mo_xO_6$ Nanostructures

XRD patterns of $Bi_2W_{1-x}Mo_xO_6$ products are shown in Figure S1 in the Supporting Information. All of the samples exhibit a single Aurivillius phase. The Mo-free product (x = 0) can be indexed to orthorhombic Bi_2WO_6 with lattice parameters of a = 5.4314(6) Å, b = 16.418(1) Å and c = 5.4505(5) Å (space group $Pca2_1$, JCPDS no. 73-1126). For x = 1.0, the γ-Bi_2MoO_6 phase with lattice parameters a = 5.4809(1) Å, b = 16.2239(5) Å and c = 5.4999(1) Å (space group $Pca2_1$, JCPDS No. 77-1246) was obtained. The lattice parameters for mixed compounds with x = 0.25, 0.50 and 0.75 fall within the range of the pristine phases: the

lengths of the a and c axes increase for higher Mo contents, whereas the b-axis lengths significantly decrease (cf. Table 1). This agrees well with previous reports by Zhang et al.[15a] and demonstrates that Bi_2WO_6 and Bi_2MoO_6 form a continuous $Bi_2W_{1-x}Mo_xO_6$ solid solution from the facile one-step hydrothermal reaction of $Bi(NO_3)_3·5H_2O$, K_2WO_4 and Na_2MoO_4 as readily available precursors.

Typical SEM images of the $Bi_2W_{1-x}Mo_xO_6$ samples are shown in Figure 1. $Bi_2W_{0.75}Mo_{0.25}O_6$ bears a strong resemblance to the morphology of hierarchical Bi_2WO_6 microspheres that consist of individual nanosheet building blocks. These hierarchical microspheres start to disintegrate upon higher Mo contents in the $Bi_2W_{1-x}Mo_xO_6$ materials (cf. Figure 1c), and this process continues until the individual nanosheet building blocks appear (cf. Figure 1d). The morphology of Bi_2MoO_6 is similar to that of $Bi_2W_{0.25}Mo_{0.75}O_6$, but the overall particle sizes are larger. The crystallite sizes of the $Bi_2W_{1-x}Mo_xO_6$ samples were determined from the (131) reflection by using the Scherrer equation as shown in Table 1. In line with the continuously sharpened peak profile, the crystallite size decreases significantly from about 38.2 nm for Bi_2MoO_6 to approximately 10.4 nm for Bi_2WO_6. This trend is also reflected in the Brunauer–Emmett–Teller (BET) surface areas (cf. Table 1). The surface area for Bi_2MoO_6 is only 9.8 m^2g^{-1}, and it increases to 18.4 m^2g^{-1} for Bi_2WO_6. Moreover, the surface area of $Bi_2W_{1-x}Mo_xO_6$ decreases from 22.6 to 16.9 m^2g^{-1} with increasing Mo content. These results indicate that $Bi_2W_{1-x}Mo_xO_6$ samples have the same structural motif in common but can be divided into two morphological types: hierarchical nanostructures (x = 0 and 0.25) and nanosheets (x = 0.50, 0.75 and 1.0).

Moreover, all solid products were collected after in situ EDXRD experiments and were analyzed by ex situ XRD and SEM. The XRD patterns of these samples agree well with those of the phases grown under ex situ experimental conditions. SEM images shown in Figure S2 in the Supporting Information demonstrate that the products isolated after the in situ EDXRD experiments already bear considerable resemblance to the fully developed materials obtained after 24 h of hydrothermal reaction (cf. Figure 1).

To understand the local structural characteristics of the $Bi_2W_{1-x}Mo_xO_6$ solid solutions, Raman spectroscopy was employed, because it can detect structural variations in the coordination polyhedra of a given material through differences in the observed modes.[22] Figure 2 shows the Raman spectra recorded for the $Bi_2W_{1-x}Mo_xO_6$ solid solution series. Generally, the resonances of Bi_2WO_6 and Bi_2MoO_6

Table 1. Unit-cell parameters and surface areas of $Bi_2W_{1-x}Mo_xO_6$ products.

Sample	a [Å]	b [Å]	c [Å]	D_{131} [nm][a]	S_{BET} [m^2g^{-1}]
Bi_2WO_6	5.4314(6)	16.418 (1)	5.4505(5)	10.4	18.4
$Bi_2W_{0.75}Mo_{0.25}O_6$	5.4553(4)	16.367(1)	5.4679(3)	11.6	22.6
$Bi_2W_{0.50}Mo_{0.50}O_6$	5.4568(4)	16.314(1)	5.4703(2)	17.9	18.8
$Bi_2W_{0.25}Mo_{0.75}O_6$	5.4762(2)	16.2584(6)	5.4898(1)	23.4	16.9
Bi_2MoO_6	5.4809(1)	16.2239(5)	5.4999(1)	38.2	9.8

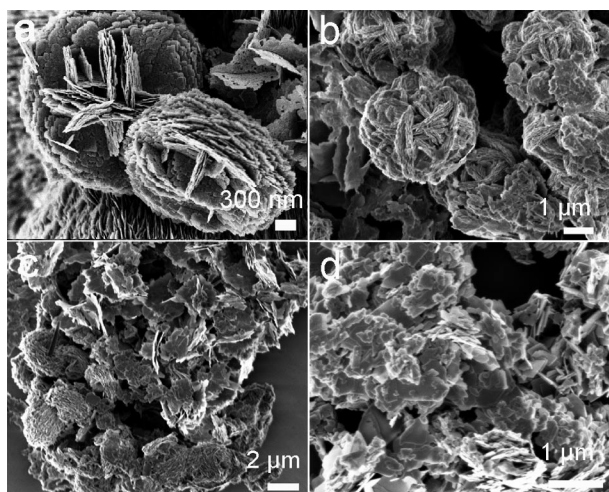[a] Crystallite size estimated from the (131) reflection with the Scherrer equation.

Figure 1. Representative SEM images of (a) Bi_2WO_6, (b) $Bi_2W_{0.75}Mo_{0.25}O_6$, (c) $Bi_2W_{0.50}Mo_{0.50}O_6$ and (d) $Bi_2W_{0.25}Mo_{0.75}O_6$.

in the range of 600–1000 cm^{-1} can be assigned to the stretching of W–O and Mo–O bonds, and those below 400 cm^{-1} arise from bending, wagging and external modes.[23] More detailed investigations show that Bi_2WO_6 and $Bi_2W_{0.75}Mo_{0.25}O_6$ exhibit very similar Raman spectra. The band at 303 cm^{-1} can be assigned to translational modes that involve simultaneous motions of Bi^{3+} and (W/Mo)O_6.[24] The strong band at 790 cm^{-1}, along with two shoulder bands at 817 and 712 cm^{-1} of Bi_2WO_6 and $Bi_2W_{0.75}Mo_{0.25}O_6$, corresponds to (W/Mo)–O stretching modes of the distorted (W/Mo)O_6 octahedra.
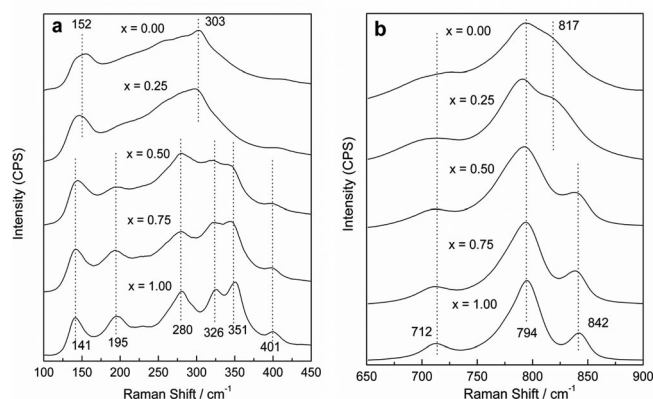

Figure 2. Raman spectra of as-prepared $Bi_2W_{1-x}Mo_xO_6$: (a) lower wavenumber range; (b) higher wavenumber range.

Interestingly, the resonance at 817 cm^{-1} is shifted to a higher wavenumber at 842 cm^{-1} with further increasing Mo content in $Bi_2W_{1-x}Mo_xO_6$ (x = 0.50, 0.75 and 1.0). It has been demonstrated in previous studies that lower frequencies of the Raman stretching bands correspond to the longer metal–oxyen bonds.[22] Therefore, Bi_2WO_6 and $Bi_2W_{0.75}Mo_{0.25}O_6$ display longer apical (W/Mo)–O bonds than $Bi_2W_{1-x}Mo_xO_6$ (x = 0.50, 0.75 and 1.0). However, the band at 712 cm^{-1} observed for all samples displays no significant shift, thus indicating that the equatorial oxygen

atoms of the (W/Mo)O_6 octahedra are not affected by increasing Mo content.[15a] It can be concluded that the amount of Mo in $Bi_2W_{1-x}Mo_xO_6$ does not only influence the final morphology (cf. Figure 1), but also the local structures of the obtained solid solutions. With increasing Mo content up to x = 0.5, the apical (W/Mo)–O bond length within the (W/Mo)O_6 octahedra decreases.

In our previous work, we studied the hydrothermal crystallization of Bi_2WO_6 with in situ EDXRD monitoring techniques.[10] We found the reaction kinetics of this hydrothermal system to be pH-dependent, accompanied by the disintegration of hierarchical nanostructures into their nanosheet building blocks. Therefore, it is to be expected that the addition of Mo precursor to the reaction medium influences the nucleation and growth of Bi_2WO_6 particle architectures. This can be a reason why hierarchical $Bi_2W_{1-x}Mo_xO_6$ (x = 0.50, 0.75 and 1.0) materials with higher Mo content have not yet been accessed. In the following, in situ XAS and EDXRD techniques were combined to elucidate the hydrothermal formation of $Bi_2W_{1-x}Mo_xO_6$ solid solutions.

In Situ XAS Investigation of $Bi_2W_{1-x}Mo_xO_6$ Formation

In our previous work, we constructed a special in situ cell that allowed us to monitor both the liquid phase and the solid–liquid interface during hydrothermal processes.[25] This provides essential insight into the formation of oxide nanomaterials and thereby indispensable information for their controlled large-scale production.

X-ray absorption near edge spectroscopy (XANES) spectra at the Mo-K edge were recorded both at the middle (liquid part in Figure 3a) and at the bottom (mainly solid part in Figure 3b) of the cell during the hydrothermal reaction. Na_2MoO_4 as the molybdenum source dissolved at a temperature as low as 50 °C under acidic reaction conditions (Figure 3a). The decrease in Mo-containing species up to 80 °C furthermore indicates the formation of solid products [i.e., the reaction onset at relatively low temperatures (Figure 3b)]. As the Bi and W species showed strong X-ray absorption at realistic concentrations needed for the experiments, high-quality in situ extended X-ray absorption fine structure (EXAFS) data were extremely difficult to obtain. In the following, we thus concentrated solely on the absorption edge with higher photon energy (Mo-K edge) rather than on the lower-energy Bi L_3 and W L_3 edges. Figure 3b shows a comparison of the in situ Mo-K edge XAS data collected in the course of the reaction with the starting material Na_2MoO_4 and the product $Bi_2W_{0.75}Mo_{0.25}O_6$ as references. Firstly, it is obvious that Mo displays completely different coordination environments in precursor and product. The Mo-K edge XAS of Na_2MoO_4 exhibits very distinctive pre-edge features close to 19995 eV, and the absorption sharply rises at 20000 eV. The pre-edge feature is due to the forbidden transition from the 1s to the 4d level, which can only be observed due to a mixing of d and p orbitals in the final state (e.g., in the case of tetrahedral

symmetry). The intensity of that feature depends on the amount of p character in the resulting state.[18] In comparison, the pre-edge intensity of the $Bi_2W_{0.75}Mo_{0.25}O_6$ product decreases sharply due to the transition from Mo in a tetrahedral environment to octahedrally coordinated Mo, even in solution. Whereas previous in situ studies on the formation of Bi_2MoO_6 had started from $(NH_4)_6Mo_7O_{24}\cdot4H_2O$ as polyoxometalate precursor with octahedrally coordinated Mo centers,[18] tetrahedral Mo coordination in the starting material is equally suitable to bring forward mixed Aurivillius-type compounds. As intermediate non-centrosymmetric tetrahedral [MoO$_4$] species have been observed prior to the formation of Bi_2MoO_6 from $(NH_4)_6Mo_7O_{24}\cdot4H_2O$ and Bi_2O_3,[17] we here demonstrate that the isostructural $Bi_2W_{1-x}Mo_xO_6$ target compounds can also be accessed directly from a precursor material with tetrahedrally coordinated molybdenum atoms. The pH influence is another key parameter, because acidic media in combination with heating obviously promote the conversion of tetrahedrally to octahedrally coordinated Mo.
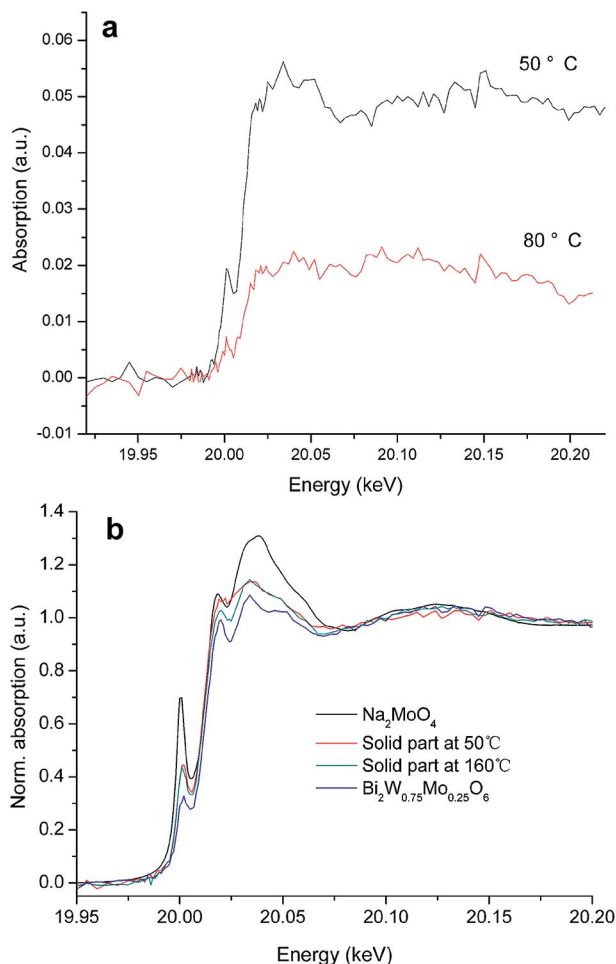

Figure 3. (a) Mo-K edge XAS spectra of the hydrothermal conversion of $Bi(NO_3)_3\cdot5H_2O/K_2WO_4/Na_2MoO_4$ to $Bi_2W_{0.75}Mo_{0.25}O_6$ (liquid phase); (b) solid-phase Mo-K edge XAS spectra of the corresponding hydrothermal $Bi_2W_{0.75}Mo_{0.25}O_6$ formation with reference spectra (Mo-K edge XAS of the Na_2MoO_4 precursor and of the $Bi_2W_{0.75}Mo_{0.25}O_6$ product).

In Situ EDXRD Studies

The time-dependent crystallization of $Bi_2W_{1-x}Mo_xO_6$ nanomaterials was studied with in situ EDXRD, and the typical evolution of the diffraction patterns of $Bi_2W_{0.75}Mo_{0.25}O_6$ is shown in Figure 4.
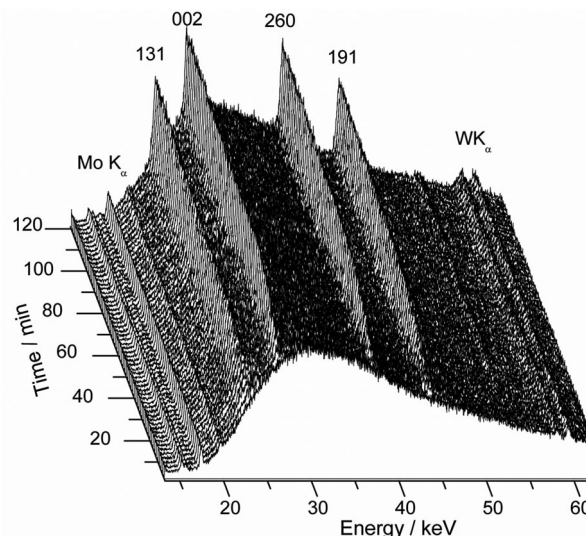
Figure 4. Time-resolved in situ EDXRD patterns recorded during the hydrothermal crystallization of $Bi_2W_{0.75}Mo_{0.25}O_6$ at 160 °C. The indices of intense lines of the product phase as well as the Mo-K_α and W-K_α fluorescence lines are marked.

The W and Mo fluorescence lines were present from the beginning of the reaction process, and several diffraction peaks of orthorhombic $Bi_2W_{0.75}Mo_{0.25}O_6$ appeared after a very short induction time. Their intensity increased over the course of the reaction, and no intermediates were detected. In situ EDXRD monitoring of the formation of $Bi_2W_{1-x}Mo_xO_6$ ($x = 0, 0.50, 0.75$ and 1.0) closely resembles the results for $Bi_2W_{0.75}Mo_{0.25}O_6$ as shown in Figure 4, but the individual induction times $t_{ind.}$ and half-life times $t_{0.5}$ strongly depend on the Mo content among the $Bi_2W_{1-x}Mo_xO_6$ series (cf. Figure 5 and Table 2). The $t_{ind.}$ and $t_{0.5}$ values for Bi_2WO_6 are 8 and 16 min, respectively, whereas the formation of Bi_2MoO_6 sets in immediately: within the time resolution of the experimental setup no induction time could be observed, and $t_{0.5}$ is only 6 min for Bi_2MoO_6. The formation processes of $Bi_2W_{1-x}Mo_xO_6$ ($x = 0.25, 0.50$ and 0.75) display intermediate kinetics. In addition, different growth curves observed (cf. Figure 5) for (a) $Bi_2W_{1-x}Mo_xO_6$ with $x = 0, 0.25$ and (b) $Bi_2W_{1-x}Mo_xO_6$ with $x = 0.50, 0.75$ and 1.0 suggest that the crystallization processes vary with the Mo content.

As the reaction kinetics of $Bi_2W_{1-x}Mo_xO_6$ materials appear to depend strongly on the degree of W/Mo substitution, kinetic analyses were performed by fitting the experimental data to a theoretical expression that related the extent of reaction α (cf. Figure 5) to time. A more detailed description of kinetic data evaluation can be found in the literature.[26] The speed of $Bi_2W_{1-x}Mo_xO_6$ formation ($x = 0.50, 0.75$ and 1) was too fast to permit detailed kinetic evaluations, so Sharp–Hancock plots based on the (260) re-
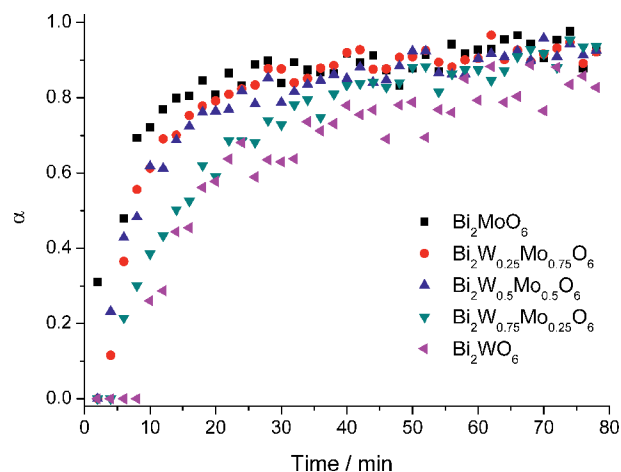
Figure 5. Extent of reaction a versus time for the growth of the $Bi_2W_{1-x}Mo_xO_6$ series at 160 °C.

Table 2. Kinetic data for the formation of $Bi_2W_{1-x}Mo_xO_6$ solid solutions.

Samples	$t_{ind.}$ [min]	$t_{0.5}$ [min]	m[a]
Bi_2WO_6	8	16	0.52
$Bi_2W_{0.75}Mo_{0.25}O_6$	4	14	0.63
$Bi_2W_{0.50}Mo_{0.50}O_6$	2	8	[b]
$Bi_2W_{0.25}Mo_{0.75}O_6$	2	8	[b]
Bi_2MoO_6	0	6	[b]

[a] Avrami exponent. [b] The reaction was too fast to generate sufficient data points for analysis.

flection were only obtained for Bi_2WO_6 and $Bi_2W_{0.75}Mo_{0.25}O_6$, respectively (Figure S3 in the Supporting Information). The linear shape of both graphs in the $0.2 < a < 0.85$ range points to a common crystallization mechanism of both Bi_2WO_6 and the $Bi_2W_{0.75}Mo_{0.25}O_6$ solid solution with respective m values of 0.52 and 0.63 (cf. Table 2).

Given that m values around 1.0 were reported for the hydrothermal formation of Bi_2MoO_6 nanoplates,[18] the formation of $Bi_2W_{0.75}Mo_{0.25}O_6$ already exhibits a clear trend towards the upper limit of m ranges for diffusion-controlled growth that were determined to be 0.54–0.62 in previous works.[27] On the basis of an Avrami exponent m close to 0.5, we had assigned a diffusion-controlled reaction mechanism to the hydrothermal formation of Bi_2WO_6 nanostructures, because m should adopt values of 1 or above for other reaction mechanisms.[10] As a consequence, $Bi_2W_{0.75}Mo_{0.25}O_6$ is formed by means of an intermediate reaction mechanism on the diffusion-controlled side, which can be explained in terms of the partial substitution of W by Mo that speeds up the reaction kinetics. An increase of the reaction exponent m from 0.5 to 1 goes hand in hand with the disintegration of Bi_2WO_6 spheres into their platelet-shaped building blocks. Therefore, the fast formation kinetics of Bi_2MoO_6 may be the reason that the organization of nanoplates into hierarchical nanostructures has not been observed. Further investigations are required to elucidate

whether the particles are formed by self-assembly or other routes, such as growth from a polycrystalline core.

Comparison with Hierarchical W/Mo Oxide Growth Mechanisms

As outlined in the Introduction, the majority of the growth mechanisms for the self-organization of oxide nanoparticles into hierarchical arrangements have been proposed on the basis of ex situ observations. Only few examples of the systematic in situ monitoring of oxide formation processes in hydrothermal systems that contain two or more cations have been reported. One of the few comprehensive studies in this field is our combined in situ EDXRD/XAS investigation on the influence of molybdenum on the growth process of hexagonal W/Mo oxide nanoarchitectures[21] in comparison with pristine hexagonal tungstates.[20] In close analogy to the stepwise W/Mo substitution strategy towards the present $Bi_2W_{1-x}Mo_xO_6$ solid solutions, we first established hydrothermal access to hierarchically nanostructured hexagonal alkali tungstates that were obtained in the presence of Rb^+ and Cs^+.[20] In situ EDXRD studies showed that they were formed by means of a nucleation-controlled mechanism with $t_{ind.}$ values of 11 min for Rb^+ and 9 min for Cs^+. This scenario changed upon addition of Mo to the hydrothermal system: hexagonal Rb–W/Mo tungstates and Cs–W/Mo tungstates with more pronounced and better organized spherical growth patterns emerged from a diffusion-controlled mechanism after shorter induction times (Rb: $t_{ind.} = 2$ min; Cs: $t_{ind.} = 6$ min) and drastically reduced $t_{0.5}$ values.[21] The introduction of Mo into the hexagonal tungstates did not alter their channel-structure motif and promoted their transformation into nanoscale hierarchical morphologies in comparison with the hydrothermal formation of hexagonal tungstates in the absence of Mo. Furthermore, the accelerated formation kinetics of the alkali W/Mo oxides with respect to the corresponding alkali tungstates can be explained by our observation that pristine MoO_3 nanorods are formed very rapidly under hydrothermal conditions (i.e., on a minute scale that does not permit further kinetic evaluations).[19] The above-described $Bi_2WO_6/Bi_2(W,Mo)O_6/Bi_2MoO_6$ series shows the same kinetic trend for the $t_{ind.}$ values: whereas bismuth molybdate formation proceeds too fast to assign a mechanistic model, tungsten-rich phases grow more slowly and under diffusion control. Therefore, the morphological difference between platelet-shaped Bi_2MoO_6 and hierarchical Bi_2WO_6 and $Bi_2(W,Mo)O_6$ is linked to the change of hydrothermal reaction kinetics (i.e., to the crystal growth mechanism). Given that hierarchical nanostructuring among W/Mo hexagonal tungstates is connected to diffusion-controlled growth as well, there are strong indications that hierarchical nanostructures are preferably formed in a "kinetic window" for the organized diffusion of the components to the growing crystals. Interestingly, the combination of a slow-growing W-oxide with a fast-growing Mo-oxide component generated optimum conditions for the hierarchical self-organi-

zation process among two structurally different systems, namely, Aurivillius-type Bi_2MO_6 compounds and hexagonal tungsten bronzes. Consequently, not only crystallographic features but also crystallization kinetics are a key steering parameter for hydrothermally obtained particle shapes. This renders kinetic monitoring a promising strategy to achieve morphology control over a wider product range, thereby covering a variety of structural motifs.

Conclusion

A series of nanostructured Aurivillius-type $Bi_2W_{1-x}Mo_xO_6$ solid solutions was obtained from the one-step hydrothermal reaction of $Bi(NO_3)_3$·$5H_2O$, K_2WO_4 and Na_2MoO_4. The extent of hierarchical organization decreases with the Mo content among the series. Whereas Bi_2WO_6 and $Bi_2W_{0.75}Mo_{0.25}O_6$ display hierarchical self-organization of individual nanoplatelets into microspheres, W/Mo ratios of 0.5 and above induce the segregation of the individual building blocks into sheet-like morphologies. Raman spectra of the $Bi_2W_{1-x}Mo_xO_6$ series show that the Mo content also influences the local structure of the (W/Mo)O_6 octahedra through a decrease in their apical bond length. In situ XAS investigations revealed that the formation of the $Bi_2W_{1-x}Mo_xO_6$ compounds sets in at as low as 80 °C, and they illustrate the conversion of the [MoO_4] tetrahedra in the Na_2MoO_4 precursor into the octahedral moieties of the mixed oxide products, even in solution. Their crystal-growth kinetics were furthermore studied with in situ EDXRD monitoring experiments. Interestingly, the different product-morphology types correlate with the observed reaction kinetics. Whereas the Mo-rich nanosheet structures among the $Bi_2W_{1-x}Mo_xO_6$ series emerge from a rapid growth process that does not permit further kinetic evaluations, the self-organization of nanoparticles into hierarchical Bi_2WO_6 and $Bi_2W_{0.75}Mo_{0.25}O_6$ microspheres proceeds by means of slower and diffusion-controlled growth. The results are in line with our previously observed kinetic and mechanistic trends for the hydrothermal formation of hierarchically nanostructured hexagonal W/Mo oxides: in analogy to the present study, the introduction of Mo into this hydrothermal W/Mo system accelerates the growth kinetics and changes the formation mechanism of the products as well. As a consequence, diffusion-controlled pathways appear to generally favor the formation of hierarchical nanoarchitectures that offer superior materials properties (e.g., sensor development and photocatalysis). The present study demonstrates how optimal morphologies of a multicomponent material can be obtained through systematic in situ monitoring of the formation of solids under hydrothermal conditions and exploiting the accompanying mechanistic changes. Further investigations on bismuth-containing sensor and catalyst materials are under way.

Experimental Section

Synthesis: In a typical procedure, $Bi(NO_3)_3$·$5H_2O$ (97 mg, 0.2 mmol), K_2WO_4 (x mmol; $x = 0$, 0.025, 0.050, 0.075 and 0.1) and Na_2MoO_4 (0.1–x mmol) were placed into acetic acid (10 mL, 20 vol.-%) at room temperature and stirred magnetically for 20 min to disperse all reagents homogeneously. The resulting precursor suspension was transferred into a Teflon-lined stainless steel autoclave with a capacity of 23 mL, maintained at 160 °C for 24 h and subsequently cooled to room temperature. The precipitate was collected after filtration, washed with distilled water and dried in air.

Characterization: PXRD was conducted with a STOE STADI P diffractometer in transmission mode (flat sample holders, Ge monochromator, Cu-$K_{\alpha 1}$ radiation) operated at 40 kV and 40 mA. The unit cells were refined with the ReflexPlus Package of Materials Studio (Accelrys Inc.). For SEM, which was performed with a Zeiss SUPRA 50VP microscope, samples were dispersed in ethanol and subsequently deposited on a silicon wafer. The specimen was investigated without conductive coating at a rather low voltage (2 kV) to minimize charging effects. BET surface area measurements were performed with a Quadrasorb SI in N_2-adsorption mode. The samples were degassed under vacuum at 150 °C for 5 h. The BET specific surface area was determined by a multipoint BET method using the adsorption data in the equilibrium relative pressure (p/p_0) range of 0.05–0.30.

In Situ XAS: In situ XAS experiments were performed at the superXAS beamline at the Swiss Light Source (SLS, Villigen, Switzerland). $Bi(NO_3)_3$·$5H_2O$ (30 mg), Na_2MoO_4 (6 mg) and K_2WO_4 (6 mg) were embedded between two glass wool plugs to fix the solid phase, and they were loaded together with acetic acid (3 mL, 20 vol.-%) into a homemade spectroscopic cell.[25] XAS scans around the Mo-K edge were recorded between 19850 and 20240 eV under stationary conditions (liquid solution and solid phase) and were calibrated with an Mo reference foil. The following procedure was applied: heating to 160 °C at a rate of 1.5 °C min^{-1} from room temp. to 50, 80, 120 and 160 °C. Background subtraction and normalization were carried out by fitting a linear polynomial to the pre-edge region and a cubic polynomial to the post-edge region of the absorption spectra using WinXAS 3.20.[28]

In Situ EDXRD Measurements: In situ EDXRD experiments were performed at HASYLAB (Hamburg) bending magnet beamline F3, which provides an energy range from 13.31 to 62.54 keV with a maximum intensity of about 26 keV. The d-spacing range is given by $d = 6.199/(E \cdot \sin\theta)$. With a detector angle of approximately 4.9°, the observable d-spacing range is 1.16–5.46 Å. The energy resolution $\Delta d/d$ is about 10^{-2} above 26 keV. The beam was collimated to 0.2 mm to give the best results. For the in situ experiments, autoclaves with glass liners of an internal diameter of 10 mm and a volume of 10 mL were used. A typical experiment was performed with $Bi(NO_3)_3$·$5H_2O$ (97 mg, 0.2 mmol), K_2WO_4 (x mmol; $x = 0$, 0.025, 0.050, 0.075 and 0.1), Na_2MoO_4 (0.1 – x mmol) and acetic acid (2 mL, 20 vol.-%) as reactants. The in situ reactions were run at 160 °C. Data collection was started immediately after the introduction of the autoclave in the oven. The acquisition time for the in situ EDXRD data measured for the given reactions was 120 s. After the in situ experiments, the solid products were collected by filtration, washed with distilled water and ethanol and dried in air for further characterization. Note that due to sedimentation effects of the (B/W)-containing products during the reaction, the in situ experiments had to be performed under rapid stirring.

Supporting Information (see footnote on the first page of this article): XRD patterns of $Bi_2W_{1-x}Mo_xO_6$ solid solutions (Figure S1); SEM images of $Bi_2W_{1-x}Mo_xO_6$ solid solutions after in situ EDXRD experiments (Figure S2); Sharp–Hancock plots derived from the kinetic data of Bi_2WO_6 and $Bi_2W_{0.75}Mo_{0.25}O_6$ recorded at 160 °C over a data range of $0.2 < \alpha < 0.85$ (Figure S3).

[1] a) J. A. Rodriguez, M. Fernandez-Garcia, *Synthesis Properties and Applications of Oxide Nanomaterials*, Wiley InterScience, **2007**; b) D. Vollath, *Nanomaterials*, Wiley-VCH, **2008**; c) H. Goesmann, C. Feldmann, *Angew. Chem.* **2010**, *122*, 1402; *Angew. Chem. Int. Ed.* **2010**, *49*, 1362; d) Y. E. Gogotsi, *Nanomaterials Handbook*, CRC Press, Taylor & Francis Group, Boca Raton, **2006**.

[2] a) M. D. Hernández-Alonso, F. Fresno, S. Suárez, J. M. Coronado, *Energ. Environ. Sci.* **2009**, *2*, 1231; b) A. Kudo, Y. Miseki, *Chem. Soc. Rev.* **2009**, *38*, 253; c) X. B. Chen, S. H. Shen, L. J. Guo, S. S. Mao, *Chem. Rev.* **2010**, *110*, 6503; d) F. E. Osterloh, *Chem. Mater.* **2008**, *20*, 35; e) I. S. Cho, D. W. Kim, S. Lee, C. H. Kwak, S. T. Bae, J. H. Noh, S. H. Yoon, H. S. Jung, D. W. Kim, K. S. Hong, *Adv. Funct. Mater.* **2008**, *18*, 2154; f) Z. G. Yi, J. H. Ye, N. Kikugawa, T. Kako, S. X. Ouyang, H. Stuart-Williams, H. Yang, J. Y. Cao, W. J. Luo, Z. S. Li, Y. Liu, R. L. Withers, *Nat. Mater.* **2010**, *9*, 559; g) A. Nikolopoulou, D. Papoulis, S. Komarneni, P. Tsolis-Katagas, D. Panagiotaras, G. H. Kacandes, P. L. Zhang, S. Yin, T. Sato, *Appl. Clay Sci.* **2009**, *46*, 363; h) A. Zuettel, A. Remhof, A. Borgschulte, O. Friedrichs, *Phil. Trans. R. Soc. A* **2010**, *368*, 3329; i) B. Ma, G. K. L. Goh, T. S. Zhang, J. Ma, *Microporous Mesoporous Mater.* **2009**, *124*, 162; j) S. G. Ebbinghaus, H. P. Abicht, R. Dronskowski, T. Mueller, A. Reller, A. Weidenkaff, *Prog. Solid State Chem.* **2009**, *37*, 173.

[3] a) G. R. Patzke, Y. Zhou, R. Kontic, F. Conrad, *Angew. Chem. Int. Ed.* **2011**, *50*, 826; b) G. A. Ozin, A. C. Arsenault, *Nanochemistry: A Chemical Approach to Nanomaterials*, RSC Publishing, Cambridge, **2005**; c) M. Yoshimura, K. Byrappa, *J. Mater. Sci.* **2008**, *43*, 2085; d) B. L. Cushing, V. L. Kolesnichenko, C. J. O'Connor, *Chem. Rev.* **2004**, *104*, 3893; e) C. N. R. Rao, A. Müller, A. K. Cheetham, *The Chemistry of Nanomaterials*, Wiley-VCH, Weinheim, **2004**.

[4] a) C. Kongmark, V. Martis, C. Pirovano, A. Löfberg, W. van Beek, G. Sankar, A. Rubbens, S. Cristol, R.-N. Vannier, E. Bordes-Richard, *Catal. Today* **2010**, *157*, 257; b) T. Ressler, *Catal. Today* **2009**, *145*, 258; c) H. P. Vu, S. Shawand, L. G. Benning, *Mineral. Mag.* **2008**, *72*, 217; d) F. Millange, R. I. Walton, D. O'Hare, *J. Mater. Chem.* **2000**, *10*, 1713; e) D. L. Chen, T. Li, L. Yin, X. X. Hou, X. J. Yu, Y. Zhang, B. B. Fan, H. L. Wang, X. J. Li, R. Zhang, T. C. Hou, H. X. Lu, H. L. Xu, J. Sun, L. A. Gao, *Mater. Chem. Phys.* **2011**, *125*, 838.

[5] a) W. Bensch, N. Pienack, *Angew. Chem. Int. Ed.* **2011**, *50*, 2014; b) G. Sankar, W. Bras, *Catal. Today* **2009**, *145*, 195; c) A. I. Frenkel, Q. Wang, N. Marinkovic, J. G. Chen, L. Barrio, R. Si, A. L. Camara, A. M. Estrella, J. A. Rodriguez, J. C. Hanson, *J. Phys. Chem. C* **2011**, *115*, 17884; d) D. Ferri, M. S. Kumar, R. Wirz, A. Eyssler, O. Korsak, P. Hug, A. Weidenkaff, M. A. Newton, *Phys. Chem. Chem. Phys.* **2010**, *12*, 5634; e) S. R. Bare, T. Ressler, *Adv. Catal.* **2009**, *52*, 339; f) J.-D. Grunwaldt, B. Kimmerle, A. Baiker, P. Boye, C. G. Schroer, P. Glatzel, C. N. Borca, F. Beckmann, *Catal. Today* **2009**, *145*, 367.

[6] M. Rehan, X. Lai, G. M. Kale, *CrystEngComm* **2011**, *3*, 3725.

[7] a) A. Kudo, K. Omori, H. Kato, *J. Am. Chem. Soc.* **1999**, *121*, 11459; b) W. Yin, W. Wang, M. Shang, L. Zhou, S. Sun, L. Wang, *Eur. J. Inorg. Chem.* **2009**, 4379.

[8] a) J. Wu, F. Duan, Y. Xie, *J. Phys. Chem. C* **2007**, *111*, 12866; b) S. Yao, J. Wei, B. Huang, S. Feng, X. Zhang, X. Qin, P. Wang, Z. Wang, Q. Zhang, X. Jing, J. Zhan, *J. Solid State Chem.* **2009**, *182*, 236; c) C. Xu, X. Wie, Y. Guo, H. Wu, Z. Ren, G. Xu, G. Shen, G. Han, *Mater. Res. Bull.* **2009**, *44*, 1635.

[9] Y. Zhou, K. Vuille, A. Heel, G. R. Patzke, *Z. Anorg. Allg. Chem.* **2009**, *635*, 1848.

[10] Y. Zhou, E. Antonova, W. Bensch, G. R. Patzke, *Nanoscale* **2010**, *2*, 2326.

[11] L. Zhou, W. Wang, H. Xu, S. Sun, M. Shang, *Chem. Eur. J.* **2009**, *15*, 1776.

[12] J. Hou, Y. Qu, D. Krsmanovic, C. Ducati, D. Eder, R. V. Kumar, *J. Mater. Chem.* **2010**, *20*, 2418.

[13] J. Xiong, G. Cheng, Z. Lu, J. Tang, X. Yu, R. Chen, *CrystEngComm* **2011**, *13*, 2381.

[14] K. Zheng, Y. Zhou, L. Gu, X. Mo, G. R. Patzke, G. Chen, *Sens. Actuators B* **2010**, *148*, 240.

[15] a) L. Zhang, Y. Man, Y. Zhu, *ACS Catal.* **2011**, *1*, 841; b) L. Zhou, M. Yu, J. Yang, Y. Wang, C. Yu, *J. Phys. Chem. C* **2010**, *114*, 18812; c) X. C. Song, Y. F. Zheng, R. Ma, Y. Y. Zhang, H. Y. Yin, *J. Hazard. Mater.* **2011**, *192*, 186; d) V. I. Voronkova, E. P. Kharitonova, O. G. Rudnitskaya, *Inorg. Mater.* **2011**, *47*, 183.

[16] A. Kudo, Y. Miseki, *Chem. Soc. Rev.* **2009**, *38*, 253.

[17] C. Kongmark, V. Martis, A. Rubbens, C. Pirovano, A. Löfberg, G. Sankar, E. Bordes-Richard, R.-N. Vannier, W. van Beek, *Chem. Commun.* **2009**, 4850.

[18] A. M. Beale, G. Sankar, *Chem. Mater.* **2003**, *15*, 146.

[19] A. Michailovski, J.-D. Grunwaldt, A. Baiker, R. Kiebach, W. Bensch, G. R. Patzke, *Angew. Chem.* **2005**, *117*, 5787; *Angew. Chem. Int. Ed.* **2005**, *44*, 5643.

[20] A. Michailovski, R. Kiebach, W. Bensch, J.-D. Grunwaldt, A. Baiker, S. Komarneni, G. R. Patzke, *Chem. Mater.* **2007**, *19*, 185.

[21] Y. Zhou, N. Pienack, W. Bensch, G. R. Patzke, *Small* **2009**, *5*, 1978.

[22] J. Yu, A. Kudo, *Adv. Funct. Mater.* **2006**, *16*, 2163.

[23] F. D. Hardcastle, I. E. Wachs, *J. Raman Spectrosc.* **1995**, *26*, 397.

[24] H. B. Fu, C. S. Pan, L. W. Zhang, Y. F. Zhu, *Mater. Res. Bull.* **2007**, *42*, 696.

[25] J.-D. Grunwaldt, M. Ramin, M. Rohr, A. Michailovski, G. R. Patzke, A. Baiker, *Rev. Sci. Instrum.* **2005**, *76*, 054104.

[26] a) L. Engelke, M. Schaefer, M. Schur, W. Bensch, *Chem. Mater.* **2001**, *13*, 1383; b) R. Kiebach, N. Pienack, M. E. Ordolff, F. Studt, W. Bensch, *Chem. Mater.* **2006**, *18*, 1196; c) L. Engelke, M. Schäfer, F. Porsch, W. Bensch, *Eur. J. Inorg. Chem.* **2003**, *3*, 506; d) R. Kiebach, M. Schaefer, F. Porsch, W. Bensch, *Z. Anorg. Allg. Chem.* **2005**, *631*, 369.

[27] B. Ma, G. K. L. Goh, J. Ma, T. J. White, *J. Electrochem. Soc.* **2007**, *154*, D557.

[28] T. Ressler, *J. Synchrotron Radiat.* **1998**, *5*, 118.

A Novel Zr-Based Porous Coordination Polymer Containing Azobenzenedicarboxylate as a Linker

Andreas Schaate,[a] Simon Dühnen,[a] Georg Platz,[a] Sebastian Lilienthal,[a] Andreas M. Schneider,[a] and Peter Behrens*[a]

A novel porous coordination polymer (PCP), Zr–abdc, composed of Zr-based secondary building units (SBUs), $[Zr_6O_4(OH)_4]^{12+}$, and 4,4′-azobenzenedicarboxylate ($abdc^{2-}$) linkers, has been synthesized by a modulated synthetic approach. In accord with the twelve-fold connecting SBU, Zr–abdc has a topology similar to the PCP series UiO-66–UiO-68, which is proposed from single-crystal XRD and powder (P)XRD experiments. The linkers are strongly disordered, which made it impossible to determine the exact structure.

The compound was further characterized by thermogravimetric analysis, scanning electron microscopy and Ar sorption measurements. Soxhlet extraction with ethanol instead of simple washing was helpful to remove guest molecules present in the pores after the synthesis. PXRD patterns measured at elevated temperatures show that a material stable up to 400 °C in air was obtained. After activation, it showed a specific surface area of $3000\ m^2\,g^{-1}$ and a pore volume of $1.41\ cm^3\,g^{-1}$.

Introduction

Hybrid porous materials that consist of metal-containing nodes linked together by organic molecules are commonly known as metal–organic frameworks (MOFs) or porous coordination polymers (PCPs).[1] Aside from the rich opportunities organic chemistry offers to design linker molecules, the concept of isoreticular chemistry is one of the most appealing characteristics of this class of materials. The idea is that the of pore size and functionality of PCPs can be systematically tuned by changing the length or functionality of the linker but retaining the metal-containing nodes or secondary building units (SBUs) and therefore the topology of the initial structure.[2] This idea was introduced with the isoreticular MOF series[3] and has been proven to be a fruitful concept by several examples.[4,5a,6,7]

In particular, PCPs based on zirconium-containing SBUs show a huge potential for many applications due to their high thermal stability and resistance towards atmospheric moisture, which can be attributed to the highly charged, oxophilic Zr^{4+} cations, the resulting strong Zr–O bonds and the high coordination number of each Zr ion.[5,7,8] Lillerud and co-workers introduced the isoreticular series UiO-66–UiO-68.[5] These compounds are constructed from the $Zr_6O_4(OH)_4(O_2C)_{12}$ SBU and linear dicarboxylate linkers

of different lengths. The SBU can be described as a Zr octahedron whose faces are capped by μ_3-OH and μ_3-O anions, which build the inner sphere of the complex, and twelve carboxylates, which complete the outer coordination sphere of the Zr cations. This high coordination number of an SBU is very unusual for PCPs and leads to a topology similar to cubic close-packing. The most prominent member of this series is UiO-66, which contains terephthalic acid (H_2bdc) as a linker. It has been shown that bdc^{2-} can be replaced by a range of different linear dicarboxylates of the same length or shorter, equipped with different functionalities.[9a,9b,10,11]

In our hands, the syntheses of Zr-based PCPs with longer, linear linkers such as biphenyldicarboxylate ($bpdc^{2-}$) were difficult to reproduce due to the formation of byproducts of low crystallinity.[8] We therefore applied the modulator approach[12] to the synthesis of Zr-based PCPs.[8] In this approach, monocarboxylic acids are added to the reaction mixture as modulators. We have proposed that a competition between the linker and modulator occurs for the complexation of Zr^{4+} cations in the reaction mixture, which reduces the rate of nucleation of the coordination polymers and enables the formation of products with higher crystallinity. By using the modulator approach, it was possible to crystallize Zr–bpdc PCP and a new Zr–tpdc–NH_2 (H_2tpdc–NH_2 = 2′-amino-1,1′:4′,1′′-terphenyl-4,4′′-dicaboxylic acid) PCP and to tune crystal sizes from nanocrystals up to single crystals suitable for single-crystal (S)XRD experiments.[8] Using even longer linkers, we have discovered a new series of porous interpenetrated zirconium–organic frameworks (PIZOFs) with this approach.[7] The structure of the PIZOFs can be derived from a twofold interpenetrated UiO topology, which is porous. These materials

[a] Institut für Anorganische Chemie and ZFM – Center for Solid State Chemistry and New Materials, Leibniz University Hannover,
Callinstrasse 9, 30167 Hannover, Germany
Fax: +49-511-762-3006
E-mail: peter.behrens@acb.uni-hannover.de

form one and the same structure with a large variety of dicarboxylic acids of the same length but with widely differing organic functionalities.[7]

We set out to use 4,4′-azobenzenedicarboxylic acid (H$_2$abdc) in the synthesis of Zr-based PCPs. We failed to synthesize UiO-68, the member of the UiO series with the largest pore size, due to the fact that the unfunctionalized terphenylenedicarboxylic acid (H$_2$tpdc) linker was completely insoluble in N,N-dimethylformamide (DMF); only with the amino-substituted derivative H$_2$tpdc–NH$_2$, which has sufficient solubility, we were able to obtain a functionalized UiO-68–NH$_2$ analogue.[8] The H$_2$abdc molecule is longer than bpdc^{2-}, the linker in UiO-67. A Zr–abdc PCP would be interesting as it should exhibit large window sizes and a high specific surface area. Unlike most of the other linkers that have been used in the synthesis of PCPs with the UiO-66–UiO-68 topology (which are linear), H$_2$abdc has a kink in its structure. The favourable synthetic accessibility of functionalized derivatives of H$_2$abdc, which start from 4-nitrobenzoic acid derivatives,[13] should allow the insertion of different organic functionalities on the linker, and, possibly, to the corresponding PCPs. H$_2$abdc and other linkers that contain azobenzene groups have already been used for the preparation of several hybrid materials, most of which are nonporous[14] and a few of which exhibit microporosity.[15]

Like other azobenzene derivatives, H$_2$abdc possesses the possibility of *cis/trans* isomerization of the azo group.[16] Recently, it was pointed out by Stock and co-workers that the successful isomerization of the azo group within a PCP can only be accomplished if it is not integrated into the backbone of the framework but present as a side chain. They provide an example of a porous interpenetrated pillared layer structure where the azo group is covalently attached to the linker and proved its *cis/trans* isomerization in the framework by UV/Vis experiments.[17]

Our main focus is to combine a linker with staggered coordination sites with the Zr SBU known from the UiO-66–UiO-68 PCPs and study the influence of its geometry on the resulting product. Such a linker with staggered coordination sites is also present in Zr-based PCPs with fumarate (fum) linkers, the synthesis and characterization of which we have recently described.[18]

Results and Discussion

For the synthesis of Zr–abdc, ZrCl$_4$, benzoic acid and H$_2$abdc were dissolved in DMF in a tightly-capped flask and heated in a preheated oven to 120 °C for 24 h. Benzoic acid was added to obtain crystalline materials. Without any modulating agent, powder XRD patterns only show broad reflections, which indicate a partially ordered product of low crystallinity (Figure S1). After this time, the reaction mixture was allowed to cool to room temperature, and the resulting red powders or crystals were isolated by centrifugation and washed with DMF and ethanol. Products that were washed by this standard procedure are denoted as

Zr–abdc (as-synt.). Some of the products were purified by Soxhlet extraction with ethanol and are denoted as Zr–abdc (Sox.).

Optical microscopy and scanning electron microscopy (SEM) images of the typical products of such syntheses are shown in Figure 1. These products show an orange-red colour similar to the free linker (the corresponding UV/Vis spectra are discussed below). Crystals with micrometer dimensions were mostly produced. In the SEM, these micrometer-sized crystals exhibited octahedral morphology but showed rough, irregular surfaces (Figure 1a). In a batch that was prepared with 30 equiv. of benzoic acid as modulator, larger crystals were produced (Figure 1b), which were suitable for the measurement of SXRD data (see below).
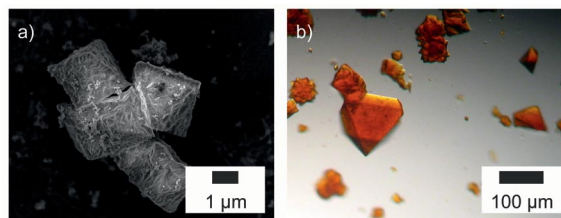
Figure 1. (a) SEM image of Zr–abdc synthesized with 10 equiv. benzoic acid as modulator; (b) image of single crystals of Zr–abdc suitable for SXRD synthesized with 30 equiv. benzoic acid (with respect to ZrCl$_4$) as modulator.

We have used the modulation approach for Zr-based PCPs with a large variety of linkers.[7,8,18] In most cases, we obtained PCPs only when a modulator was added in the synthesis; an exception is simple UiO-66 with the bdc^{2-} linker (bdc: benzenedicarboxylate). For this and other compounds, such as the Zr–fum PCP, we were able to show that an increasing modulator concentration in the reaction mixture led to increasing sizes of the product particles.[8,18] This, however, was not the case for UiO-67 with the bpdc^{2-} linker. Although it was possible to obtain highly crystalline, individual particles of micrometer dimension by using benzoic acid as a modulator, it was not possible to regulate the size of the crystallites by varying the amount of the modulator.[8] The case of the Zr–abdc PCP presented here is similar. After examination of the SEM images and the line widths in PXRD patterns carried out on products from several experiments with varying modulator concentrations, we can say that the concentration of modulator does not control the size of the product particles.

The possibility of size control by modulation may be linked to the solubility of the linker. Whereas H$_2$bdc and H$_2$fum are highly soluble in DMF, the solubility of H$_2$bpdc and H$_2$abdc is much lower. In a typical Zr PCP synthetic system, various equilibria decide the outcome of a reaction, which possibly involves the formation of highly stable [Zr$_6$O$_4$(OH)$_4$]$^{12+}$ SBUs to which either carboxylate groups from the modulator or linker molecules coordinate. When the linker and the modulator both have a high solubility, they will effectively participate in these equilibria, so that the concentration of the modulator can influence the final result. When the solubility of the linker is small, however,

it should also have a strong tendency to stay coordinated to the growing crystallites. Then, the modulator molecules cannot exert any influence on the size of these particles.

PXRD patterns, such as that in Figure 2a, show a general similarity to the patterns of other compounds with the UiO-66 topology with regard to the sequence of the reflections and their approximate intensity distribution. The reflections can be indexed within a face-centred cubic cell, and the lattice constant was refined to $a = 29.4227(4)$ Å. A comparison with cell parameters of other PCPs with UiO-66 topology shows that the size of the unit cell lies between that of Zr–bpdc and of Zr–tpdc–NH$_2$, as expected (Table 1).
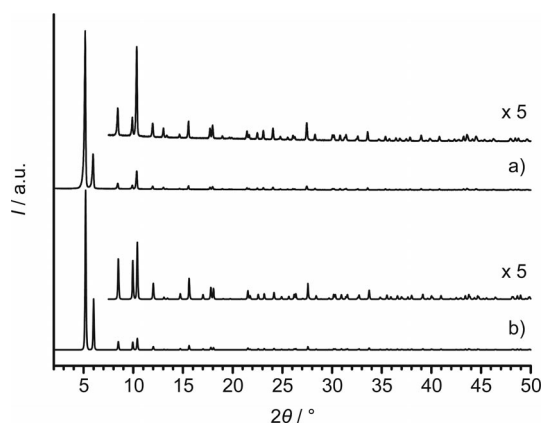

Figure 2. (a) Experimental PXRD pattern of Zr–abdc; (b) theoretical PXRD pattern simulated on the basis of the partial structure derived from SXRD data, i.e. a face-centered cubic arrangement of SBUs.

Table 1. Cell parameters a and V [Å] of different Zr-based PCPs in the space group $Fm\bar{3}m$. Data were obtained from SXRD or refined from PXRD patterns.

PCP	a/Å	V/Å^3	Method	Ref.
Zr–bdc	20.7551(5)	8870.3(2)	PXRD	[5a]
Zr–muconic dicarboxylate	20.9550(23)	9201.6(30)	PXRD	[11]
Zr–bpdc	26.8499(15)	19356.6(18)	PXRD	[8]
Zr–abdc	29.4227(4)	25471.1(10)	SXRD	this work
Zr–tpdc–NH$_2$	32.7767(5)	35212.4(9)	SXRD	[8]

Although we successfully synthesized single crystals of Zr–abdc and carried out SXRD experiments on them, it was not possible to determine their exact structure from these measurements. In all these experiments we found the space group $Fm\bar{3}m$ [$a = 29.4433(4)$ Å in good agreement with PXRD results]. In the analysis of the data, the atoms of the SBUs (Figure 3b) were readily found (atomic positions are given in Table S1). As expected, and similar to the arrangement found in UiO-66, their centres lie at the lattice points of a face-centred cubic lattice (Figure 3c and d). However, all attempts to further refine the structure gave unsatisfactory results. A possible reason for this is the staggered shape of the linker (Figure 3a).
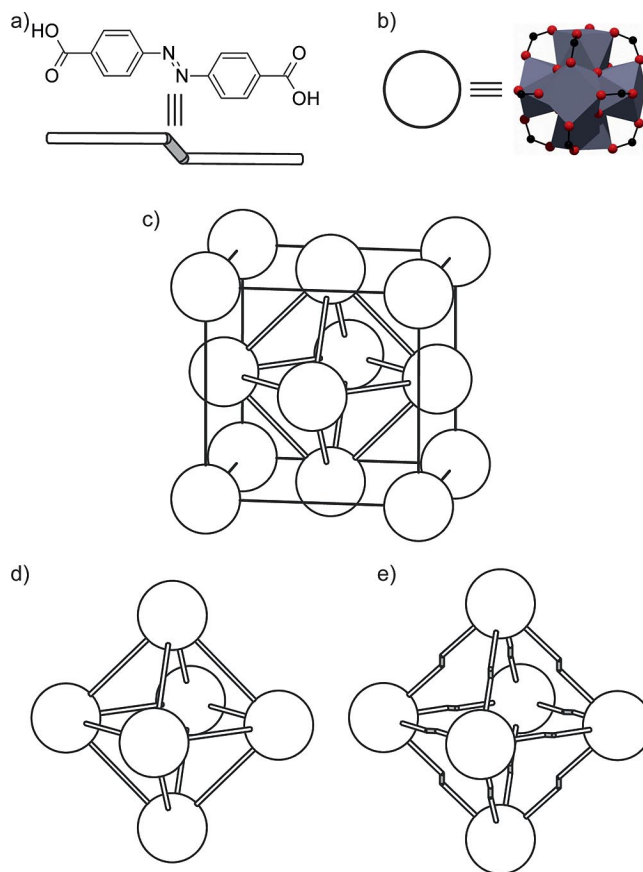
Figure 3. (a) Structural formula and schematic representation of H$_2$abdc; (b) SBU of Zr–abdc (blue: coordination polyhedral around zirconium; black: carbon; red: oxygen); (c) schematic representation of cubic close-packed spheres, which shows the arrangement of the SBUs in a PCP with UiO-66 topology (the octahedral cavity is emphasized by connections between the SBUs); (d) schematic representation of an octahedral cavity of a PCP with UiO-66 topology and with linear linkers in space group $Fm\bar{3}m$; (e) schematic representation of an octahedral cavity of Zr–abdc with an ordered arrangement of the linkers that possess staggered shapes; the specific order pattern shown here would result in a lowering of the symmetry to space group $I4/m$.

Based on the high symmetry of the space group, it was not possible to locate the atoms of the linker. Either their positions are highly disordered so that the effective electron density at certain atomic positions is too small to be detected or the linkers with their specific nonlinear shape are ordered, which breaks the high symmetry of $Fm\bar{3}m$. With regard to the former case, we can state that a comparison of the experimental PXRD data with a simulated PXRD pattern based on the partial structure derived from the SXRD data shows a very good agreement (Figure 2). For the latter case we tried to derive ordered arrangements of the linkers, one of which is shown in Figure 3e. This ordering of the linkers with their staggered structure resulted in a structure with a space group of lower symmetry ($I4/m$; $a = 20.6533$ Å, $c = 29.7535$ Å, atomic positions in Table S2), which allows the representation of the positions of the atoms of the linkers in a coherent fashion, i.e. without the need for disorder models (Figure 3e). We are aware that

lowering the symmetry during such a procedure strongly depends on the forcefield used for the modelling. The deviations between the simulated PXRD pattern of such a structure and an experimental PXRD pattern of Zr–abdc showed that a structure in which the linkers are ordered in this way cannot be justified (Figure S2). Altogether these are strong indications that the structure of the new Zr–abdc PCP has an analogous topology to the UiO-66–UiO-68 Zr-based PCPs, however, with disordered linkers. Accordingly, the new compound should have the empirical formula $Zr_6O_4(OH)_4(abdc)_6$.

To further substantiate this composition, we performed thermogravimetric analysis (TGA) on the obtained Zr–abdc materials. TGA of Zr–abdc (as-synt.) in a flow of air (Figure 4) revealed that the mass loss of the material occurs in two steps. The mass loss that occurred up to 300 °C is assigned to guest molecules that are released from the cavities. Above 400 °C, the curve shows a strong drop, which may tentatively be assigned to the combustion of the linker molecules. The final product is monoclinic ZrO_2, as identified by PXRD. As the guest contents of PCPs can differ depending on the drying procedure and guest-exchange history, the measured mass losses were corrected for the removal of guest molecules and were compared to the theoretical mass losses calculated from the empirical formula of Zr–abdc (Table 2). The comparison shows a discrepancy of about 4% between the corrected and calculated mass losses for Zr–abdc (as-synt.), i.e. the mass loss of the step tentatively ascribed to the linker decomposition is too high. We assumed that the as-synthesized compound still contained guest molecules that can only leave when the framework is destroyed (which, in turn, lowers the decomposition temperature of the compound, see the discussion below).

Table 2. Comparison of measured and calculated TGA mass loss data [%] obtained in a flow of air for Zr–abdc (as-synt.) and Zr–abdc (Sox.).

Step	Calculated	Zr–abdc (as-synt.)		Zr–abdc (Sox.)	
		Measured	Guest-free[a]	Measured	Guest-free[a]
Guests	–	19.7	–	9.8	–
Linker	67.7	57.5	71.6	61.1	67.7
Residue	32.3	22.8	28.4	29.2	32.3

[a] Mass loss after correction for removal of guest molecules.

We previously found[8] that the activation of PCP materials obtained from modulated syntheses can be difficult due to the partial occlusion of modulator molecules in the cavities of the porous materials. When the activation of the material is carried out simply by heating, trapped modulator molecules can destroy the PCP, which happens in Zr–bdc prepared with benzoic acid as the modulator.[8] The reason for this is the small window size of this PCP, which cannot let the modulator molecules pass through. With larger windows, as in Zr–bpdc, this problem disappears, because enclosed benzoic acid molecules can leave the material without hindrance. Zr–abdc should have larger windows than Zr–bpdc judging from the lattice dimensions. However, the thermal activation of Zr–abdc in the as-synthesized state appears to be difficult, which can be judged from variable-temperature PXRD patterns (Figure 5a). Zr–abdc (as-synt.) appears stable up to about 280 °C. Beyond this, the reflections of the material are broadened but do not completely disappear until 440 °C. This is an indication of partial degradation of the material above 280 °C. The reason for this could be that not all of the guest molecules were removed from Zr–abdc (as-synt.) by the standard washing procedure with DMF and ethanol. Higher than 280 °C, these remain-

Figure 4. TGA in air of Zr–abdc (as-synt.) and Zr–abdc (Sox.).
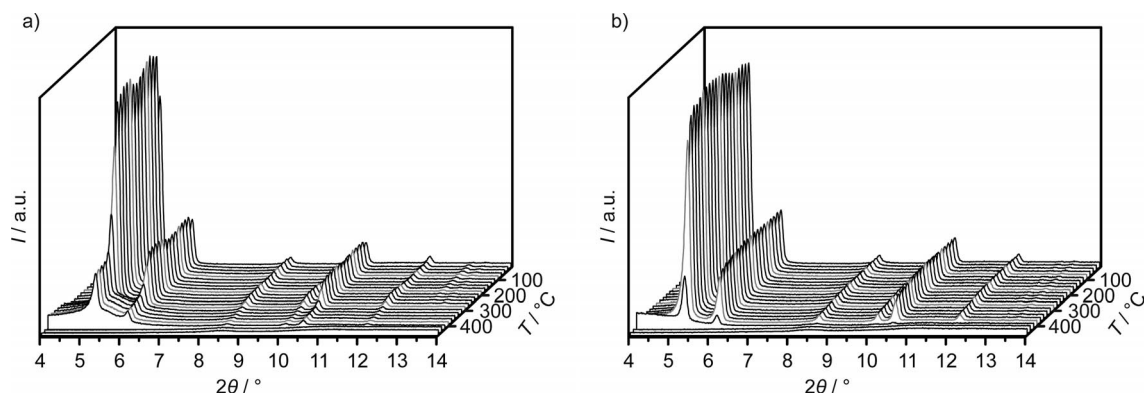
Figure 5. Variable-temperature PXRD patterns of (a) Zr–abdc (as-synt.) and (b) a Zr–abdc (Sox.).

ing guests could then destroy the framework as they leave the material and would be responsible for the increased mass loss in the TGA step that was assigned to the degradation of the linker.

We therefore chose to apply a more efficient washing procedure to remove guest molecules from Zr–abdc (as-synt.), which consisted of a Soxhlet extraction with ethanol for 24 h. The TGA of Zr–abdc (Sox.) again proceeded in two steps (Figure 4). The first step of Zr–abdc (Sox.) is assigned to the loss of guests up to 300 °C, which is considerably smaller than that of Zr–abdc (as-synt.). This shows that extraction with ethanol reduced the guest content effectively. We also found that Soxhlet extraction saves time compared to other guest removal or exchange procedures that have been applied to purify Zr PCPs.[9a] The second step that corresponds to the oxidation of the linkers again starts at ca. 400 °C. For Zr–abdc (Sox.), the corrected mass loss is in perfect accordance with the calculated mass loss of Zr–abdc (Table 2). Variable-temperature PXRD patterns of Zr–abdc (Sox.) (Figure 5b) show that the material withstands the conditions of the Soxhlet extraction. The intensities and line widths of the reflections do not change significantly up to about 400 °C, which shows that the Soxhlet extraction has led to higher thermal stability of Zr–abdc. Although Zr–abdc is stable to ambient air and moisture in the as-synthesized and the Soxhlet-extracted state, it is not stable in aqueous solution, which can be judged from a PXRD pattern measured on a sample after immersion in water for 24 h (Figure S3).

The UV/Vis spectra of H$_2$abdc and Zr–abdc (Figure S4) are similar. Both can be attributed to azobenzene chromophores with a *trans* configuration. Under irradiation at 355 nm, the *trans* isomer of free H$_2$abdc, in an aqueous solution at pH = 11, can be switched to the *cis* isomer, which results in a drastic change in the absorption properties of H$_2$abdc.[16] The *cis* isomer can relax back to the *trans* form by a thermally activated process or by irradiation at 430 nm. As our syntheses were carried out at elevated temperatures, it is not surprising that the azo group is present in its *trans* form in H$_2$abdc. Carrying out the crystallization of the Zr–abdc PCP under irradiation with UV light did not result in abdc linkers with *cis* configuration due to thermal relaxation at the high synthetic temperature. Attempts to induce *cis/trans* isomerization of the abdc linkers incorporated into the Zr–abdc PCP by using UV light were unsuccessful, because such isomerizations are impossible when the azobenzene chromophore is restrained in a rigid framework. As Stock and co-workers have explained,[17] isomerization reactions of azobenzene moieties in PCPs can only occur when the switching unit is present as a side chain to the linker (or as part of an unrestrained guest molecule).

Ar sorption experiments were carried out on Zr–abdc (Sox.) to prove the microporosity of the purified product. The Ar sorption curve shows a typical type-I isotherm with a steep increase of the curve at low P/P_0 values (Figure 6a). The specific surface area is 3000 m^2 g^{-1}, which was determined by applying the Brunauer–Emmett–Teller equation to the data. As expected, this value is similar to the specific

surface area of Zr–bpdc.[8] The pore size distribution, evaluated by nonlocal (NL) DFT fitting of the data (Figure S5), shows a maximum at 13 Å (Figure 6b). From the modelled Zr–abdc structure, the largest spheres that would fit into the voids that correspond to the octahedral and tetrahedral sites of a cubic close-packing have diameters of 15 and 11 Å, respectively. The pore size distribution gives a reasonable average of these pore sizes, and the total pore volume is 1.41 cm^3 g^{-1}.
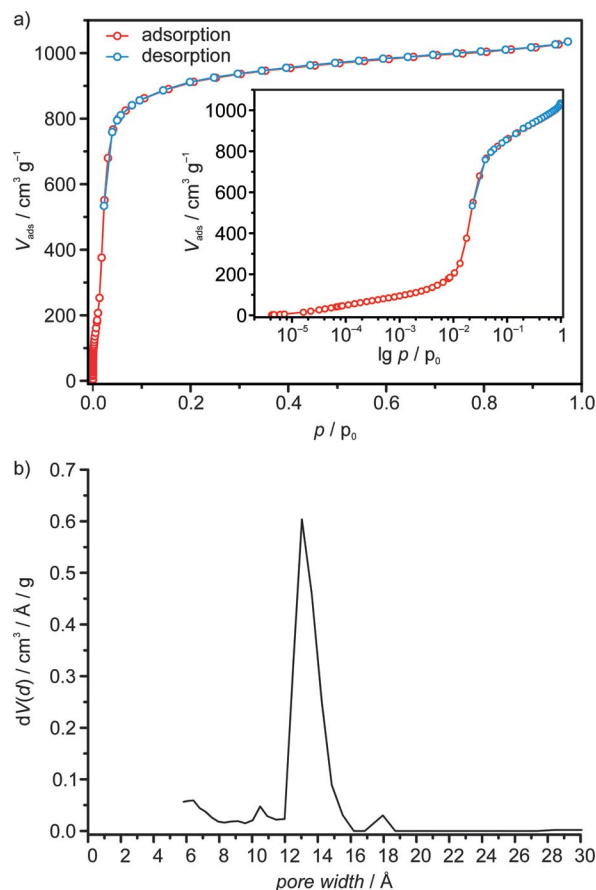
Figure 6. (a) Argon gas sorption isotherms of Zr–abdc (Sox.) (activated at 120 °C prior to sorption experiment) at –186.15 °C as linear scale plot; inset: logarithmic scale plot; red: adsorption, blue: desorption. (b) Pore size distribution of Zr–abdc (Sox.) calculated from the data given in Figure 6a.

Conclusions

We have presented the synthesis and characterization of a new Zr PCP with abdc dianions as linkers. The new compound was obtained from a synthesis modulated with benzoic acid. Evaluation of powder and single-crystal XRD data suggests that the Zr–abdc PCP has the same topology as the PCPs from the UiO-66–UiO-68 series, but the staggered structure of the linker seems to lead to high disorder and makes it impossible to determine the exact structure from SXRD experiments. TGA data and the results from sorption measurements support the proposal of the structure. For activation, it is crucial to purify Zr–abdc exten-

sively prior to thermal activation. For this purpose, Soxhlet extraction with ethanol proved to be a helpful and convenient tool, which also increased the thermal stability of the compound. As the synthesis of H$_2$abdc derivatives is modular with regard to the introduction of different organic functionalities, this compound could be the first of an isostructural series of Zr-based azo-PCPs with tuneable properties.

Experimental Section

General: All chemicals and solvents were purchased from commercial sources and were used without further purification. PXRD was carried out with a Stoe Stadi P diffractometer operated with Ge(111)-monochromatized Cu-K_α radiation (λ = 1.54060 Å) in transmission mode. Field-emission (FE) SEM images were recorded with a JEOL JESM-6700F with a semi-in-lens detector (working distance 3 mm; acceleration voltage 2 kV). Samples were prepared by dispersing in ethanol, dropping onto a carbon block and drying under reduced pressure. TGA measurements were performed with a Netzsch STA 429 thermoanalyzer. For this purpose, alumina crucibles were filled with the samples and heated under a flow of air at a rate of 5 °C/min up to 1000 °C. UV/Vis measurements of powder samples were carried out with a Varian Cary 4000 UV/Vis spectrometer in diffuse reflectance with Teflon powder as the white standard. Ar sorption isotherms were measured with a Quantachrome Autosorb-1 instrument. The sample was purified by Soxhlet extraction and activated in vacuo at 120 °C for 54 h prior to the sorption measurement. The specific surface area was determined by applying the Brunauer–Emmett–Teller equation to the P/P_0 range from 0.04 to 0.08. The measured data were fitted with the calculation model Ar at 87 K zeolites/silica (cylinder pores, NLDFT ads.) of the AS 1 Win software from Quantachrome to obtain the pore size distribution and the total pore volume. SXRD studies were carried out with a Bruker KAPPA APEX II CCD diffractometer equipped with a graphite crystal monochromator situated in the incident beam, which produces Cu-K_α radiation (λ = 1.54178 Å). Data collection was carried out at –100 °C. The SAINT program was used for integration of the diffraction profiles,[19] and adsorption corrections were applied by using the SADABS routine.[20] The structure was solved by direct methods and refined by full-matrix least squares on F^2 with anisotropic displacement using the SHELXTL software package.[21] The modelling of Zr–abdc to a structure that shows the kink in abdc$^{2–}$ was done as follows: the partial structure obtained from SXRD experiments (which contained the atoms of the SBUs) was used as a starting point. The space group was set to $P1$ and the disordered linkers were substituted by complete abdc$^{2–}$ molecules. The constructed model was submitted to a full energy minimization, which included optimization of the unit cell dimensions and metric, with parameters from the Universal Force Field as implemented in Materials Studio 5.5. The geometry optimization converged to result in a plausible tetragonal structure with the space group $I/4m$, No. 87 ($a = b = 20.6533$, $c = 29.7535$ Å, $a = \beta = \gamma = 90°$, $V = 12692$ Å^3).

Preparation of 4,4-Azobenzenedicarboxylic Acid (H$_2$abdc): H$_2$abdc was prepared according to a literature procedure.[22]

Preparation of Zr–abdc: All reactions were performed in 100 mL Teflon-capped glass flasks. In a typical synthesis, zirconium(IV) chloride (0.120 g, 0.51 mmol) and different amounts of benzoic acid (e.g. 1.884 g, 15.43 mmol) were dissolved in DMF (20 mL) by using ultrasound for ca. 1 min. To the clear solution, H$_2$abdc

(0.139 g, 0.51 mmol) was added and dispersed by ultrasound for ca. 5 min. Water (0.037 mL, 2.06 mmol) was added to the suspension, and the flask was tightly capped. The orange suspension was kept in an oven at 120 °C under static conditions. After 30 min, the linker was completely dissolved, and the solution was bright red. After 24 h, the solution was cooled to room temperature, and the precipitate was isolated by centrifugation. The solid was suspended in DMF (20 mL). After standing at room temperature for 2–6 h, the suspension was centrifuged, and the solvent was decanted. The particles were washed with ethanol (20 mL) in the same way as described for washing with DMF. Afterwards, the solids were dried in an oven at 120 °C for 2 h. Zr–abdc (as-synt.) refers to products that were produced in this way. Further purification of the PCPs was carried out by Soxhlet extraction with ethanol for 24 h and subsequent drying in an oven at 120 °C for 2 h. Zr–abdc (Sox.) refers to products that were purified in this way.

Supporting Information (see footnote on the first page of this article): Additional PXRD patterns, tables with atomic coordinates of the structural model, UV/Vis spectra of H$_2$abdc and Zr–abdc and the NLDFT fitting plot for the sorption data.

[1] S. Kitagawa, R. Kitaura, S. Noro, *Angew. Chem.* **2004**, *116*, 2388; *Angew. Chem. Int. Ed.* **2004**, *43*, 2334–2375.

[2] O. M. Yaghi, M. O'Keeffe, N. W. Ockwig, H. K. Chae, M. Eddaoudi, J. Kim, *Nature* **2003**, *423*, 705–714.

[3] M. Eddaoudi, J. Kim, N. Rosi, D. Vodak, J. Wachter, M. O'Keeffe, O. M. Yaghi, *Science* **2002**, *295*, 469–472.

[4] L. Ma, J. M. Falkowski, C. Abney, W. Lin, *Nat. Chem.* **2010**, *2*, 838–846.

[5] a) J. H. Cavka, S. Jakobsen, U. Olsbye, N. Guillou, C. Lamberti, S. Bordiga, K. P. Lillerud, *J. Am. Chem. Soc.* **2008**, *130*, 13850–13851; b) L. Valenzano, B. Civalleri, S. Chavan, S. Bordiga, M. H. Nilsen, S. Jakobsen, K. P. Lillerud, C. Lamberti, *Chem. Mater.* **2011**, *23*, 1700–1718.

[6] S. Surblé, C. Serre, C. Mellot-Draznieks, F. Millange, G. Férey, *Chem. Commun.* **2006**, 284–286.

[7] A. Schaate, P. Roy, T. Preuße, S. J. Lohmeier, A. Godt, P. Behrens, *Chem. Eur. J.* **2011**, *17*, 9320–9325.

[8] A. Schaate, P. Roy, A. Godt, J. Lippke, F. Waltz, M. Wiebcke, P. Behrens, *Chem. Eur. J.* **2011**, *17*, 6643–6651.

[9] a) S. J. Garibay, S. M. Cohen, *Chem. Commun.* **2010**, *46*, 7700–7702; b) M. Kim, S. J. Garibay, S. M. Cohen, *Inorg. Chem.* **2011**, *50*, 729–731; c) M. Kandiah, S. Usseglio, S. Svelle, U. Olsbye, K. P. Lillerud, M. Tilset, *J. Mater. Chem.* **2010**, *20*, 9848–9851.

[10] M. Kandiah, M. H. Nilsen, S. Usseglio, S. Jakobsen, U. Olsbye, M. Tilset, C. Larabi, E. A. Quadrelli, F. Bonino, K. P. Lillerud, *Chem. Mater.* **2010**, *22*, 6632–6640.

[11] V. Guillerm, S. Gross, C. Serre, T. Devic, M. Bauer, G. Férey, *Chem. Commun.* **2010**, *46*, 767–769.

[12] a) S. Diring, S. Furukawa, Y. Takashima, T. Tsuruoka, S. Kitagawa, *Chem. Mater.* **2010**, *22*, 4531–4538; b) T. Tsuruoka, S. Furukawa, Y. Takashima, K. Yoshida, S. Isoda, S. Kitagawa, *Angew. Chem.* **2009**, *121*, 4833; *Angew. Chem. Int. Ed.* **2009**, *48*, 4739–4743.

[13] F. Rakotondradany, M. A. Whitehead, A.-M. Lebuis, H. F. Sleiman, *Chem. Eur. J.* **2003**, *9*, 4471–4780.

[14] a) X. Lin, T. Liu, J. Lin, H. Yang, J. Lü, B. Xu, R. Cao, *Inorg. Chem. Commun.* **2010**, *13*, 388–391; b) B. Liu, Q. Xu, *Acta Crystallogr., Sect. E* **2009**, *65*, m509; c) C. Volkringer, T.

Loiseau, T. Devic, G. Férey, D. Popov, M. Burghammer, C. Riekel, *CrystEngComm* **2010**, *12*, 3225–3228; d) H. Furukawa, J. Kim, N. W. Ockwig, M. O'Keeffe, O. M. Yaghi, *J. Am. Chem. Soc.* **2008**, *130*, 11650–11661; e) B. Chen, S. Ma, E. J. Hurtado, E. B. Lobkovsky, H.-C. Zhou, *Inorg. Chem.* **2007**, *46*, 8490–8492; f) Z.-F. Chen, R.-G. Xiong, B. F. Abrahams, X.-Z. You, C.-M. Che, *J. Chem. Soc., Dalton Trans.* **2001**, *17*, 2453–2455; g) C.-M. Jin, Z. Zhu, Z.-F. Chen, Y.-J. Hu, X.-G. Meng, *Cryst. Growth Des.* **2010**, *10*, 2054–2056.

[15] a) Z.-F. Chen, Z.-L. Zhang, Y.-H. Tan, Y.-Z. Tang, H.-K. Fun, Z.-Y. Zhou, B. F. Abrahams, H. Liang, *CrystEngComm* **2008**, *10*, 217–231; b) Y. Liu, J. F. Eubank, A. J. Cairns, J. Eckert, V. C. Kravtsov, R. Luebke, M. Eddaoudi, *Angew. Chem.* **2007**, *119*, 3342; *Angew. Chem. Int. Ed.* **2007**, *46*, 3278–3283; c) T. M. Reineke, M. Eddaoudi, D. Moler, M. O'Keeffe, O. M. Yaghi, *J. Am. Chem. Soc.* **2000**, *122*, 4843–4844; d) V. Zeleňák, Z. Vargová, M. Almáši, A. Zeleňáková, J. Kuchár, *Microporous Mesoporous Mater.* **2010**, *129*, 354–359.

[16] G. Abellán, H. García, C. J. Gómez-García, A. Ribera, *J. Photochem. Photobiol. A: Chem.* **2011**, *217*, 157–163.

[17] A. Modrow, D. Zargani, R. Herges, N. Stock, *Dalton Trans.* **2011**, *40*, 4217–4222.

[18] G. Wißmann, A. Schaate, S. Lilienthal, I. Bremer, A. M. Schneider, P. Behrens, *Microporous Mesoporous Mater.* **2012**, *152*, 64–70.

[19] *SAINT Integration Engine*, version 7.68A, Bruker AXS, Inc., **2009**.

[20] G. M. Sheldrick, *SADABS – Area Detector Adsorption and Other Corrections*, version 2.03, Bruker AXS, Inc., **2008**.

[21] G. M. Sheldrick, *SHELXTL – Program for Solution and Refinement of Crystal Structures*, version 5.1, University of Göttingen, **1997**.

[22] P. S. Mukherjee, N. Das, Y. K. Kryschenko, A. M. Arif, P. J. Stang, *J. Am. Chem. Soc.* **2004**, *126*, 2464–2473.

 © 2012 Wiley-VCH Verlag GmbH & Co. KGaA, Weinheim

On the Coordination of Dinitrogen to Group 4 Metallocenes
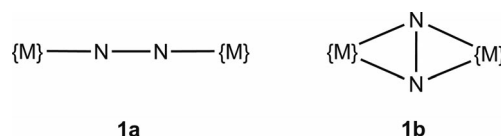
Benjamin Peigné,[a] Joan Cano,[a,b] and Gabriel Aullón*[a]

A theoretical study on the basis of DFT calculations for complexes with the general formula [{MCp$_2$}$_2$N$_2$] (M = Ti, Zr, or Hf; Cp = cyclopentadienyl ligand) is presented. The relative stability of side-on and end-on isomers is determined for each metal atom. A survey of the electronic structure and molecular orbitals provides a simple interpretation of the chemical bonding within the M$_2$N$_2$ unit and reveals the factors that determine the choice of the coordination mode of dinitrogen to metallocenes. These results have been confirmed by vibrational calculations and topological analysis of the electron density together with a structural database study. The influence of the conformational changes on some molecular properties and their implications for the N–N bonding character will be discussed.

Introduction

Ammonia is a molecule that has changed our world in the past century.[1] However, the industrial production of ammonia generated by the well-known Haber–Bosch process from its constituent elements has high energy costs.[2,3] Clearly, the best source for N$_2$ is atmospheric nitrogen, but an alternative method of N≡N triple-bond cleavage could provide a new energy-efficient synthesis. As an example of this successful result, one must take note of the biologic analogue nitrogenase, which can transform dinitrogen into ammonia under mild conditions such as room temperature and atmospheric pressure. Experimental and computational studies on homogeneous catalysis with transition-metal complexes have been made in an attempt to search for low-cost alternative mechanisms.[4]

One could consider two steps in the transformation of dinitrogen into ammonia. Initially, the molecule would be fixed to an active center; subsequently, it should be hydrogenated, and then a cleavage of the N–N bond should occur. The process of fixation can be associated with the coordination of dinitrogen to a transition metal, although its binding mode is an open question.[5–7] In a dinuclear complex, two main possibilities can be contemplated (Scheme 1): end-on coordination (**1a**) in which each nitrogen atom is coordinated to one metal atom, and side-on mode (**1b**) in which four atoms form a diamond with standard N–N bond lengths.[8] We notice that group 4 elements present either structure, without any clear preference, and display a wide range of N–N distances.

[a] Departament de Química Inorgànica and
Institut de Química Teòrica i Computacional (IQTCUB),
Universitat de Barcelona,
Avda. Diagonal 647, 08028 Barcelona, Spain
[b] Institució Catalana de Recerca i Estudis Avançats (ICREA),
Passeig Lluís Companys, 23, 08010 Barcelona, Spain
Supporting information for this article is available on the WWW under http://dx.doi.org/10.1002/ejic.201100788.

Scheme 1. Coordination modes of dinitrogen in binuclear complexes.

Some zirconium complexes have been able to coordinate N$_2$, which is subsequently hydrogenated at 1 atm of H$_2$ pressure and room temperature.[9,10] On the other hand, several group 4 metallocenes have a strong propensity to coordinate the dinitrogen molecule.[11] Hydrogenation and cleavage of dinitrogen by metallocenes have been reported recently in which the catalytic species is [Zr(η^5-C$_5$-Me$_4$H)$_2$].[12] In general, the chemistry of group 4 elements is dominated by the M^{IV} state, which is a d^0 ion, although low-valent M^{II} and M^{III} complexes promote unusual reactions. Electron-rich [MCp$_2$] (Cp = cyclopentadienyl ligand) complexes can be applied in activation reactions of small molecules such as dinitrogen.[13] However, only experimental infrared and theoretical studies for the coordination of dinitrogen to naked group 4 elements in an argon matrix have been reported up to this moment.[14]

In this paper, we apply computational methods on the basis of density functional theory to study the bonding on [M$_2$(μ-N)$_2$Cp$_4$] compounds (Cp denotes a general cyclopentadienyl ring). We present a theoretical study to analyze the influence of the metal in the relative stability of isomers, an analysis of molecular geometry, a description of the electronic structure, and stretching frequencies for the nitrogen–nitrogen bond. This study has also been completed with a structural analysis from the available experimental data. At present, only a theoretical study of the electronic structure and vibrational characterization of an end-on titanium complex has been published by Tuczek et al.[15] Con-

sequently, the goal of this article is to systematically investigate the coordination mode of dinitrogen to metallocene fragments in $[M_2Cp_4N_2]$ (M = Ti, Zr, and Hf) complexes.

Results and Discussion

Relative Stability of Isomers

A comparison of the relative energies between end-on and side-on isomers in $[M_2(C_5H_5)_4N_2]$ complexes shows a dramatic influence of the metals on the stability of these isomers (Table 1). Whereas in the Ti compound an end-on arrangement is observed for the most stable isomer, the Zr and Hf complexes prefer the side-on form. However, the replacement of C_5H_5 ligands by bulkier C_5Me_5 ones produces an extra stabilization of the end-on isomer in all cases, and even leads to a change in the order for Zr species.[16] This effect can be related to the repulsion between the two metallocene units in the side-on isomer that favors a lengthening of the metal–metal distance (about 1 Å).

Our results show the following preferential trends: (a) the side-on isomer is more stable for the heavier metals (Ti < Zr < Hf), and (b) bulky substituents in the cyclopendienyl ring destabilize the side-on isomer. These conclusions are corroborated by experimental data that show that the dinitrogen fragment adopts an end-on coordination in most titanium complexes (6 of 7 structures), whereas the side-on isomer is always observed for zirconium and hafnium species.

Table 1. Energy [kcal mol^{-1}] of the side-on isomer of $[M_2Cp_4N_2]$ complexes relative to that of the end-on form (**1a**).[a]

Cp, M	Ti	Zr	Hf
C_5H_5	+11.4	–6.7	–13.7
C_5Me_5	+36.2	+9.6	+0.3

[a] Positive and negative values correspond to the most stable end-on and side-on isomer, respectively.

Molecular Geometry

The first analyzed isomer of compounds $[M_2(C_5H_5)_4N_2]$ is the end-on one in which each nitrogen atom is coordinated to one metal atom (**1a**). The main structural parameters for the calculated geometries are shown in Table 2 together with the available experimental data. In this case, the geometries with the three studied metals are very similar.

The N–N distance of the end-on form has values of about 1.20 Å in all cases, thereby confirming a persistence of the multiple-bond character. These values are in agreement with the experimental data (1.15–1.18 Å). On the other hand, M–N distances are relatively shorter than the sum of atomic radii,[21] and the angles around the nitrogen atoms are perfectly lineal. The coordination of each metal is completed by two cyclopentadienyl ligands from the centroid of the Cp rings. The Cp ligands have a η^5 mode and Cp–M–Cp angles calculated to be about 143°. These parameters remain invariable when C_5H_5 rings are substituted by C_5Me_5 ones. However, an important change is found in the relative orientation of the cyclopentadienyl rings from different metal atoms, described by angle ω in Scheme 2. All molecular models with C_5H_5 present values equal to 0° by corresponding to an eclipsed conformation of the two MCp_2 fragments. However, a staggered conformation is observed when using C_5Me_5 (from 82 to 89°). In relation to the available experimental data retrieved from

2

Scheme 2. Definition of the relative orientation of the two metallocenes.

Table 2. Main geometric parameters[a] for experimental and optimized structures in the singlet state of $[M_2Cp_4N_2]$ complexes of group 4 with end-on coordination of dinitrogen (see **1a**).
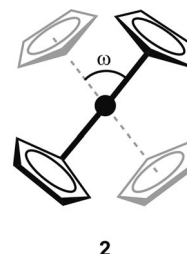
Cp	M	N–N	M–N	M–X[b]	M···M	M–N–N	X–M–X[b]	ω[c]	Ref. code	Ref.
C_5Me_5	Ti	1.155	2.023	2.067	5.198	177	146	87	NPMCTI	[17]
	Ti	1.166	2.010	2.067	5.182	177	146	85		
C_5HMe_4	Ti	1.170	1.987	2.035	5.143	179	141	7	RARMAY	[18]
$C_5H_3(SiMe_3)_2$	Ti	1.163	1.993	2.039	5.147	176	145	8	NACKAE	[19]
	Ti	1.165	1.994	2.035	5.152	177	145	2		
$C_5H_2Me_2iPr$	Ti	1.168	1.971	2.023	5.109	177	144	4	SIGJAU	[20]
C_5H_3tBu–R[d]	Ti	1.165	1.990	2.014	5.118	172	136	40	SIGJIC	[20]
$C_5H_2tBu(SiMe_3)$–R[d]	Ti	1.174	2.010	2.051	5.192	179	135	43	SIGJEY	[20]
C_5H_5	Ti	1.195	1.944	2.075	5.082	180	143	0	calcd.	
C_5Me_5	Ti	1.196	2.004	2.127	5.203	180	143	82	calcd.	
C_5H_5	Zr	1.201	2.093	2.245	5.387	180	143	0	calcd.	
C_5Me_5	Zr	1.211	2.117	2.281	5.446	180	143	82	calcd.	
C_5H_5	Hf	1.181	2.094	2.210	5.370	180	143	0	calcd.	
C_5Me_5	Hf	1.238	1.983	2.269	5.204	180	142	89	calcd.	

[a] Distances [Å] and angles [°]. [b] X is defined as the centroid of the cyclopentadienyl ring. [c] The ω value is defined as the dihedral angle X–M···M–X that shows the relative orientation of the two metallocene units. [d] A bridging $SiMe_2$ group between both rings of the same metallocene unit.

the Cambridge Structural Database, staggered, eclipsed, and intermediate conformations have been observed in titanium complexes depending on the substituents at the cyclopentadienyl rings. According to our theoretical results, the partial substitutions of the cyclopentadienyl ring ($C_5H_{5-x}R_x$) lead to a nearly eclipsed conformation ($\omega <$ 10°), whereas fully substituted rings prefer a staggered one ($\omega \approx$ 86–87°). Some exceptions are observed in two cases due to the presence of the linking chain between cyclopendienyl rings ($\omega \approx$ 40–43°).

The main structural parameters for the calculated and experimental geometries for the side-on isomer are shown in Table 3. The M_2N_2 unit makes a regular ring (1b), which in all complexes has a planar diamond core ($\theta = 180°$ in Scheme 3). However, dramatic differences are found depending on the transition metal. The calculated N–N distances in $[M_2(C_5H_5)_4N_2]$ (M = Ti, Zr, and Hf) complexes are 1.25, 1.55, and 1.42 Å, respectively. These distances can be classified as intermediate between double- and single-bond characters, and a detailed study of the electronic structure of complexes will be presented to interpret them (see below). Even a good correlation is not easy to find from the theoretical results; we can expect the staggered nature of the geometry to increase from C_5H_5 to C_5Me_5 groups ($\omega \approx$ 77°). This structural change reflects the importance of the repulsion between cyclopentadienyl rings because the metal···metal distances are now shorter than the end-on isomer due to the coordination mode adopted by the dinitrogen fragment. Whereas a quasi-eclipsed conformation is predicted for the titanium model, large ω values are expected for zirconium and hafnium. In this way, theoretical calculations on titanium models show the largest bending around metal (Cp–M–Cp angle). These conclusions could also be envisaged with the experimental data if some exceptions were considered due to the presence of steric requirements in the cyclopentadienyl rings.
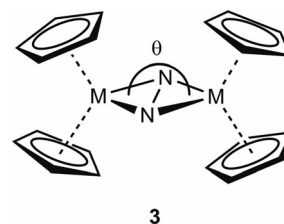
Scheme 3. Definition of the degree of planarity for the M_2N_2 core.

Vibrational Analysis

We have found optimized molecular geometries for the end-on and side-on isomers in all studied models. Thereby, the synthesis of each isomer is feasible a priori. In fact, depending on substituent groups, both isomers could be structurally characterized. Along these lines, we analyzed the vibrational frequency that corresponds to the nitrogen–nitrogen stretching mode and its relation with those distances.[8] These values are shown together with available experimental data in Table 4. As an example of the relation between stretching frequency and bond order, we have also included simple molecules that are perfectly defined such as dinitrogen, diazene, and hydrazine, as they can provide

Table 4. Values [cm^{-1}][a] for the calculated stretching mode ν_{NN} for the two isomers of $[M_2Cp_4N_2]$ complexes in the singlet state. Available experimental data are also shown.[b]

M	End-on (1a)	Side-on (1b)	Exptl.[b]
Ti	1785	1524	1755 (1a)
Zr	1817	696	775 (1b)
Hf	1676	863	n.a.

[a] Calculated values for reference: N_2: 2372 cm^{-1}; N_2H_2: 1614 cm^{-1}; N_2H_4: 1122 cm^{-1} (experimental values at 2331, 1529, and 1087 cm^{-1}, respectively).[27–29] [b] Coordination mode of the experimental structure is in parentheses.

Table 3. Main geometric parameters[a] for experimental and optimized structures in the singlet state of $[M_2Cp_4N_2]$ complexes of group 4 with side-on coordination of dinitrogen (see 1b).

Cp	M	N–N	M–N	M–X[b]	M···M	N–M–N	X–M–X	ω[c]	θ[d]	Ref. code	Ref.
$C_5H_2Me_3$	Ti	1.216	2.151	2.052	4.126	32.8	136	11	180	SIGHUM	[20]
C_5HMe_4	Zr	1.377	2.125	2.262	4.020	37.8	128	65	180	ERIJAQ	[12]
$C_5H_3(SiMe_3)_2$	Zr	1.466	2.114	2.231	3.966	40.6	133	3	180	IJIHUE	[22]
$C_5H_2Me_2Ph, C_5Me_5$	Zr	1.379	2.095	2.263	3.956	38.4	131	73	177	QAWBEW	[23]
C_5H_3tBu-R, C_5Me_4-R[e]	Zr	1.407	2.089	2.246	3.911	39.3	125	58	167	WEZVED	[24]
$C_5H_2tBu(SiMe_3)-R$[e]	Zr	1.241	2.281	2.250	4.373	31.5	125	46	180	QIDYOR	[25]
C_5HMe_4	Hf	1.423	2.081	2.237	3.910	40.0	127	65	180	REBREW	[26]
C_5H_5	Ti	1.249	2.138	2.101	4.090	34.0	136	2	180	calcd.	
C_5Me_5	Ti	1.251	2.182	2.207	4.180	33.3	131	76	180	calcd.	
C_5H_5	Zr	1.555	2.080	2.312	3.858	43.9	128	49	180	calcd.	
C_5Me_5	Zr	1.506	2.110	2.382	3.940	41.8	128	77	180	calcd.	
C_5H_5	Hf	1.421	2.079	2.272	3.908	40.0	129	52	180	calcd.	
C_5Me_5	Hf	1.404	2.102	2.352	3.965	39.0	128	78	180	calcd.	

[a] Distances [Å] and angles [°]. [b] X is defined as the centroid of the cyclopentadienyl ring. [c] The ω value is defined as the dihedral angle X–M···M–X that shows the relative orientation of the two metallocene units. [d] The θ value is defined as the bent angle between both MN_2 planes to measure the bending degree of the M_2N_2 diamond. [e] A bridging $SiMe_2$ group between both rings of the same metallocene unit.

interesting information when analyzing our theoretical results.

For titanium complexes, the calculated stretching frequencies show the existence of an N–N multiple bond close to a double bond in the side-on isomer and strongest in the end-on mode. It can be seen that the experimental frequencies agree with an end-on arrangement, as previously reported by Tuczek et al.[15] Similar results were obtained for zirconium models with an end-on form that display the highest frequency and the greatest multiple-bond character for the dinitrogen fragment. However, the zirconium side-on complex clearly shows an N–N bond that is weaker than the Ti one, which is reflected in the larger bond length and lower vibrational frequency than the hydrazine molecule. Analogous values, but closer to the hydrazine, have been predicted for the hafnium complexes.

Orbital Analysis

In an attempt to understand the different behavior of end-on and side-on isomers, we present here an analysis of the molecular-orbital diagram. From the molecular-orbital interaction, we will propose a description of the bond between metallocenes and dinitrogen. Finally, we contrast the results of population analysis to verify our interpretation of the bonding in the $\{M_2N_2\}^{4+}$ unit. Since the s orbital of nitrogen atoms is very low in energy, the interactions between dinitrogen and metallocene fragments were analyzed by using the p orbitals.[30] The combinations of these orbitals are classified according to their σ and π character. The latter are degenerate in a free molecule, but they can be differentiated in the complex as $\pi_{\parallel}$ (parallel) and $\pi_{\perp}$ (perpendicular) depending on their relative orientation with respect to the arene ligands.

Since similar results were found for the end-on isomer with the three metal atoms, we only discuss here the results of the $[Ti_2(C_5H_5)_4N_2]$ complex. However, comments for the other two transition metals are added when significant variations appear. The molecular orbitals of the Ti_2N_2 core for the interaction between dinitrogen and metallocene fragments are represented in Figure 1.[30] Among the six orbitals of dinitrogen unit, three bonding (σ + 2π) and only one antibonding (π*) orbitals can be considered to be fully occupied in the model complex. As a result of this electron configuration, one can formally suggest a value equal to two for the bond order of the dinitrogen fragment, which acquires a diazenide character, N_2^{2-}.[15]

A complete population analysis for all complexes is shown in Table 5, including atomic charges, spin densities, and orbital occupations of metal and nitrogen atoms. These data are complemented by analogous information for mononuclear complexes of the type $[M(C_5H_5)_2]$ in the Supporting Information. In the end-on $[Ti_2(C_5H_5)_4N_2]$ complex, the population analysis shows that atomic charges of Ti and N are +0.9 and –0.2, respectively, and thus only 0.4 is transferred from the metals to dinitrogen molecule (from free dinitrogen). However, this low electron transfer is re-
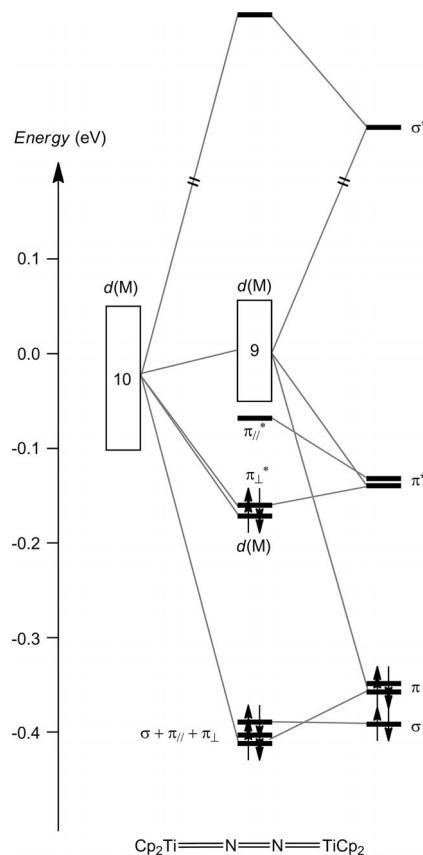

Figure 1. Diagram of the interaction between the d orbitals of two MCp_2 fragments and the dinitrogen molecule for the end-on isomer (**1a**). The number in each box indicates the quantity of molecular orbitals.

lated to a decrease in spin density on each metal of 0.7, whereas a null value is found for the nitrogen atoms. This result would be interpreted as a double-bond character of nitrogen–nitrogen, although a high degree of delocalization in the Ti=N=N=Ti unit was found when the molecular orbitals were analyzed. This formulation implies that one electron remains in a d orbital of each metal, which is assigned as Ti^{III} (d^1) in agreement with the paramagnetic nature of available experimental compounds,[17,19,20] and related ones.[31] However, our model complex has a singlet as ground state, and the optimized triplet and quintuplet excited states are placed at 9.9 and 6.9 kcal mol^{-1} (3462 and 2427 cm^{-1}), respectively. Although our calculations incorrectly predicted a strong antiferromagnetic coupling between the two metal ions, we notice that their geometries have minimal structural changes without affecting their chemical significance. Similar results were obtained for analogous compounds of Zr and Hf, and an equivalent electronic description should apply (the triplet state was only at 0.24 kcal mol^{-1}, 84 cm^{-1}, in the Zr derivative), although neither experimental compound was available to corroborate our result.

We have continued with the side-on arrangement of the $[Ti_2(C_5H_5)_4N_2]$ model complex. The molecular-orbital analysis of the Ti_2N_2 fragment in Figure 2 (left) shows an

Table 5. Population analysis (from natural population analysis) for the optimized structures of $[M_2Cp_4N_2]$ complexes in the singlet state.

	End-on isomer (**1a**)			Side-on isomer (**1b**)		
	Ti	Zr	Hf	Ti	Zr	Hf
Charges						
M	+0.87	+1.10	+1.31	+0.97	+1.56	+1.76
N	−0.19	−0.28	−0.31	−0.29	−0.74	−0.78
Spin densities[a]						
M	1.21	1.00	0.95	0.97	0.00	0.00
N	0.00	0.05	0.04	0.00	0.00	0.00
Orbital occupations						
s(M)	0.17	0.21	0.29	0.17	0.18	0.22
p(M)	0.01	0.01	0.01	0.01	0.01	0.01
d(M)	2.91	2.64	2.35	2.77	2.21	1.95
s(N)	1.42	1.44	1.42	1.54	1.63	1.57
p(N)	3.74	3.81	3.85	3.73	4.10	4.19

[a] Absolute values for each metal and nitrogen atom: antiferromagnetism or diamagnetism (see text).

electron configuration of $\sigma^2\pi^4\pi^{*2}$ for the dinitrogen ligand. Despite the different orientation of the dinitrogen, the results are similar to those obtained in end-on forms that have nearly identical populations (see Table 5). Consequently, a Ti^{III}/N_2^{2-} electron configuration should be assigned in accordance with the experimental distances.[20] These results are in agreement with those previously reported by the presence of bond lengths between bridging atoms in M_2X_2 rings and the description of the bonding in the diamond for binuclear complexes.[32,33]

However, significant changes were found in the electronic structure of zirconium and hafnium derivatives with a side-on form. Figure 2 (right) shows the molecular diagram for the zirconium complex, and an identical picture can be displayed for the hafnium one. The molecular-orbital diagram reveals that the two π orbitals are now fully occupied, thereby suggesting a $\sigma^2\pi^4\pi^{*4}$ electron configuration for the dinitrogen fragment. This result implies the presence of a single bond, perfectly supported by the large optimized N–N bond length (1.56 Å). Spin densities of Zr and N atoms take null values, and the metal has lost all the d electrons to formally become a Zr^{IV} ion, in contrast to 1.9 in the mononuclear $Zr^{II}Cp_2$ complex. Consequently, we propose that the dinitrogen group displays a hydrazinide character, N_2^{4-}.[8] A closed-shell configuration is obtained as the ground state with an optimized triplet one 6.1 kcal mol^{-1} higher in energy (2120 cm^{-1}, in which one electron remains in each metal center like the titanium complex), which is in agreement with its diamagnetic behavior. Similar conclusions were reached for the hafnium model complex. Experimental data based on line broadening in the ^1H, ^{13}C, and ^{15}N NMR spectra for Zr[12,23–25] and Hf[26] complexes confirm their diamagnetism. Finally, the different electron configuration in the heavy metals must be related as shown by the smaller fourth ionization potential of Zr (34.3) and Hf (33.3) than Ti (43.3 eV).[34]

In an attempt to evaluate the factors that govern the activation of dinitrogen by transition metals, we have compared
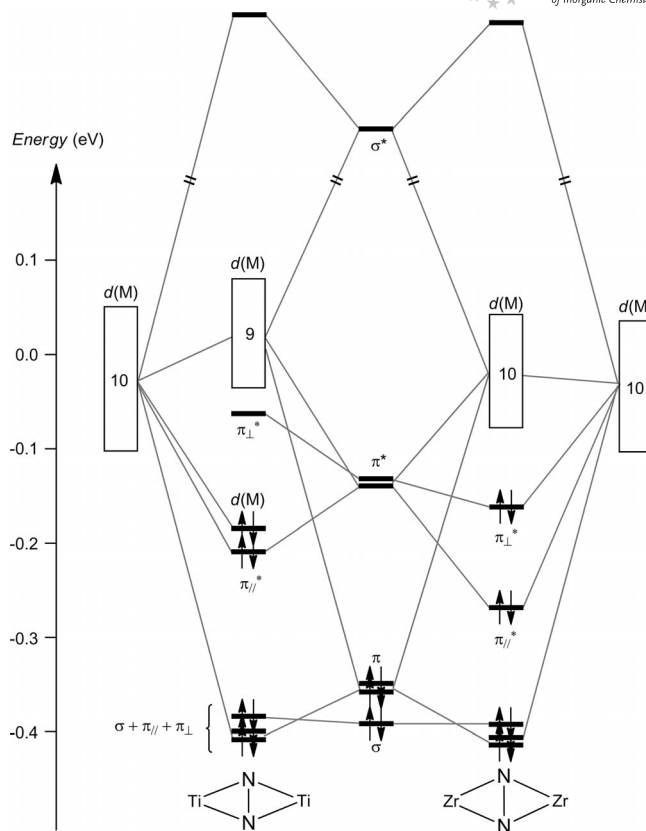

Figure 2. Diagram of the interaction between the d orbitals of two MCp_2 fragments and the dinitrogen molecule for the side-on isomer (**1b**): M = Ti (left) and M = Zr (right). The number in each box indicates the quantity of molecular orbitals.

the molecular orbitals involved in the $\{M_2N_2\}^{4+}$ unit depending on the metal atom. A detailed analysis of Figure 2 shows that the electronic configuration can be associated to the relative energy of $\pi_\perp^*(N_2)$ or d(M) molecular orbitals in a given system (see Figure 3). Despite the wide range of experimental data for the N–N distance (i.e., 1.24–1.47 Å for Zr complexes), the correlation with the electronic structure is unclear. However, those complexes with diamagnetic behavior have ω values greater than 46°, whereas for the eclipsed conformation with ω = 3° only a paramagnetic compound with a Zr_2N_2 core is observed,[22] even though it has the largest N–N distance (1.47 Å). In this case, and also for the paramagnetic side-on Ti compound, the diminished overlap between $\pi_\perp^*(N_2)$ and d(M) orbitals prevents electron transfer, thereby keeping one in each metal atom and the increase N–N double-bond character. Previous theoretical studies have confirmed the importance of the conformational angle in the mechanistic study of hydrogenation of the $[Zr_2(C_5HMe_4)_4N_2]$ complex,[35] or by comparing hydrogenated compounds such as $[Zr_2(C_5HMe_4)_4-(N_2H_2)]$.[36] The different behavior found for $[M_2Cp_4N_2]$ complexes should be related to the conformational angle ω and its subtle influence on the orbital levels. Small geometric variations in the M_2N_2 unit can modify the relative energy of the orbitals involved.[30]
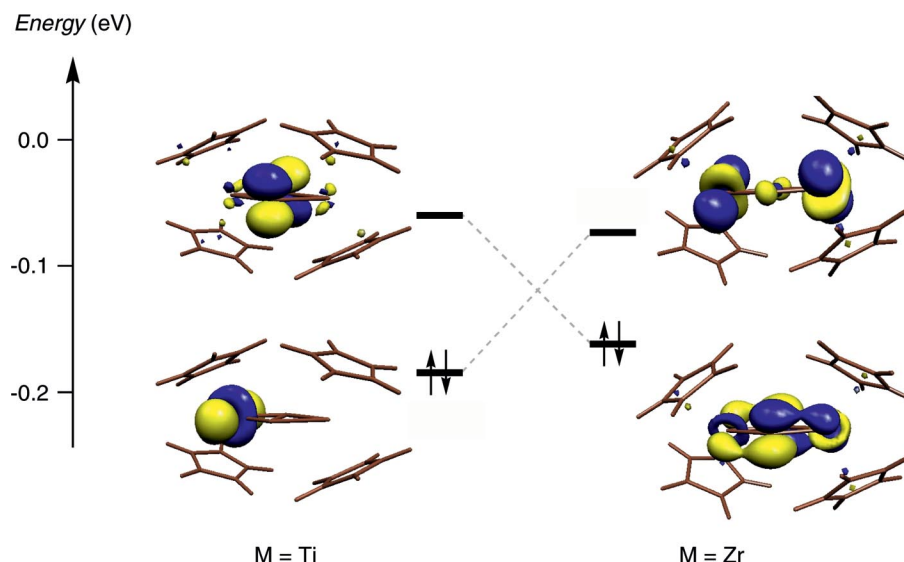
Figure 3. Composition of two of molecular orbitals that results in mixing between δd(M) and $\pi_\perp$*(N$_2$) in the side-on complexes of [M$_2$Cp$_4$N$_2$] with M = Ti and Zr.

Analysis of the Electron Density

To further characterize the electronic structure of the studied compounds, we performed a topological analysis of the electron charge density $\rho(r)$ for the optimized geometries, according to the atoms-in-molecules theory.[37,38] As pointed out by Bader, the main properties of the electron density can be summarized in terms of critical points and its number of curvatures. A bond critical point, referred to as a (3,–1) critical point, is taken as an indication of the presence of a chemical bond. In this point, the ellipticity parameter ε reflects the deviation from the circularity for this chemical bond and its relationship with multiple-bond character.

A complete list of critical points can be made, but only data from those involved in the M$_2$N$_2$ unit are shown in Table 6 and analyzed in this work. Similar values for the three metals were obtained for the end-on isomer. A critical point that corresponds to the N–N interaction has an electron density about 0.5 and a negative value of $\nabla^2\rho(r)$, thus indicating covalent character. Moreover, its low ellipticity (ε < 0.04) suggests that the triple-bond character is maintained in these species. In addition, two bond-critical points between each M–N pair with positive values of $\nabla^2\rho(r)$ are in accordance with the common feature of donor–acceptor interactions, which show great asymmetry in the electron density due to the presence of cyclopentadienyl ligands.

The side-on isomers of [M$_2$(C$_5$H$_5$)$_4$N$_2$] complexes have a cyclic structure, in which four bond-critical points between each side of the diamond contribute to donor–acceptor M–N interactions, as well as an additional bond-critical point for the N–N covalent bond across it. For the Ti compound, the Ti–N critical point has similar values to those of the end-on one but with a decrease in $\nabla^2\rho(r)$, which should indicate a weaker bond in this isomer because of the poor directionality of the bonding orbitals in the ring, according

Table 6. Properties of (3,–1) bond-critical points in the optimized structures of [M$_2$Cp$_4$N$_2$] complexes in the singlet state.[a]

| M	End-on isomer (**1a**)			Side-on isomer (**1b**)		
	Ti	Zr	Hf	Ti	Zr	Hf
M–N bonds:						
$\rho(r)$	0.10	0.09	0.09	0.07	0.10	0.10
$\nabla^2\rho(r)$	0.51	0.44	0.43	0.26	0.36	0.38
ε	0.34	0.31	0.32	0.30	0.07	0.13
N–N bonds:						
$\rho(r)$	0.48	0.47	0.53	0.43	0.21	0.31
$\nabla^2\rho(r)$	–0.98	–0.96	–1.35	–0.74	–0.03	–0.46
ε	0.03	0.02	0.04	0.02	0.12	0.09

[a] Units: ρ in e a$_o^{-3}$ (= 6.748 e Å^{-3}); $\nabla^2\rho$ in e a$_o^{-5}$ (= 24.098 e Å^{-5}).

to the longest distances found (2.14 and 1.94 Å, respectively). However, no significant variations in the N–N bond can be expected for the change in coordination mode for Ti complexes. For the Zr compound, it shows a decrease in the ellipticity of the M–N bonds that can be related to the lower contribution of the π orbital in the Zr$_2$N$_2$ ring bonding. On the other hand, for the N–N bond, $\rho(r)$ decreases and $\nabla^2\rho(r)$ is practically zero, according to the weak interaction through the diamond (1.55, which is in agreement with a larger distance for typical single bonds of 1.45 Å).[39] For the Hf complex, similar values to the Zr compound were found for M–N bonds, whereas intermediates between Ti and Zr complexes were found for the N–N one.

Mechanism for the Formation of Complexes

To analyze the formation of [M$_2$Cp$_4$N$_2$] complexes, we have studied the steps described in Scheme 4. For each one, we calculated the free-energy changes (electronic energy is in the Supporting Information) associated with pathways
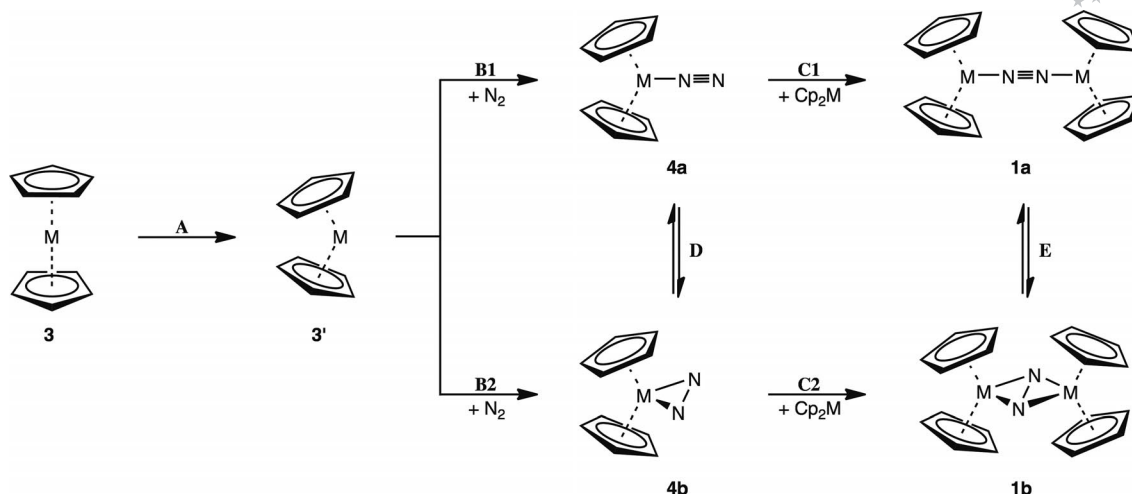
Scheme 4. Proposed stepwise mechanism to generate $[M_2Cp_4N_2]$ species.

A–E for M = Ti, Zr, and Hf in an attempt to try to unravel the factors that determine the different stabilities obtained for each metal.

The first step prior to coordination of dinitrogen to metallocene is the bending of an MCp_2 fragment (**A**). Given the centroid of the cyclopentadienyl ring, the bending of metallocenes is always unfavorable for triplet and singlet states. We have estimated that the destabilization upon bending the geometry of the MCp_2 fragment to the dinuclear complexes has values of less than 10 kcal mol^{-1}. A correlated diagram for molecular orbitals from lineal to bent geometry of MCp_2 units can be found in the Supporting Information, with a similar behavior for all three metals. The small difference in energy between the single occupied orbitals with $\delta(M–Cp)$ character explains that the triplet state is more stable than the singlet one.[40]

The second step of our system involves the coordination of dinitrogen to a bent MCp_2 fragment (**B**), thereby resulting in two alternative isomers (Scheme 5). This process is clearly favored for the two forms, with the order Ti < Zr << Hf in both cases, and the triplet state is always more stable than the singlet one. The data for equilibrium **D** shows the higher stability of **4a**, reported previously for the Zr compound,[16] but it decreases down the group. In concordance with this trend, only one end-on structure with titanium has been structurally characterized,[41] though some analogous fragments with triple bonding such as carbonyl[41] or acetylide[42–45] have similar structural trends. The geometric structures show that N–N distances are slightly shorter in the end-on isomer than in the side-on one.[16] However, they clearly indicate the presence of a strong multiple-bonding character (<1.18 Å in all cases) according to experimental data (1.12 versus 1.15 Å for the end-on titanium complex). The electronic structure presents small changes, which reduces the electron transfer in the order Ti > Zr ≈ Hf (between 0.1 and 0.3). As a result of the coordination of dinitrogen, a spin density of about 0.4 appears on the terminal nitrogen atom in the end-on form,

whereas smaller values are obtained for these atoms in the side-on one.
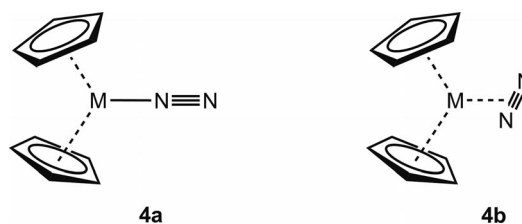
Scheme 5. Mononuclear complexes with dinitrogen ligands.

The following step in our proposed method is the addition of a second MCp_2 fragment to the dinitrogen complex. The coordination of MCp_2N_2 to a new bent MCp_2 fragment to build $M_2Cp_4N_2$ species (called **C**) is always more favorable than the previous one (**B**, from MCp_2 to MCp_2N_2). This synergic effect of the coordination of both metal fragments to the dinitrogen molecule increases when the metal decreases in group 4 (see Table 7) according to a single isolated Ti compound with the geometry of **4a**. A surprising result was obtained for Hf isomers that have values larger than 120 kcal mol^{-1}; it indicates that they should present a high affinity for the generation of Hf_2N_2 species. The analysis of the geometric structure of end-on coordination shows slight variations when a second MCp_2 is added, which can explain a shortening in the M–N distance of about 0.1 Å due to the electron delocalization from the Ti=N=N=Ti fragment (see above). However, the most important changes are detected in side-on complexes, especially for Zr and Hf complexes, due to the electron transfer that occurs only when a second MCp_2 fragment is added. These dramatic variations are a shortening in the M–N distance (>0.3 Å) and a lengthening of N–N and M–X ones (>0.3 and ca. 0.08 Å, respectively).

To analyze the effect of the first coordination of an MCp_2 fragment on the addition of a second group, we compared the energetic difference between both processes in

B. Peigné, J. Cano, G. Aullón

Table 7. Calculated free energies [kcal mol^{-1}] for the processes of formation of [M$_2$Cp$_4$N$_2$] complexes from MCp$_2$ ones and N$_2$.

Reaction[a]	Path	Ti	Zr	Hf
Planar-[MCp$_2$] (**3**) → *Bent*-[MCp$_2$] (**3′**)	**A**	+9.4 (+6.9)	+6.0 (+5.2)	+8.6 (+3.9)
Bent-[MCp$_2$] (**3′**) + N$_2$ → [MCp$_2$(η^1-N$_2$)] (**4a**)	**B1**	−14.0 (−20.3)	−22.6 (−26.4)	−126.0 (−131.2)
Bent-[MCp$_2$] (**3′**) + N$_2$ → [MCp$_2$(η^2-N$_2$)] (**4b**)	**B2**	−0.3 (−11.8)	−12.6 (−22.4)	−119.6 (−130.7)
[MCp$_2$(η^1-N$_2$)] (**4a**) + *Bent*-[MCp$_2$] (**3′**) → [M$_2$Cp$_4$(μ,η^1:η^1-N$_2$)] (**1a**)	**C1**	−22.3	−35.6	−108.9
[MCp$_2$(η^2-N$_2$)] (**4b**) + *Bent*-[MCp$_2$] (**3′**) → [M$_2$Cp$_4$(μ,η^2:η^2-N$_2$)] (**1b**)	**C2**	−22.6	−50.5	−126.1
[MCp$_2$(η^1-N$_2$)] (**4a**) → [MCp$_2$(η^2-N$_2$)] (**4b**)	**D**	+13.7 (+8.5)	+10.0 (+4.0)	+6.3 (+0.5)
[M$_2$Cp$_4$(μ,η^1:η^1-N$_2$)] (**1a**) → [M$_2$Cp$_4$(μ,η^2:η^2-N$_2$)] (**1b**)	**E**	+13.4	−5.0	−10.9

[a] Dinuclear complexes have a singlet as the ground state. Mononuclear complexes have a triplet as the ground state. Values for the singlet state are shown in parentheses in the second entry.

each case. We concluded that the binding of the second metal is generally more favorable than the former, especially for side-on isomers, which explains the high value obtained for the Zr complex (ca. 40 kcal mol^{-1}). Moreover, by combining the coordination of two MCp$_2$ fragments to the dinitrogen molecule (**B** + **C**), one can conclude that Ti prefers the end-on coordination, whereas Zr and Hf favor the side-on one. Although both process are favorable, our results reveal that the coordination of the second metal fragments is the origin of the differences in behavior between the metals. Finally, these values are slightly modified by the bending of metallocenes (**A**) to obtain the relative stability of M$_2$N$_2$ complexes shown in **E**.

Ligand-Design Complexes

According to the different distances found in the isomers, we have designed substituted cyclopentadienyl ligands to impose a specific range of metal···metal distances and to modify the relative stability of two forms. In this field, we have calculated the following molecular models with methylene bridges between cyclopentadienyl rings such as [Ti$_2$(C$_5$H$_4$\{CH$_2$\}$_n$C$_5$H$_4$)$_2$N$_2$] (Figure 4). For n = 1, the shortest Ti···Ti distances are obtained with values of 3.48 and 4.48 Å for side-on and end-on forms respectively, the former being more stable by 6.0 kcal mol^{-1}. Similarly, the larger stabilization of the side-on structure by 20.4 kcal mol^{-1} is found for n = 2, despite the fact that Ti···Ti bonds are similar to those obtained in an unbridged
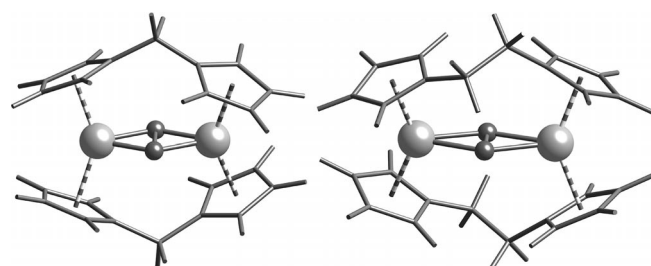
model (4.03 and 5.17 Å, respectively). We conclude that geometric restrictions can favor an unexpected isomer predicted by simple models. In summary, these models could predict the stability of a disadvantageous isomer in the presence of geometrical constraints.

Conclusion

The present theoretical studies have allowed us to understand the structural choice of the dinitrogen molecule in [M$_2$Cp$_4$N$_2$] compounds depending on the transition metal. Complexes with zirconium or hafnium prefer a side-on structure for the M$_2$N$_2$ unit, whereas titanium prefers an end-on one. The relative stability of the side-on isomer over the end-on one increases down group 4, but is not favored by bulky substituents on the cyclopentadienyl rings. However, selected bridges between terminal ligands can stabilize the side-on form for Ti complexes.

In the end-on isomer, the electronic structure shows a double-bond character between both nitrogen atoms (N$_2^{2-}$) and paramagnetic center M^{III} (d^1) ions. A similar description is obtained for the Ti complex in a side-on form, whereas Zr and Hf complexes show a d^0 center together with a hydrazinide ligand (N$_2^{4-}$). The effect of the metal is clearly significant in this isomer, in which only the III state for titanium is found. Titanium is the metal with the largest fourth ionization potential, which leaves it in a worse position to give a single N–N bond due to its ease in reaching the formal oxidation state M^{III}. This different behavior can be rationalized in terms of molecular orbitals and the relative orientation between MCp$_2$ fragments. Whereas the staggered conformation favors the largest overlap between orbitals and best electron transfer from metal to dinitrogen, an eclipsed one avoids it. These formal orders for the nitrogen–nitrogen bond are consistent with the results obtained by vibrational and atoms-in-molecules analysis.

Finally, we have investigated a series of steps to analyze the factors that determine the formation mechanism of these complexes. Although the bending of metallocenes is slightly disfavored, the coordination of dinitrogen to metal centers compensates this. The union of metallocenes to the

Figure 4. Optimized side-on structures of [Ti$_2$(C$_5$H$_4$–\{CH$_2$\}$_n$–C$_5$H$_4$)$_2$N$_2$] for n = 1 and 2.

nitrogen molecule has a synergic effect by which the first fragment enhances the coordination of the second. These two processes differentiate the preferential behavior between the three metals of group 4, although major changes in geometric and electronic structures are detected when a second fragment is bound.

Experimental Section

Computational Details: Density functional calculations were carried out using the Gaussian 03 package.[46] Open-shell calculations were performed in all cases with an unrestricted scheme in which the broken-symmetry approach was used for singlet states.[47] The hybrid DFT method known as B3LYP was applied, in which the Becke three-parameters exchange functional[48] and the Lee–Yang–Parr correlation functional were used.[49] Relativistic effective core potentials from Stuttgart–Dresden group were used to represent the innermost electrons of the transition-metal atoms and their corresponding basis set with valence double-ζ quality.[50] The basis set for the light elements (N, C, and H) was also double-ζ split-valence and included a polarization function in all atoms, proposed by Ahlrichs et al.[51] Geometry optimizations were carried out on the full potential-energy surface, without symmetry restrictions, and they were confirmed as minima by a vibrational analysis. For the topological analysis of the electron density, critical points were generated with the Xaim routine.[52]

Structural Analysis: For the experimental collection, structural data were retrieved from the Cambridge Structural Database (Version 5.31, November 2009).[53]

Supporting Information (see footnote on the first page of this article): Comparison of the main geometric and electronic data for [MCp$_2$] and [MCp$_2$N$_2$] complexes.

Acknowledgments

[1] V. Smil, *Enriching the Earth: Fritz Haber, Carl Bosch and the Transformation of World Food Production*, MIT Press, Cambridge, **2001**.

[2] K. Tamaru in *Catalytic Ammonia Synthesis* (Ed.: J. R. Jennings), Plenum, New York, **1991**.

[3] R. Schlögl, *Angew. Chem.* **2003**, *115*, 2050; *Angew. Chem. Int. Ed.* **2003**, *42*, 2004–2008.

[4] H.-J. Himmel, M. Reiher, *Angew. Chem.* **2006**, *118*, 6412; *Angew. Chem. Int. Ed.* **2006**, *45*, 6264–6288.

[5] F. Barriére, *Coord. Chem. Rev.* **2003**, *236*, 71–89.

[6] B. A. MacKay, M. D. Fryzuk, *Chem. Rev.* **2004**, *104*, 385–401.

[7] M. D. Fryzuk, *Acc. Chem. Res.* **2009**, *42*, 127–133.

[8] F. Studt, F. Tuczek, *J. Comput. Chem.* **2006**, *27*, 1278–1291.

[9] M. D. Fryzuk, J. B. Love, S. J. Rettig, *Science* **1997**, *275*, 1445–1447.

[10] Y. Ohki, M. D. Fryzuk, *Angew. Chem.* **2007**, *119*, 3242; *Angew. Chem. Int. Ed.* **2007**, *46*, 3180–3183.

[11] P. J. Chirik, *Dalton Trans.* **2007**, 16–25.

[12] J. A. Pool, E. Lobkovsky, P. J. Chirik, *Nature* **2004**, *427*, 527–530.

[13] M. D. Fryzuk, S. A. Johnson, *Coord. Chem. Rev.* **2000**, *200–202*, 379–409.

[14] G. P. Kushto, P. F. Souter, G. V. Chertihin, L. Andrews, *J. Chem. Phys.* **1999**, *110*, 9020–9031.

[15] F. Studt, N. Lehnert, B. E. Wiesler, A. Scherer, R. Beckhaus, F. Tuczek, *Eur. J. Inorg. Chem.* **2006**, 291–297.

[16] P. Bobadova-Parvanova, Q. Wang, K. Morokuma, D. G. Musaev, *Angew. Chem.* **2005**, *117*, 7263; *Angew. Chem. Int. Ed.* **2005**, *44*, 7101–7103.

[17] R. D. Sanner, D. M. Duggan, T. C. McKenzie, R. E. Marsh, J. E. Bercaw, *J. Am. Chem. Soc.* **1976**, *98*, 8358–8365.

[18] J. M. de Wolf, R. Blaauw, A. Meetsma, J. H. Teuben, R. Gyepes, V. Varga, K. Mach, N. Vledman, A. L. Spek, *Organometallics* **1996**, *15*, 4977–4983.

[19] T. E. Hanna, I. Keresztes, E. Lobkovsky, W. H. Bernskoetter, P. J. Chirik, *Organometallics* **2004**, *23*, 3448–3458.

[20] T. E. Hanna, W. H. Bernskoetter, M. W. Bouwkamp, E. Lobkovsky, P. J. Chirik, *Organometallics* **2007**, *26*, 2431–2438.

[21] B. Cordero, V. Gómez, A. E. Platero-Prats, M. Revés, J. Echeverría, E. Cremades, F. Barragán, S. Alvarez, *Dalton Trans.* **2008**, 2832–2838.

[22] J. A. Pool, E. Lobkovsky, P. J. Chirik, *J. Am. Chem. Soc.* **2003**, *125*, 2241–2251.

[23] W. H. Bernskoetter, E. Lobkovsky, P. J. Chirik, *J. Am. Chem. Soc.* **2005**, *127*, 14051–14061.

[24] T. E. Hanna, I. Keresztes, E. Lobkovsky, P. J. Chirik, *Inorg. Chem.* **2007**, *46*, 1675–1683.

[25] P. J. Chirik, L. M. Henling, J. E. Bercaw, *Organometallics* **2001**, *20*, 534–544.

[26] W. H. Bernskoetter, A. V. Olmos, E. Lobkovsky, P. J. Chirik, *Organometallics* **2006**, *25*, 1021–1027.

[27] F. Rasetti, *Proc. Natl. Acad. Sci. USA* **1929**, *15*, 234–237.

[28] V. E. Bondybey, J. W. Nibler, *J. Chem. Phys.* **1973**, *58*, 2125–2134.

[29] J. R. Durig, S. F. Bush, E. E. Mercer, *J. Chem. Phys.* **1966**, *44*, 4238–4247.

[30] A. A. Palacios, G. Aullón, P. Alemany, S. Alvarez, *Inorg. Chem.* **2000**, *39*, 3166–3175.

[31] A. Scherer, K. Kollak, A. Lützen, M. Friedemann, D. Haase, W. Saak, R. Beckhaus, *Eur. J. Inorg. Chem.* **2005**, 1003–1010.

[32] G. Aullón, P. Alemany, S. Alvarez, *J. Organomet. Chem.* **1994**, *478*, 75–82.

[33] R. S. Simons, K. J. Galat, J. D. Bradshaw, W. J. Youngs, C. A. Tessier, G. Aullón, S. Alvarez, *J. Organomet. Chem.* **2001**, *628*, 241–254.

[34] G. Aullón, M. Hamidi, A. Lledós, S. Alvarez, *Inorg. Chem.* **2004**, *43*, 3702–3714.

[35] H. Miyachi, Y. Shigeta, K. Hirao, *J. Phys. Chem. A* **2005**, *109*, 8800–8808.

[36] J. A. Pool, W. H. Bernskoetter, P. J. Chirik, *J. Am. Chem. Soc.* **2004**, *126*, 14326–14327.

[37] R. F. W. Bader, *Chem. Rev.* **1991**, *91*, 893–928.

[38] R. F. W. Bader, *Atoms in Molecules: A Quantum Theory*, Clarendon Press, Oxford, **1995**.

[39] F. H. Allen, O. Kennard, D. G. Watson, L. Brammer, A. G. Orpen, R. Taylor, *J. Chem. Soc. Perkin Trans. 2* **1987**, S1–S19.

[40] T. A. Albright, J. K. Burdett, M.-H. Whangbo, *Orbital Interactions in Chemistry*, Wiley, New York, **1985**, p. 395.

[41] T. E. Hanna, E. Lobkovsky, P. J. Chirik, *J. Am. Chem. Soc.* **2006**, *128*, 6018–6019.

[42] F. G. Kirchbauer, P.-M. Pellny, H. Sun, V. V. Burlakov, P. Arndt, W. Baumann, A. Spannenberg, U. Rosenthal, *Organometallics* **2001**, *20*, 5289–5296.

[43] K. Mach, R. Gyepes, M. Horacek, L. Petrusova, J. Kubista, *Collect. Czech. Chem. Commun.* **2003**, *68*, 1877–1896.

[44] M. Horacek, I. Cisarova, L. Lukesova, J. Kubista, K. Mach, *Inorg. Chem. Commun.* **2004**, *7*, 713–717.

[45] L. Lukesova, M. Horacek, R. Gyepes, I. Cisarova, P. Step-nicka, J. Kubista, K. Mach, *Collect. Czech. Chem. Commun.* **2005**, *70*, 11–33.

[46] M. J. Frisch, G. W. Trucks, H. B. Schlegel, G. E. Scuseria, M. A. Robb, J. R. Cheeseman, J. A. Montgomery Jr., T. Vreven, K. N. Kudin, J. C. Burant, J. M. Millam, S. S. Iyengar, J. Tomasi, V. Barone, B. Mennucci, M. Cossi, G. Scalmani, N. Rega, G. A. Petersson, H. Nakatsuji, M. Hada, M. Ehara, K. Toyota, R. Fukuda, J. Hasegawa, M. Ishida, T. Nakajima, Y. Honda, O. Kitao, H. Nakai, M. Klene, X. Li, J. E. Knox, H. P. Hratchian, J. B. Cross, C. Adamo, J. Jaramillo, R. Gomperts, R. E. Stratmann, O. Yazyev, A. J. Austin, R. Cammi, C. Pomelli, J. W. Ochterski, P. Y. Ayala, K. Morokuma, G. A. Voth, P. Salvador, J. J. Dannenberg, V. G. Zakrzewski, S. Dapprich, A. D. Daniels, M. C. Strain, O. Farkas, D. K. Malick, A. D. Rabuck, K. Raghavachari, J. B. Foresman, J. V. Ortiz, Q. Cui, A. G. Baboul, S. Clifford, J. Cioslowski, B. B. Stefanov, G. Liu, A. Liashenko, P. Piskorz, I. Komaromi, R. L. Martin, D. J. Fox, T. Keith, M. A. Al-Laham, C. Y. Peng, A. Nanayakkara, M. Challacombe, P. M. W. Gill, B. Johnson, W. Chen, M. W. Wong, C. Gonzalez, J. A. Pople, *Gaussian 03*, Revision C.2, Gaussian Inc., Wallingford, CT, **2004**.

[47] E. Ruiz, P. Alemany, S. Alvarez, J. Cano, *J. Am. Chem. Soc.* **1997**, *119*, 1297–1303.

[48] A. D. Becke, *J. Chem. Phys.* **1993**, *98*, 5648–5652.

[49] C. Lee, W. Yang, R. G. Parr, *Phys. Rev. B* **1988**, *37*, 785–789.

[50] D. Andrae, U. Haeussermann, M. Dolg, H. Stoll, H. Preuss, *Theor. Chim. Acta* **1990**, *77*, 123–141.

[51] A. Schaefer, H. Horn, R. Ahlrichs, *J. Chem. Phys.* **1992**, *97*, 2571–2577.

[52] J. C. Ortiz, C. Bo, *XAIM*, Departament de Química Física i Inorgànica (Universitat Rovira i Virgili), Tarragona (Spain), **1998**.

[53] F. H. Allen, O. Kennard, *Chem. Des. Autom. News* **1993**, *8*, 31–37.

Synthesis, Crystal Structure and Gas Adsorption Properties of Four Pd–Zn Coordination Polymers Containing Potential Catalytic Active Sites

Yuhei Miyazaki,[a] Yusuke Kataoka,[b] Tatsuya Kawamoto,*[a] and Wasuke Mori[a]

New Pd–Zn coordination polymers incorporating a Pd^{II} complex were prepared in one-pot reactions from isonicotinic acid, $K_2[PdCl_4]$ and Zn^{II} ions in water. Depending on the reaction conditions, four new types of Pd–Zn coordination polymers (one-, two- and three-dimensional networks), which consist of a Pd^{II} complex coordinated by two or four isonicotinic acids, were formed. The structures were determined by single-crystal X-ray diffraction, X-ray powder diffraction,

TGA and CHN elemental analysis. Interestingly, for the N_2 and H_2 gas adsorption measurements at 77 K and 760 Torr, two of the new Pd–Zn coordination polymers show selective H_2 gas adsorption performances. Therefore, these complexes may be potentially attractive materials for heterogeneous catalysts or for H_2 gas separation for hydrogenation reactions.

Introduction

State-of-the-art crystal engineering involves the design and synthesis of new crystalline materials with specific properties that are dictated by desired applications. Recently, the coordination polymers and metal–organic frameworks (MOFs) constructed from transition metals and organic ligands, which are crystalline porous materials, have attracted considerable attention. The control of topology and geometry of the coordination polymers makes it possible to construct the materials with different properties. Actually, such coordination polymers have been investigated with regard to their potential applications as gas storage,[1] heterogeneous catalysts,[2] magnetism,[3] sensing materials[4] and so on. Specifically, synthesis of hetero-dimetallic coordination polymers with selected complex ligands in place of organic ligands is a very attractive research area concerning applications as catalysts or sensing materials. In homogeneous systems, decomposition and elution of these functional complexes may occur in the presence of a large quantity of solvent. Accordingly, selective reaction with substances and separation of the catalyst from the solvent and products are very difficult. From this point of view, heterogeneous systems have claimed our attention. In practice, most coordination polymers are insoluble in common solvents except for water. The insolubility may result in high

stability and separation of catalysts and solvents by preventing the elution and decomposition of the polymers. Thus, in the novel highly selective and stable catalyst design, introduction of isolated complex units into a well-defined coordination sphere of a coordination polymer network is an important approach. However, heterodimetallic coordination polymers are still rare compared with the extensively studied monometallic coordination polymers and are under development.[5]

As a result, we attempted to design novel heterodimetallic coordination polymers containing Pd^{II} complex–ligand sites as potential active sites. The Pd^{II} complex is widely used in catalytic reactions such as the hydrogenation reaction,[6] Suzuki–Miyaura reaction[7] and photo-hydrogen production reaction.[8] Here, we report on the synthesis, characterization and gas adsorption properties of four Pd–Zn coordination polymers. Coordination polymers containing Pd^{II} complex–ligand sites are also extremely unexplored in heterodimetallic coordination polymers[9] (recently, our group reported on the water photo-reduction reaction using coordination polymers reported herein[10]). In the coordination polymer reported herein, complex–ligands selected as potential catalytic active sites are $[PdCl_2(H\text{-INA})_2]$[11] (H-INA = isonicotinic acid) coordinated by two N atoms of isonicotinic acid and $[Pd(H\text{-INA})_2(INA)_2]$[12] coordinated by four N atoms of H-INA and INA (Scheme 1). These units are linked through the coordination of the carboxylate group to Zn^{II} atoms to form extended frameworks: $[Zn\{PdCl_2(INA)_2\}(H_2O)_4]_n$ (**1**), $[Zn\{Pd(INA)_4\}(H_2O)_{8.5}]_n$ (**2**), $[Zn\{Pd(INA)_4\}(H_2O)_6]$ (**3**) and $[\{Zn_2(\mu_2\text{-OH})\}\{Pd(INA)_4\}Cl(H_2O)_3]_n$ (**4**). In this work, we succeeded in synthesizing these four Zn–Pd coordination polymers under different reaction conditions (temperature, addition of benzene and molar ratio of the H-INA ligand), and they were

[a] Department of Chemistry, Faculty of Science, Kanagawa University,
Hiratsuka, Kanagawa 259-1293, Japan
Fax: +81-463-58-9684
E-mail: kaw@kanagawa-u.ac.jp
[b] Department of Chemistry, Graduate School of Science, Osaka University,
Osaka 560-0043, Japan

characterized by single-crystal X-ray analysis, XRPD, elemental analysis and thermogravimetric analysis. In addition, the N_2 and H_2 gas adsorption performances of the four Zn–Pd coordination polymers are also discussed in detail.
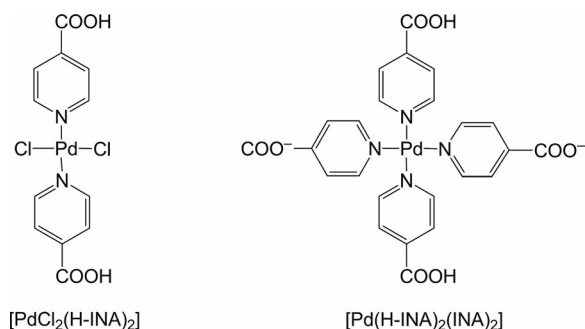
Scheme 1. Structure of the complex–ligand.

Results and Discussion

Crystal Structure of [Zn{PdCl$_2$(INA)$_2$}(H$_2$O)$_4$]$_n$ (1)

Complex **1** was prepared by a solvothermal method of a water solution containing $K_2[PdCl_2]$, H-INA and Zn-$(NO_3)_2$. The structure is a 1-D coordination polymer in which the complex–ligand [PdCl$_2$(H-INA)$_2$] acts as linear bridging ligand. The crystal view around the Zn^{II} and Pd^{II} metal centres is shown in Figure 1a. X-ray analysis reveals that the Zn^{II} atom is not bridged by the carboxylic group but by the carboxylate O atom of [PdCl$_2$(INA)$_2$] [C–O 1.260(7) and 1.268(8) Å]. In Figure 1a, the Zn^{II} atom is coordinated by four H$_2$O molecules and two carboxylate oxygen atoms of the [PdCl$_2$(INA)$_2$] units to form a 1-D chain

polymer structure. Therefore, the charge of Zn^{II} is balanced by the carboxylate groups of the [PdCl$_2$(INA)$_2$] units. The packing structure of complex **1** is shown in Figure 1b. The 1-D chain polymers are stacked along the a axis through hydrogen bonds between the coordinated H$_2$O molecules [O–O 3.007(6) Å]. Moreover, these 1-D chains are connected by hydrogen bonds between the noncoordinate carboxylate O atoms and H$_2$O molecules coordinated to the Zn^{II} atom [O–O 2.737(7) Å]. The coordination space formed by these 1-D chain polymers is too small to be filled with guest molecules. The interchain distance of Pd^{II}–Pd^{II} is 5.570(2) Å.

Crystal Structure of [Zn{Pd(INA)$_4$}(H$_2$O)$_{8.5}$]$_n$ (2)

Complex **2** was prepared by slow concentration of a water solution containing $K_2[PdCl_4]$, H-INA and Zn-$(NO_3)_2$. Complex **2** is a 3-D polymer constructed from [Pd(INA)$_4$] units and Zn^{II} atoms. The crystal structure around the metal centres is shown in Figure 2a. The Zn^{II} atom is coordinated by four different carboxylate O atoms of the [Pd(INA)$_4$] units [C–O 1.207(1)–1.266(1) Å]. The charge balance for the Zn^{II} and Pd^{II} atoms is maintained by the carboxylate groups. The 3-D network is a PtS type as shown in Figure 2b, and the open pore is almost isostructural with the previously reported Cu-MOF.[13] However, complex **2** has a twofold interpenetrated PtS network structure (Figure 2c), whereas Cu-MOFs have a non-interpenetrated structure. Therefore, complex **2** has smaller open pores and 1-D channels along the c axis (Figure 2d). The neighbouring Pd^{II}–Pd^{II} distances are 12.576 Å.

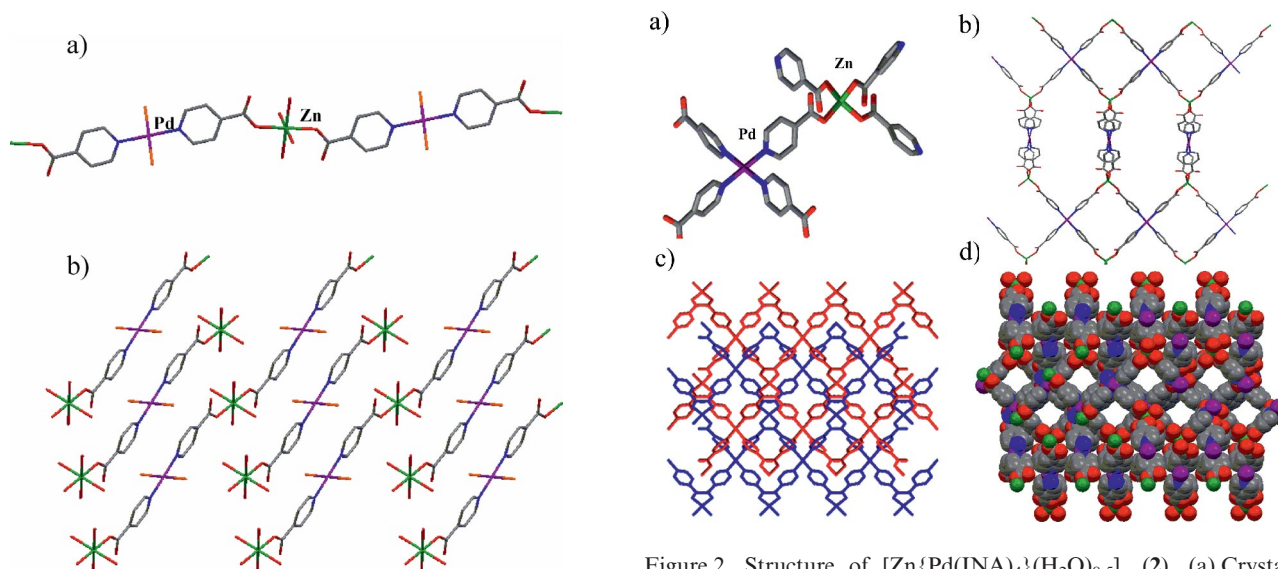Figure 1. Structure of [Zn{PdCl$_2$(INA)$_2$}(H$_2$O)$_4$]$_n$ (**1**). (a) Crystal structure around the Pd^{II} and Zn^{II} metal centres. (b) Packing view along the b axis. Hydrogen atoms are omitted for clarity. Pd atoms are shown in purple, Zn in green, C in gray, N in blue, O in red and Cl in orange.

Figure 2. Structure of [Zn{Pd(INA)$_4$}(H$_2$O)$_{8.5}$]$_n$ (**2**). (a) Crystal structure around the Pd^{II} and Zn^{II} metal centres. (b) Packing view along the c axis. (c) Two-fold PtS network structure along the c axis. (d) Space-filling model of the twofold PtS network structure. Hydrogen atoms and guest H$_2$O molecules are omitted for clarity. Pd atoms are shown in purple, Zn in green, C in gray, N in blue and O in red.

Crystal Structure of [Zn{Pd(INA)₄}(H₂O)₆] (3)

Complex **3** was synthesized by a procedure similar to that of complex **2** except for the addition of benzene. Recently, work concerning interpenetrated and non-interpenetrated isomeric structures by template molecules (benzene, oxalic acid and so on) was reported.[14] In the process of the synthesis of non-interpenetrated complex **2**, we added benzene as a template molecule to the reaction solution. Complex **3** has not a non-interpenetrated 3-D structure of complex **2** as we expected but a 0-D structure, which is constructed from mononuclear Zn^{II} atoms and [Pd(INA)₄] complex ligands. The crystal structure around the metal centres is shown in Figure 3a. Each Zn^{II} atom is tetrahedrally coordinated by two H_2O molecules and two carboxylate O atoms of the [Pd(INA)₄] units. Two Zn^{II} atoms are bridged by the two carboxylate O atoms of the four isonicotinic acids coordinated to the Pd^{II} atoms in *cis* positions [C–O 1.288(2) and 1.238(16) Å], and the other two carboxylate O atoms are noncoordinate O atoms [C–O 1.258(18) and 1.262(3) Å]. The packing view in Figure 3b shows that complex **3** forms a 2-D network through hydrogen bonds between H_2O molecules coordinated to Zn^{II} atoms and free carboxylate O atoms [O–O 2.642(2) and 2.618(2) Å], and also 1-D channels along the *a* axis by weak π–π interaction [3.712(3) Å].

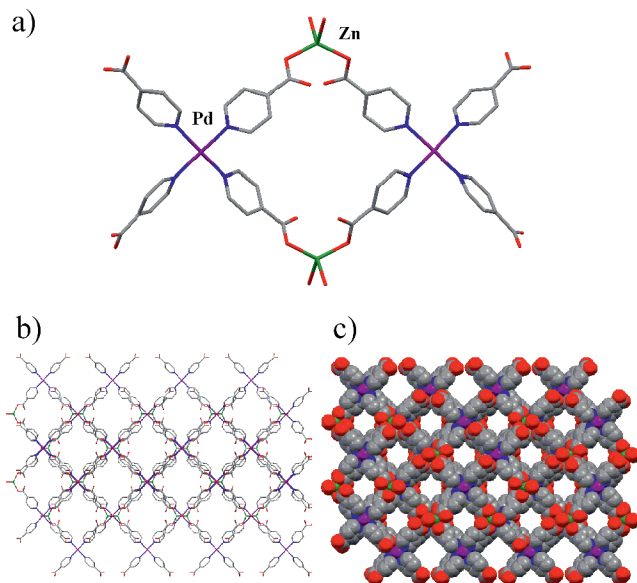Figure 3. Structure of [Zn{Pd(INA)₄}(H₂O)₆] (**3**). (a) Crystal structure around the Pd^{II} and Zn^{II} metal centres. (b) Packing view along *b* axis. (c) Space-filling model of the hydrogen network. Hydrogen atoms and guest H_2O molecules are omitted for clarity. Pd atoms are shown in purple, Zn in green, C in gray, N in blue and O in red.

Crystal Structure of [{Zn₂(μ₂-OH)}{Pd(INA)₄}Cl(H₂O)₃]ₙ (4)

This complex is constructed from Zn(OH)Zn and [Pd(INA)₄] units, a Cl counter anion and water molecules,

and the two Zn metal centres adopt different configurations. One Zn^{II} atom is tetrahedrally coordinated by one metal-bridging hydroxide anion, one H_2O molecule and two carboxylate O atoms. The other Zn atom is octahedrally coordinated by one metal-bridging hydroxide anion, one H_2O molecule and four carboxylate O atoms. The bridging Zn–O–Zn angle is 93.3(9)° and the Zn–Zn separation is 3.283(4) Å. The charge of the Zn(OH)Zn and [Pd(INA)₄] units is balanced by one free Cl anion, one hydroxide anion, two semi-chelating carboxylate anions and two monodentate carboxylate anions.

The wave-like 2-D sheet layers are stacked together along the *a* axis as shown in Figure 4c and are separated by 4.71(3) Å from each other. The shortest Pd^{II}–Pd^{II} distances are 9.561(5) Å. The 2-D sheet frameworks have 1-D channels along the *c* axis as shown in Figure 4b and d. The 1-D pores are occupied by Cl counter anions and H_2O molecules. Therefore, it is possible that the pores are opened by removing H_2O molecules.
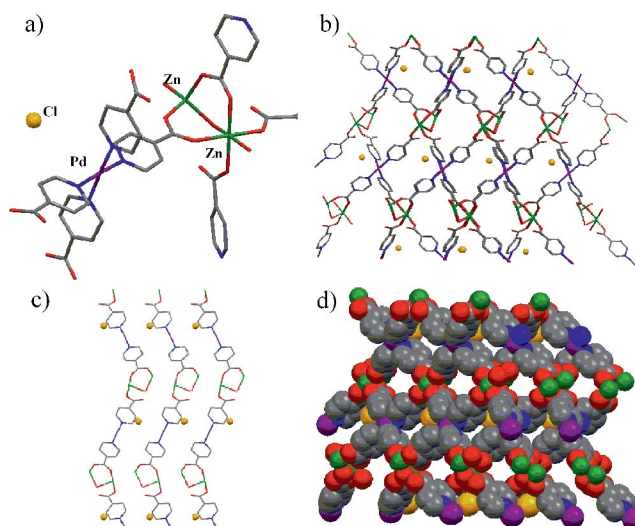

Figure 4. Structure of [Zn₂(μ₂-OH){Pd(INA)₄}Cl(H₂O)₃]ₙ (**4**). (a) Crystal structure around the Pd^{II} and Zn^{II} metal centres. (b) Packing view along the *c* axis. (c) Packing view along the *b* axis. (d) Space-filling model of the packing view. Hydrogen atoms and H_2O molecules are omitted for clarity. Pd atoms are shown in purple, Zn in green, C in gray, N in blue, O in red and Cl in orange.

Characterization of the Pd–Zn Coordination Polymers

Bulk samples of the complexes **1**–**4** are stable in air and insoluble in common organic solvents. The IR spectra show no characteristic absorption bands for any protonated H-INA, indicative of complete deprotonation of these ligands. Moreover, XRPD patterns derived from crystal structure data are fairly consistent with experimental XRPD patterns of complexes **1**–**4**, ground before measurement, although the intensities and positions of all observed peaks were not in complete agreement with those of simulated peaks. These results indicate that the bulk samples of complexes **1**–**4** have structures similar to those of their crystals (Figure S1–S4). However, the number of guest H_2O molecules was not accu-

Y. Miyazaki, Y. Kataoka, T. Kawamoto, W. Mori

rately determined by single-crystal X-ray diffraction analysis, because the guest H_2O molecules are disordered. In order to elucidate the problem, CHN elemental analysis and TGA (see Exp. Sect.) were performed. The TGA curve shows that H_2O molecules were eliminated around 373 K, and the number of H_2O molecules determined from weight loss and elemental analysis was 4.0 molecules per formula unit for complex **1**, 8.5 molecules for complex **2**, 6.0 molecules for complex **3** and 3.0 molecules for complex **4**.

N₂ and H₂ Gas Adsorption Properties

The permanent porosity of these activated Pd–Zn coordination polymers was confirmed by both N_2 and H_2. Freshly synthesized samples were activated under high vacuum at room temperature overnight and at 373 K for 4 h. Both N_2 and H_2 gas were not adsorbed by complex **1** and complex **3**. A reason for such behaviour might be that complex **1** has closed pores for gas adsorption and that the 2-D network structure of complex **3** may collapse from the removal of H_2O molecules. A small amount of N_2 gas was occupied in complexes **2** and **4** (Figure 5). As shown in Figure 5, the N_2 gas isotherms at 77 K show typical type-I adsorption behaviour with a saturated N_2 gas adsorption amount of 38.1 cm³ g⁻¹ [STP (standard temperature and pressure)] for complex **2** and 15.0 cm³ g⁻¹ (STP) for complex

4. The Langmuir surface area calculated from the N_2 gas adsorption was 111 m² g⁻¹ for complex **2** and 14.1 m² g⁻¹ for complex **4**. The surface area is small, compared with those of general coordination polymers, because both complexes lack the open pores for N_2 gas (3.64 Å)[16] adsorption. However, complexes **2** and **4** show high H_2 gas (2.80 Å) adsorption compared with N_2 gas. At low pressure, the amount of N_2 gas adsorbed is higher than that of H_2 gas. As pressure increases, both complexes have a higher H_2 gas than N_2 gas performance, and finally the adsorbed H_2 gas amounts reached 0.713 cm³ g⁻¹ (0.635wt.-%) for complex **2** and 0.401 cm³ g⁻¹ (0.357wt.-%) for complex **4**. N_2 and H_2 gas adsorption parameters are summarized in Table 1. Such selective H_2 gas adsorption behaviour versus other gases such as N_2, CH_4 and CO_2 is of interest for applications in small molecule separation and purification.[17] Complexes **2** and **4** consist of [Pd(INA)₄] units as potential catalyst sites. Therefore, these complexes may be useful as heterogeneous catalysts in hydrogenation reactions and so on.

Table 1. Gas adsorption parameters of complexes **2** and **4**.

	SA[a] [m² g⁻¹]	N₂ uptake [cm³ g⁻¹ (STP)]	Pore volume[b] [cm³ g⁻¹]	H₂ uptake[c] [wt.-%]
2	111	38.1	0.0361	0.635
4	14.1	15.0	0.0047	0.357

[a] Langmuir plots were constructed for N_2 gas adsorption isotherms, and the surface area (SA) was determined by using a linear region in the range of P/P_0 = 0.001–0.50. [b] The pore volume was calculated by the Harvous–Kawazoe method.[18] [c] The wt.-% of H_2 uptake is a multiple factor of 0.0089 [cm³ g⁻¹, STP].
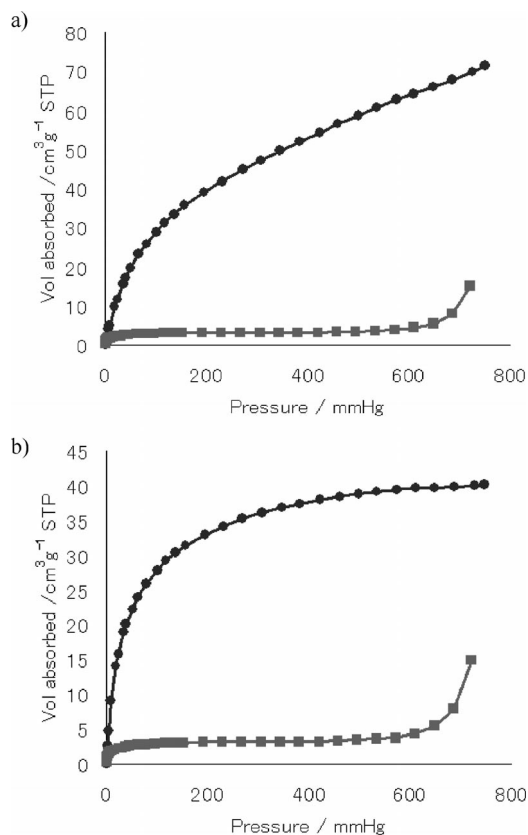
Conclusions

Four Pd–Zn coordination polymers constructed from [PdCl₂(H-INA)₂] or [Pd(H-INA)₂(INA)₂] building units as potential catalyst active sites have been prepared and structurally characterized by single-crystal X-ray structure determination, X-ray powder diffraction and so on. For the N_2 and H_2 gas measurements, gas adsorption performances were not observed for both complexes **1** and **3**. However, complexes **2** and **4** exhibit selective H_2 over N_2 gas adsorption behaviour. Therefore, it is worth noting that both of these microporous materials provide a special interest with regard to their potential applications for separation or purification of H_2 gas and for heterogeneous catalysts.

Figure 5. N_2 and H_2 gas isotherms at 77 K and 760 Torr (filled circles H_2 gas adsorption, filled squares N_2 gas adsorption) of (a) complex **2** and (b) complex **4**.

Experimental Section

Material and Physical Measurements: All reagents and solvents were used as received from commercial suppliers without further purification. FTIR spectra were measured with a JASCO FTIR 650 in the form of KBr plates in the range 4000–400 cm⁻¹. Thermogravimetric analyses (TGA) were performed with a Rigaku TG-8101D in air from 298 to 773 K with a heating rate of 5 K min⁻¹. X-ray powder diffraction (XRPD) patterns were measured with a Bruker spectrometer at 35 kV, 200 mA for Cu-K_α radiation (λ = 1.5418 Å). The elemental analyses for C, H, N were performed with a Perkin–Elmer 240 CHN Analyzer.

Table 2. Crystal data of complexes **1**–**4**.

	1	**2**	**3**	**4**
Empirical formula	$C_{12}H_{18}Cl_2N_2O_8PdZn$	$C_{24}H_{16}N_4O_8PdZn$	$C_{48}H_{40}N_8O_{22}Pd_2Zn_2$	$C_{24}H_{24}ClN_4O_{10}PdZn_2$
M_r [g mol^{-1}]	558.95	694.33	1424.44	801.09
Crystal system	triclinic	orthorhombic	monoclinic	orthorhombic
Space group	$P\bar{1}$	$Ccca$	$C2/c$	$Cmc2_1$
a [Å]	5.570(2)	16.958(9)	18.749(5)	12.903(6)
b [Å]	6.6885(18)	18.523(4)	27.465(6)	11.864(4)
c [Å]	12.863(3)	25.085(12)	16.390(4)	24.7645(10)
α [°]	71.51(2)	90	90	90
β [°]	79.41(3)	90	125.015(5)	90
γ [°]	83.69(3)	90	90	90
V [Å^3]	446.0(3)	7934(9)	6912(3)	3791(2)
Z	1	8	4	4
$D_{calcd.}$ [mg m^{-3}]	2.081	1.163	1.769	1.403
$F(000)$	278	3894	3720	1569
GOF	1.009	1.007	1.001	1.586[15]
R_{int}	0.057	0.039	0.037	0.048[15]
R_1[a] [$I > 2\sigma(I)$]	0.0484	0.1007	0.0431	0.1170[15]
wR_2[b] (all data)	0.1488	0.1878	0.1317	0.3111[15]

[a] $R_1 = \Sigma(||F_o| - |F_c||)/\Sigma|F_o|$. [b] $wR_2 = \{\Sigma[w(F_o^2 - F_c^2)^2]/\Sigma[w(F_o^2)^2]\}^{1/2}$.

Synthesis of [Zn{PdCl$_2$(INA)$_2$}(H$_2$O)$_4$]$_n$ (1): A mixture of K$_2$[PdCl$_4$] (0.05 mmol), H-INA (0.10 mmol) and Zn(NO$_3$)$_2$ (0.10 mmol) was dissolved in distilled water (6 mL) at room temperature. The solution was placed into the stainless-steel container and heated at 373 K for 24 h. After cooling to room temperature, yellow, plate-like crystals were filtered, washed with distilled water and dried at room temperature. [Zn{PdCl$_2$(INA)$_2$}(H$_2$O)$_4$] (560.0): calcd. C 25.78, H 2.89, N 5.01; found C 26.13, H 2.92, N 5.07. Solvent content calcd. from the proposed formula: H$_2$O 12.88; found (determined by TGA): 12.85.

Synthesis of [Zn{Pd(INA)$_4$(H$_2$O)$_{8.5}$]$_n$ (2): A mixture of K$_2$[PdCl$_4$] (0.05 mmol), H-INA (0.20 mmol) and Zn(NO$_3$)$_2$ (0.10 mmol) was dissolved in distilled water (6 mL) at room temperature. The solution was transferred into a 20 mL sample vial and allowed to stand for 2 weeks. The obtained colourless, block-like crystals were filtered, washed with distilled water and dried at room temperature. [Zn{Pd(INA)$_4$}(H$_2$O)$_{8.5}$] (813.4): calcd. C 35.73, H 4.09, N 6.82; found C 35.44, H 4.39, N 6.89. Solvent content calcd. from the proposed formula: H$_2$O 18.81; found (determined by TGA): 21.97.

Synthesis of [Zn{Pd(INA)$_4$}(H$_2$O)$_6$] (3): A mixture of K$_2$[PdCl$_4$] (0.05 mmol), H-INA (0.20 mmol) and Zn(NO$_3$)$_2$ (0.10 mmol) was dissolved in distilled water (6 mL) and benzene (1 mL) at room temperature. The solution was transferred into a 20 mL sample vial and allowed to stand for 1 week. The obtained colourless, block-like crystals were filtered, washed with distilled water and dried at room temperature. [Zn{Pd(INA)$_4$}(H$_2$O)$_6$] (768.3): calcd. C 37.28, H 4.18, N 7.25; found C 37.32, H 4.32, N 7.25. Solvent content calcd. from the proposed formula: H$_2$O 13.99; found (determined by TGA): 13.65.

Synthesis of [{Zn$_2$(μ_2-OH)}{Pd(INA)$_4$}Cl(H$_2$O)$_3$]$_n$ (4): A mixture of K$_2$[PdCl$_4$] (0.05 mmol), H-INA (0.20 mmol) and Zn(NO$_3$)$_2$ (0.10 mmol) was dissolved in distilled water (6 mL) at room temperature. The solution was transferred into the stainless-steel container and heated at 373 K for 24 h. After cooling to room temperature, colourless, block-like crystals were filtered, washed with distilled water and dried at room temperature. [{Zn$_2$(μ_2-OH)}{Pd(INA)$_4$}Cl(H$_2$O)$_3$] (832.1): calcd. C 35.02, H 2.69, N 6.81; found C 35.44, H 3.34, N 6.89. Solvent content calcd. from the proposed formula: H$_2$O 5.41; found (determined by TGA): 5.97.

Gas Adsorption Measurements: The gas adsorption measurements were carried out with a Micromeritics ASAP 2010 instrument, and from these sorption curves the specific surface area was determined. Freshly prepared samples were activated at room temperature under high vacuum for 20 h and at 373 K for 4 h prior to measurements. The adsorption isotherms for the N$_2$ and H$_2$ gas were recorded at liquid N$_2$ temperature (77.35 K).

Single-Crystal X-ray Structure Determination: Intensity data for the reported Pd–Zn coordination polymers were collected at 100 K with a Rigaku Mercury diffractometer equipped with graphite-monochromated Mo-K_α radiation ($\lambda = 0.71073$ Å). The structure was solved by direct methods and subsequent difference Fourier syntheses and refined on F^2 by full-matrix least squares using the SIR-92 program package.[19] All non-hydrogen atoms were refined anisotropically. Hydrogen atoms were located in the calculated positions and refined by using a riding model. The H atoms of the noncoordinated H$_2$O molecules could not be located but are included in the formula. The detailed crystal data of complexes **1**–**4** are shown in Table 2. CCDC-841702 (**1**), -770549 (**2**), -871700 (**3**), and -871701 (**4**) contain the supplementary crystallographic data for this paper. These data can be obtained free of charge from The Cambridge Crystallographic Data Centre from www.ccdc.cam.ac.uk/data_request/cif.

Supporting Information (see footnote on the first page of this article): XRPD patterns of complexes **1**–**4**.

Acknowledgments

[1] a) W. Mori, F. Inoue, K. Yoshida, H. Nakayama, S. Takamizawa, M. Kishita, *Chem. Lett.* **1997**, 1291; b) H. K. Chae, D. Y. Siberio-perez, J. Kim, Y. Go, M. Eddaoudi, A. J. Matzger, M. O'Keeffe, O. M. Yaghi, *Nature* **2004**, *427*, 523; c) S. Takamiz-

awa, E. Nakata, H. Yokoyama, K. Mochizuki, W. Mori, *Angew. Chem.* **2003**, *115*, 4467; *Angew. Chem. Int. Ed.* **2003**, *42*, 4331; d) S. Kitagawa, R. Kitaura, S. Noro, *Angew. Chem.* **2004**, *116*, 2388; *Angew. Chem. Int. Ed.* **2004**, *43*, 2334; e) K. Seki, W. Mori, *J. Phys. Chem. B* **2002**, *106*, 1380; f) S. Xiang, Z. Zhang, C.-G. Zhao, K. Hong, X. Zhao, D.-R. Ding, M.-H. Xie, C.-D. Wu, M. C. Das, R. Gill, K. M. Thomas, B. Chen, *Nat. Commun.* **2011**, *2*, 204; g) B. Chen, X. Zhao, A. Putkham, K. Hong, E. B. Lobkovsky, E. J. Hurtado, A. J. Fletcher, K. M. Thomas, *J. Am. Chem. Soc.* **2008**, *130*, 6411.

[2] a) S. Naito, T. Tanibe, E. Saito, T. Miyao, W. Mori, *Chem. Lett.* **2001**, 1178; b) C. N. Kato, M. Hasegawa, T. Sato, A. Yoshizawa, T. Inoue, W. Mori, *J. Catal.* **2005**, *230*, 226; c) Y. Kataoka, K. Sato, Y. Miyazaki, K. Masuda, H. Tanaka, S. Naito, W. Mori, *Energy Environ. Sci.* **2009**, *2*, 397; d) Y. Kataoka, K. Sato, Y. Miyazaki, Y. Suzuki, H. Tanaka, Y. Kitagawa, T. Kawakami, M. Okumura, W. Mori, *Chem. Lett.* **2010**, *39*, 358; e) C. D. Wu, W. Lin, *Angew. Chem.* **2007**, *119*, 1093; *Angew. Chem. Int. Ed.* **2007**, *46*, 1075.

[3] a) K. Barthelet, K. Adil, F. Millange, C. Serre, D. Riou, G. Ferey, *J. Mater. Chem.* **2003**, *13*, 2208; b) T. Ohmura, W. Mori, M. Hasegawa, T. Takei, T. Ikeda, E. Hasegawa, *Bull. Chem. Soc. Jpn.* **2003**, *76*, 1387; c) S. Konar, P. S. Mukherjee, E. Zangrando, F. Lloret, N. R. Chaudhuri, *Angew. Chem.* **2002**, *114*, 1631; *Angew. Chem. Int. Ed.* **2002**, *41*, 1561.

[4] a) A. Kobayashi, H. Hara, S. Noro, M. Kato, *Dalton Trans.* **2010**, *39*, 3400; b) J. W. Yoon, S. H. Jhung, Y. K. Hwang, S. M. Humphrey, P. T. Wood, J.-S. Chang, *Adv. Mater.* **2007**, *19*, 1830.

[5] a) K. C. Szeto, K. O. Kongshaug, S. Jakobsen, M. Tilset, K. P. Lillerud, *Dalton Trans.* **2008**, 2055; b) R. Kitaura, G. Onoyama, H. Sakamoto, R. Matsuda, S. Noro, S. Kitagawa, *Angew. Chem. Int. Ed.* **2004**, *43*, 2643; c) S. Noro, H. Miyasaka, S. Kitagawa, T. Wada, T. Okubo, M. Yamashita, T. Mitani, *Inorg. Chem.* **2005**, *44*, 1; d) S. H. Cho, B. Ma, S. T. Nguyen, J. T. Hupp, T. E. Albercht-Schmitt, *Chem. Commun.* **2006**, 2563; e) M. C. Das, S. Xiang, Z. Zhang, B. Chen, *Angew. Chem. Int. Ed.* **2011**, *50*, 10510–10520.

[6] a) Y. Q. Wang, S. M. Lu, Y. G. Zhou, *J. Org. Chem.* **2007**, *72*, 3729; b) Y. Z. Hao, Z. X. Li, J. L. Tian, *J. Mol. Catal. A* **2007**, *256*, 258.

[7] a) S. Gulcemal, I. Kani, F. Yilmaz, B. Cetinkaya, *Tetrahedron* **2010**, *66*, 5602; b) N. Miyaura, A. Suzuki, *Chem. Rev.* **1995**, *95*, 2457; c) A. Suzuki, *J. Organomet. Chem.* **1999**, *576*, 147.

[8] a) S. Rau, B. S. D. Gleich, E. Anders, M. Rudolph, M. Friendrich, H. Gorls, W. Henry, J. G. Vos, *Angew. Chem.* **2006**, *118*, 6361; *Angew. Chem. Int. Ed.* **2006**, *45*, 6215; b) P. Lei, M. Hedlund, R. Lomoth, H. Rensmo, O. Johansson, L. Hammarstrom, *J. Am. Chem. Soc.* **2008**, *130*, 27; c) P. N. Curtin, L. Tinker, C. M. Burgess, E. D. Cline, S. Bernhard, *Inorg. Chem.* **2010**, *49*, 210.

[9] a) J. Hafizovic, A. Krivokapic, K. C. Szeto, S. Jakobsen, K. P. Lillerud, U. Olsbye, M. Tilser, *Cryst. Growth Des.* **2007**, *7*, 2302; b) A. D. Burrows, M. F. Mahon, C. T. F. Wong, *CrystEngComm* **2008**, *10*, 48; c) L. A. Gerrard, P. T. Wood, *Chem. Commun.* **2000**, 2107.

[10] Y. Miyazaki, Y. Kataoka, Y. Kitagawa, M. Okumura, W. Mori, *Chem. Lett.* **2010**, *39*, 878.

[11] Z. Qin, M. C. Jennings, R. J. Puddephat, K. W. Muir, *Inorg. Chem.* **2002**, *41*, 5174.

[12] C. B. Aakeroy, A. M. Beatty, D. S. Leinen, *Angew. Chem. Int. Ed.* **1999**, *38*, 12.

[13] L. Ma, A. Jin, Z. Xie, W. Lin, *Angew. Chem.* **2009**, *121*, 10089; *Angew. Chem. Int. Ed.* **2009**, *48*, 9905.

[14] a) S. Bureekaew, H. Sato, R. Matsuda, Y. Kubota, R. Hirose, J. Kim, K. Kato, M. Tanaka, S. Kitagawa, *Angew. Chem.* **2010**, *122*, 1; *Angew. Chem. Int. Ed.* **2010**, *49*, 1; b) L. Ma, W. Lin, *J. Am. Chem. Soc.* **2008**, *130*, 13834; c) S. Ma, D. Sun, M. Ambrogio, J. A. Fillinger, S. Parkin, H. C. Zhou, *J. Am. Chem. Soc.* **2007**, *129*, 1858.

[15] The GOF and *R* values of complex **4** are relatively high compared with those of the other Zn–Pd complexes. We assume that the results are derived from the large disorder of the Cl counter anion, because the R_{int} value is similar to those of the other complexes.

[16] B. Chen, S. Ma, F. Zapata, F. R. Fronczek, E. B. Lobkovsky, H. C. Zhou, *Inorg. Chem.* **2007**, *46*, 1233.

[17] a) T, S. Ma, F. Zapata, E. B. Lobkovsky, J. Yang, *Inorg. Chem.* **2006**, *45*, 5718; b) J. A. R. Nvaro, E. Barea, A. R. Dieguez, J. M. Salas, C. O. Ania, J. B. Parra, N. Masciocchi, S. Galli, A. Sironi, *J. Am. Chem. Soc.* **2008**, *130*, 3978; c) D. K. Samsoneko, H. Kim, Y. Sun, G. H. Kim, H. S. Kim, K. Kim, *Chem. Asian J.* **2007**, *1*, 484; d) Z. Chen, S. Xiang, H. D. Arman, P. Li, S. Tidrow, D. Zhao, B. Chen, *Eur. J. Inorg. Chem.* **2010**, *24*, 3475.

[18] G. Horvath, K. Kawazoe, *J. Chem. Eng. Jpn.* **1983**, *16*, 470.

[19] A. Altomare, G. Cascarano, C. Giacovazzo, A. Guagliardi, M. C. Burla, G. Polidori, M. Camalli, *J. Appl. Cryst.* **1994**, *27*, 435.

Pyridocarbazole-Rhodium(III) Complexes as Protein Kinase Inhibitors

Sandra Dieckmann,[a] Radostan Riedel,[a] Klaus Harms,[a] and Eric Meggers*[a]

Inert metal complexes are sophisticated structural scaffolds for the design of enzyme inhibitors. Whereas previous work from our laboratory was predominantly based on ruthenium(II), this study evaluates the suitability of rhodium in the +3 oxidation state to serve as a structural centre for the design of inert metal-based enzyme inhibitors. Based on our established staurosporine-inspired metallo-pyridocarbazole scaffold, strategies for the convenient synthesis of rhodium(III)-pyridocarbazole complexes were developed and applied to the synthesis of protein kinase inhibitors. The structures of several rhodium complexes were investigated by X-ray crystallography. A stability study confirmed the high kinetic inertness of such rhodium complexes under biologically relevant conditions, such as the presence of millimolar concentrations of thiols. Finally, an extremely potent, picomolar rhodium inhibitor for the protein kinase Pim1 was discovered. Thus, it can be concluded that rhodium(III) expands the toolbox for the design of inert metal complexes with biological activity.

Introduction

The development of small synthetic compounds for biomedical research and drug development is predominantly based on organic scaffolds, whereas metal-based compounds play only a niche role.[1] However, our laboratory is focused on exploiting kinetically inert metal complexes – especially octahedral coordination compounds – as sophisticated structural scaffolds for the design of enzyme inhibitors.[2] Metal complexes offer a very rich stereochemistry with high structural diversity and thus provide the opportunity to access unexplored chemical space together with the prospect for the discovery of compounds with new biological properties.[3] In this metal-templated design, the metal exerts a solely structural role by serving as a substitutionally inert centre around which mostly organic ligands are assembled to form defined shapes which can occupy protein pockets such as enzyme-active sites in unique fashions and, according to our experiences, with astonishing target selectivities that can be traced back to the mostly rigid globular nature of the structures.[4]

Along these lines, we successfully established half-sandwich[5] and octahedral metal complexes[4,6,7] as highly potent and selective inhibitors of protein and lipid kinases. The overall design of metal-containing kinase inhibitors was initially inspired by the potent but unselective natural ATP-competitive kinase inhibitor staurosporine, in which the bidentate pyridocarbazole ligand replaces the indolocarbazole aglycon of staurosporine, whereas the carbohydrate moiety is formally replaced by a metal complex fragment (Figure 1).[2,8,9] Interestingly, the kinase inhibition properties of such metallo-pyridocarbazole complexes differ markedly from staurosporine, even though several crystal structures confirmed a staurosporine-like binding of metallo-pyridocarbazoles in the ATP binding sites of the respective protein and lipid kinases.[4–8]
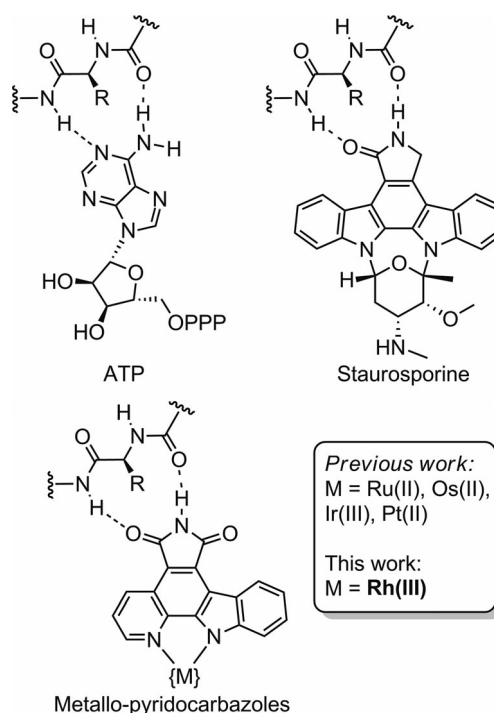

Figure 1. Pyridocarbazole metal complexes as protein kinase inhibitors inspired by the natural product staurosporine. Shown are the binding of ATP (PPP = triphosphate), staurosporine and metallo-pyridocarbazoles to the hinge region of protein kinases.

[a] Fachbereich Chemie, Philipps-Universität Marburg,
Hans-Meerwein-Straße, 35043 Marburg, Germany
E-mail: meggers@chemie.uni-marburg.de

A prerequisite for the outlined metal-based strategy is high stability of the metal complexes when exposed to the biological environment. Previous work from our group was mainly based on ruthenium(II)[4–8] but we also reported inhibitors with the late transition metals osmium(II),[10] iridium(III)[4,11] and platinum(II).[12] Reports from several groups over the last few years have revealed the suitability of rhodium for the design of metal-based anticancer candidates and here we now demonstrate that rhodium in the oxidation state III also serves as a powerful structural centre for designing inert metal-based enzyme inhibitors.[13] We report strategies for the rapid synthesis of octahedral rhodium(III) complexes bearing the pyridocarbazole heterocycle, investigations of the structures of several complexes by X-ray crystallography and demonstrate the high kinetic stability of such complexes under biologically relevant conditions. Furthermore, we reveal the highly potent inhibition of protein kinases by pyridocarbazole-rhodium(III) complexes.

Results and Discussion

Rhodium(III) Precursor Complexes

All rhodium(III) complexes discussed here contain a bidntate pyridocarbazole ligand (1a–c)[14] in its mono-anionic, indole-deprotonated form (Scheme 1). The benzyl or methyl groups of the pyridocarbazoles 1a and 1b, respectively, served as a crystallisation handle for model studies, whereas the TBS-protected pyridocarbazole 1c was employed for the synthesis of bioactive rhodium complexes which are capable of interacting with the ATP-binding site of kinases. As indicated in Figure 1, the free imide function is important for the bioactivity through its hydrogen bonding to the hinge region of protein kinases.
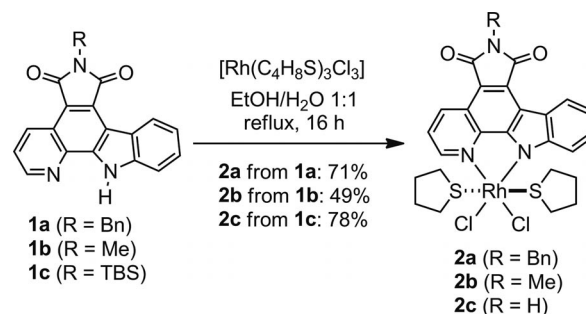
Scheme 1. Synthesis of reactive pyridocarbazole-Rh^III precursor complexes; TBS = *tert*-butyldimethsilyl.

Previous related studies with ruthenium(II) revealed that it is desirable to gain access to reactive metal-pyridocarbazole complexes in which the four remaining sites of the octahedral coordination sphere are occupied by labile monodentate ligands.[6] Such precursor complexes then enable the convenient and rapid synthesis of a large variety of different metal pyridocarbazole complexes either in individual or combinatorial reactions by ligand substitutions with other mono-, bi- and tridentate ligands or combinations thereof.[6] We achieved the synthesis of such a pyridocarbazole-Rh^III precursor complex as shown in Scheme 1. Accordingly, the reaction of the heterocycles 1a–c with [Rh(C₄H₈S)₃Cl₃][15] in 1:1 EtOH/H₂O under reflux for 16 h provided the complexes 2a–c in yields of 49–78%. The benzyl group at the maleimide moiety of complex 2a enabled us to obtain a crystal structure of 2a (Figure 2, Table 1). The structure reveals that rhodium is coordinated in a bidentate fashion to the deprotonated pyridocarbazole ligand 1a, in addition to the coordination of two chlorides in a *cis* and two tetrahydrothiophene ligands in a *trans* fashion. Complexes 2a–c are fairly stable at room temperature but undergo ligand exchange reactions under elevated temperature as outlined below.
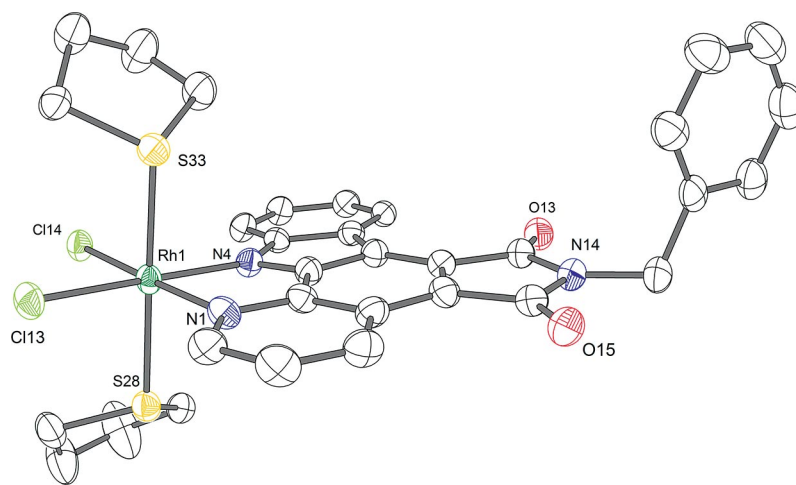

Figure 2. Molecular structure of precursor complex 2a. Only one of two independent complexes is shown. Positions of disorder and solvent molecules are not displayed. ORTEP drawing with 50% probability thermal ellipsoids. Selected bond lengths [Å] and angles [°]: N1–Rh1 2.086(3), N4–Rh1 2.052(3), S28-Rh1 2.3519(11), S33–Rh1 2.3509(11), Rh1–Cl13 2.3485(9), Rh1–Cl14 2.3365(10), N4–Rh1–S28 92.16(9), N1–Rh1–S28 88.05(9), S33–Rh1–S28 174.34(4).

Table 1. Crystallographic data for complexes **2a**, **4c**, and **4d**.

	2a	**4c**	**4d**
Chemical formula	2($C_{32}H_{30}Cl_2N_3O_2RhS_2$)·3($CH_2Cl_2$)	$C_{24}H_{22}ClN_3O_2RhS_3$·$NO_3$·$C_2H_3N$·0.64($H_2O$)	$C_{33}H_{35}ClN_6O_2Rh$·2(C_3H_7NO)·NO_3·0.5($C_4H_{10}O$)
M_r	1707.82	733.57	931.29
Crystal system, space group	triclinic, $P\bar{1}$	triclinic, $P\bar{1}$	triclinic, $P\bar{1}$
a, b, c [Å]	11.3103(4), 14.1291(5), 23.3075(9)	7.6910(4), 12.3776(8), 15.7267 (10)	12.2205 (13), 12.4496 (12), 16.8685(13)
α, β, γ [°]	90.941 (3), 99.237 (3), 111.070 (3)	76.532 (5), 79.311 (5), 84.183 (5)	104.090 (7), 99.220(8), 116.357 (7)
V [Å^3]	3419.4 (2)	1428.04 (15)	2121.5 (3)
Z	2	2	2
μ [mm^{-1}]	1.05	0.96	0.53
Crystal size [mm]	$0.26 \times 0.24 \times 0.09$	$0.10 \times 0.07 \times 0.07$	$0.18 \times 0.05 \times 0.05$
T_{min}, T_{max}	0.607, 1.189	0.904, 0.95	0.927, 0.992
Measured, independent and observed $[I > 2\sigma(I)]$ reflections	52878, 14472, 8583	10088, 4966, 3498	6861, 6861, 2536
R_{int}	0.095	0.050	0.00, data have been "squeezed"[b]
$R[F^2 > 2\sigma(F^2)]$, $wR(F^2)$, S[a]	0.045, 0.102, 0.86	0.035, 0.059, 0.87	0.067, 0.162, 0.78
Reflections	14472	4966	6861
Parameters	1135	449	518
Restraints	1944	6	6
$\rho_{max}, \Delta\rho_{min}$ (e Å^{-3})	0.97, –0.96	0.43, –0.43	0.10, –0.53
CCDC number[c]	846315	846317	846316

[a] $R_1 = \Sigma||F_o| - |F_c||/\Sigma|F_o|$; $wR_2 = [w(F_o^2 - F_c^2)^2/\Sigma w(F_o^2)^2]^{1/2}$; $S = \{\Sigma [w(F_o^2 - F_c^2)^2]/(n-p)\}^{1/2}$. [b] PLATON program; see ref.[24] [c] Crystallographic data (excluding structure factors) have been deposited in the Cambridge Crystallographic Data Centre (CCDC). CIF files can be obtained from the CCDC free of charge via http://www.ccdc.cam.ac.uk/data_request/cif.

Rhodium(III) Complexes with Cyclic Tridentate Ligands

Next, we investigated the coordination chemistry of these precursor complexes and focused on the reaction with cyclic tridentate ligands in order to reduce the number of possible stereoisomers. For example, the reaction of **2a**–**c** with 1,4,7-trithiacyclononane (**3a**),[16] 1,4,7-triazacyclononane (**3b**)[17] or 1,4,7-trimethyl-1,4,7-triazacyclononane (**3c**)[18] in DMF at 120 °C for 16 hours afforded the complexes **4a**–**g** in yields of 20–50%. All complexes formed as a single diastereomer in racemic forms in which the tridentate ligands each replaced two tetrahydrothiophenes and one chloride

(Scheme 2). The remaining chloride can be further subjected to substitution, albeit only under forcing conditions. For example, the reaction of **4a** with NaI in DMF at 120 °C for 16 hours resulted in the formation of the complex **4h** in which the chloride was substituted by an iodide (38%). Whereas the coordination of 1,4,7-trithiacyclononane leads to rhodium complexes with the expected almost perfect octahedral geometry as demonstrated by the X-ray crystal structure of complex **4d** (Figure 3), the X-ray structure of the 1,4,7-trimethyl-1,4,7-triazacyclononane complex **4c** displayed in Figure 4 reveals a highly distorted coordination sphere around the rhodium centre in which the pyridocarbazole heterocycle is significantly bent out of the plane spanned by the rhodium(III)-coordinated nitrogen atoms N1, N4, N31 and N34. This distortion is most likely the
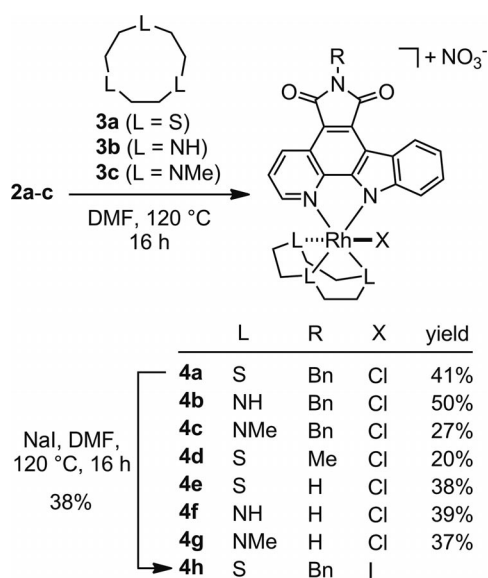
Scheme 2. Synthesis of pyridocarbazole-Rh^{III} complexes **4a**–**h** with cyclic tridentate ligands starting from the precursor complexes **2a**–**c**.
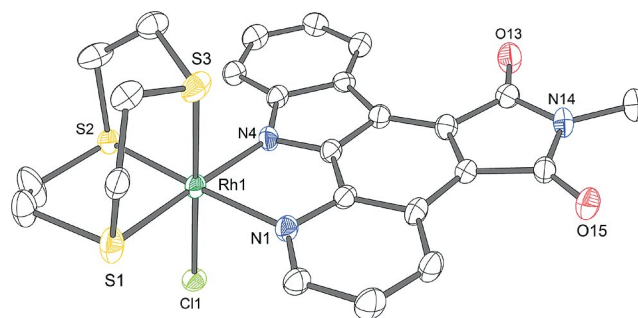
Figure 3. Molecular structure of complex **4d**. Solvent molecules and the nitrate counterion have been omitted. The 1,4,7-trithiacyclononane ligand is disordered. ORTEP drawing with 50% probability thermal ellipsoids. Selected bond lengths (Å) and angles (°): N1–Rh1 2.103(3), N4–Rh1 2.081(3), S1–Rh1 2.2905(11), S2–Rh1 2.2759(10), S3–Rh1 2.2653(12), Cl1–Rh1 2.3567(11), S2–Rh1–S1 89.89(4), N1–Rh1–Cl1 89.79(9), S3–Rh1–Cl1 179.52(5).
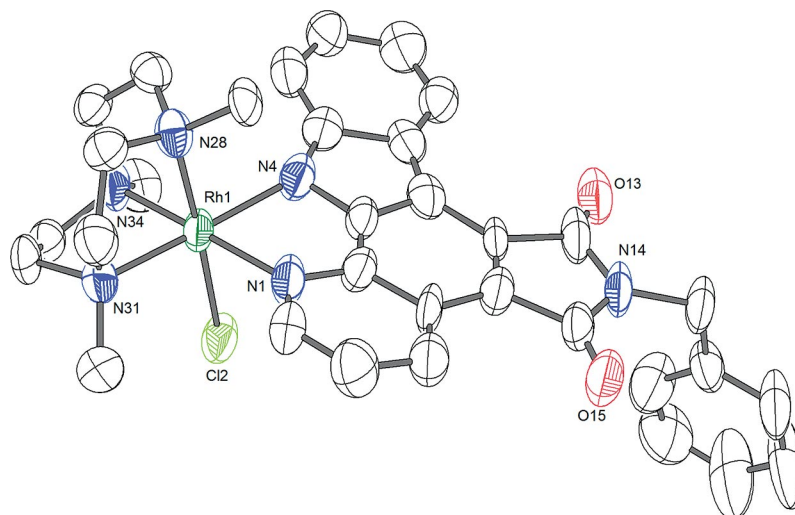
Figure 4. Molecular structure of the distorted 1,4,7-trimethyl-1,4,7-triazacyclononane complex **4c**. The counterion and solvent molecules have been omitted. ORTEP drawing with 50% probability thermal ellipsoids. Selected bond lengths (Å) and angles (°): N1–Rh1 2.101(9), N4–Rh1 2.119(9), N28–Rh1 2.040(7), N31–Rh1 2.099(8), N34–Rh1 2.066(8), Cl2–Rh1 2.344(2), N28–Rh1–N1 97.6(3), N28–Rh1–N4 92.7(3), N1–Rh1–Cl2 84.6(2), N4–Rh1–Cl2 89.3(2).

consequence of steric crowding resulting from a combination of relatively short Rh–N bonds together with the steric demand of the three methyl groups.

Stability Studies

A requirement for such rhodium(III) complexes to be employed as structural scaffolds for the design of bioactive compounds in chemical biology studies or as drug candidates in medicine is their chemical stability under biological conditions. In this respect, the biggest obstacle for transition metal complexes is typically the millimolar cellular concentration of nucleophilic thiols such as the natural tripeptide glutathione or cysteine. In order to evaluate the inertness of the here synthesised pyridocarbazole-rhodium(III) complexes, we incubated the complexes **4a** and **4h** as exemplary members of this class in 9:1 [D_6]DMSO/D_2O and in the presence of 5 mM β-mercaptoethanol and monitored their stability by ^{1}H NMR spectroscopy. As shown for complex **4h** in Figure 5, no additional signals or peak shifts were detected after 24 hours, thus confirming the inertness of this class of rhodium(III) complexes.
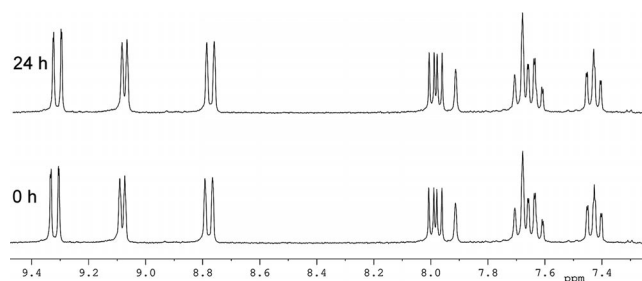

Figure 5. Stability evaluation of compound **4h** (5 mM) in 9:1 [D_6]-DMSO/D_2O in the presence of β-mercaptoethanol (5 mM). Shown are the aromatic regions of the ^{1}H NMR spectra right after the addition of β-mercaptoethanol (0 h) and after 24 h.

Kinase Inhibition Properties

Finally, we investigated the protein kinase inhibition properties of the synthesised rhodium pyridocarbazole complexes and selected the protein kinase Pim1 as our target since it has been demonstrated by us to display a general affinity for pyridocarbazole metal complexes.[4,5a,6] Accordingly, the rhodium complexes containing unmodified maleimide moieties (**4e–g**) were tested for their inhibition of Pim1 at a concentration of 100 nM. Revealingly, whereas the 1,4,7-triazacyclononane complex **4f** was only a moderate inhibitor for Pim1 (26% remaining Pim1 activity at 100 nM), the 1,4,7-trimethyl-1,4,7-triazacyclononane complex **4g** (2.1% remaining Pim1 activity at 100 nM) and the 1,4,7-trithiacyclononane complex **4e** (0% remaining Pim1 activity at 100 nM) displayed very potent Pim1 inhibition. We further investigated the Pim1 inhibition of the most potent complex **4e** and determined from concentration dependent inhibition data an IC$_{50}$ (concentration of compound at which the enzyme activity is reduced to 50%) value of 0.16 nM at 100 μM ATP (Figure 6). Thus, the simple complex **4e** constitutes one of the most potent reported inhibitors of the protein kinase Pim1 to date. To further evaluate if complex **4e** binds as designed to the hinge region of the ATP binding site, we tested two derivatives of **4e** in which the imide hydrogen had been replaced by a methyl (**4d**) or benzyl group (**4a**). As shown in Figure 6, these alkylations dramatically reduce the activity by factors of 469 (**4d**: IC$_{50}$ = 75 nM) or 8125 (**4a**: IC$_{50}$ = 1300 nM), consistent with the expectation that the imide hydrogen forms a hydrogen bond with a carbonyl oxygen of the hinge region as indicated in Figure 1.

To gain insight into the protein kinase inhibition selectivity of the extremely potent Pim1 inhibitor **4e**, we tested racemic **4e** for its protein kinase binding affinity profile against the majority of the human protein kinases encoded in the human genome (human kinome).[19] This was ac-
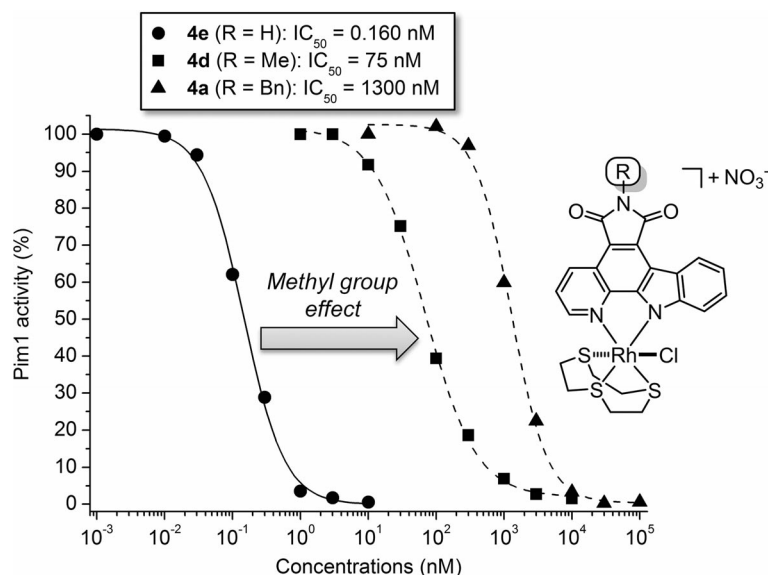
Figure 6. IC$_{50}$ curves of complex **4e**, the *N*-methylated derivative **4d** and the *N*-benzylated derivative **4a** against Pim1 at ATP concentrations of 100 µM. For the IC$_{50}$ determination of **4e**, the Pim1 concentration was ca. 0.3 nM.

complished by using an active-site-directed competition binding assay with 451 different protein kinases (KINOME*scan*, DiscoveRx) which provides primary data

(%ctrl = percent of control: 0% = highest affinity, 100% = no affinity) that correlate with binding constants (K_d).[20] As a result, out of the tested 451 enzymes, three protein
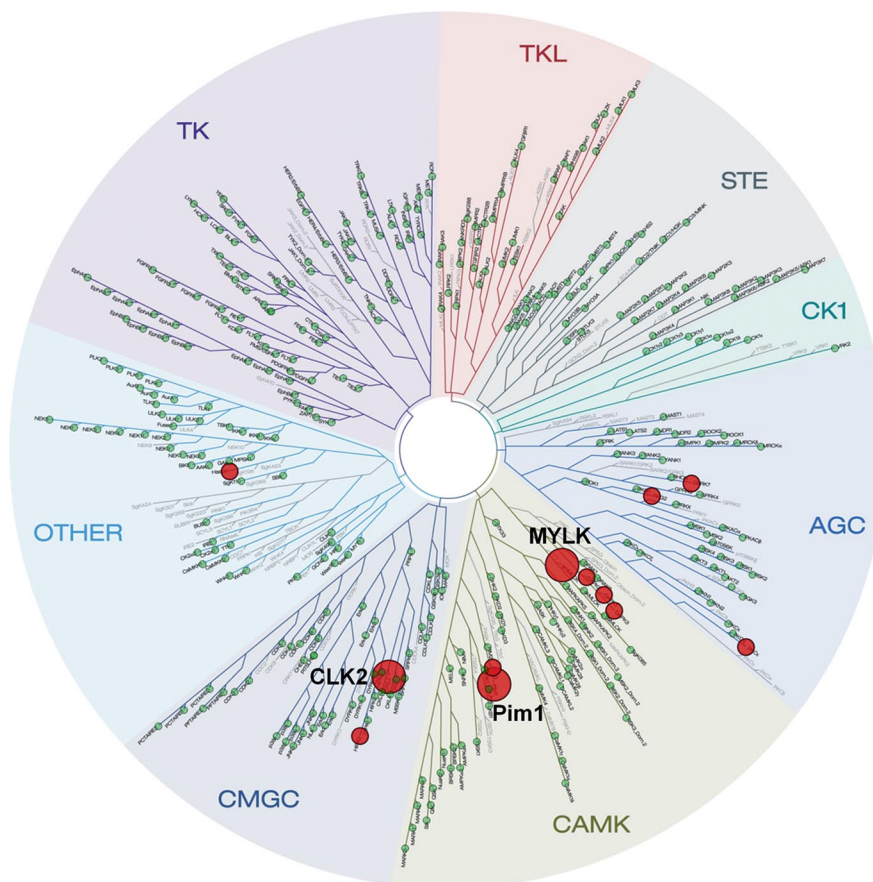

Figure 7. Protein kinase selectivity of complex **4e** (1 nM) as determined by an active-site-directed affinity screening (KINOME*scan*, DiscoveRx) against 451 human protein kinases. Representation of the main hits (< 5% of control, large red circles) within the human kinase dendrogram which displays the protein kinase families and the evolutionary relationships between the individual kinases. Weak or no hits are labelled with small red circles (10–35% of control) and smaller green circles (> 35% of control).

kinases, namely CLK2, MYLK and Pim1, were identified as the main hits with %ctrl values below 5% at a concentration of 1 nM **4e**. The human kinase dendrogram shown in Figure 7 demonstrates the high degree of kinase selectivity of rhodium complex **4e**.

Conclusions

We presented here our first study using rhodium complexes as structural scaffolds for the design of enzyme inhibitors and we discovered a surprisingly potent, picomolar rhodium(III)-based inhibitor for the protein kinase Pim1. Since the majority of our previous work was based on using ruthenium in the diamagnetic oxidation state II as our preferred structural centre for building enzyme inhibitors, a comparison of the suitability of the metals ruthenium(II) and rhodium(III) for our approach seems appropriate. Compared with ruthenium, rhodium chemistry has two main disadvantages: The price for rhodium is extremely high and in our experience the coordination chemistry of octahedral rhodium(III) complexes is not well understood which is for example reflected by the overall modest yields presented in this work. However, despite these drawbacks, rhodium offers properties that render it an attractive complement to the much less expensive ruthenium. First, the rhodium complexes investigated here are highly inert under biologically relevant conditions as can be seen for the fact that even the monodentate chloride and iodide ligands in the complexes **4a** and **4h**, respectively, do not exchange in the presence of millimolar concentrations of thiols. This inertness seems to even surpass the stability of related ruthenium complexes. Second, and most importantly, rhodium in the oxidation state III forms very kinetically stable complexes with hard ligands such amines as found in the ligands **3b** and **3c**, for example, whereas ruthenium(II) would become prone to oxidation to the undesired paramagnetic ruthenium(III) with these and related ligands. Thus, it can be concluded that rhodium(III) expands the toolbox for the design of inert metal complexes with biological activity.

Experimental Section

General Methods: Reactions were carried out using oven-dried glassware and conducted under a positive pressure of nitrogen unless stated otherwise. The pyridocarbazole ligands **1a–c**,[14] 1,4,7-trithiacyclononane,[21] 1,4,7-triazacyclononane,[22] 1,4,7-trimethyl-1,4,7-triazacyclononane[23] and [Rh(C$_4$H$_8$S)$_3$Cl$_3$][15] were synthesised according to published procedures. Other chemicals as well as all solvents were used as received from standard suppliers or distilled prior to use. All synthesised compounds were purified by silica gel chromatography (230–400 mesh) and their high purities confirmed by ^{1}H and ^{13}C NMR spectroscopy. NMR spectra were recorded on a DPX-250 (250 MHz), Avance 300 (300 MHz), DRX-400 (400 MHz) or Avance 500 (500 MHz) spectrometer. Infrared spectra were recorded on a Bruker Alpha FTIR instrument. High resolution mass spectra were obtained with a Finnigan LTQ-FT instrument using either APCI or ESI.

Compound 2a: An orange suspension of ligand **1a** (40 mg, 106 µmol) and [Rh(C$_4$H$_8$S)$_3$Cl$_3$] (50 mg, 106 µg) in degassed EtOH/

H$_2$O, 1:1 (4 mL) was heated at reflux (90 °C) for 16 h. Afterwards, the red-brown suspension was cooled to room temperature and the solvent was evaporated. The red residue was purified by silica gel chromatography with CH$_2$Cl$_2$/MeOH, 100:1 to obtain **2a** (54.7 mg, 71%) as a red solid. ^{1}H NMR (300 MHz, CDCl$_3$): δ = 9.34 (dd, J = 8.3, 1.2 Hz, 1 H), 9.31 (d, J = 5.3 Hz, 1 H), 8.90 (d, J = 7.9 Hz, 1 H), 8.62 (d, J = 8.4 Hz, 1 H), 7.75 (dd, J = 8.3, 5.4 Hz, 1 H), 7.60–7.52 (m, 3 H), 7.45–7.27 (m, 4 H), 4.98 (s, 2 H), 3.69–3.58 (m, 2 H), 2.86–2.79 (m, 2 H), 2.75–2.66 (m, 2 H), 2.16–1.80 (m, 8 H), 1.75–1.66 (m, 2 H) ppm. ^{13}C NMR (75 MHz, CDCl$_3$): δ = 169.5, 169.0, 153.1, 149.8, 149.7, 149.2, 142.7, 137.1, 135.8, 130.9, 128.8, 128.7, 127.8, 127.5, 125.4, 124.1, 123.0, 122.1, 120.9, 116.7, 115.8, 114.0, 41.7, 37.3, 37.0, 30.2, 29.8 ppm. IR (film): ṽ = 3062, 2938, 2861, 1751, 1697, 1624, 1583, 1554, 1524, 1496, 1474, 1420, 1387, 1340, 1264, 1228, 1141, 1105, 1061, 1031, 948, 900, 855, 823, 799, 752, 700, 660, 630, 501 cm^{-1}. HRMS (ESI): calcd. for C$_{32}$H$_{30}$Cl$_2$N$_3$O$_2$RhS$_2$ (M)$^+$ 725.0206; found 725.0201.

Compound 2b: An orange suspension of ligand **1b** (20 mg, 66 µmol) and [Rh(C$_6$H$_{12}$S$_3$)$_3$Cl$_3$] (31.3 mg, 66 µmol) in degassed EtOH/H$_2$O, 1:1 (4 mL) was heated at reflux (90 °C) for 16 h. Afterwards the red suspension was cooled to room temperature and the solvent was removed. The red residue was purified by silica gel chromatography with CH$_2$Cl$_2$/MeOH, 100:1 to obtain **2b** (20.8 mg, 49%) as a red solid. ^{1}H NMR (300 MHz, CDCl$_3$): δ = 9.36–9.30 (m, 2 H), 8.89 (d, J = 8.0 Hz, 1 H), 8.63 (d, J = 8.4 Hz, 1 H), 7.76 (dd, J = 8.3, 5.3 Hz, 1 H), 7.57 (ddd, J = 8.4, 7.0, 1.3 Hz, 1 H), 7.42 (ddd, J = 8.5, 7.1, 1.1 Hz, 1 H), 3.71–3.58 (m, 2 H), 3.30 (s, 3 H), 2.92–2.79 (m, 2 H), 2.78–2.65 (m, 2 H), 2.18–1.81 (m, 8 H), 1.77–1.65 (m, 2 H) ppm. ^{13}C NMR (63 MHz, [D$_6$]DMSO): δ = 170.0, 169.5, 153.0, 149.8, 149.2, 142.7, 135.8, 131.0, 127.5, 125.4, 124.2, 123.0, 122.0, 120.9, 116.7, 115.8, 114.2, 37.3, 37.1, 30.2, 29.8, 24.0 ppm. IR (film): ṽ = 3061, 2956, 2924, 2854, 1752, 1698, 1622, 1585, 1524, 1490, 1445, 1412, 1377, 1334, 1307, 1260, 1227, 1138, 1084, 1021, 875, 845, 800, 744, 698, 663, 618 cm^{-1}. HRMS (ESI): calcd. for C$_{26}$H$_{26}$Cl$_2$N$_3$O$_2$RhS$_2$ [M + Na]$^+$ 671.9791; found 671.9817.

Compound 2c: An orange suspension of ligand **1c** (43 mg, 106 µmol) and [Rh(C$_4$H$_8$S)$_3$Cl$_3$] (50 mg, 106 µmol) in degassed EtOH/H$_2$O, 1:1 (4 mL) was heated at reflux (90 °C) for 16 h. Afterwards the red suspension was cooled to room temperature and the solvent was evaporated. The red residue was purified by silica gel chromatography with CH$_2$Cl$_2$/MeOH (gradient 100:1 to 30:1) to obtain **2c** (52.8 mg, 78%) as a red solid. ^{1}H NMR (300 MHz, [D$_6$]-DMSO): δ = 11.30 (s, 1 H), 9.29–9.24 (m, 2 H), 8.72 (d, J = 7.9 Hz, 1 H), 8.53 (d, J = 8.4 Hz, 1 H), 8.05 (dd, J = 8.3, 5.4 Hz, 1 H), 7.56 (ddd, J = 8.3, 7.1, 0.8 Hz, 1 H), 7.37 (ddd, J = 8.0, 7.1, 0.8 Hz, 1 H), 3.14–3.01 (m, 2 H), 2.66–2.53 (m, 4 H), 2.23–2.11 (m, 2 H), 1.81–1.60 (m, 8 H) ppm. ^{13}C NMR (125 MHz, [D$_6$]DMSO): δ = 170.5, 170.1, 152.1, 149.7, 149.2, 142.1, 135.4, 131.2, 126.7, 124.5, 124.3, 123.4, 121.3, 120.1, 115.3, 115.04, 115.02, 36.4, 36.2, 29.5, 29.3 ppm. IR (film): ṽ = 3242, 2959, 2927, 2855, 1755, 1705, 1623, 1584, 1524, 1497, 1470, 1419, 1344, 1261, 1228, 1085, 1018, 872, 798, 751, 705, 641, 494, 403 cm^{-1}. HRMS (ESI): calcd. for C$_{25}$H$_{24}$Cl$_2$N$_3$O$_2$RhS$_2$ (M)$^+$ 634.9737; found 634.9755.

Compounds 4a–g. General Synthetic Procedure: Compound **2a**, **2b** or **2c** (1.0 equiv.) and ligand **3a**, **3b** or **3c** (1.5 equiv.) were dissolved in freshly distilled DMF (0.07 mmol mL^{-1}) and stirred at 120 °C for 16 h. The solvent was removed under vacuum and the red residue was purified by silica gel chromatography with MeCN/H$_2$O/KNO$_3$(satd.) 50:3:1. The solvent of the combined product eluents was removed and the residue dissolved in a minimum amount of acetonitrile/water and precipitated with an excess of water. The red solid was isolated by centrifugation, washed four times with water

(6 mL) and dried in vacuo to obtain the compounds **4a**–**g** as red nitrate salts. Yields: **4a** (41%), **4b** (50%), **4c** (27%), **4d** (20%), **4e** (38%), **4f** (39%), **4g** (37%).

4a: ^{1}H NMR (250 MHz, [D$_6$]DMSO): δ = 9.35 (d, J = 8.5 Hz, 1 H), 9.18 (d, J = 4.8 Hz, 1 H), 8.82 (d, J = 7.8 Hz, 1 H), 8.04 (dd, J = 8.3, 5.5 Hz, 1 H), 7.77 (d, J = 8.1 Hz, 1 H), 7.65 (t, J = 7.1 Hz, 1 H), 7.48–7.23 (m, 6 H), 4.90 (s, 2 H), 3.95–3.23 (m, 11 H), 3.03–2.86 (m, 1 H) ppm. ^{13}C NMR (63 MHz, [D$_6$]DMSO): δ = 168.8, 168.5, 152.0, 151.9, 149.91, 148.88, 141.2, 137.1, 135.9, 130.1, 128.6, 127.44, 127.36, 125.3, 124.9, 123.6, 121.7, 120.3, 115.6, 113.9, 113.8, 40.9, 37.0, 36.3, 32.4 ppm. IR (film): $\tilde{\nu}$ = 3425, 2934, 1751, 1692, 1624, 1583, 1521, 1493, 1384, 1334, 1225, 1178, 1141, 1107, 1077, 1030, 940, 905, 823, 798, 736, 697, 657, 628, 496, 429 cm^{-1}. HRMS (ESI): calcd. for C$_{30}$H$_{26}$ClN$_3$O$_2$RhS$_3$ (M − NO$_3$)$^+$ 693.9925; found 693.9922.

4b: ^{1}H NMR: (500 MHz, [D$_6$]DMSO): δ = 9.28 (d, J = 8.6 Hz, 1 H), 9.26 (d, J = 5.5 Hz, 1 H), 8.80 (d, J = 8.0 Hz, 1 H), 8.79 (br. s, 1 H), 8.59 (br. s, 1 H), 8.06 (dd, J = 8.3, 5.2 Hz, 1 H), 7.98 (d, J = 8.4 Hz, 1 H), 7.63 (ddd, J = 8.2, 7.2, 1.2 Hz, 1 H), 7.44–7.33 (m, 6 H), 7.27 (t, J = 7.2 Hz, 1 H), 4.93 (s, 2 H), 3.74–3.65 (m, 2 H), 3.64–356 (m, 1 H), 3.52–3.43 (m, 1 H), 3.31–3.24 (m, 1 H), 3.22–3.09 (m, 3 H), 2.93–2.80 (m, 4 H) ppm. ^{13}C NMR: (125 MHz, [D$_6$]DMSO): δ = 169.0, 168.8, 153.4, 151.2, 148.82, 148.80, 142.7, 137.2, 134.7, 129.8, 128.6, 127.3, 127.1, 126.5, 124.4, 124.1, 123.5, 121.0, 119.8, 115.1, 112.2, 52.4, 52.1, 51.8, 51.4, 50.5, 49.7, 40.7 ppm. IR (film): $\tilde{\nu}$ = 3420, 3192, 3115, 2924, 1746, 1685, 1625, 1583, 1526, 1495, 1416, 1384, 1324, 1293, 1226, 1147, 1109, 1052, 1023, 980, 935, 898, 819, 739, 696, 659, 628, 560, 498, 481, 428 cm^{-1}. HRMS (ESI): calcd. for C$_{30}$H$_{29}$ClN$_6$O$_2$Rh (M − NO$_3$)$^+$ 643.1090; found 643.1087.

4c: ^{1}H NMR (300 MHz, [D$_6$]DMSO): δ = 9.47 (d, J = 5.4 Hz, 1 H), 9.40 (d, J = 8.3 Hz, 1 H), 8.99 (d, J = 7.9 Hz, 1 H), 8.12–8.01 (m, 2 H), 7.64 (t, J = 7.5 Hz, 1 H), 7.48–7.24 (m, 6 H), 4.90 (s, 2 H), 4.34–4.25 (m, 1 H), 3.97–3.80 (m, 2 H), 3.72–3.33 (m, 10 H), 3.32–3.14 (m, 5 H), 2.05 (s, 3 H) ppm. ^{13}C NMR (63 MHz, [D$_6$]DMSO): δ = 168.8, 168.6, 152.9, 150.7, 147.04, 147.01, 142.7, 137.1, 135.7, 129.1, 128.6, 127.4, 126.6, 125.2, 124.4, 123.8, 121.6, 119.9, 116.5, 115.8, 113.6, 64.3, 63.7, 62.5, 61.6, 61.2, 60.5, 55.6, 52.3, 51.8, 40.8 ppm. IR (film): $\tilde{\nu}$ = 3362, 2960, 2924, 2854, 1749, 1696, 1613, 1587, 1530, 1489, 1459, 1384, 1337, 1260, 1210, 1085, 1015, 866, 796, 749, 699, 630 cm^{-1}. HRMS (ESI): calcd. for C$_{33}$H$_{35}$ClN$_6$O$_2$Rh (M − NO$_3$)$^+$ 685.1560; found 685.1561.

4d: ^{1}H NMR (300 MHz, [D$_6$]DMSO): δ = 9.36 (d, J = 8.5 Hz, 1 H), 9.16 (d, J = 5.2 Hz, 1 H), 8.83 (d, J = 7.7 Hz, 1 H), 8.03 (dd, J = 8.3, 5.2 Hz, 1 H), 7.76 (d, J = 8.5 Hz, 1 H), 7.64 (ddd, J = 8.2, 7.1, 1.1 Hz, 1 H), 7.44 (t, J = 7.5 Hz, 1 H), 3.94–3.27 (m, 11 H), 3.18 (s, 3 H), 3.01–2.88 (m, 1 H) ppm. ^{13}C NMR (75 MHz, [D$_6$]DMSO): δ = 169.2, 168.8, 151.8, 151.6, 148.9, 141.1, 135.9, 130.4, 127.3, 125.2, 124.9, 123.6, 121.6, 120.2, 115.5, 114.1, 113.8, 38.5, 38.4, 37.0, 36.3, 32.4, 23.8 ppm. IR (film): $\tilde{\nu}$ = 3355, 2960, 1752, 1691, 1626, 1584, 1524, 1493, 1439, 1407, 1380, 1334, 1259, 1223, 1085, 1014, 795, 739, 693, 658, 614, 551, 489 cm^{-1}. HRMS (ESI): calcd. for C$_{24}$H$_{22}$ClN$_3$O$_2$RhS$_3$ (M − NO$_3$)$^+$ 617.9612; found 617.9607.

4e: ^{1}H NMR (300 MHz, [D$_6$]DMSO): δ = 11.34 (s, 1 H) 9.35 (d, J = 8.2 Hz, 1 H), 9.16 (d, J = 5.0 Hz, 1 H), 8.81 (d, J = 7.7 Hz, 1 H), 8.02 (dd, J = 8.3, 5.3 Hz, 1 H), 7.75 (d, J = 8.2 Hz, 1 H), 7.63 (t, J = 7.3 Hz, 1 H), 7.43 (t, J = 7.5 Hz, 1 H), 3.94–3.25 (m, 11 H), 3.00–2.87 (m, 1 H) ppm. ^{13}C NMR (63 MHz, [D$_6$]DMSO): δ = 170.5, 170.0, 151.8, 148.7, 141.4, 136.0, 131.1, 127.2, 125.1, 125.0, 123.6, 121.7, 120.1, 115.4, 115.1, 113.8, 37.0, 36.3, 32.3 ppm. IR (film): $\tilde{\nu}$ = 3412, 3226, 2927, 2851, 1752, 1705, 1618, 1584, 1524,

1493, 1448, 1410, 1336, 1261, 1223, 1175, 1134, 1079, 1008, 946, 911, 875, 824, 795, 743, 706, 635, 487, 434 cm^{-1}. HRMS (ESI): calcd. for C$_{23}$H$_{20}$ClN$_3$O$_2$RhS$_3$ (M − NO$_3$)$^+$ 603.9467; found 603.9454.

4f: ^{1}H NMR (500 MHz, [D$_6$]DMSO): δ = 11.21 (s, 1 H), 9.27 (d, J = 8.3 Hz, 1 H), 9.24 (d, J = 5.1 Hz, 1 H), 8.79 (d, J = 7.8 Hz, 1 H), 8.77 (br. s, 1 H), 8.57 (br. s, 1 H), 8.04 (dd, J = 8.3, 5.2 Hz, 1 H), 7.96 (d, J = 8.4 Hz, 1 H), 7.61 (ddd, J = 8.2, 7.1, 1.1 Hz, 1 H), 7.43–7.37 (m, 2 H), 3.74–3.64 (m, 2 H), 3.64–3.55 (m, 1 H), 3.52–3.42 (m, 1 H), 3.30–3.25 (m, 1 H), 3.20–3.07 (m, 3 H), 2.92–2.81 (m, 4 H) ppm. ^{13}C NMR (125 MHz, [D$_6$]DMSO): δ = 170.7, 170.4, 153.1, 151.0, 148.7, 142.8, 134.8, 130.8, 126.2, 124.5, 123.8, 123.6, 121.0, 119.6, 114.9, 114.8, 113.6, 52.4, 52.1, 51.7, 51.4, 50.5, 49.6 ppm. IR (film): $\tilde{\nu}$ = 3154, 2923, 2854, 1744, 1699, 1584, 1494, 1345, 1288, 1227, 1150, 1020, 808, 744, 705, 639, 559, 483, 423 cm^{-1}. HRMS (ESI): calcd. for C$_{23}$H$_{23}$ClN$_6$O$_2$Rh (M − NO$_3$)$^+$ 553.0621; found 553.0620.

4g: ^{1}H NMR (300 MHz, [D$_6$]DMSO): δ = 11.29 (s, 1 H), 9.45 (d, J = 5.5 Hz, 1 H), 9.40 (d, J = 8.2 Hz, 1 H), 8.98 (d, J = 7.9 Hz, 1 H), 8.09–7.99 (m, 2 H), 7.62 (t, J = 7.5 Hz, 1 H), 7.43 (t, J = 7.5 Hz, 1 H), 4.34–4.22 (m, 1 H), 3.96–3.80 (m, 2 H), 3.72–3.33 (m, 10 H), 3.32–3.13 (m, 5 H), 2.05 (s, 3 H) ppm. ^{13}C NMR (125 MHz, [D$_6$]DMSO): δ = 170.5, 170.2, 152.7, 150.5, 146.9, 142.9, 135.8, 130.1, 126.4, 125.3, 124.5, 123.6, 121.5, 119.6, 116.3, 115.6, 114.8, 64.2, 63.6, 62.5, 61.6, 61.2, 60.5, 55.5, 52.3, 51.7 ppm. IR (film): $\tilde{\nu}$ = 3244, 2958, 2923, 2853, 1748, 1708, 1583, 1530, 1461, 1414, 1378, 1342, 1259, 1229, 1090, 1018, 867, 799, 749, 701, 641, 491 cm^{-1}. HRMS (ESI): calcd. for C$_{26}$H$_{29}$ClN$_6$O$_2$Rh (M − NO$_3$)$^+$ 595.1090; found 595.1095.

Compound 4h: A solution of compound **4a** (13.0 mg, 17 µmol) and NaI (25.8 mg, 172 µmol) was dissolved in freshly distilled DMF (2 mL) and stirred at 120 °C for 16 h. The solvent was removed and the red residue was purified by silica gel chromatography with MeCN/H$_2$O/KNO$_3$(satd.) 50:3:1. The solvent of the combined product eluents were removed and the residue dissolved in a mini-muml amount of acetonitrile/water and subsequently precipitated with an excess of water. The product was isolated by centrifugation, washed four times with water and dried in vacuo to obtain **4h** as a red nitrate salt (5.5 mg, 38%). ^{1}H NMR (300 MHz, [D$_6$]DMSO): δ = 9.32 (d, J = 8.5 Hz, 1 H), 9.14 (d, J = 5.1 Hz, 1 H), 8.81 (d, J = 7.9 Hz, 1 H), 8.01 (dd, J = 7.9, 5.2 Hz, 1 H), 7.73–7.60 (m, 2 H), 7.47–7.24 (m, 6 H), 4.90 (s, 2 H), 4.07–3.95 (m, 1 H), 3.94–3.66 (m, 6 H), 3.65–3.51 (m, 1 H), 3.30–3.15 (m, 2 H), 3.07–2.95 (m, 1 H), 2.81–2.67 (m, 1 H) ppm. ^{13}C NMR (63 MHz, [D$_6$]DMSO): δ = 168.7, 168.5, 152.1, 151.8, 149.2, 149.1, 141.4, 137.1, 135.8, 130.1, 128.6, 127.45, 127.36, 125.3, 124.9, 123.7, 121.7, 120.3, 115.7, 113.8, 42.8, 40.9, 36.8, 35.8, 33.4 ppm. IR (film): $\tilde{\nu}$ = 3443, 2925, 1751, 1700, 1621, 1584, 1525, 1494, 1387, 1343, 1228, 1180, 1143, 1108, 942, 909, 825, 794, 747, 700, 658, 630, 498, 440 cm^{-1}. HRMS: calcd. for C$_{30}$H$_{26}$IN$_3$O$_2$RhS$_3$ (M − NO$_3$)$^+$ 785.9281; found 785.9275.

Protein Kinase Assays. Kinase Profiling: The protein kinase selectivity profile of complex **4e** at an assay concentration of 1 nM was derived from an active-site-directed affinity screening against 451 human protein kinases (KINOME*scan*, DiscoeRx). *Pim1 inhibition*: Inhibition data were obtained by a conventional radioactive assay in which Pim1 activity was measured by the degree of phosphorylation of the P70 S6 kinase substrate with [γ-^{33}P]ATP (Perkin–Elmer). Accordingly, different concentrations of the rhodium complexes were preincubated at room temperature for 30 min with Pim1 (Millipore) and P70 S6 kinase substrate (AnaSpec) and the phosphorylation reaction was subsequently initiated by adding

ATP and [γ-^{33}P]ATP to a final volume of 25 µL, which consisted of MOPS (10 mм, pH 7.0), Mg(OAc)$_2$ (10 mм), DMSO (5%), Pim1 (1.6 nM, except for the IC$_{50}$ curve of **4e**: 0.3 nM), P70 S6 kinase substrate (50 µM), EDTA (0.1 mм), Brij-35 (0.001%), glycerol (0.5%), β-mercaptoethanol (0.01%), BSA (0.1 mg mL^{-1}) and ATP (100 µM) including [γ-^{33}P]ATP (approximately 0.1 µCi µL^{-1}). After incubation for 30 min, the reaction was terminated by spotting 14 µL onto circular P81 phosphocellulose paper (diameter 2.1 cm, Whatman), followed by washing with 0.75% phosphoric acid and acetone. The dried P81 papers were transferred to scintillation vials and 5 mL of scintillation cocktail were added. The counts per minute (CPM) were measured with a Beckmann Coulter LS6500 Multi Purpose Scintillation Counter and corrected by the background CPM. The IC$_{50}$ values were determined in triplicate from sigmoidal curve fits.

Single-Crystal X-ray Diffraction Studies: Single crystals of the individual complexes were obtained as follows: **2a** from a solution of CH$_2$Cl$_2$ layered with hexane, **4c** from a solution in DMF layered with hexane and **4d** from a mixture of DMF and H$_2$O. The intensity data sets were collected at 100 K using a STOE IPDS-2T or STOE IPDS2 system with Mo-K_α radiation (λ = 0.71073 Å). The data were corrected for absorption effects using multi scanned reflections.[24] The structures were solved by direct methods by using SIR-92[25] or SIR2008[26] and refined using the full-matrix least-squares procedure implemented in SHELX-97.[27] Hydrogen atoms were included in calculated positions. In **2a** both the solvent molecules (CH$_2$Cl$_2$) and the two independent complex molecules show disorder. In **4d** the 1,4,7-trithiacyclononane ligand was disordered. The crystal of **4c** was twinned and only data of one domain were used during structure refinement. In **4c**, heavily disordered solvent was present. The data set has been treated by the "squeeze" procedure implemented in the PLATON program.[24]

[1] a) K. H. Thompson, C. Orvig, *Science* **2003**, *300*, 936–939; b) W. H. Ang, P. J. Dyson, *Eur. J. Inorg. Chem.* **2006**, 4003–4018; c) T. W. Hambley, *Dalton Trans.* **2007**, 4929–4937; d) T. W. Hambley, *Science* **2007**, *318*, 1392–1393; e) A. Mukherjee, P. J. Sadler, *Wiley Encycl. Chem. Biol.* **2009**, 1–47; f) K. L. Haas, K. J. Franz, *Chem. Rev.* **2009**, *109*, 4921–4960; g) A. Levina, A. Mitra, P. A. Lay, *Metallomics* **2009**, *1*, 458–470; h) C.-M. Che, F.-M. Siu, *Curr. Opin. Chem. Biol.* **2010**, *14*, 255–261; i) E. A. Hillard, G. Jaouen, *Organometallics* **2011**, *30*, 20–27; j) G. Gasser, I. Ott, N. Metzler-Nolte, *J. Med. Chem.* **2011**, *54*, 3–25.

[2] E. Meggers, G. E. Atilla-Gokcumen, H. Bregman, J. Maksimoska, S. P. Mulcahy, N. Pagano, D. S. Williams, *Synlett* **2007**, *8*, 1177–1189.

[3] a) E. Meggers, *Curr. Opin. Chem. Biol.* **2007**, *11*, 287–292; b) E. Meggers, *Chem. Commun.* **2009**, 1001–1010; c) C. L. Davies, E. L. Dux, A.-K. Duhme-Klair, *Dalton Trans.* **2009**, 10141–10154.

[4] For a recent example, see: L. Feng, Y. Geisselbrecht, S. Blanck, A. Wilbuer, G. E. Atilla-Gokcumen, P. Filippakopoulos, K. Kräling, M. A. Celik, K. Harms, J. Maksimoska, R. Marmorstein, G. Frenking, S. Knapp, L.-O. Essen, E. Meggers, *J. Am. Chem. Soc.* **2011**, *133*, 5976–5986.

[5] a) J. É. Debreczeni, A. N. Bullock, G. E. Atilla, D. S. Williams, H. Bregman, S. Knapp, E. Meggers, *Angew. Chem.* **2006**, *118*, 1610; *Angew. Chem. Int. Ed.* **2006**, *45*, 1580–1585; b) H. Bregman, E. Meggers, *Org. Lett.* **2006**, *8*, 5465–5468; c) G. E. Atilla, D. S. Williams, H. Bregman, N. Pagano, E. Meggers, *ChemBioChem* **2006**, *7*, 1443–1450; d) P. Xie, D. S. Williams, G. E. Atilla-Gokcumen, L. Milk, M. Xiao, K. S. M. Smalley, M. Herlyn, E. Meggers, R. Marmorstein, *ACS Chem. Biol.* **2008**, *3*, 305–316; e) G. E. Atilla-Gokcumen, L. Di Costanzo, E. Meggers, *J. Biol. Inorg. Chem.* **2011**, *16*, 45–50.

[6] H. Bregman, P. J. Carroll, E. Meggers, *J. Am. Chem. Soc.* **2006**, *128*, 877–884.

[7] J. Maksimoska, L. Feng, K. Harms, C. Yi, J. Kissil, R. Marmorstein, E. Meggers, *J. Am. Chem. Soc.* **2008**, *130*, 15764–15765.

[8] H. Bregman, D. S. Williams, G. E. Atilla, P. J. Carroll, E. Meggers, *J. Am. Chem. Soc.* **2004**, *126*, 13594–13595.

[9] For different designs of metal-containing protein kinase inhibitors, see: a) J. Spencer, A. P. Mendham, A. K. Kotha, S. C. W. Richardson, E. A. Hillard, G. Jaouen, L. Male, M. B. Hursthouse, *Dalton Trans.* **2009**, 918–921; b) B. Biersack, M. Zoldakova, K. Effenberger, R. Schobert, *Eur. J. Med. Chem.* **2010**, *45*, 1972–1975; c) S. Blanck, T. Cruchter, A. Vultur, R. Riedel, K. Harms, M. Herlyn, E. Meggers, *Organometallics* **2011**, *30*, 4598–4606.

[10] J. Maksimoska, D. S. Williams, G. E. Atilla-Gokcumen, K. S. M. Smalley, P. J. Carroll, R. D. Webster, P. Filippakopoulos, S. Knapp, M. Herlyn, E. Meggers, *Chem. Eur. J.* **2008**, *14*, 4816–4822.

[11] A. Wilbuer, D. H. Vlecken, D. J. Schmitz, K. Kräling, K. Harms, C. P. Bagowski, E. Meggers, *Angew. Chem. Int. Ed.* **2010**, *49*, 3839–3842.

[12] D. S. Williams, P. J. Carroll, E. Meggers, *Inorg. Chem.* **2007**, *46*, 2944–2946.

[13] For rhodium complexes with biological activities, see: a) B. Weber, A. Serafin, J. Michie, C. van Rensburg, J. C. Swarts, L. Bohm, *Anticancer Res.* **2004**, *24*, 763–770; b) A. Dorcier, W. H. Ang, S. Bolaño, L. Gonsalvi, L. Juillerat-Jeannerat, G. Laurenczy, M. Peruzzini, A. D. Phillips, F. Zanobini, P. J. Dyson, *Organometallics* **2006**, *25*, 4090–4096; c) A. M. Angeles-Boza, H. T. Chifotides, J. D. Aguirre, A. Chouai, P. K.-L. Fu, K. R. Dunbar, C. Turro, *J. Med. Chem.* **2006**, *49*, 6841–6847; d) A. Dorcier, C. G. Hartinger, R. Scopelliti, R. H. Fish, B. K. Keppler, P. J. Dyson, *J. Inorg. Biochem.* **2008**, *102*, 1066–1076; e) M. A. Scharwitz, I. Ott, Y. Geldmacher, R. Gust, W. S. Sheldrick, *J. Organomet. Chem.* **2008**, *693*, 2299–2309; f) J. D. Aguirre, A. M. Angeles-Boza, A. Chouai, C. Turro, J.-P. Pellois, K. R. Dunbar, *Dalton Trans.* **2009**, 10806–10812; g) R. Bieda, M. Dobroschke, A. Triller, I. Ott, M. Spehr, R. Gust, A. Prokop, W. S. Sheldrick, *ChemMedChem* **2010**, *5*, 1123–1133; h) Y. Geldmacher, R. Rubbiani, P. Wefelmeier, A. Prokop, I. Ott, W. S. Sheldrick, *J. Organomet. Chem.* **2011**, *696*, 1023–1031; i) R. J. Ernst, A. C. Komor, J. K. Barton, *Biochemistry* **2011**, *50*, 10919–10928.

[14] a) H. Bregman, D. S. Williams, E. Meggers, *Synthesis* **2005**, 1521–1527; b) N. Pagano, J. Maksimoska, H. Bregman, D. S. Williams, R. D. Webster, F. Xue, E. Meggers, *Org. Biomol. Chem.* **2007**, *5*, 1218–1227.

[15] K. D. John, K. V. Salszar, B. L. Scott, R. T. Baker, A. P. Sattelberger, *Organometallics* **2001**, *20*, 296–304.

[16] For rhodium(III) complexes with 1,4,7-trithiacyclononane, see for example: a) S. C. Rawle, R. Yagbasan, K. Prout, S. R. Cooper, *J. Am. Chem. Soc.* **1987**, *109*, 6181–6182; b) K. Brandt, W. S. Sheldrick, *J. Chem. Soc., Dalton Trans.* **1996**, 1237–1243.

[17] For rhodium(III) complexes with 1,4,7-triazacyclononane, see for example: K. Wieghardt, W. Schmidt, B. Nuber, B. Prikner, J. Weiss, *Chem. Ber.* **1980**, *113*, 36–41.

[18] For rhodium(III) complexes with 1,4,7-trimethyl-1,4,7-triazacyclononane, see for example: K. Wieghardt, P. Chaudhuri, B. Nuber, J. Weiss, *Inorg. Chem.* **1982**, *21*, 3086–3090.

[19] G. Manning, D. B. Whyte, R. Martinez, T. Hunter, S. Sudarsanam, *Science* **2002**, *298*, 1912–1934.

[20] a) M. A. Fabian, W. H. Biggs III, D. K. Treiber, C. E. Atteridge, M. D. Azimoara, M. G. Benedetti, T. A. Carter, P. Ciceri, P. T. Edeen, M. Floyd, J. M. Ford, M. Galvin, J. L. Gerlach, R. M. Grotzfeld, S. Herrgard, D. E. Insko, A. G. Lai, J.-M. Lélias, S. A. Mehta, Z. V. Milanov, A. M. Velasco, L. M. Wodicka, H. K. Patel, P. P. Zarrinkar, D. J. Lockhardt, *Nat. Biotechnol.* **2005**, *23*, 329–336; b) M. W. Karaman, S. Herrgard, D. K. Treiber, P. Gallant, C. E. Atteridge, B. T. Campbell,

K. W. Chan, P. Ciceri, M. I. Davis, P. T. Edeen, R. Faraoni, M. Floyd, J. P. Hunt, D. J. Lockhardt, Z. V. Milanov, M. J. Morrison, G. Pallares, H. K. Patel, S. Pritchard, L. M. Wodicka, P. P. Zarrinkar, *Nat. Biotechnol.* **2008**, *26*, 127–132.

[21] P. J. Blower, S. R. Cooper, *Inorg. Chem.* **1987**, *26*, 2009–2010.

[22] S. Niibayashi, H. Hayakawa, R.-H. Jin, H. Nagashima, *Chem. Commun.* **2007**, 1855–1857.

[23] V. Stavila, M. Allali, L. Canaple, Y. Stortz, C. Franc, P. Maurin, O. Beuf, O. Dufay, J. Samarut, M. Janier, J. Hasserodt, *New J. Chem.* **2008**, *32*, 428–435.

[24] A. L. Spek, *PLATON, A Multipurpose Crystallographic Tool*, Utrecht University, The Netherlands, **1998**.

[25] A. Altomare, G. Cascarano, C. Giacovazzo, A. Guagliardi, *J. Appl. Crystallogr.* **1993**, *26*, 343–350.

[26] M. C. Burla, R. Caliandro, M. Camalli, B. Carrozzini, G. L. Cascarano, L. De Caro, C. Giacovazzo, G. Polidori, D. Siliqi, R. Spagna, *J. Appl. Crystallogr.* **2007**, *40*, 609–613.

[27] G. M. Sheldrick, *Acta Crystallogr., Sect. A* **2008**, *64*, 112–122.

FULL PAPER

Syntheses, Structure, and Reactivity of Amino(azido)stibanes

Mathias Lehmann,[a] Axel Schulz,*[a,b] and Alexander Villinger[a]

Amino(azido)stibanes Mes*N(SiMe$_3$)Sb(N$_3$)X (X = N$_3$, Cl, OTf) were synthesized and fully characterized. Their structures were determined by single-crystal X-ray diffraction and are rare examples of antimony azides. On account of weak Sb···X van der Waals interactions, centrosymmetric dimers are observed in the solid state. Mes*N(SiMe$_3$)Sb(OTf)X species (X = Cl, N$_3$, and OTf; OTf = triflate = CF$_3$SO$_3^-$) are labile with respect to Me$_3$Si–OTf elimination even at ambient temperatures and form in situ the highly reactive iminostibane Mes*N=SbX, which rapidly decomposes. Diazide Mes*N(SiMe$_3$)Sb(N$_3$)$_2$ slowly decomposes when a Lewis acid such as B(C$_6$F$_5$)$_3$ is present, thus leading to the formation of a salt that bears a heterocyclic Sb–N dication and an [N$_3$–B(C$_6$F$_5$)$_3$]$^-$ adduct anion in good yields.

Introduction

Four-membered heterocycles of the type [X–Sb(μ-NR)]$_2$ are known as cyclo-1,3-distiba(III)-2,4-diazanes (X = halogen, R = organic group). These ring systems are good starting materials for polycyclic inorganic and organometallic compounds.[1–3] The cyclo-distiba(III)-diazane [Cl–Sb(μ-NtBu)]$_2$ was first generated by the treatment of SbCl$_3$ with LiN(SiMe$_3$)(tBu).[4] Stahl introduced a simple one-pot synthesis of [Cl–Sb(μ-NtBu)]$_2$ by using SbCl$_3$ and tBuNH$_2$. The structure was determined by Chivers et al.[5,6]

Recently, a series of four-membered rings of the type [X–Sb(μ-NR)]$_2$, which contain alternating antimony(III) and nitrogen centers, were synthesized and fully characterized (X = halogen, R = supermesityl = 2,4,6-tri-tert-butylphenyl = Mes*), and represent rare examples of cyclo-distibadiazanes.[7] The synthesis was carried out by starting from the triflate (triflate = CF$_3$SO$_3^-$ = OTf) species [TfO–Sb(μ-NR)]$_2$ (Scheme 1). By means of Me$_3$Si–OTf elimination, reactions of [TfO–Sb(μ-NR)]$_2$ with Me$_3$Si–X yielded the halogen compounds [X–Sb(μ-NR)]$_2$, except for the fluorine species, for which an iodine/fluorine exchange reaction with AgF was successfully applied.

Niecke et al. reported the first monomeric iminochlorophosphane Mes*–N=E–Cl (E = P).[8] The stabilities of the monomeric species R–N=E^{III}–X (E = P, As, Sb; X = Cl, OTf) with respect to the corresponding dimers by using Mes* groups (Mes* = 2,4,6-tri-tert-butylphenyl) on N and a chloro or triflate substituent on the pnictogen was only recently studied.[9–11]
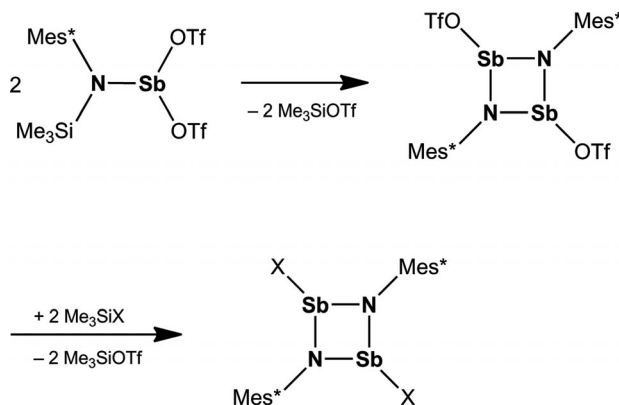
Scheme 1. Synthesis of halogen-substituted cyclo-1,3-distiba-2,4-diazane (X = Cl, Br, I).

We are interested in heterocycles of the type [X–E(μ-NR)]$_2$ with a central E$_2$N$_2$ ring (E = element of group 15) as building blocks for cyclic 1,3-dipnicata-2,4-diazenium cations[12] (Scheme 2) and nitrogen-rich compounds such as cyclic or acyclic pnictogen azides[13] or binary heterocycles such as tetraazapnictoles, which can be generated from pnictogen azides by means of Lewis acids such as GaCl$_3$ or B(C$_6$F$_5$)$_3$ (Scheme 3).[14]

Particularly useful for the synthesis of imino-stibanes R–N=Sb–X (X = Cl, N$_3$) are triflate-substituted species, RN(SiMe$_3$)Sb(OTf)X (X = Cl, N$_3$), since intrinsic elimination of Me$_3$Si–OTf (Scheme 1 and Scheme 4) may lead to the in situ formation of an azido(imino)stibane, which can either dimerize to give 1,3-diazido-cyclo-1,3-distiba-2,4-diazane or isomerize to a tetraazastibole when a Lewis acid is added (Scheme 3). Here we report on the synthesis and full characterization of Mes*N(SiMe$_3$)Sb(N$_3$)(OTf), Mes*N(SiMe$_3$)Sb(Cl)(N$_3$), and Mes*N(SiMe$_3$)Sb(N$_3$)$_2$ as possible candidates.

[a] Universität Rostock Institut für Chemie
Albert-Einstein-Strasse 3a, 18059 Rostock, Germany
E-mail: axel.schulz@uni-rostock.de
[b] Leibniz-Institut für Katalyse e.V. an der Universität Rostock,
Albert-Einstein-Strasse 29a, 18059 Rostock, Germany
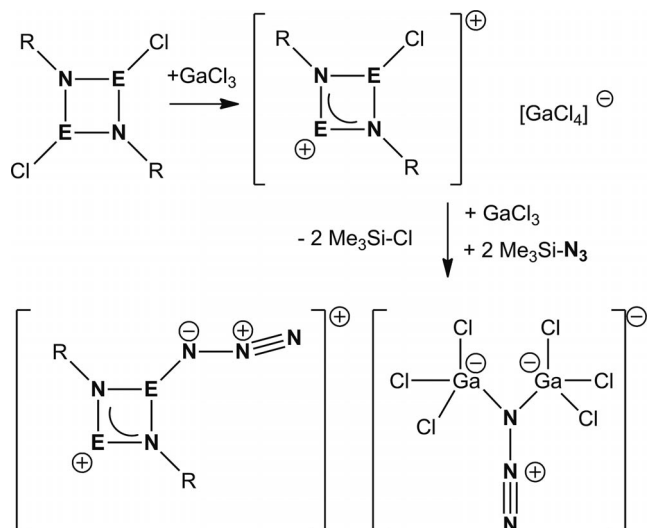
Scheme 2. Synthesis of nitrogen-rich *cyclo*-1,3-dipnicta-2,4-diazenium cations (E = P, As).
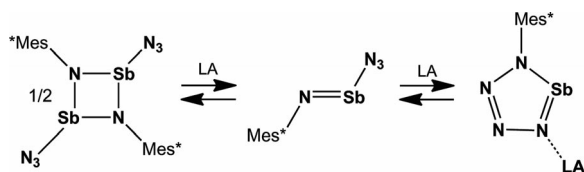
Scheme 3. Synthesis of tetrazastiboles (LA = Lewis acid).
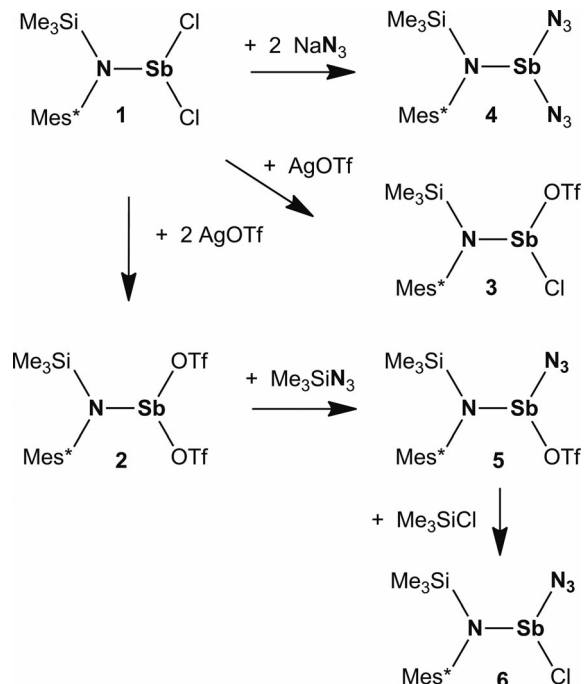
Scheme 4. Synthesis of amino(azido)stibanes.

Results and Discussion

To the best of our knowledge, monomeric acyclic amino-(azido)stibanes of the type R^1–$N(R^2)$–$Sb(X)$–N_3 (X = halogen, pseudohalogen, OTf; $R^{1,2}$ = organic substituents) are

not yet known. The only known acyclic antimony azides reported are $Sb(N_3)_3$,[15,16] $ClSb(N_3)_2$,[17] $[Sb(N_3)_4]^-$,[18] $[Sb(N_3)_4]^+$,[18] $Sb(N_3)_5$,[19] $[Sb(N_3)_6]^-$,[19] and $Sb(C_6H_5)_4$-(N_3).[20] Thus it was of interest to study R^1–$N(R^2)$–$Sb(X)$–N_3 species and their reactivity (e.g., with Lewis acids).

Synthesis

As shown in Scheme 4, amino(dichloro)stibane Mes*$N(SiMe_3)SbCl_2$ (**1**) was used as starting material for the synthesis of azido species of the type R^1–$N(R^2)$–$Sb(X)$–N_3 (X = Cl or OTf; R^1 = Mes*, R^2 = $SiMe_3$). The amino-(diazido)stibane Mes*$N(SiMe_3)Sb(N_3)_2$ (**4**) is easily obtained when a small excess amount of NaN_3 is added in one portion to a stirred solution of Mes*$N(SiMe_3)SbCl_2$ in THF at ambient temperatures. Removal of the solvent, extraction with *n*-hexane, and concentration finally resulted in the deposition of colorless crystals of Mes*$N(SiMe_3)$-$Sb(N_3)_2$ (**4**) in good yields (76%).

In a second series of experiments, we studied the synthesis of monoazido-stibanes Mes*$N(SiMe_3)Sb(N_3)X$, which were substituted by either a triflate or chloride ion (species **5**: X = OTf; **6**: X = Cl). Mes*$N(SiMe_3)Sb(N_3)(OTf)$ can be obtained in a two-step reaction: Treatment of Mes*N-$(SiMe_3)SbCl_2$ (**1**) with one equivalent of AgOTf gives Mes*$N(SiMe_3)Sb(Cl)(OTf)$ (**3**) in good yields (65%), whereas addition of a second equivalent of AgOTf leads to the formation of Mes*$N(SiMe_3)Sb(OTf)_2$ (**2**), which is an ideal precursor for the generation of monoazide **5**. Triflate-substituted aminostibanes are especially suitable for the generation of halogen- and pseudohalogen-substituted compounds by means of Me_3Si–OTf elimination upon ad-
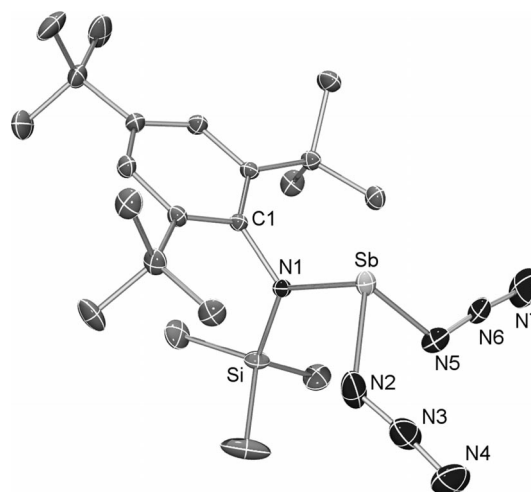

Figure 1. ORTEP drawing of the molecular structure of **4** in the crystal. Thermal ellipsoids with 30% probability at 173 K (hydrogen atoms omitted for clarity). Selected bond lengths [Å] and angles [°]: Sb1–N1 2.008(2), Sb–N5 2.085(2), Sb1–N2 2.089(3), Si1–N1 1.766(2), N1–C1 1.467(2), N2–N3 1.204(4), N3–N4 1.134(4), N5–N6 1.151(3), N6–N7 1.170(4); N1–Sb1–N5 99.19(9), N1–Sb1–N2 98.22(9), N5–Sb1–N2 84.3(1), C1–N1–Si1 116.0(1), C1–N1–Sb1 115.9(1), Si1–N1–Sb1 128.14(9), N3–N2–Sb1 119.2(2), N4–N3–N2 174.0(4), N6–N5–Sb1 122.2(2), N5–N6–N7 173.4(3).

dition of Me₃Si–X (X = halogen or pseudohalogen). For instance, when one equivalent of Me₃Si–N₃ was added to a solution of Mes*N(SiMe₃)Sb(OTf)₂ in CH₂Cl₂ at –60 °C, within 20 min the monoazido species **5** was formed upon Me₃Si–OTf elimination after warming to ambient temperatures (yield: 85%). Even monoazide **6** can now easily be generated from Mes*N(SiMe₃)Sb(N₃)(OTf) (**5**) simply by addition of Me₃Si–Cl, which triggers the elimination of Me₃Si–OTf and the exchange of OTf by Cl. It should be noted that species **2** and **5** already slowly eliminate Me₃Si–OTf at ambient temperatures in polar solvents such as CH₂Cl₂.

Properties and Characterization

Azidostibanes **4**, **5**, and **6** were fully characterized by NMR, IR, and Raman spectroscopy, elemental analysis, and single-crystal structure elucidation (Figures 1, 2, 3, and 4). As illustrated in Scheme 4, there are different synthetic routes but all afford species **4**, **5**, and **6** as colorless microcrystalline solids in good yields (>60%). Azide formation can easily be detected by means of IR spectroscopy. The vibrational spectra of all three azides feature the presence of covalently bound azido ligands as shown by the asymmetrical stretching mode in the range 2200–2000 cm⁻¹

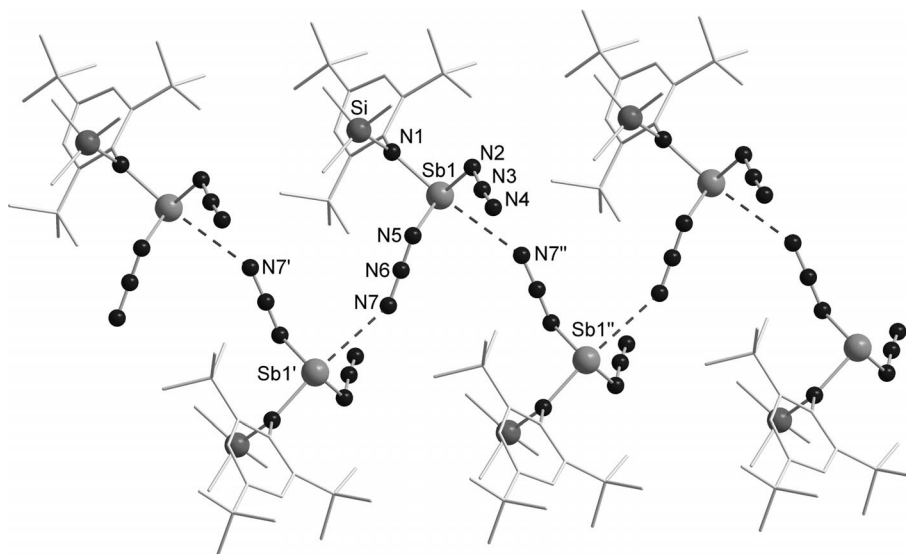Figure 2. Section of the chain composed of [···Sb–NNN···Sb–] units in the crystal in **4**. Two types of bonds form the chain: Sb1–N5 2.085(2) and Sb1···N7′ 3.196(4) Å.
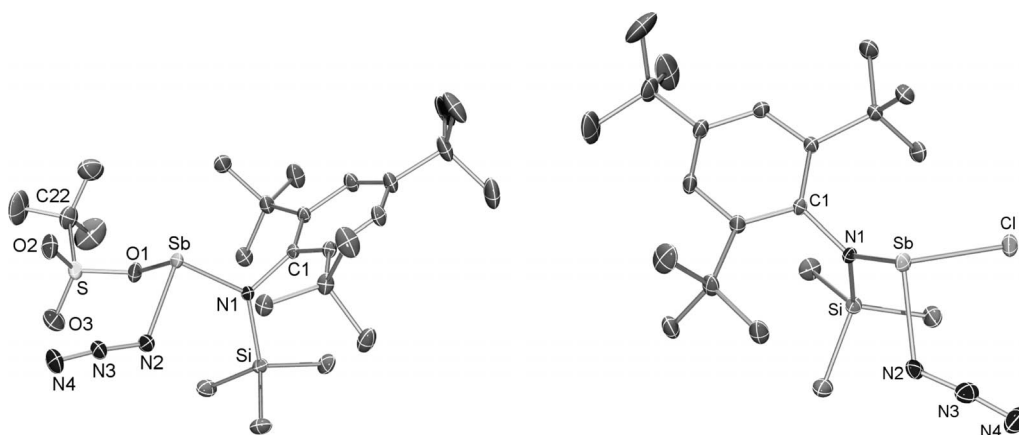

Figure 3. ORTEP drawing of the molecular structure of **5** (left) and **6** (right) in the crystal. Thermal ellipsoids with 30% probability at 173 K (hydrogen atoms omitted for clarity). Selected bond lengths [Å] and angles [°]; **5**: Sb1–N1 1.985(1), Sb1–N2 2.052(1), Sb1–O1 2.178(1), Si3–N1 1.789(1), N1–C1 1.466(2), N2–N3 1.223(2), N3–N4 1.133(2); N1–Sb1–N2 92.90(5), N1–Sb1–O1 95.26(4), N2–Sb1–O1 87.07(5), S1–O1–Sb1 121.57(7), C1–N1–Sb1 112.67(8), Si3–N1–Sb1 127.33(6), N3–N2–Sb1 121.4(1), N4–N3–N2 174.7(2); **6**: Sb1–Cl1 2.4347(5), Sb1–N2 2.105(2), Sb1–N1 2.007(1), N2–N3 1.166(2), N3–N4 1.138(3), Si1–N1 1.769(2), N1–C1 1.454(2), N1–Sb1–N2 93.53(6), N1–Sb1–Cl1 103.31(4), N2–Sb1–Cl1 89.94(5), C1–N1–Si1 116.5(1), C1–N1–Sb1 116.4(1), Si1–N1–Sb1 126.7(7), N3–N2–Sb1 117.6(1), N4–N3–N2 174.9(2).
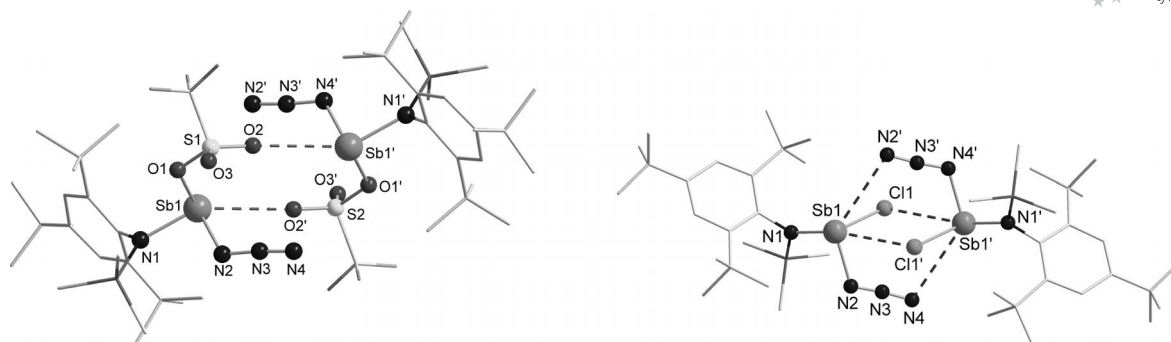
Figure 4. Formation of centrosymmetric dimers through small intermolecular interactions in monoazides **5** (left) and **6** (right).

$[v_{as}(N_3) = 2092$ (**4**), 2095 (**5**), 2103 cm^{-1} (**6**)], the symmetrical stretching mode at 1400–1200 cm^{-1}, and the deformation mode at 700–600 cm^{-1}. The Sb–N stretching modes are found in the range 450–350 cm^{-1} [414–455 (**4**), 423 (**5**), 407 (**6**), cf. 382–421 cm^{-1} in $Sb(N_3)_5$ and 370–386 cm^{-1} in $Sb(N_3)_3$].[16a,19] The presence of more than one azido ligand results in in-phase and out-of-phase coupling.

Compounds **4**, **5**, and **6** are air- and moisture-sensitive but stable under an argon atmosphere over a long period as solid; however, they slowly decompose in solvents such as THF even at ambient temperatures. Both the mono- and the diazides are neither heat- nor shock-sensitive and are thermally stable up to over 90 °C. Presumably decomposition starts with the intrinsic elimination of Me$_3$Si–OTf. In the solid state, the thermally most stable compound is diazido species **4** with a decomposition temperature of 148 °C, followed by compound **6** ($T_{dec.}$ = 120 °C). Monoazide **5** already decomposes at 95 °C without explosion. All three azidostibanes can be prepared in bulk.

X-ray Crystallography

The structures of compounds **2**–**6**, **9**, and **10** (compounds **9** and **10** will be introduced in the next chapter) have been determined. Tables 1 and 2 present the X-ray crystallographic data. X-ray-quality crystals of all considered species were selected in Kel-F-oil (Riedel-de Haën) or Fomblin YR-1800 (Alfa Aesar) at ambient temperature. All samples were cooled to –100(2) °C during the measurement.

The molecular structures of azides **4**, **5**, and **6** are shown in Figures 1, 2, 3, and 4, and of starting materials **2** and **3** in Figures 5 and 6, respectively, along with selected bond lengths and angles. More details are found in the Supporting Information.

Diazide Mes*N(SiMe$_3$)Sb(N$_3$)$_2$ (**4**) crystallizes in the triclinic space group $P\bar{1}$ with two formula units per cell. The structure consists of separated Mes*N(SiMe$_3$)Sb-(N$_3$)$_2$ molecules with two disordered *t*Bu groups. In contrast to the trigonal pyramidal Sb atom, the nitrogen atom

Table 1. Crystallographic details of **2**, **3**, and **4**.

	Mes*N(SiMe$_3$)Sb(OTf)$_2$ (**2**)	Mes*N(SiMe$_3$)Sb(Cl)(OTf) (**3**)	Mes*N(SiMe$_3$)Sb(N$_3$)$_2$ (**4**)
Formula	C$_{23}$H$_{38}$F$_6$NO$_6$S$_2$SbSi·0.5(C$_6$H$_{14}$)	C$_{22}$H$_{38}$ClF$_3$NO$_3$SSbSi	C$_{21}$H$_{38}$N$_7$SbSi
M_r [g mol^{-1}]	795.59	638.88	538.42
Color	colorless	colorless	colorless
Crystal system	triclinic	triclinic	monoclinic
Space group	$P\bar{1}$	$P\bar{1}$	$P2_1/c$
a [Å]	10.5338(4)	10.1239(3)	12.2068(4)
b [Å]	12.8586(5)	16.8725(5)	8.4027(3)
c [Å]	14.8720(5)	26.5485(8)	25.5240(9)
α [°]	77.470(2)	108.099(1)	90
β [°]	74.657(2)	100.612(1)	101.248(1)
γ [°]	65.953(2)	90.3640(10)	90
V [Å^3]	1760.4(1)	4227.0(2)	2567.7(2)
Z	2	6	4
$\rho_{calcd.}$ [g cm^{-3}]	1.501	1.506	1.393
μ [mm^{-1}]	1.005	1.233	1.142
T [K]	173(2)	173(2)	173(2)
Measured reflections	42168	81600	44137
Independent reflections	11844	22306	9299
Reflections [$I > 2\sigma(I)$]	10119	18109	6996
R_{int}	0.0317	0.0261	0.0376
$F(000)$	814	1956	1112
R_1 {$R[I > 2\sigma(I)]$}	0.0286	0.0285	0.0379
wR_2 (F^2)	0.077	0.0760	0.0950
GoF	1.075	1.064	1.063
Parameters	401	928	345

M. Lehmann, A. Schulz, A. Villinger

Table 2. Crystallographic details of **5**, **6**, and **10**.

	Mes*N(SiMe₃)Sb(N₃)(OTf) (**5**)	Mes*N(SiMe₃)Sb(Cl)(N₃) (**6**)	Compound **10**
Formula	$C_{22}H_{38}F_3N_4O_3SSbSi \cdot CH_2Cl_2$	$C_{21}H_{38}ClN_4SbSi$	$C_{30}H_{48}N_4Sb_2 \cdot 2(C_{18}BF_{15}N_3)$
M_r [g mol⁻¹]	730.39	531.84	1816.26
Color	colorless	colorless	red
Crystal system	monoclinic	monoclinic	monoclinic
Space group	$P2_1/n$	$P2_1/c$	$P2_1/c$
a [Å]	10.4273(4)	10.2880(4)	9.8897(3)
b [Å]	16.8836(5)	25.179(1)	17.0327(5)
c [Å]	19.0314(6)	10.4115(4)	20.4230(7)
α [°]	90	90	90
β [°]	103.313(2)	103.855(1)	94.453(2)
γ [°]	90	90	90
V [Å³]	3260.5(2)	2618.5(2)	3429.8(2)
Z	4	4	2
$\rho_{calcd.}$ [g cm⁻³]	1.488	1.349	1.759
μ [mm⁻¹]	1.158	1.215	0.920
T [K]	173(2)	173(2)	173(2)
Measured reflections	43552	29673	56893
Independent reflections	11626	7606	12057
Reflections [$I > 2\sigma(I)$]	9504	6266	9585
R_{int}	0.0232	0.0361	0.0363
$F(000)$	1488	1096	1792
R_1 {$R[I > 2\sigma(I)]$}	0.0259	0.0269	0.0362
wR_2 (F^2)	0.0695	0.0657	0.0827
GoF	1.070	1.038	1.043
Parameters	395	265	515

sits in a trigonal-planar environment ($\Sigma\sphericalangle = 360.0°$) with an Sb–N$_{amino}$ single bond of 2.008(2) Å (Sb–N1), whereas the two Sb–N$_{azide}$ single bonds are considerably longer with values of 2.085(2) (Sb–N5) and 2.089(3) Å (Sb1–N2), respectively. These Sb–N$_{amino}$ and Sb–N$_{azide}$ bonds lie in the expected range for aminostibanes, for example, d(Sb–N$_{amino}$) = 2.056(3) in Mes*N(SiMe₃)SbCl₂,[7] d(Sb–N$_{amino}$) = 2.092(2) and d(Sb–N$_{azide}$) = 2.104(2) in [tBuC-(iPrN)₂]Sb(N₃)₂,[21] and d(Sb–N$_{azide}$) = 2.119(4) Å in Sb(N₃)₃[16] [cf. $\Sigma r_{cov.}$(Sb–N) = 2.11 Å].[22] The angles around the antimony center vary strongly from 99.19(9) (N1–Sb1–N5)/98.22(9) (N1–Sb1–N2) to 84.3(1)° (N5–Sb1–N2), which gives a difference of around 14°. For both azido ligands, the typical *trans*-bent structure with N–N–N angles of about 173–174° is observed.[23] The N$_\alpha$–N$_\beta$ bonds differ significantly [1.204(4) versus 1.151(3) Å], and also the N$_\beta$–N$_\gamma$ bond length is slightly different with values of 1.134(4) (N3–N4) and 1.170(4) Å (N6–N7). This difference in bond lengths can be attributed to intermolecular interactions (Figure 1). A closer look at the intermolecular interactions in **4** reveals an expansion of the Sb coordination number by the formation of nitrogen bridges that involves the γ-nitrogen atom (N7) of only one azido ligand. These interionic distances are rather long with values of 3.196(4) Å [cf. Σr_{vdW}(Sb···N) = 3.8 Å];[24] however, they are responsible for the formation of a chainlike structure as depicted in Figure 2. A similar situation was found by Stahl et al. in diazido-*cyclo*-distibadiazane [N₃–Sb(μ-NtBu)]₂, which forms a layer structure of associated molecules, with intermolecular Sb···N contacts of 3.226 Å.

Monoazides **5**·CH₂Cl₂ and **6** crystallize in the monoclinic space groups $P2_1/n$ and $P2_1/c$, respectively, with four formula units per cell. As discussed before for diazide **4**, also

in compounds **5** and **6** the antimony adopts a trigonal-pyramidal geometry attached to a planar nitrogen atom (Figure 3). Since the structural parameters for all three azide compounds (**4**, **5**, and **6**) are very similar with respect to the Mes*N–Sb–N₃ moiety, we would like to focus only on the differences. Although the Sb–Cl bond length of 2.4347(5) Å is in the typical range for a single bond [cf. $\Sigma r_{cov.}$(Sb–Cl) = 2.39 Å] in azide **6**, the Sb–O distance [2.178(1) Å] is rather long compared to sum of the covalent radii (2.04 Å). This might partly be attributed to an intramolecular donor–acceptor interaction (negative hyperconjugation)[25] between the lone pair (which occupies a p-type atomic orbital) located at the amino-nitrogen atom (N1) and the antibonding Sb–O bond, which results in a weakening of the latter bond while introducing a small amount of π bonding along the Sb–N$_{amino}$ unit in accord with a short Sb–N1 bond [1.985(1) Å; cf. $\Sigma r_{cov.}$(Sb–N) = 2.11 Å].[22]

The asymmetric unit of **5** and **6** consists of a Mes*NSb(N₃)(OTf) (and one molecule of CH₂Cl₂) and a Mes*NSb(Cl)(N₃) molecule, respectively, but with small but significant symmetric intermolecular interactions that lead to the formation of centrosymmetric dimers (Figure 4). Whereas in **5** only one stronger Sb1···O2′ interaction [3.009(1); cf. Σr_{vdW}(Sb···O) = 3.7 Å and d(Sb···N5′) = 3.715(2) Å] between the Sb center and one oxygen atom of an adjacent triflate group is observed, in **6** both the Cl and the N$_{γ,azide}$ atom display weak contacts with the Sb centers [Sb1···Cl1′ 3.4902(5) Å, cf. Σr_{vdW}(Sb···Cl) = 4.0 Å and Sb1···N2′ 3.627(2) Å, cf. Σr_{vdW}(Sb···N) = 3.8 Å].

Mes*N(SiMe₃)Sb(OTf)₂·0.5 C₆H₁₄ (**2**·0.5n-hexane) and Mes*N(SiMe₃)Sb(Cl)(OTf) (**3**) crystallize in the triclinic space group $P\bar{1}$ with two and six formula units per cell, respectively. Furthermore, chlorotriflate **3** was also crys-

tallized from toluene, which led to the formation of mono-clinic crystals (space group $P2_1$) with an asymmetric unit
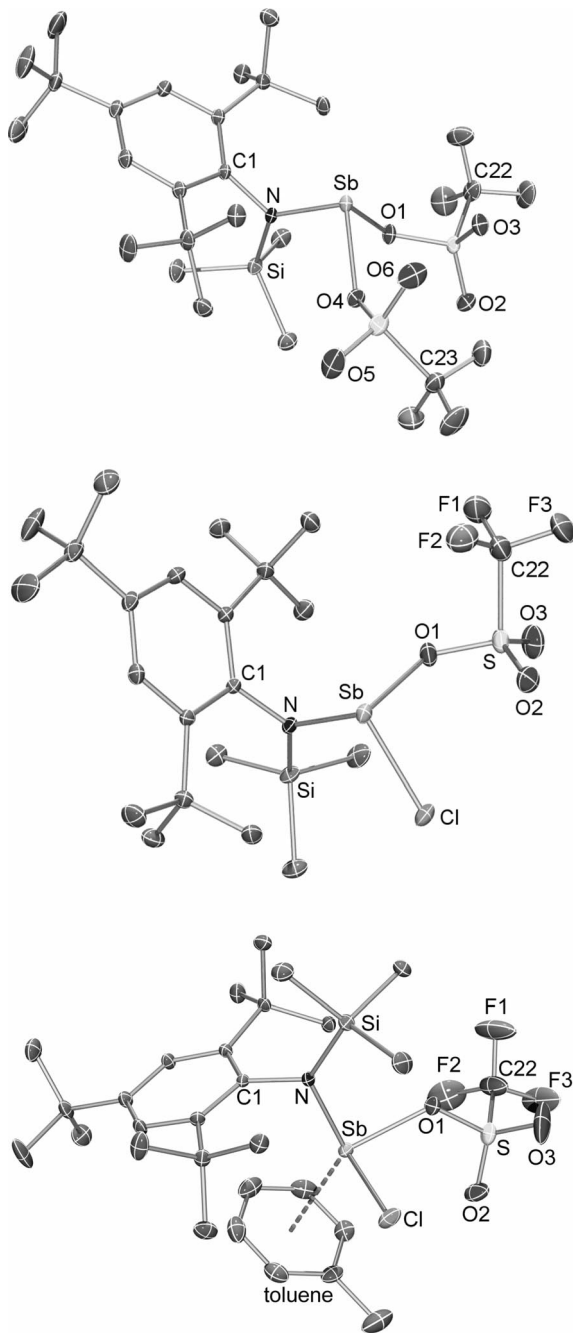

Figure 5. ORTEP drawing of the molecular structure of $2 \cdot 0.5 n$-hexane (top), **3** (middle), and $3 \cdot$toluene (bottom) in the crystal. Thermal ellipsoids with 30% probability at 173 K (hydrogen atoms omitted for clarity). Selected bond lengths [Å] and angles [°]: **2**: Sb–N 1.965(1), Sb–O1 2.069(1), Sb–O4 2.095(1), N–C1 1.467(2), N–Si 1.803(1); C1–N–Sb 115.73(9), Si–N–Sb 128.80(7), N–Sb–O1 91.22(5), N–Sb–O4 95.90(5), O1–Sb–O4 82.22(5), S1–O1–Sb 121.58(6), S2–O4–Sb 126.49(7). **3**C Sb1–N1 1.998(1), Sb1–O1 2.159(1), Sb1–Cl1 2.338(5); N1–Sb1–O1 98.67(6), N1–Sb1–Cl1 98.74(4), O1–Sb1–Cl1 88.49(4), S1–O1–Sb1 125.35(9), C1–N1–Si1 126.3(1), C1–N1–Sb1 105.7(1). $3 \cdot$toluene: Sb–N 2.005(2), Sb–O1 2.117(2), Sb–Cl 2.375(1), Sb···centroid 3.203(1); N–Sb–O1 91.61(6), N–Sb–Cl 104.44(5), O1–Sb–Cl 87.38(5), S1–O1–Sb 124.7(1), C1–N–Si 128.0(2), C1–N–Sb 103.2(2).

that consists of one Mes*N(SiMe$_3$)Sb(Cl)(OTf) molecule along with one toluene molecule (Figure 5). In $3 \cdot$toluene, significant solvent···antimony interaction in an η^6 fashion [Sb···C$_{aryl}$ distances between 3.42–3.57 Å, cf. Σr_{vdW}(Sb···C) = 3.9 Å] but no dimer formation due to intermolecular interactions between adjacent Mes*N(SiMe$_3$)Sb(Cl)(OTf) molecules is observed. In contrast, for $2 \cdot 0.5 n$-hexane, no solvent interactions but centrosymmetric dimer formation due to strong Sb···O interactions are found (Figure 6).[7] Besides two intermolecular van der Waals contacts [Sb1···O3′ 3.541(1) and Sb1···O6′ 3.546(2) Å], two intramolecular contacts [Sb1···O3′ 3.135(2) and Sb1···O6′ 3.311(2) Å] can also be found. By these four interactions a Sb$_2$O$_4$ octahedron is built (Figure 6, right). Also Mes*N(SiMe$_3$)Sb(Cl)(OTf) (**3**) forms a centrosymmetric dimer due to intra- and intermolecular interactions [Sb1···O2 3.314(2) and Sb1···O2′ 3.145(1) Å] as depicted in Figure 6 (left), however, no significant Sb···Cl′ contacts are observed [Sb···Cl′ 4.713(5) Å]. Compared to compounds **5** and **6**, similar structural features with respect to bond lengths and angles are found for **2** and **3** (Figure 5).

Reactivity – Decomposition

Amino(azido)stibanes of the type Mes*N(SiMe$_3$)–Sb(N$_3$)Y (**4**: Y = N$_3$, **5**: OTf, and **6**: Cl) were synthesized to study the possibility of an intrinsic Me$_3$Si–Y elimination, which generates in situ a reactive imino(azido)stibane as illustrated in Scheme 5. Imino(azido)stibanes that bear an Sb=N double bond can either dimerize along this double bond forming a [N$_3$–Sb(μ-NMes*)]$_2$ heterocycle (**7**) or cyclize to give a tetraazastibole (**8**), a compound which was recently obtained by an unusual isomerization reaction starting from **7** upon addition of a Lewis acid (Scheme 5).[10,13] Like Mes*N(SiMe$_3$)Sb(OTf)$_2$ (**2**), which eliminates Me$_3$Si–OTf at ambient temperatures to lead finally to the formation of the corresponding cyclo-1,3-distiba-2,4-diazane [OTf–Sb(μ-NMes*)]$_2$,[7] Mes*N(SiMe$_3$)-Sb(Cl)(OTf) (**3**) isomerizes at 70 °C in n-hexane to result in the formation of a mixture of Mes*N(SiMe$_3$)SbCl$_2$ (**1**) and **2**, which further eliminates Me$_3$Si–OTf to yield [OTf–Sb-(μ-NMes*)]$_2$ (Schemes 1 and 6). Also monoazide Mes*N(SiMe$_3$)Sb(N$_3$)(OTf) (**5**) slowly decomposes in CH$_2$Cl$_2$ and releases Me$_3$Si–OTf. In this case, only Mes*–N$_3$ (**9**) (yield: 42%) and Me$_3$Si–OTf could be observed as products in this decomposition reaction (Scheme 6), which suggests the elimination of Me$_3$Si–OTf at the beginning followed by formation and decomposition of a tetrazastibole. Mes*–N$_3$ (**9**) was characterized by an X-ray structure determination. In addition to the known triclinic structure (**9a**), a new monoclinic modification was obtained (**9b**) (see the Supporting Information).[26] In contrast to compound **5**, species **1**, **4**, and **6** do not eliminate Me$_3$Si–Y even at elevated temperatures. Diazide **4** is thermally relatively stable. For this reason, we added the Lewis acid B(C$_6$F$_5$)$_3$ to trigger the intrinsic elimination of Me$_3$Si–N$_3$. But even under these conditions the decomposition reaction is rather slow.
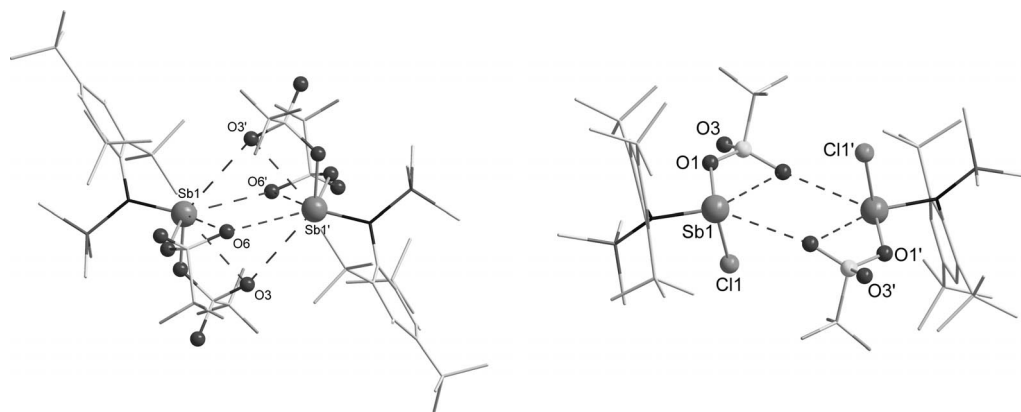
Figure 6. Formation of centrosymmetric dimers through small intermolecular interactions in **5** (left) and **6** (right).

It took about five days for a complete decomposition in CH_2Cl_2 at ambient temperatures to lead in good yields (>50%) to an intriguing dimeric heterocyclic Sb–N dication with an azide–borane adduct anion, $[N_3–B(C_6F_5)_3]^−$, as de-

picted in Scheme 7. The anion was first described by Klapötke et al. in 2002.[27] We do want to stress that the preparation of the salt that contains the heterocyclic Sb–N dication (**10**) can be reproduced in good yields although we know only very little about its formation. Sb–N dication with the $[N_3–B(C_6F_5)_3]^−$ counterion (**10**) can be isolated as deep red crystals from CH_2Cl_2. Crystals of **10** are neither heat- nor shock-sensitive and decompose above 173 °C.

The dimeric cyclic Sb–N ion represents one of the rare examples of nitrogen–antimony cations.[28] Formally, the dication from **10** can be regarded as a dimer of a diazastibolium monocation (Scheme 7). Compound **10** crystallizes in the monoclinic space group $P2_1/c$ with two formula units per cell. The structure consists of separated centrosymmetric dications and $[N_3–B(C_6F_5)_3]^−$ anions (Figure 7). Only two weak $Sb\cdots F_{C_6F_5}$ [Sb$\cdots$F11 3.216(1), Sb$\cdots$F1′ 3.439(1) Å] and two $Sb\cdots N_{azide}$ [Sb$\cdots$N3 3.302(2), Sb$\cdots$N5′ 3.600(2) Å] contacts are found. The central Sb_2N_2 ring is planar with two significant different Sb–N distances [Sb1–N1 2.103(2), Sb1–N1′ 2.315(2) Å] as well as all other cycles to form a planar framework of five condensed cycles in the dication. The Sb–N2 distance amounts to Sb1–N2 2.239(2) Å [cf. Σr_{cov}(Sb–N) = 2.11 Å].[22] The coordination sphere around the antimony(III) can be best understood as a strongly distorted bisphenoidal arrangement with the axial unit along N2–Sb–N1′ [N1–Sb1–C1 91.15(9), N1–Sb1–N2 73.35(6), C1–Sb1–N2 85.42(9), N1–Sb1–N1′ 71.12(6), C1–Sb1–N1′ 86.82(9), N2–Sb1–N1′ 143.41(6)°] when the weak van der Waals interactions are not considered.
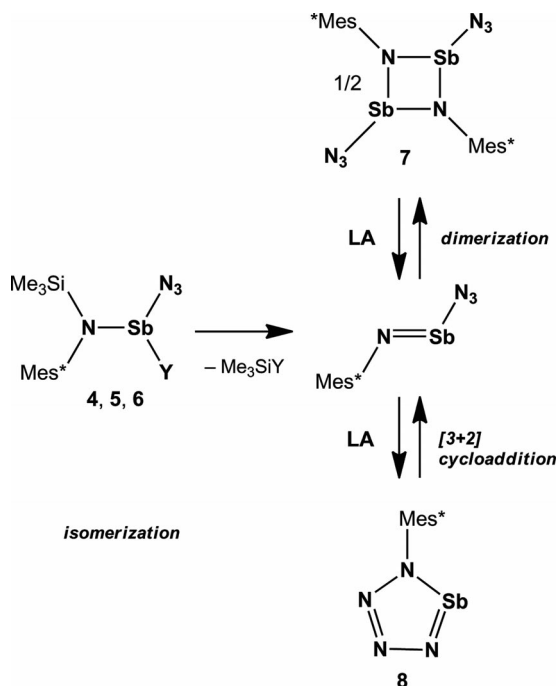
Scheme 5. Application of amino(azido)stibanes (**4**: Y = N_3, **5**: Y = OTf, **6**: Y = Cl; LA = Lewis acid).
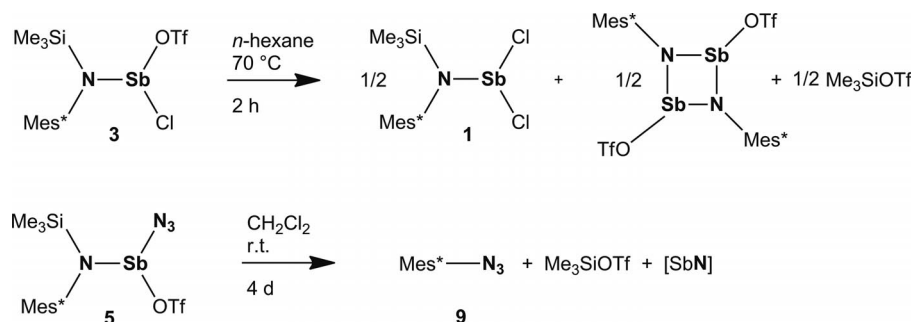
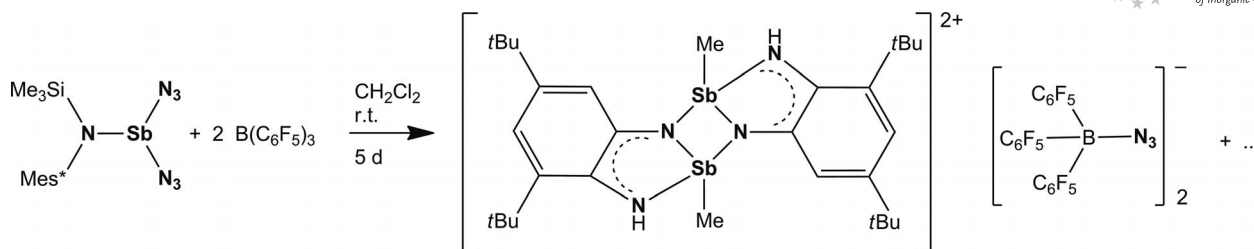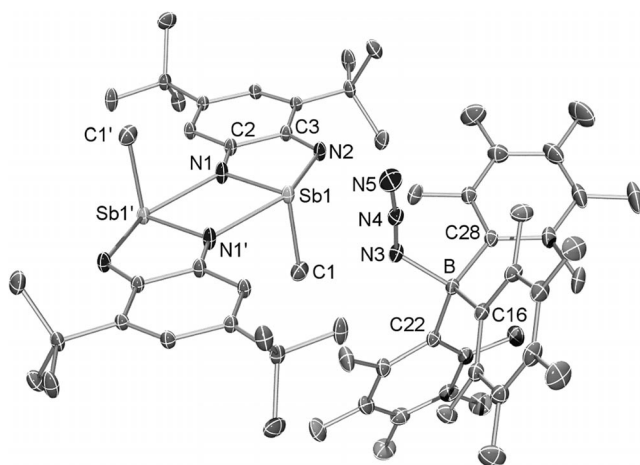Scheme 6. Decomposition of **3** and **5**.

Scheme 7. Reaction of **4** with B(C₆F₅)₃ to **10**.

Figure 7. ORTEP drawing of the decomposition product **10** in the crystal. Thermal ellipsoids with 30% probability at 173 K (hydrogen atoms omitted for clarity). Selected bond lengths [Å] and angles [°]: Sb1–N1 2.103(2), Sb1–N2 2.239(2), Sb1–N1′ 2.315(2), Sb1–C1 2.133(2), N1–C2 1.290(2), N2–C3 1.288(2), B1–N3 1.590(2), B1–C22 1.644(3), B1–C28 1.648(3), B1–C16 1.650(3), N3–N4 1.208(2), N4–N5 1.138(2); N1–Sb1–C1 91.15(9), N1–Sb1–N2 73.35(6), C1–Sb1–N2 85.42(9), N1–Sb1–N1′ 71.12(6), C1–Sb1–N1′ 86.82(9), N2–Sb1–N1′ 143.41(6), C2–N1–Sb1 119.3(1), C2–N1–Sb1′ 131.3(1), C3–N2–Sb1 117.3(1), N3–B1–C22 106.4(1), N3–B1–C28 107.3(1), C22–B1–C28 109.8(1), N3–B1–C16 105.7(1), C22–B1–C16 114.13(2), C28–B1–C16 113.0(2), N4–N3–B1 120.4(2), N5–N4–N3 174.6(2).

The adduct anion [N₃–B(C₆F₅)₃]⁻ belongs to a class of adduct anions of strong Lewis acids such as [(F₅C₆)₃B(μ-X)-B(C₆F₅)₃]⁻ (X = CN, OH),[29–31] [Y–B(C₆F₅)₃]⁻ (OH),[32–36] [N{CN·B(C₆F₅)₃}₂]⁻, [C{CN·B(C₆F₅)₃}₃]⁻, [B{CN·B-(C₆F₅)₃}₄]⁻,[37] [NO₃·B(C₆F₅)₃]⁻, or even [SO₄·2B-(C₆F₅)₃]²⁻.[38] These anions are easily prepared in a simple acid/base reaction. For example, an excess amount of B(C₆F₅)₃ is added to basic anions such as dicyanoamide or nitrate to give in almost quantitative yields adduct anions with astonishingly stable borate units. An example of an azide-diadduct anion is [N₃(GaCl₃)₂]⁻ with two GaCl₃ units attached to the same N atom (Scheme 2).[12a,12f,39]

The azide ion distorts upon complexation from $D_{\infty h}$ to C_s symmetry with two different N–N bond lengths [N3–N4 1.208(2), N4–N5 1.138(2) Å; N1–N2–N3 174.6(2)°]. The azide anion (Figure 7) and the B(C₆F₅)₃ group are connected by means of a strong B–N bond {B1–N3 1.590(2) Å; cf. 1.616(3) Å in CH₃CN·B(C₆F₅)₃;[40] 1.658 Å in H₃N–BH₃;[41] 1.987(3) and 1.974(3) Å in [N₃(GaCl₃)₂]⁻}.[39] The central boron atom is tetracoordinate with an average B–

C(aryl) bond length of 1.647 Å. The coordination geometry around boron in the tetrahedral BC₃N core is slightly distorted with the smallest angle of 105.7, and the largest 114.1°. The B1–N3–N4 angle amounts to 120.4(2)°.

Conclusion

Amino(azido)stibanes of the type Mes*N(SiMe₃)Sb-(N₃)Y (Y = N₃, OTf, and Cl) were synthesized to study the possibility of an intrinsic Me₃Si–Y elimination. They are easily obtained either by Cl/N₃ substitution reactions or the elimination of Me₃Si–OTf when triflate-substituted precursors are treated with Me₃Si–N₃. The solid-state structures of the monoazides **5** and **6** as well as diazide **4** revealed the formation of centrosymmetric dimers facilitated by weak Sb···Z van der Waals interactions (Z = O, N, Cl atoms).

Triflate-substituted amino(azido)stibanes slowly decompose even at ambient temperatures in CH₂Cl₂ to form in situ a highly reactive iminostibane when an adjacent Me₃Si group is available. Without a triflate group such as in diazide **4**, amino(azido)stibanes are relatively stable with respect to Me₃Si–N₃ elimination. However, by addition of a Lewis acid, decomposition is strongly enhanced, thereby resulting in the formation of a salt that bears an intriguing dimeric cyclic Sb–N dication and the adduct anion [N₃–B(C₆F₅)₃]⁻. The dimeric cyclic Sb–N ion represents one of the rare examples of antimony dication.

Experimental Details

General Information: All manipulations were carried out under oxygen- and moisture-free conditions by using standard Schlenk and drybox techniques.

Dichloromethane was purified according to a literature procedure,[42] dried first with P₄O₁₀ and secondly with CaH₂, then freshly distilled prior to use. CH₃CN was dried with P₄O₁₀ and freshly distilled prior to use. Tetrahydrofuran (THF) and toluene were dried with Na/benzophenone and freshly distilled prior to use. *n*-Hexane was dried with Na/benzophenone/tetraglyme and freshly distilled prior to use.

Trimethylsilyl chloride (99%, Merck) and trimethylsilyl azide (99%, Fluka) were distilled prior to use. NaN₃ (99%, Acros) was used as received. Silver trifluoromethylsulfonate (AgOTf),[43] dichloro-[(2,4,6-tri-*tert*-butylphenyl)(trimethylsilyl)amino]stibane (Mes*N-(SiMe₃)SbCl₂, **1**), [(2,4,6-tri-*tert*-butylphenyl)(trimethylsilyl)amino]-bis(trifluoromethylsulfonyl)stibane (Mes*N(SiMe₃)Sb(OTf)₂, **2**),[7] and B(C₆F₅)₃[44] were prepared according to literature procedures.

$^{13}C\{^1H\}$, ^{13}C DEPT, ^1H, $^{19}F\{^1H\}$, and ^{29}Si INEPT NMR spectra were obtained with a Bruker AVANCE 300 spectrometer or a Bruker AVANCE 500 spectrometer and were referenced internally to the deuterated solvent [^{13}C, CD_2Cl_2: δ_{ref} = 54.0 ppm, $CDCl_3$: δ_{ref} = 77.0 ppm, OC_4D_8 ([D_8]THF): δ_{ref} = 67.4 ppm] or to protic impurities in the deuterated solvent (^1H, $CDHCl_2$: δ_{ref} = 5.31 ppm, $CHCl_3$: δ_{ref} = 7.26 ppm, OC_4D_7H: δ_{ref} = 3.57 ppm). CD_2Cl_2 and $CDCl_3$ were dried with P_4O_{10}, [D_8]THF was dried with Na/benzophenone. A Nicolet 380 FTIR with a Smart Orbit ATR device was used for IR spectroscopy. For Raman spectroscopy, a Bruker VERTEX 70 FTIR instrument with a RAM II FT-Raman module and equipped with an Nd:YAG laser (1064 nm) was used. An Analysator Flash EA 1112 from Thermo Quest or a C/H/N/S-Mikronalysator TruSpec-932 from Leco was used for C, H, N analyses. Melting points: EZ-Melt, Stanford Research Systems, heating rate 20 °C min^{-1} (clearing-points are reported). Mass spectrometry was carried out with a Finnigan MAT 95-XP from Thermo Electron.

X-ray Structure Determination: X-ray-quality crystals of **2**, **3**, **3**·toluene, **4**, **5**, **6**, **9a**, **9b**, and **10** were selected in Kel-F-oil (Riedel deHaen) or Fomblin YR-1800 (Alfa Aesar) at ambient temperatures. All samples were cooled to 173(2) K during measurement. The data were collected with a Bruker Apex Kappa-II diffractometer using graphite-monochromated Mo-K_α radiation (λ = 0.71073 Å). The structures were solved by direct methods (SHELXS-97)[45] and refined by full-matrix least-squares procedures (SHELXL-97).[46] Semiempirical absorption corrections were applied (SADABS).[47] All non-hydrogen atoms were refined anisotropically; hydrogen atoms were included in the refinement at calculated positions using a riding model.

CCDC-852780 (for **2**), -852781 (for **3**), -852783 (for **4**), -852784 (for **5**), -852785 (for **6**), and -852786 (for **10**) contain the supplementary crystallographic data for this paper. These data can be obtained free of charge from The Cambridge Crystallographic Data Centre via www.ccdc.cam.ac.uk/data_request/cif.

Mes*N(SiMe₃)SbCl(OTf) (3): AgOTf (1 mmol, 0.26 g) in toluene (5 mL) was added over a period of five minutes at 0 °C to a stirred solution of Mes*N(SiMe₃)SbCl₂ (1 mmol, 0.53 g) in toluene (10 mL), and the resulting colorless suspension was stirred for two hours. The solvent was removed under vacuum, and the colorless residue was extracted with *n*-hexane (10 mL) and filtered (F4). The colorless solution was concentrated to about 2 mL and stored at +5 °C for several hours to result in the deposition of colorless crystals. Removal of solvent by syringe and drying yielded 0.42 g (0.65 mmol, 65%) of Mes*N(SiMe₃)SbCl(OTf) (**3**) as a colorless crystalline solid; m.p. 113 °C (dec.). $C_{22}H_{38}NClF_3O_3SSbSi$ (638.88): calcd. C 41.36, H 5.99, N 2.19; found C 41.49, H 5.96, N 2.11. ^1H NMR (25 °C, CD_2Cl_2, 300.13 MHz): δ = 0.29 [s, 9 H, Si(CH_3)₃], 1.30 (s, 9 H, *p-t*Bu), 1.56 (s, 18 H, *o-t*Bu), 7.51 (s, 2 H, CH) ppm. $^{13}C\{^1H\}$ NMR (25 °C, CD_2Cl_2, 75.48 MHz): δ = 4.57 [Si(CH_3)₃], 31.50 [C(CH_3)₃], 35.51 [C(CH₃)₃], 36.11 [C(CH_3)₃], 38.74 [C(CH₃)₃], 119.10 [q, $^1J(^{13}C,^{19}F)$ = 318.4 Hz, CF_3], 126.46 (CH), 135.79 (Ar–C), 149.00 (Ar–C), 150.23 (Ar–C) ppm. ^{19}F NMR (25 °C, CD_2Cl_2, 282.38 MHz): δ = –77.51 (CF_3) ppm. ^{29}Si INEPT NMR (25 °C, CD_2Cl_2, 49.70 MHz): δ = 19.8 [Si(CH₃)₃] ppm. IR (ATR, 25 °C, 32 scans): $\tilde{\nu}$ = 2960 (m), 2906 (m), 2872 (m), 1598 (m), 1514 (m), 1496 (w), 1478 (m), 1469 (w), 1464 (w), 1436 (w), 1404 (w), 1393 (w), 1381 (w), 1364 (m), 1250 (s), 1222 (s), 1172 (s), 1100 (m), 1020 (s), 992 (m), 936 (w), 911 (m), 883 (m), 864 (s), 853 (m), 836 (m), 812 (m), 781 (m), 760 (m), 753 (m), 749 (m), 730 (m), 711 (m), 689 (m), 671 (m), 665 (m), 627 (s), 612 (s), 575 (s), 542 (m) cm^{-1}. Raman (75 mW, 25 °C, 500 scans): $\tilde{\nu}$ = 3059 (2), 2961 (8), 2907 (10), 2780 (1), 2712 (1), 1602 (3), 1464 (2), 1448 (2), 1415

(2), 1392 (1), 1287 (2), 1235 (2), 1213 (3), 1202 (3), 1180 (2), 1144 (2), 1099 (1), 1029 (1), 1003 (2), 936 (1), 923 (1), 868 (1), 821 (2), 785 (1), 765 (2), 712 (1), 634 (1), 572 (2), 469 (1), 374 (1), 339 (2), 318 (4), 245 (2), 148 (1), 118 (1) cm^{-1}.

Mes*N(SiMe₃)Sb(N₃)₂ (4): NaN₃ (2 mmol, 0.13 g) was added in one portion at ambient temperatures to a stirred solution of Mes*N(SiMe₃)SbCl₂ (1 mmol, 0.53 g) in THF (10 mL), and the resulting colorless suspension was stirred for 20 h. The solvent was removed under vacuum, and the colorless residue was extracted with *n*-hexane (10 mL) and filtered (F4). The colorless solution was concentrated to about 2 mL and stored at +5 °C for several hours, which resulted in the deposition of colorless crystals of solvent by syringe. Drying yielded 0.41 g (0.76 mmol, 76%) of Mes*N(SiMe₃)Sb(N₃)₂ (**4**) as a colorless crystalline solid; m.p. 148 °C (dec.). $C_{21}H_{38}N_7SbSi$ (538.42): calcd. C 46.85, H 7.11, N 18.21; found C 47.75, H 7.39, N 18.06. ^1H NMR (25 °C, CD_2Cl_2, 300.13 MHz): δ = 0.20 [s, 9 H, Si(CH_3)₃], 1.29 (s, 9 H, *p-t*Bu), 1.55 (s, 18 H, *o-t*Bu), 7.45 (s, 2 H, CH) ppm. $^{13}C\{^1H\}$ NMR (25 °C, CD_2Cl_2, 75.48 MHz): δ = 4.06 [Si(CH_3)₃], 31.56 [C(CH_3)₃], 35.05 [C(CH_3)₃], 35.62 [C(CH₃)₃], 38.51 [C(CH₃)₃], 125.86 (CH), 139.27 (Ar–C), 147.57 (Ar–C), 149.77 (Ar–C) ppm. ^{29}Si INEPT NMR (25 °C, CD_2Cl_2, 49.70 MHz): δ = 14.6 [Si(CH₃)₃] ppm. IR (ATR, 25 °C, 32 scans): $\tilde{\nu}$ = 3390 (vw), 3334 (vw), 2957 (m), 2905 (m), 2863 (m), 2092 (s), 2078 (s), 1599 (w), 1556 (vw), 1539 (vw), 1520 (vw), 1505 (vw), 1487 (w), 1471 (m), 1461 (m), 1457 (m), 1435 (w), 1404 (m), 1391 (m), 1361 (m), 1314 (m), 1263 (m), 1250 (s), 1213 (m), 1198 (m), 1172 (m), 1140 (m), 1030 (vw), 1020 (vw), 939 (vw), 910 (w), 887 (m), 850 (s), 832 (s), 768 (m), 749 (s), 727 (s), 683 (m), 673 (m), 643 (s), 578 (m), 550 (w), 538 (m) cm^{-1}. Raman (75 mW, 25 °C, 500 scans): $\tilde{\nu}$ = 3479 (1), 3069 (1), 2963 (9), 2905 (10), 2866 (5), 2777 (1), 2708 (1), 2095 (6), 2079 (3), 1600 (4), 1453 (3), 1406 (1), 1362 (1), 1317 (1), 1287 (1), 1249 (2), 1200 (2), 1175 (3), 1140 (3), 1101 (2), 1025 (1), 922 (1), 824 (2), 748 (1), 729 (2), 684 (1), 645 (1), 632 (1), 570 (2), 508 (1), 488 (1), 455 (1), 414 (6), 274 (1), 237 (1), 220 (1), 181 (1), 130 (1) cm^{-1}.

Mes*N(SiMe₃)Sb(N₃)(OTf) (5): Me₃SiN₃ (1 mmol, 0.12 g) in CH₂Cl₂ (3 mL) was added over a period of five minutes at –60 °C to a stirred solution of Mes*N(SiMe₃)Sb(OTf)₂ (1 mmol, 0.75 g) in CH₂Cl₂ (10 mL). The resulting colorless solution was warmed to room temperature over a period of 20 min. The solvent was removed under vacuum, and the colorless residue was recrystalized from *n*-hexane. Removal of solvent by syringe and drying yielded 0.55 g (0.85 mmol, 85%) of Mes*N(SiMe₃)SbN₃(OTf) (**5**) as a colorless crystalline solid; m.p. 95 °C (dec.). $C_{22}H_{38}N_4F_3O_3SSbSi$ (645.47): calcd. C 40.94, H 5.93, N 8.68; found C 40.75, H 5.84, N 7.26. ^1H NMR (25 °C, CD_2Cl_2, 300.13 MHz): δ = 0.23 [s, 9 H, Si(CH_3)₃], 1.29 (s, 9 H, *p-t*Bu), 1.54 (s, 18 H, *o-t*Bu), 7.48 (s, 2 H, CH) ppm. $^{13}C\{^1H\}$ NMR (25 °C, CD_2Cl_2, 75.48 MHz): δ = 4.10 [Si(CH_3)₃], 31.49 [C(CH_3)₃], 35.12 [C(CH₃)₃], 35.94 [C(CH_3)₃], 38.60 [C(CH₃)₃], 119.30 [q, $^1J(^{13}C,^{19}F)$ = 318.2 Hz, CF_3], 126.20 (CH), 136.37 (Ar–C), 148.62 (Ar–C), 149.71 (Ar–C) ppm. ^{19}F NMR: δ = (25 °C, CD_2Cl_2, 282.38 MHz): –77.17 (CF_3) ppm. ^{29}Si INEPT NMR (25 °C, CD_2Cl_2, 49.70 MHz): δ = 18.8 [Si(CH₃)₃] ppm. IR (ATR, 25 °C, 32 scans): $\tilde{\nu}$ = 2958 (m), 2912 (m), 2870 (m), 2103 (s), 1600 (w), 1478 (w), 1462 (w), 1405 (w), 1393 (m), 1350 (m), 1313 (m), 1256 (m), 1229 (m), 1196 (s), 1171 (m), 1149 (m), 1097 (m), 1023 (m), 960 (s), 908 (w), 882 (m), 840 (s), 768 (m), 748 (m), 739 (m), 689 (m), 678 (m), 630 (s), 586 (m), 573 (m), 541 (m) cm^{-1}. Raman (250 mW, 25 °C, 1000 scans): $\tilde{\nu}$ = 3090 (1), 2995 (3), 2964 (8), 2907 (10), 2783 (1), 2712 (1), 2094 (4), 1601 (4), 1547 (1), 1455 (2), 1408 (2), 1356 (1), 1290 (1), 1247 (1), 1229 (2), 1197 (2), 1173 (2), 1139 (3), 1098 (2), 1022 (1), 959 (1), 937 (1), 920 (1), 862

(1), 816 (2), 767 (2), 740 (2), 690 (1), 634 (2), 570 (2), 542 (1), 481 (1), 423 (6), 323 (1), 255 (1), 182 (2) cm^{-1}.

Mes*N(SiMe₃)SbCl(N₃) (6): Me₃SiCl (1 mmol, 0.11 g) in CH₂Cl₂ (3 mL) was added over a period of five minutes at –60 °C to a stirred solution of Mes*N(SiMe₃)Sb(N₃)(OTf) (1 mmol, 0.65 g) in CH₂Cl₂ (10 mL). The resulting colorless solution was warmed to room temperature over a period of 20 min. The solvent was removed under vacuum and the colorless residue was recrystallized from *n*-hexane. Removal of solvent by syringe and drying yielded 0.38 g (0.72 mmol, 72%) of Mes*N(SiMe₃)SbCl(N₃) (6) as a colorless crystalline solid; m.p. 120 °C (dec.). C₂₁H₃₈N₄ClSbSi (531.84): calcd. C 47.42, H 7.20, N 10.53; found C 47.56, H 7.20, N 10.38. ¹H NMR (25 °C, CD₂Cl₂, 300.13 MHz): δ = 0.23 [s, 9 H, Si(C*H*₃)₃], 1.28 (s, 9 H, *p-t*Bu), 1.56 (s, 18 H, *o-t*Bu), 7.45 (s, 2 H, C*H*) ppm. IR (ATR, 25 °C, 32 scans): ṽ = 3390 (vw), 3334 (vw), 2956 (m), 2911 (m), 2859 (m), 2095 (s), 2078 (s), 1603 (m), 1484 (m), 1476 (m), 1462 (m), 1404 (m), 1391 (m), 1361 (m), 1311 (m), 1260 (s), 1254 (s), 1245 (m), 1213 (m), 1193 (m), 1170 (m), 1135 (m), 1099 (s), 1026 (w), 1019 (w), 942 (w), 923 (w), 908 (w), 896 (w), 883 (m), 851 (s), 833 (s), 769 (m), 750 (s), 731 (s), 686 (m), 671 (m), 644 (s), 634 (m), 605 (w), 580 (m), 569 (w), 540 (m) cm^{-1}.

Compound 10: A solution of B(C₆F₅)₃ (1 mmol, 0.52 g) in CH₂Cl₂ (5 mL) was added at –60 °C over a period of five minutes to a stirred solution of Mes*N(SiMe₃)Sb(N₃)₂ (1 mmol, 0.56 g) in CH₂Cl₂ (10 mL). The resulting orange solution was stirred for seven days at ambient temperature. The dark red solution was concentrated to about 2 mL and stored at +5 °C for several hours, which resulted in the deposition of red crystals. Removal of solvent by syringe and drying yielded 0.51 g (0.28 mmol, 56%) of *N*-(6-imino-3,5-di-*tert*-butyl-cyclohexa-2,4-dienyl)iminomethylstibenium azidotris(pentafluorphenyl)borate (10) as a red crystalline solid; m.p. 173 °C (dec.). C₆₆H₄₈N₁₀BF₃₀Sb₂ (1816.26): calcd. C 43.65, H 2.66, N 7.71; found C 43.32, H 2.69, N 7.50. ¹H NMR (25 °C, [D₈]-THF, 300.13 MHz): δ = 1.16 (s, 6 H, Me), 1.28 (s, 18 H, *t*Bu), 1.44 (s, 18 H, *t*Bu), 6.77 [d, ^1J(^{1}H,^{1}H) = 1.93 Hz, 2 H, C*H*], 7.03 [d, ^1J(^{1}H,^{1}H) = 1.93 Hz, 2 H, C*H*], 11.81 (s, 2 H, N*H*) ppm. ¹³C{¹H} NMR (25 °C, [D₈]THF, 75.48 MHz): δ = 12.77 (*C*H₃), 28.81 [C(*C*H₃)₃], 30.64 [C(*C*H₃)₃], 37.46 [*C*(CH₃)₃] 117.12 (*C*H), 127.17 (*C*H), 137.7 [m, ^1J(^{13}C,^{19}F) = 250 Hz, Ar–*C*F], 139.8 [m, ^1J(^{13}C,^{19}F) = 243 Hz, Ar–*C*F], 149.3 [m, ^1J(^{13}C,^{19}F) = 243 Hz, Ar–*C*F], 151.50 (Ar–*C*), 164.84 (Ar–*C*), 166.22 (Ar–*C*), 169.16 (Ar–*C*) ppm. ¹¹B NMR (25 °C, [D₈]THF, 96.29 MHz): δ = –8.3 ppm. ¹⁹F NMR (25 °C, [D₈]THF, 282.38 MHz): δ = –167.75 [m, ^3J(^{19}F,^{19}F) = 22 Hz, 12 F, *m*C*F*], –163.53 [t, ^3J(^{19}F,^{19}F) = 20.2 Hz, 6 F, *p*-C*F*], –143.03 [d, ^3J(^{19}F,^{19}F) = 21.0 Hz, 12 F, *o*-C*F*] ppm. IR (ATR, 25 °C, 32 scans): ṽ = 3347 (m), 3071 (vw), 2972 (m), 2965 (m), 2912 (w), 2879 (w), 2123 (s), 2003 (w), 1643 (m), 1624 (m), 1592 (w), 1565 (vw), 1556 (vw), 1514 (s), 1493 (m), 1461 (s), 1455 (s), 1403 (m), 1385 (m), 1372 (m), 1350 (m), 1333 (m), 1318 (m), 1275 (m), 1245 (m), 1199 (m), 1121 (m), 1091 (s), 1086 (s), 1026 (w), 1020 (w), 1012 (w), 972 (s), 927 (m), 910 (m), 890 (m), 862 (s), 838 (m), 824 (m), 802 (m), 767 (m), 756 (m), 745 (m), 733 (m), 670 (s), 665 (m), 648 (m), 617 (m), 604 (m), 593 (m), 574 (m), 534 (w) cm^{-1}. Raman (250 mW, 25 °C, 1500 scans): ṽ = 3085 (1), 2973 (2), 2922 (2), 2811 (1), 2118 (1), 1624 (3), 1591 (2), 1560 (2), 1513 (10), 1400 (1), 1384 (1), 1335 (2), 1320 (1), 1267 (1), 1237 (1), 1199 (3), 1122 (1), 1086 (1), 1026 (1), 971 (1), 928 (1), 892 (1), 870 (1), 823 (1), 790 (1), 778 (1), 702 (1), 623 (2), 583 (1), 516 (2), 493 (2), 478 (1), 448 (1), 431 (1), 409 (1), 395 (1), 356 (1), 308 (1), 288 (1), 242 (1), 217 (1), 202 (1), 171 (1), 122 (2), 110 (1) cm^{-1}.

Supporting Information (see footnote on the first page of this article): Experimental details, details of X-ray structure analysis.

[1] M. S. Balakrishna, D. J. Eisler, T. Chivers, *Chem. Soc. Rev.* **2007**, *36*, 650–664, and references cited therein.

[2] L. Stahl, *Coord. Chem. Rev.* **2000**, *210*, 203–250, and references cited therein.

[3] a) E. L. Doyle, L. Riera, D. S. Wright, *Eur. J. Inorg. Chem.* **2003**, 3279–3289; b) M. A. Beswick, D. S. Wright, *Coord. Chem. Rev.* **1998**, *176*, 373–406.

[4] N. Kuhn, O. J. Scherer, *Z. Naturforsch. B* **1979**, *34*, 888.

[5] D. C. Haagenson, L. Stahl, R. J. Staples, *Inorg. Chem.* **2001**, *40*, 4491–4493.

[6] D. J. Eisler, T. Chivers, *Inorg. Chem.* **2006**, *45*, 10734–10742.

[7] M. Lehmann, A. Schulz, A. Villinger, *Eur. J. Inorg. Chem.* **2010**, *35*, 5501–5508.

[8] a) E. Niecke, M. Nieger, F. Reichert, *Angew. Chem.* **1988**, *100*, 1781; *Angew. Chem. Int. Ed. Engl.* **1988**, *27*, 1715–1716; b) E. Niecke, R. Detsch, M. Nieger, F. Reichert, W. W. Schoeller, *Bull. Soc. Chim. Fr.* **1993**, *130*, 25–31.

[9] a) N. Burford, T. S. Cameron, K. D. Conroy, B. Ellis, M. Lumsden, C. L. B. Macdonald, R. McDonald, A. D. Phillips, P. J. Ragogna, R. W. Schurko, D. Walsh, R. E. Wasylishen, *J. Am. Chem. Soc.* **2002**, *124*, 14012–14013; b) N. Burford, T. S. Cameron, C. L. B. Macdonald, K. N. Robertson, R. Schurko, D. Walsh, *Inorg. Chem.* **2005**, *44*, 8058–8064; c) N. Burford, C. A. Dyker, A. D. Phillips, H. A. Spinney, A. Deckon, R. McDonald, P. J. Ragogna, A. L. Rheingold, *Inorg. Chem.* **2004**, *43*, 7502–7507; d) N. Burford, K. D. Conroy, J. C. Landry, P. J. Ragogna, M. J. Ferguson, R. McDonald, *Inorg. Chem.* **2004**, *43*, 8245–8251.

[10] M. Lehmann, A. Schulz, A. Villinger, *Struct. Chem.* **2011**, *22*, 35–43.

[11] A. Schulz, A. Villinger, *Angew. Chem.* **2008**, *120*, 614–617; *Angew. Chem. Int. Ed.* **2008**, *47*, 603–606.

[12] a) D. Michalik, A. Schulz, A. Villinger, N. Weding, *Angew. Chem.* **2008**, *120*, 6565–6568; *Angew. Chem. Int. Ed.* **2008**, *47*, 6465–6468; b) A. Schulz, A. Villinger, A. Westenkirchner, R. Wustrack, *Inorg. Chem.* **2008**, *47*, 9140–9142; c) W. Baumann, A. Schulz, A. Villinger, *Angew. Chem.* **2008**, *120*, 9672–9675; *Angew. Chem. Int. Ed.* **2008**, *47*, 9530–9532; d) D. Michalik, A. Schulz, A. Villinger, *Inorg. Chem.* **2008**, *47*, 8316–8322; e) R. Kuzora, A. Schulz, A. Villinger, R. Wustrack, *Dalton Trans.* **2009**, 9304–9311; f) A. Schulz, A. Villinger, *Inorg. Chem.* **2009**, *48*, 7359–7367.

[13] a) A. Schulz, A. Villinger, *Angew. Chem.* **2010**, *122*, 8190–8194; *Angew. Chem. Int. Ed.* **2010**, *49*, 8017–8020; b) D. Michalik, A. Schulz, A. Villinger, *Angew. Chem.* **2010**, *122*, 7737–7740; *Angew. Chem. Int. Ed.* **2010**, *49*, 7575–7577.

[14] M. Lehmann, A. Schulz, A. Villinger, *Angew. Chem.* **2011**, *123*, 5327–5331; *Angew. Chem. Int. Ed.* **2011**, *50*, 5221–5224.

[15] T. M. Klapötke, A. Schulz, J. McNamara, *J. Chem. Soc., Dalton Trans.* **1996**, 2985–2987.

[16] a) K. O. Christe, R. Haiges, A. Vij, J. A. Boatz, S. Schneider, T. Schroer, M. Gerken, *Chem. Eur. J.* **2004**, *10*, 508–517; b) S. Schulz, B. Lyhs, G. Jansen, D. Bläser, C. Wölper, *Chem. Commun.* **2011**, *47*, 3401–3403.

[17] T. M. Klapötke, H. Nöth, T. Schütt, M. Warchold, *Z. Anorg. Allg. Chem.* **2001**, *627*, 81–84.

[18] K. Karaghiosoff, T. M. Klapötke, B. Krumm, H. Nöth, T. Schütt, M. Suter, *Inorg. Chem.* **2002**, *41*, 170–179.

[19] K. O. Christe, R. Haiges, J. A. Boatz, A. Vij, V. Vij, M. Gerken, S. Schneider, T. Schroer, M. Yousufuddin, *Angew. Chem.* **2004**, *116*, 6844–6848; *Angew. Chem. Int. Ed.* **2004**, *43*, 6676–6680.

[20] a) K. O. Christe, R. Haiges, J. A. Boatz, H. D. B. Jenkins, E. B. Garner, D. A. Dixon, *Inorg. Chem.* **2011**, *50*, 3752–3756; b)

K. O. Christe, R. Haiges, T. Schroer, M. Yousufuddin, *Z. Anorg. Allg. Chem.* **2005**, *631*, 2691–2655.

[21] D. Bläser, B. Lyhs, S. Schulz, C. Wöpler, *Chem. Eur. J.* **2011**, *17*, 4914–4920.

[22] P. Pyykkö, M. Atsumi, *Chem. Eur. J.* **2009**, *15*, 12770–12779.

[23] I. C. Tornieporth-Oetting, T. M. Klapötke, *Angew. Chem.* **1995**, *107*, 559–568; *Angew. Chem. Int. Ed. Engl.* **1995**, *34*, 511–520.

[24] A. F. Holleman, N. Wiberg, *Lehrbuch der Anorganischen Chemie*, 102nd ed., Walter de Gruyter, Berlin, **2007**, Appendix V.

[25] a) E. D. Glendening, A. E. Reed, J. E. Carpenter, F. Weinhold, *NBO*, version 3.1; b) J. E. Carpenter, F. Weinhold, *J. Mol. Struc. (Theochem)* **1988**, *169*, 41–62; c) F. Weinhold, J. E. Carpenter, *The Structure of Small Molecules and Ions*, Plenum Press, **1988**, p. 227; d) F. Weinhold, C. Landis, *Valency and Bonding. A Natural Bond Orbital Donor-Acceptor Perspective*, Cambridge University Press, **2005**, and references cited therein.

[26] K. Peters, E.-M. Peters, J. Balthasar, H. Quast, *Z. Kristallogr. New Cryst. Struct.* **1988**, *213*, 723.

[27] W. Fraenk, T. M. Klapötke, B. Krumm, H. Nöth, M. Suter, M. Vogt, M. Warchhold, *Can. J. Chem.* **2002**, *80*, 1444–1450.

[28] M. Veith, B. Bertsch, V. Huch, *Z. Anorg. Allg. Chem.* **1988**, *559*, 73–88.

[29] S. J. Lancaster, A. Rodriguez, A. Lara-Sanchez, M. D. Hannant, D. A. Walker, D. H. Hughes, M. Bochmann, *Organometallics* **2002**, *21*, 451.

[30] R. E. LaPointe, *WO99/42467*, **1999**.

[31] R. E. LaPointe, G. R. Roof, K. A. Abbboud, J. Klosin, *J. Am. Chem. Soc.* **2000**, *122*, 9560.

[32] a) I. C. Vei, S. I. Pascu, M. L. H. Green, J. C. Green, R. E. Schilling, G. D. Anderson, R. L. Rees, *Dalton Trans.* **2003**, 2550; b) L. H. Doerrer, J. R. Galsworthy, M. L. H. Green, M. A. Leech, M. Müller, *J. Chem. Soc., Dalton Trans.* **1998**, 3191; c) L. H. Doerrer, J. R. Galsworthy, M. L. H. Green, M. A. Leech, *J. Chem. Soc., Dalton Trans.* **1998**, 2483; d) L. H. Doerrer, A. J. Graham, M. L. H. Green, *J. Chem. Soc., Dalton Trans.* **1998**, 3941; e) L. H. Doerrer, M. L. H. Green, *J. Chem. Soc., Dalton Trans.* **1999**, 4325.

[33] T. Beringhelli, D. Maggioni, G. D'Alfonso, *Organometallics* **2001**, *20*, 4927.

[34] I. D. G. Watson, A. K. Yudin, *J. Org. Chem.* **2003**, *68*, 5160.

[35] C. Janiak, L. Braun, T. G. Scharmann, F. Girgsdies, *Acta Crystallogr., Sect. C* **1998**, *54*, 1722.

[36] A. Di Saverio, F. Focante, I. Camurati, L. Resconi, T. Beringhelli, G. D'Alfonso, D. Donghi, D. Maggioni, P. Mercandelli, A. Sironi, *Inorg. Chem.* **2005**, *44*, 5030.

[37] A. Bernsdorf, H. Brand, R. Hellmann, M. Köckerling, A. Schulz, A. Villinger, K. Voss, *J. Am. Chem. Soc.* **2009**, *131*, 8958–8970.

[38] M. Becker, A. Schulz, A. Villinger, K. Voss, *RSC Adv.* **2011**, *1*, 128–134.

[39] A. Schulz, A. Villinger, *Chem. Eur. J.* **2010**, *16*, 7276–7281.

[40] H. Jacobsen, H. Berke, S. Doering, G. Kehr, G. Erker, R. Froehlich, O. Meyer, *Organometallics* **1999**, *18*, 1724.

[41] L. R. Thorne, R. D. Suenram, F. J. Lovas, *J. Chem. Phys.* **1983**, *78*, 167.

[42] C. B. Fischer, S. Xu, H. Zipse, *Chem. Eur. J.* **2006**, *12*, 5779.

[43] G. M. Whitesides, F. D. Gutowski, *J. Org. Chem.* **1976**, *41*, 2882–2885.

[44] M. Kuprat, M. Lehmann, A. Schulz, A. Villinger, *Organometallics* **2010**, *29*, 1421–1427.

[45] G. M. Sheldrick: *SHELXS-97: Program for the Solution of Crystal Structures*, University of Göttingen, Germany, **1997**.

[46] G. M. Sheldrick: *SHELXL-97: Program for the Refinement of Crystal Structures*, University of Göttingen, Germany, **1997**.

[47] G. M. Sheldrick, *SADABS*, version 2, University of Göttingen, Germany, **2004**.

L-Proline-Derived Dendritic Tetrakis(diperoxotungsto)phosphate: Synthesis and Enantioselective Oxidation Catalysis

Claire Jahier[a] and Sylvain Nlate*[a]

As a part of our ongoing research towards the synthesis of chiral dendritic polyoxometalate (DENDRI-POM) hybrids that are able to catalyze oxidation of organic substrates with high selectivity and enantioselectivity, we have prepared an enantiopure DENDRI-POM salt by coupling a well-defined L-proline-derived tetrapropylammonium dendron with the tetrakis(diperoxotungsto)phosphate $[PO_4\{WO(O_2)_2\}_4]^{3-}$. This DENDRI-POM hybrid was characterized by infrared, NMR spectroscopy, polarimetry, and elemental analysis. The data obtained are consistent with the structure in which the trianionic POM is surrounded by three L-proline-based dendrons. This DENDRI-POM oxidized sulfides with moderate activity and very low enantioselectivities (up to 4 %), whereas alkenes were efficiently oxidized with up to 37 % enantiomeric excess (ee), and good yields. Although these

ee values are still not satisfactory for practical asymmetric synthesis, 37 % ee represents the best enantioselectivity reported to date in the oxidation of organic substrate with chiral POM hybrids. Studies of temperature, solvent, and catalyst loading effects on the outcome of the reaction indicate that the ee is sensitive to the nature of the solvent. Moreover, the catalyst was recovered at low temperature and reused while retaining its activity and enantioselectivity. These results contrast and complement our reported results in which DENDRI-POMs based on phenylethylamine-derived ligands efficiently oxidize sulfides with up to 14 % ee, whereas alkenes were not oxidized with this family of chiral POM compounds. Thus, the influence of the nature of the chiral countercation on the POM properties is again observed.

Introduction

Polyoxometalates (POMs)[1] are an important class of inorganic compounds with highly interesting properties that render them attractive candidates for potential applications in a variety of fields such as catalysis, biology, magnetism, optics, and medicine.[2–6] In this context, the construction of enantiomerically pure inorganic–organic materials have received much more attention due to their potential use in the area of medicine and asymmetric catalysis.[7] Among numerous application of POMs, catalysis is by far the most studied on account of the enormous versatility that POMs offer in the clean synthesis of fine chemicals, including their ability to catalyze environmentally friendly reactions. Although a wide variety of chiral catalysts (including transition-metal-based complexes and organocatalysts) have been developed for the asymmetric oxidation of organic substrates with high activity and enantioselectivity,[8] few of them are based on POM clusters.[7,9] Among those reported so far, dendritic structures are rare,[10] although the properties of POMs such as their stability, solubility, their recycl-

ing potential, and overall their catalytic efficiency are closely related to the structure of the dendritic wedge. Recently, we have reported a series of chiral dendritic polyoxometalates (DENDRI-POMs) constructed by electrostatic interactions between enantiopure dendritic ammonium ions and an achiral polyanion that efficiently catalyze the asymmetric oxidation of sulfides with up to 14 % enantiomeric excess (ee), thereby highlighting the transfer of chirality from the dendritic wedges to the inorganic cluster.[10] Shortly after this report, the group of Bonchio published a report on nondendritic, optically active polyoxotungstophosphonates prepared by covalent functionalization of a Keggin-type POM with a chiral organophosphonate, which oxidized methyl p-tolyl sulfide to the corresponding chiral sulfoxide with up to 75 % conversion and a maximum of 8 % ee.[11] With these promising results, our attention was turned to improve the catalytic efficiency of these hybrids, in terms of reactivity and stereoselectivity, by tuning the structure of the chiral dendritic countercation. Thus, we have studied the catalytic properties of enantiopure DENDRI-POM hybrids constructed by electrostatic coupling of an achiral trianionic POM with enantiopure dendritic cations that bear one and three ammonium groups, respectively.[10] We discovered a substantial improvement in the stability, activity, and selectivity of the oxidation of sulfides with catalysts built with the monocationic ligand versus the triammonium ligand, but the asymmetric induction was not

[a] IECB-CBMN, UMR CNRS No. 5248,
Université Bordeaux 1,
2 Rue Robert Escarpit, 33607 Pessac Cedex, France
Fax: +33-5-4000-2215
E-mail: s.nlate@iecb.u-bordeaux.fr
Supporting information for this article is available on the WWW under http://dx.doi.org/10.1002/ejic.201101145.

significantly affected by this modification of the chiral ethylamine-based dendritic structure. Being interested in the development of highly enantioselective DENDRI-POM catalysts, we herein report the synthesis and characterization of an enantiopure POM salt by coupling the pyrrolidinylmethanol-based dendritic cation to the Venturello polyanion $[PO_4\{WO(O_2)_2\}_4]^{3-}$. We focused on this trianionic POM to compare the work described in this manuscript with that previously reported in our group.[10] This POM hybrid was used as catalyst in the asymmetric oxidation of aromatic alkenes with a better *ee*.

Results and Discussion

Preparation and Characterization of L-Proline-Derived DENDRI-POM 7

The L-proline-derived DENDRI-POM **7** was prepared by electrostatic assembly of the L-proline-based dendron **6** with the Venturello polyanion $[PO_4\{WO(O_2)_2\}_4]^{3-}$ by treatment of **6** with the commercially available heteropolyacid $H_3PW_{12}O_{40}$ and an excess amount of hydrogen peroxide in a biphasic medium of water and dichloromethane. To compare the work described in this manuscript with that reported in the literature,[10] we focused on the Venturello polyanion. L-2-(Hydroxydipropylmethyl)-1-{[4-(hydroxydipropylmethyl)phenyl}pyrrolidine (**6**) was obtained from the L-proline methyl ester **1**, as summarized in Scheme 1.

The L-proline methyl ester **1** was first synthesized according to the published method.[12] The allylation of **1** with allylmagnesium bromide gives the enantiopure L-2-(diallylhydroxymethyl)pyrrolidine **2** in 97% yield. The coupling of **2** with methyl 4-(bromomethyl)benzoate (**3**) affords the corresponding (diallylhydroxymethyl)pyrrolidinyl-substituted methyl benzoate **4** in 94% yield. The latter was allylated with allylmagnesium bromide to give the correspond-

ing tetraallyl–pyrrolidine compound **5**. Attempts to prepare the triaallyl derivative of **2** or the hexaallyl derivative of **5** by allylation of the corresponding carbinol with allyltrimethylsilane in the presence of BF_3 failed. The hydrogenation of **5** in the presence of Pd/C as catalyst gave the corresponding tetrapropyl compound **6** in 93% yield.

All these compounds were characterized by NMR spectroscopy, mass spectrometry, and elemental analysis. The data obtained are consistent with the proposed pyrrolidine-based structure. The enantiopure DENDRI-POM salt **7** (Scheme 2) was prepared from the commercially available Keggin heteropolyacid $H_3PW_{12}O_{40}$ and the tetrapropyl–pyrrolidine **6**, in the presence of an excess amount of H_2O_2, following the procedure that involves peroxide-mediated decomposition of $H_3PW_{12}O_{40}$. According to reported studies, $H_3PW_{12}O_{40}$ is decomposed in the presence of H_2O_2 to form the dinuclear peroxotungstate $[\{WO(O_2)_2(H_2O)\}_2O]^{2-}$ and the trianionic peroxophosphotungstate $[PO_4\{WO(O_2)_2\}_4]^{3-}$.[10,13] The latter reacts selectively with **6** in a biphasic mixture of water and dichloromethane to give the DENDRI-POM **7**, whereas the dinuclear peroxotungstate $[\{WO(O_2)_2(H_2O)\}_2O]^{2-}$ remained in the aqueous phase of the reaction mixture and was isolated as a potassium salt in the presence of potassium chloride. DENDRI-POM **7** was obtained as a light yellow solid in 90% yield. Spectroscopic studies, and infrared and elemental analysis data reported for **7** are consistent with the proposed structure in which the polyanion $[PO_4\{WO(O_2)_2\}_4]^{3-}$ is surrounded by three tetrapropyl–pyrrolidine–ammonium dendrons (Scheme 2). Only one signal was observed in the ^{31}P NMR spectrum for **7** ($\delta = 2.85$ ppm, $CDCl_3$).

To evaluate the catalytic efficiency of DENDRI-POM **7** and demonstrate the chiroptical properties of the POM unit in an asymmetric reaction, we have performed the oxidation of methyl phenyl sulfide and selected alkenes in the presence of H_2O_2.
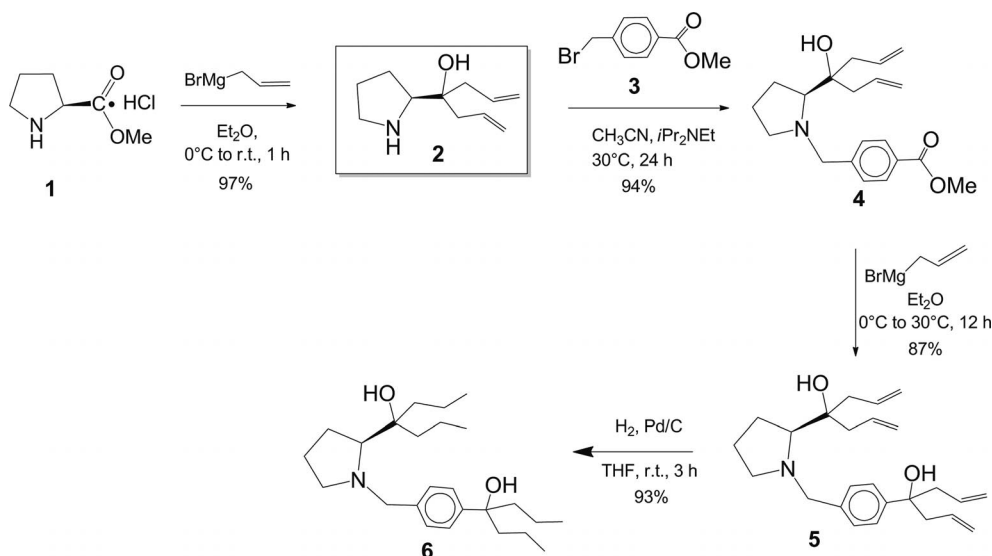
Scheme 1. Synthesis of L-proline-derived dendron **6**.
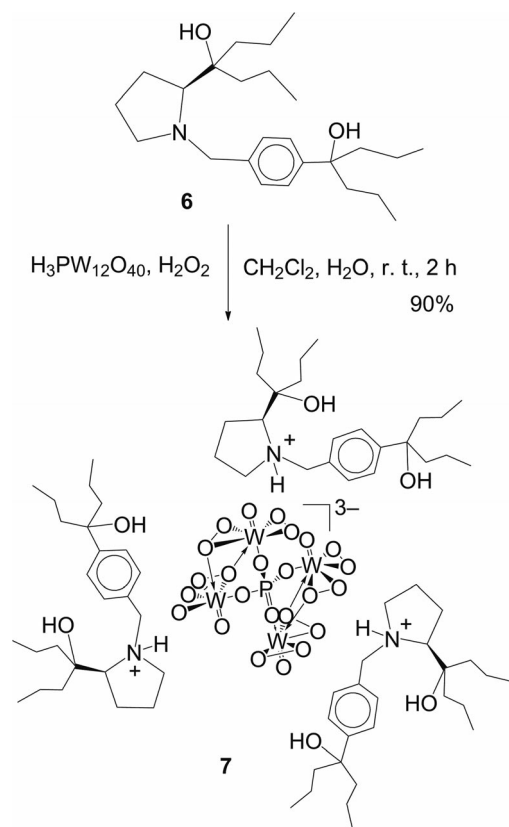
Scheme 2. Synthesis of DENDRI-POM salt **7**.

## Catalytic Oxidation of Methyl Phenyl Sulfide and Selected Alkenes with L-Proline-Derived DENDRI-POM 7 and H₂O₂

To evaluate the catalytic performance of enantiopure DENDRI-POM **7**, we performed the asymmetric oxidation of methyl phenyl sulfide **8** and selected aromatic alkenes by using aqueous hydrogen peroxide (35%) in a biphasic mixture of water and organic solvents. The results summarized in Table 1 show that hybrid **7** catalyzed the oxidation of methyl phenyl sulfide **8** to the corresponding methyl phenyl sulfoxide **9** and a small amount of sulfone **10**, with 100% conversion and only 2% enantioselectivity (_ee_), after 2 h at room temperature (Table 1, entry 1). Whereas the reactivity of **7** toward methyl phenyl sulfide **8** decreased with a decrease in the reaction temperature to –50 °C, no significant change in the _ee_ value was observed (2 versus 4%, entries 1 and 2). These results contrast with our recently reported work with a series of DENDRI-POM salts prepared from ethylamine-based dendrons.[10] These DENDRI-POM catalysts efficiently oxidized sulfides to the corresponding sulfoxides with generally 100% conversion and up to 14% _ee_ after times that range from 5 to 360 min, even at low temperature (–50 °C). In the work described in this manuscript, the proline-based DENDRI-POM **7** oxidized methyl phenyl sulfide **8** with only 73% conversion and 4% _ee_ after 10 h at –50 °C. These results showed once again the influence of the structure of the cation on the properties of the POM anion. Furthermore, optically active oxiranes represent key

building blocks for the synthesis of fine chemicals and pharmaceuticals.[15] Thus, asymmetric epoxidation of alkenes is an interesting alternative to the kinetic resolution of such compounds.[16] To compare the catalytic efficiency of hybrid **7** to those of DENDRI-POMs prepared from ethylamine-based dendritic ligands described in the literature,[10] we have evaluated the performance of POM hybrid **7** in the asymmetric epoxidation of _trans_-stilbene (**11**), α-_trans_-methylstilbene (**12**), styrene (**13**), α-methylstyrene (**14**), and methyl cinnamate (**15**) with aqueous hydrogen peroxide (35%) under similar conditions. As shown in Table 1, the oxidation of aromatic alkenes **11**, **12**, **13**, and **14** with hybrid **7** gave the corresponding _trans_-stilbene oxide (**16**), α-_trans_-methylstilbene oxide (**17**), phenyloxirane (**18**), and 2-methyl-2-phenyloxirane (**19**) if the reaction was performed at 50 °C.

Low substrate conversion was observed at room temp. in the case of **11**, whereas **12** led quantitatively to the corresponding oxide **17** even at room temperature. An enantiomeric excess (_ee_) of 37 and 11% was respectively obtained in the oxidation of **11** and **12** (Table 1, entries 3–6). Interestingly, the enantioselectivity was not dependent upon the reaction temperature, contrary to the oxidation of sulfides. Compounds **13** and **14** were inert at room temp. However, significant substrate conversion was obtained by heating the reaction mixture to 50 °C, unfortunately with almost no enantioselectivity (_ee_ values up to 2% were obtained; entries 8 and 10). Compound **15** was totally inert under the experimental conditions used. Thus, epoxide **20** was not obtained, even by increasing respectively the reaction temperature above 50 °C, the reaction time and the catalyst concentration (entries 11 and 12). It is clearly shown in Table 1 that the enantioselectivity depends on the nature of the substrate. Whereas the oxidation of **11** gave the corresponding epoxide **16** with 37% _ee_ and 44% yield at room temp. in 48 h, **12** was quantitatively oxidized to epoxide **17** in 24 h, but with low _ee_ (11%). The same trend was observed in the oxidation of **13** and **14**, as the latter was slightly more reactive than **13**, but with very low _ee_ (entries 7–10). In addition, **15**, which bears a withdrawing substituent on the alkene group, is not oxidized under these conditions (entries 11 and 12). These results indicate that the reaction kinetics and enantioselectivity in the oxidation of alkenes with hybrid **7** and H₂O₂ are controlled by the electronic structure and the bulkiness of the alkene. These results are in agreement with those reported by Beller's group in the asymmetric epoxidation of aromatic alkenes with iron-based catalysts and H₂O₂.[18] Beller has demonstrated that the enantioselectivity in alkene epoxidation is controlled by steric and electronic factors. The mechanism that operates in our system is in agreement with an electrophilic oxygen transfer, as previously observed for oxidation reactions with DENDRI-POM salts of the Venturello ion,[10] as **12** is a more nucleophilic and more reactive substrate than **11**, **13**, **14**, and **15**.

To evaluate the influence of the polarity of solvents on the reaction kinetics and the enantioselectivity, we examined the oxidation of **11** by POM hybrid **7** in chloroform,

Table 1. Catalytic oxidation of methyl phenyl sulfide 8[a] and representative aromatic alkenes[b] by proline-derived DENDRI-POM 7, using H$_2$O$_2$.
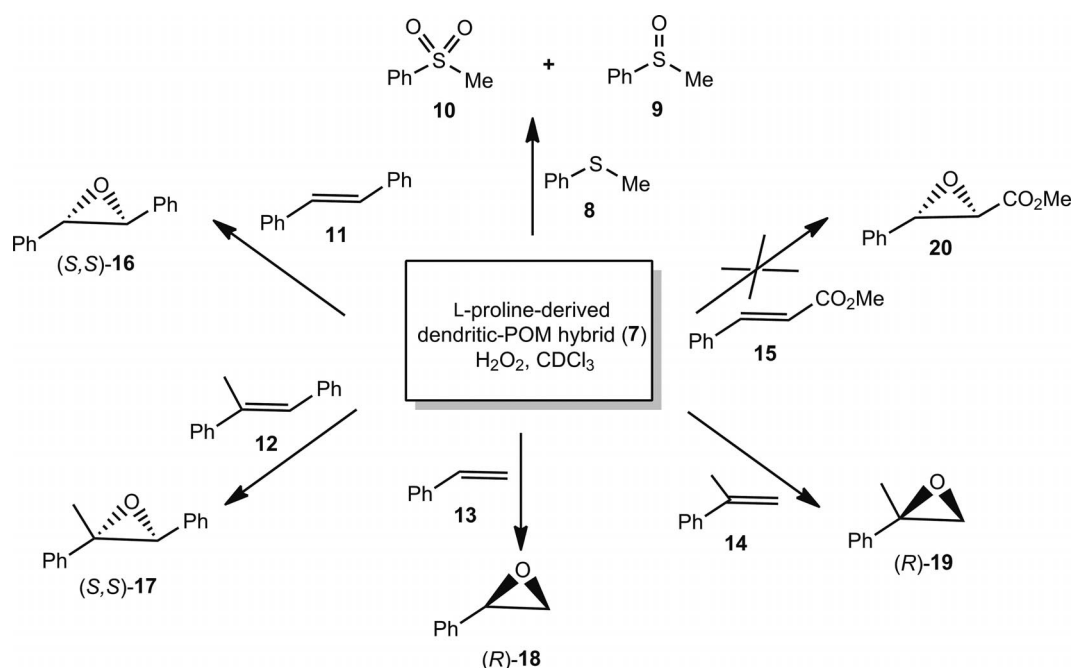
Entry	Substrate	T [°C]	t [h][c]	Conv. [%][d]	Products	ee [%][e]
1	8	r.t.	2	100	9 (83); 10 (17)	2[f]
2		−50	10	73	9 (70); 10 (3)	4[f]
3	11	r.t.	48	44	16	37 (S,S)
4		50	48	100		37 (S,S)
5	12	r.t.	24	97	17	11 (S,S)
6		50	24	100		11
7	13	r.t.	72	0	18	–
8		50	72	76		1 (R)
9	14	r.t.	72	0	19	–
10		50	48	89		2 (R)
11	15	r.t.	72	0	20	–
12		50	72	0		–

[a] Reaction conditions: catalyst (0.4 mol-%), substrate (250 equiv.), 35% H$_2$O$_2$ (800 equiv.), CDCl$_3$ (1 mL). [b] Reaction conditions: catalyst (1 mol-%), substrate (250 equiv.), 35% H$_2$O$_2$ (800 equiv.), solvent CDCl$_3$ (1 mL). [c] Reactions were monitored by ^{1}H NMR spectroscopy. [d] Conversion determined from the relative intensities of the ^{1}H NMR spectroscopic signals of the substrate and the product. [e] Enantiomeric excess determined by chiral HPLC using a Chiralcel ASH column, UV detection (254 nm), eluting with hexane/2-propanol (9.5:0.5) at a flow rate of 0.5 mL min^{-1}.[14] [f] Enantiomeric excess determined by chiral HPLC using a Chiralcel ASH column, UV detection (254 nm), eluting with hexane/2-propanol (1:1) at a flow rate of 0.5 mL min^{-1}.[17]
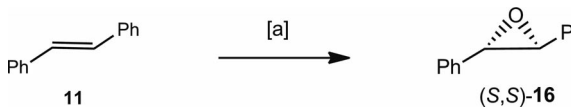
dichloromethane, toluene, acetonitrile, acetone, and tetrahydrofuran in the presence of H$_2$O$_2$ at 50 °C. For better comparison, the reaction time (48 h) and the catalyst concentration (1 mol-%) were kept constant for all experiments. As detailed in Table 2, it is noteworthy that the nature of the solvent has a dramatic effect on the reaction kinetics and the ee values. In CH$_3$CN, acetone, and THF, for example, no oxidation of 11 to the corresponding epoxide 16 occurred (entries 4–6). However, in CDCl$_3$, CH$_2$Cl$_2$, and toluene, 11 was oxidized to epoxide 16 with conversions that ranged from 43 to 100% and ee values that ranged from 19 to 37% (Table 2, entries 1–3).

The reaction seemed to be favorable in less polar and noncoordinating solvents. It becomes apparent that out of all solvents evaluated in the oxidation of sulfides and alkenes with POM hybrid 7, the reaction in CDCl$_3$ was found

to be accelerated to some extend compared with that in CH$_2$Cl$_2$ and toluene, and the ee was increased from 19 and 28%, respectively, in CH$_2$Cl$_2$ and toluene, to 37% in CDCl$_3$ (Table 2, entries 1–3).

We also investigated the influence of the catalyst concentration on the reaction kinetics and ee values. Thus, 11 was oxidized with hybrid 7 in chloroform in the presence of H$_2$O$_2$ at 50 °C. The results, which are summarized in Table 3, showed that increasing the catalyst concentration increased the reaction kinetics without affecting the ee. At a low catalyst concentration (0.4 mol-%), no substrate conversion was observed after 96 h at 30 °C, whereas only 14% conversion was obtained after 48 h at 50 °C (Table 3, entries 1 and 5). By using 2 mol-% of catalyst, the conversion was complete after 48 h at 50 °C (entry 7). In all cases, the ee value of epoxide 16 (37%) was not affected by the catalyst

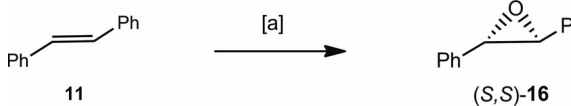Table 2. Effects of solvents on yield and *ee* values of (*S*,*S*)-**16**.[a]

Entry	Solvent	Conv. [%][b]	*ee* [%][c]
1	CDCl$_3$	100	37 (*S*,*S*)
2	CH$_2$Cl$_2$	71	19 (*S*,*S*)
3	toluene	43	28 (*S*,*S*)
4	CH$_3$CN	0	–
5	acetone	0	–
6	THF	0	–

[a] Reaction conditions: catalyst (1 mol-%), substrate (250 equiv.), 35% H$_2$O$_2$ (800 equiv.), solvent (1 mL). [b] Conversion determined from the relative intensities of the ^{1}H NMR spectroscopic signals of the substrate and the product. [c] Enantiomeric excess determined by chiral HPLC using a Chiralcel ASH column, UV detection (254 nm), eluting with hexane/2-propanol (9.5:0.5) at a flow rate of 0.5 mL min^{-1}.[14]

concentration. Increasing the catalyst loading from 2 to 5 mol-% did not increase significantly the reaction kinetics (entries 3 and 4), which is an interesting feature in terms of the development of environmentally friendly processes.

Table 3. Effects of catalyst concentration on the reaction efficiency and *ee* values of (*S*,*S*)-**16**.[a]

Entry	Cat. [%]	*T* [°C]	*t* [h][b]	Conv. [%][c]	*ee* [%][d]
1	0.4	30	96	0	–
2	1		48	8	37
3	2		48	44	37
4	5		48	53	37
5	0.4	50	48	14	37
6	1		48	53	37
7	2		48	100	37

[a] Reaction conditions: catalyst, substrate (250 equiv.), 35% H$_2$O$_2$ (800 equiv.), solvent (1 mL). [b] Reactions were monitored by ^{1}H NMR spectroscopy. [c] Conversion determined from the relative intensities of the ^{1}H NMR spectroscopic signals of the substrate and the product. [d] Enantiomeric excess determined by chiral HPLC using a Chiralcel ASH column, UV detection (254 nm), eluting with hexane/2-propanol (9.5:0.5) at a flow rate of 0.5 mL min^{-1}.[14]

By varying the oxidant/substrate ratio, no significant change was observed in either the reaction kinetics and the enantioselectivity. It thus appears that the best reaction conditions identified up to now to achieve a high yield and a maximum *ee* in the oxidation reactions with POM-based catalysts are the oxidation of **11** to the corresponding **16**, with 2 mol-% of L-proline-based dendritic hybrid **7**, a ratio of 1:3.2 substrate/hydrogen peroxide, and 1 mL of CDCl$_3$ at 50 °C. It is interesting to note that all the reactions performed did not proceed in the absence of POM catalyst when carried out under similar conditions. In addition, the L-proline-derived ligand **5** and its hydrochloride salt

(**5**·HCl) were found to be inert in oxidation reactions under similar conditions. Thus the presence of the polyoxometalate unit is essential to the catalytic activity.

Catalyst Recovery and Reutilization

A significant advantage of dendritic catalysts is that they can be easily separated from substrates and product through precipitation due to the solubility properties of these macromolecules. Therefore, four catalytic cycles were performed at room temperature and at 50 °C to test the stability of the L-proline-based DENDRI-POM **7** in the oxidation of **11** with 1 mol-% of catalyst and H$_2$O$_2$. The catalyst was recovered by precipitation after each catalytic cycle and checked by ^{1}H and ^{31}P NMR spectroscopy before a new catalytic experiment was performed. At room temperature, *trans*-stilbene **11** was oxidized without any discernible loss in activity and enantioselectivity over at least four cycles, whereas at 50 °C, the conversion (34 to 15%) and the isolated yield (62 to 21%) of the recycled catalyst decreased significantly after the first cycle. The ^{31}P NMR spectrum of the recovered catalyst showed the appearance of new peaks at δ = –0.2 and –16.1 ppm, thus indicating a structural change of the polyanion. This structural change is probably due to the decomposition of the POM unit at 50 °C. It was noticed, however, that the decomposition of the catalyst did not affect the *ee* value of 37%.

Conclusion

In the quest for efficient enantioselective POM-based catalysts, we have designed and synthesized an L-proline-derived enantiopure ligand and assembled it with the Venturello trianion [PO$_4${WO(O$_2$)$_2$}$_4$]$^{3-}$ by electrostatic interaction. This DENDRI-POM oxidized methyl phenyl sulfide with low activity and very low *ee* (up to 4%), whereas aromatic alkenes were efficiently oxidized to the corresponding oxirane with up to 37% *ee*. These results are not comparable with those previously reported in our group, in which DENDRI-POM salts based on the Venturello anion and enantiopure phenylethylamine-derived dendrons oxidized phenyl methyl sulfide with better activity and *ee* (up to 14%), whereas alkenes were not oxidized with this family of POM catalysts.[10] Although the enantioselectivity (37%) of the reaction is still not satisfactory for practical asymmetric synthesis, to the best of our knowledge, this *ee* value represents the best enantioselectivity obtained up to now with POM-based frameworks in enantioselective transformations. To improve this *ee* value by varying the reaction parameters, we found that, in contrast to the reaction temperature, the nature of the solvent could dramatically influence the *ee* of the reaction. These new results complement our previous work and clearly confirm that some key parameters in catalysis with POMs, such as activity, selectivity, and enantioselectivity, can be improved by modifying the local environment of polyanions. Further studies are being carried out in our laboratory.

Experimental Section

General: Reagent-grade THF and diethyl ether were predried with Na foil and distilled using sodium–benzophenone under argon immediately before use. Acetonitrile (CH_3CN) was stirred under argon overnight over phosphorus pentoxide, distilled from sodium carbonate, and stored under argon. Methylene chloride (CH_2Cl_2) was distilled from calcium hydride just before use. All other chemicals were used as received. The ^1H, ^{13}C, ^{31}P NMR spectra were recorded at 25 °C with a Bruker AC 250 FT spectrometer (^1H: 250.13 MHz; ^{13}C: 62.91 MHz) and a Bruker AC 200 FT spectrometer (^1H: 200.16 MHz; ^{13}C: 50.33 MHz; ^{31}P: 81.02 MHz) at CESAMO (Bordeaux, France). All chemical shifts are referenced to Me_4Si (TMS). Mass spectra were performed by the CESAMO with a QStar Elite mass spectrometer (Applied Biosystems). The instrument is required to have an ESI source, and spectra were recorded in the positive mode. The electrospray needle was maintained at 4500 V and operated at room temperature. Samples were introduced by injection through a 10 µL sample loop into a 200 µL min^{-1} flow of methanol from the LC pump. Elemental analyses were performed at the Vernaison CNRS center at Lyon-Villeurbanne (France). The infrared spectra were recorded in KBr pellets with a FTIR Paragon 1000 Perkin–Elmer spectrometer unless otherwise indicated. Organic oxidation products were identified by correlation to authentic samples.

L-2-(Diallylhydroxymethyl)pyrrolidine (2): In a Schlenk tube, allyl bromide (4.2 mL, 5.90 g, 48.61 mmol) was slowly added to a mixture of magnesium (1.40 g, 58.33 mmol) in anhydrous diethyl ether (25 mL) cooled to 0 °C. Then a solution of L-proline methyl ester[12] (**1**; 1.61 g, 9.72 mmol) in anhydrous diethyl ether (10 mL) was added to the reaction mixture at 0 °C. The mixture was stirred for 1 h at room temperature. Then a solution of 6 M NH_4Cl (25 mL) was added to the reaction mixture. The product was extracted with diethyl ether (3 × 30 mL) and dried with sodium sulfate. The solvent was removed under vacuum and the product was purified by silica gel column chromatography and eluted with petroleum ether/diethyl ether (9:1 v/v) to give compound **2** as colorless oil in 97% yield (1.71 g). ^1H NMR (200.16 MHz, CDCl$_3$, TMS): δ = 5.90–5.82 (m, 2 H, CH=CH$_2$), 5.12–5.06 (m, 4 H, CH=CH$_2$), 3.16–3.09 (m, 1 H, CH), 2.99–2.90 (m, 2 H, CH$_2$–N), 2.67 (br., 2 H, OH and NH), 2.40–2.07 (m, 4 H, CH$_2$–CH=CH$_2$), 1.79–1.69 (m, 4 H, CH$_2$) ppm. ^{13}C NMR (50.33 MHz, CDCl$_3$, TMS): δ = 134.0 (CH=CH$_2$), 117.6 (CH=CH$_2$), 73.4 (Cq–OH), 63.7 (CH–N), 46.4 (CH$_2$–N), 42.8 (CH$_2$), 40.3 (CH$_2$), 25.6 (CH$_2$–CH=CH$_2$) ppm. MS (ESI): m/z = 182.10 [M + H]$^+$; found 182.29. C$_{11}$H$_{19}$NO: calcd. C 72.88, H 10.56; found: C 72.67, H 10.44. $[a]_D^{20}$ = –114.0 (c = 10^{-2} g mL^{-1}, CHCl$_3$).

Methyl L-4-[2-(Diallylhydroxymethyl)pyrrolidin-1-yl]benzoate (4): A mixture of L-proline diallyl carbinol **2** (0.95 g, 5.24 mmol), methyl 4-(bromomethyl)benzoate **3** (1.60 g, 6.81 mmol), and N,N-diisopropylethylamine (0.88 g, 6.81 mmol) in CH$_3$CN was stirred for 24 h at 30 °C. After removal of the solvent under vacuum, the residue was extracted with diethyl ether, washed with water, and dried with sodium sulfate. The solvent was removed under vacuum and the product purified by silica gel column chromatography and eluting with petroleum ether/diethyl ether (7:3 v/v). Compound **4** was obtained as a colorless oil in 94% (1.62 g) yield. ^1H NMR (200.16 MHz, CDCl$_3$, TMS): δ = 7.98 (d, $^3J_{H,H}$ = 6.88 Hz, 2 H, Har), 7.41 (d, $^3J_{H,H}$ = 6.75 Hz, 2 H, Har), 5.91–5.84 (m, 2 H, CH=CH$_2$), 5.13–5.03 (m, 4 H, CH=CH$_2$), 3.88 (dd, $^2J_{H,H}$ = 12.08 Hz, 2 H, CH$_2$–N), 3.89 (s, 3 H, O–CH$_3$), 2.91–2.82 (m, 2 H, CH and CH$_2$–N), 2.67 (br., 2 H, OH and NH), 2.36–2.32 (dm, 4 H, CH$_2$–CH=CH$_2$), 2.19–2.17 (m, 1 H, CH$_2$–N), 1.88–1.81 (m, 2

H, CH$_2$), 1.72–1.69 (m, 2 H, CH$_2$) ppm. ^{13}C NMR (50.33 MHz, CDCl$_3$, TMS): δ = 166.9 (C=O), 145.9 (Cq, Ar), 134.1 (d, $^1J_{C,H}$ = 23.06 Hz, CH=CH$_2$), 129.6 (CH, Ar), 128.6 (Cq, Ar), 127.8 (CH, Ar), 117.9 (CH=CH$_2$), 75.8 (Cq–OH), 70.2 (CH–N), 62.3 (CH$_2$-N), 54.1 (CH$_2$–N), 51.9 (O–CH$_3$), 41.0 (CH$_2$–CH=CH$_2$), 27.2 (CH$_2$), 24.8 (CH$_2$) ppm. MS (ESI): m/z = 330.21 [M + H]$^+$; found 330.45. C$_{20}$H$_{27}$NO$_3$: calcd. C 72.92, H 8.26; found: C 72.47, H 8.02. $[a]_D^{20}$ = –136.5 (c = 10^{-2} g mL^{-1}, CHCl$_3$).

Tetraallyl–Pyrrolidine Compound 5: In a Schlenk tube, allyl bromide (0.40 mL, 0.56 g, 4.64 mmol) was slowly added to a mixture of magnesium (0.135 g, 5.57 mmol) in anhydrous diethyl ether (10 mL) cooled to 0 °C. Then a solution of methyl benzoate derivative **4** (0.61 g, 1.86 mmol) in anhydrous diethyl ether (5 mL) was added to the reaction mixture at 0 °C. The mixture was stirred for 12 h at 30 °C. A solution of 6 M NH$_4$Cl (15 mL) was then added to the reaction mixture. The product was extracted with diethyl ether (3 × 15 mL), and dried with Na$_2$SO$_4$. The solvent was removed under vacuum, and the product was purified by silica gel column chromatography and eluted with petroleum ether/diethyl ether (9:1 v/v). Compound **5** was isolated as colorless oil in 87% (617 mg) yield. ^1H NMR: δ = 7.36–7.29 (m, 4 H, Har), 5.99–5.81 (m, 2 H, CH=CH$_2$), 5.70–5.57 (m, 2 H, CH=CH$_2$), 5.13–5.01 (m, 8 H, CH=CH$_2$), 3.82 (dd, $^2J_{H,H}$ = 11.31 Hz, 2 H, CH$_2$–N), 2.88–2.69 (m, 2 H, CH and CH$_2$–N), 2.71–2.51 (dm, 4 H, CH$_2$–CH=CH$_2$), 2.49–2.33 (m, 1 H, CH$_2$–N), 2.34–2.18 (dm, 4 H, CH$_2$–CH=CH$_2$), 1.89–1.84 (m, 2 H, CH$_2$), 1.71–1.67 (m, 2 H, CH$_2$) ppm. ^{13}C NMR (50.33 MHz, CDCl$_3$, TMS): δ = 144.4 (Cq, Ar), 138.6 (Cq, Ar), 134.2 (CH=CH$_2$), 133.4 (CH=CH$_2$), 127.9 (CH, Ar), 125.2 (CH, Ar), 119.0 (CH=CH$_2$), 117.7 (CH=CH$_2$), 75.6 (Cq–OH), 74.9 (Cq–OH), 70.1 (CH–N), 62.4 (CH$_2$–N), 55.0 (CH$_2$–N), 46.7 (CH$_2$–CH=CH$_2$), 41.0 (CH$_2$–CH=CH$_2$), 27.2 (CH$_2$), 24.8 (CH$_2$) ppm. MS (ESI): m/z = 382.27 [M + H]$^+$; found 382.57. C$_{25}$H$_{35}$NO$_2$: calcd. C 78.70, H 9.25; found C 78.54, H 8.89. $[a]_D^{20}$ = –140.0 (c = 10^{-2} g mL^{-1}, CHCl$_3$).

Tetrapropyl–Pyrrolidine Compound 6: Pd/C catalyst (10%) was added to a solution of **5** (0.52 g, 1.36 mmol) in THF (20 mL) in a thick-walled tube capped with a Young stopcock. The tube was flushed, pressurized with hydrogen, sealed, and stirred at room temperature for 3 h. The solvent was removed under vacuum. The residue was extracted with diethyl ether and filtered through Celite. The solvent was removed under vacuum and the product was purified by chromatography on a silica gel column and eluted with petroleum ether/diethyl ether (4:6 v/v). Compound **6** was obtained as colorless oil in 93% (493 mg) yield. ^1H NMR (200.16 MHz, CDCl$_3$, TMS): δ = 7.33 (s, 4 H, Har), 3.78 (dd, $^3J_{H,H}$ = 11.31 Hz, 2 H, CH$_2$–N), 2.90–2.79 (m, 3 H, CH and CH$_2$–N), 2.51–2.49 (m, 1 H, CH$_2$–N), 1.86–1.72 (m, 6 H, CH$_2$), 1.70–1.65 (m, 2 H, CH$_2$), 1.55–1.52 (m, 2 H, CH$_2$), 1.37–1.28 (m, 8 H, CH$_2$), 1.12–1.10 (m, 2 H, CH$_2$), 0.91 (t, $^3J_{H,H}$ = 7.90 Hz, 6 H, CH$_3$), 0.85 (t, $^3J_{H,H}$ = 5.98 Hz, 6 H, CH$_3$) ppm. ^{13}C NMR (50.33 MHz, CDCl$_3$, TMS): δ = 145.1 (Cq, Ar), 138.3 (Cq, Ar), 127.8 (CH, Ar), 125.1 (CH, Ar), 76.9 (Cq–OH), 75.6 (Cq–OH), 70.2 (CH–N), 62.8 (CH$_2$–N), 54.9 (CH$_2$–N), 45.2 (CH$_2$), 38.5 (CH$_2$–CH–CH$_2$), 27.2 (CH$_2$), 24.9 (CH$_2$), 17.0 (d, CH$_2$), 16.7 (CH$_2$), 14.9 (d, CH$_3$), 14.4 (CH$_3$) ppm. MS (ESI): m/z = 390.34 [M + H]$^+$; found 390.63. C$_{25}$H$_{35}$NO$_2$: calcd. C 77.07, H 11.12; found C 76.89, H 11.19. $[a]_D^{20}$ = –135.5 (c = 10^{-2} g mL^{-1}, CHCl$_3$).

Enantiopure Dendritic POM Hybrid 7: H$_2$O$_2$ (4.6 mL, 35% in water) was added to a solution of commercial heteropolyacid H$_3$PW$_{12}$O$_{40}$ (0.098 mmol) in water. The mixture was stirred at room temperature for 30 min. A solution of **6** (100 mg, 0.256 mmol) in CH$_2$Cl$_2$ (5 mL) was added, and the mixture was

stirred for 30 min. The CH_2Cl_2 layer was washed with water and dried with sodium sulfate. The product was obtained by removing the solvent under vacuum to give a yellow solid in 90% (204 mg) yield. ^1H NMR (200.16 MHz, CDCl$_3$, TMS): δ = 7.32 (br., 12 H, Har), 4.32 (br., 6 H, CH$_2$–N), 3.64 (br., 6 H, CH$_2$–N), 3.28 (br., 3 H, CH–N), 2.32 (br., 6 H, CH$_2$), 2.11 (br., 12 H, CH$_2$), 1.82 (br., 18 H, CH$_2$), 1.31 (br., 24 H, CH$_2$), 0.91 (br., 6 H, CH$_2$), 0.88 (br., 36 H, CH$_3$) ppm. ^{13}C NMR (50.33 MHz, CDCl$_3$,TMS): δ = 148.9 (Cq, Ar), 131.3 (CH, Ar), 126.7 (Cq, Ar), 126.2 (CH, Ar), 76.9 (Cq–OH), 74.2 (Cq–OH), 74.0 (CH–N), 60.3 (CH$_2$–N), 54.8 (CH$_2$–N), 45.0 (CH$_2$), 37.7 (d, CH$_2$–CH=CH$_2$), 26.3 (CH$_2$), 23.5 (CH$_2$), 16.6 (CH$_2$), 16.4 (d, CH$_2$), 14.4 (d, CH$_3$), 14.2 (CH$_3$) ppm. ^{31}P NMR (121.49 MHz, CDCl$_3$): δ = 2.85 (PO$_4$) ppm. FTIR (KBr plates): $\tilde{v}$ = 2965.7 (s), 1461.8 (m), 1114.7 (m, P–O), 1083.6 (m, P–O), 954.9 (s, W=O), 839.5 (m, O–O). $C_{75}H_{132}N_3O_{30}PW_4$: calcd. C 38.79, H 5.73, P 1.33, W 31.67; found C 39.43, H 6.03, P 1.29, W 32.01. $[a]_D^{20}$ = –112.4 (c = 10^{-2} g mL^{-1}, CHCl$_3$).

General Procedure for the Catalytic Oxidation Reactions with Dendritic POM 7 and for the Catalyst Recovery Experiment: The POM catalyst and the substrate (250 equiv.) were dissolved in solvent (1 mL). An aqueous solution of H_2O_2 (35% in water) was added to the reaction mixture at the appropriate temperature. The latter was stirred and monitored by ^1H NMR spectroscopy. Upon completion of the reaction, the organic layer was separated and concentrated under vacuum to about 0.2 mL. The catalyst was precipitated by addition of Et$_2$O (5 mL). The solid was filtered, washed with diethyl ether (3 × 1 mL), and dried under vacuum to yield the POM catalyst as a white solid, which was analyzed by ^1H and ^{31}P NMR spectroscopy before its use in a new catalytic experiment. The diethyl ether solution was evaporated under vacuum, and the oxidized product was purified by chromatography on a silica gel column [petroleum ether/diethyl ether (1:9 v/v)]. The enantiomeric excesses were determined by chiral HPLC using a Chiralcel ASH column, UV detector (254 nm), and eluting with hexane-2-propanol (1:1) in the case of methyl phenyl sulfide (**8**) and (9.5:0.5) in the case of alkenes, at a flow rate of 0.5 mL min^{-1}. The catalyst was recovered following the typical procedure and conditions described above for the first cycle. The organic solvent and the reactants were adjusted to the amount of the catalyst used.

Supporting Information (see footnote on the first page of this article): NMR and IR spectra of compounds **4**, **5**, **6**, and **7**.

Acknowledgments

[1] a) M. T. Pope, A. Müller, *Angew. Chem.* **1991**, *103*, 56; *Angew. Chem. Int. Ed. Engl.* **1991**, *30*, 34–48; b) J. T. Rhule, C. L. Hill, D. A. Rud, R. F. Schinazi, *Chem. Rev.* **1998**, *98*, 327–358; c) D. E. Katsoulis, *Chem. Rev.* **1998**, *98*, 359–388; d) M. T. Pope, A. Müller (Eds.), *Polyoxometalate Chemistry: From Topology via Self-Assembly to Applications*, Kluwer Academic, Dordrecht, **2001**.

[2] a) M. T. Pope, A. Müller (Eds.), *Polyoxometalates Chemistry: From Topology via Self-Assembly to Applications*, Kluwer Academic Publishers, Dordrecht, The Netherlands, **2001**; b) J. J. Borra-Almenar, E. Coronado, A. Müller, M. T. Pope (Eds.), *Polyoxometalate Molecular Science*, Kluwer Academic Publishers, Dordrecht, The Netherlands, **2003**; c) D. L. Long, E. Burkholder, L. Cronin, *Chem. Soc. Rev.* **2007**, *36*, 105–121.

[3] a) K. Kamata, K. Yonehara, Y. Sumida, K. Yamaguchi, S. Hikichi, N. Mizuno, *Science* **2003**, *300*, 964–966; b) M. Bonchio, M. Carraro, G. Scorrano, U. Kortz, *Adv. Synth. Catal.* **2005**, *347*, 1909–1912; c) A. Sartorel, M. Carraro, A. Bagno, G. Scorrano, M. Bonchio, *Angew. Chem.* **2007**, *119*, 3319; *Angew. Chem. Int. Ed.* **2007**, *46*, 3255–3258; d) A. Sartorel, M. Carraro, R. De Zorzi, S. Geremia, N. D. McDaniel, S. Bernhard, G. Scorrano, M. Bonchio, *J. Am. Chem. Soc.* **2008**, *130*, 5006–5007.

[4] A. Proust, R. Thouvenot, P. Gouzerh, *Chem. Commun.* **2008**, *16*, 1837–1852.

[5] a) D. A. Judd, J. H. Nettles, J. P. Snyder, D. C. Liotta, J. Tang, J. Ermolieff, R. F. Schinazi, C. L. Hill, *J. Am. Chem. Soc.* **2001**, *123*, 886–897; b) S. Shigeta, S. Mori, E. Kodama, J. Kodama, K. Takahashi, T. Yamase, *Antiviral Res.* **2003**, *58*, 265–271; c) X. Wang, J. Liu, M. T. Pope, *Dalton Trans.* **2003**, *5*, 957–960; d) Y. Tajima, *Microbiol. Immunol.* **2003**, *47*, 207–212.

[6] C. Sanchez, G. J. de Soler-Illia, F. Ribot, T. Lalot, C. R. Mayer, V. Cabuil, *Chem. Mater.* **2001**, *13*, 3061–3083.

[7] a) D. A. J. Judd, H. Nettles, N. Nevins, J. P. Snyder, D. C. Liotta, J. Tang, J. Ermolieff, R. F. Schinazi, C. L. Hill, *J. Am. Chem. Soc.* **2001**, *123*, 886–897; b) A. Müller, F. Peters, M. T. Pope, D. Gattesschi, *Chem. Rev.* **1998**, *98*, 239–271; c) B. Hasenknopf, K. Micoine, E. Lacôte, S. Thorimbert, M. Malacria, R. Thouvenot, *Eur. J. Inorg. Chem.* **2008**, 5001–5013, and references cited therein) M. Carraro, A. Sartorel, G. Scorrano, C. Maccato, M. H. Dickman, U. Kortz, M. Bonchio, *Angew. Chem.* **2008**, *120*, 7385; *Angew. Chem. Int. Ed.* **2008**, *47*, 7275–7279; e) C. Boglio, B. Hasenknopf, G. Lenoble, P. Rémy, P. Gouzerh, S. Thorimbert, E. Lacôte, M. Malacria, R. Thouvenot, *Chem. Eur. J.* **2008**, *14*, 1532–1540.

[8] For review, see: a) A. Berkessel, H. Gröger, *Asymmetric Organocatalysis*, Wiley-VCH, Weinheim, Germany, **2005**; b) T. Katsuki, in: *Comprehensive Coordination Chemistry II*, vol. 9 (Ed.: J. McCleverty), Elsevier Science, Oxford, **2003**; c) T. Katsuki, in: *Catalytic Asymmetric Synthesis*, 2nd ed. (Ed.: I. Ojima), Wiley-VCH, New York, **2000**; d) E. N. Jacobsen, M. H. Wu, in: *Comprehensive Asymmetric Catalysis* (Eds.: E. N. Jacobsen, A. Pfaltz, H. Yamamoto), Springer, Berlin, **1999**.

[9] a) M. Inoue, T. Yamase, *Bull. Chem. Soc. Jpn.* **1995**, *68*, 3055–3063; b) F. B. Xin, M. T. Pope, *J. Am. Chem. Soc.* **1996**, *118*, 7731–7736; c) M. Inoue, T. Yamase, *Bull. Chem. Soc. Jpn.* **1996**, *69*, 2863–2868; d) D. L. Long, P. Kögerler, L. J. Farrugia, L. Cronin, *Chem. Asian J.* **2006**, *1*, 352–357; e) D. L. Long, E. Burkholder, L. Cronin, *Chem. Soc. Rev.* **2007**, *36*, 105–121; f) C. Streb, D. L. Long, L. Cronin, *Chem. Commun.* **2007**, *5*, 471–473; g) U. Kortz, M. G. Savelieff, F. Y. A. Ghali, L. M. Khalil, S. A. Maalouf, D. I. Sinno, *Angew. Chem.* **2002**, *114*, 4246; *Angew. Chem. Int. Ed.* **2002**, *41*, 4070–4073; h) X. K. Fang, T. M. Anderson, C. L. Hill, *Angew. Chem.* **2005**, *117*, 3606; *Angew. Chem. Int. Ed.* **2005**, *44*, 3540–3544; i) X. K. Fang, T. M. Anderson, Y. Hou, C. L. Hill, *Chem. Commun.* **2005**, *40*, 5044–5046; j) L. M. Zheng, T. Whitfield, X. Wang, A. J. Jacobson, *Angew. Chem.* **2000**, *112*, 4702; *Angew. Chem. Int. Ed.* **2000**, *39*, 4528–4531; k) H. Y. An, E. B. Wang, D. R. Xiao, Y. G. Li, Z. M. Su, L. Xu, *Angew. Chem.* **2006**, *118*, 918; *Angew. Chem. Int. Ed.* **2006**, *45*, 904–908.

[10] a) C. Jahier, M. Cantuel, N. D. McClenaghan, T. Buffeteau, D. Cavagnat, F. Agbossou, M. Carraro, M. Bonchio, S. Nlate, *Chem. Eur. J.* **2009**, *15*, 8703–8708; b) C. Jahier, M.-F. Coustou, M. Cantuel, N. D. McClenaghan, T. Buffeteau, D. Cavagnat, M. Carraro, S. Nlate, *Eur. J. Inorg. Chem.* **2011**, 727–738.

[11] M. Carraro, G. Modugno, A. Sartorel, G. Scorrano, M. Bonchio, *Eur. J. Inorg. Chem.* **2009**, 5164–5174.

[12] W. Wan, B. Mao, S. Zhu, X. Jiang, Z. Liu, R. Wang, *Eur. J. Org. Chem.* **2009**, 3790–3794.

[13] D. C. Duncan, R. C. Chambers, E. Hecht, C. Hill, *J. Am. Chem. Soc.* **1995**, *117*, 681–691.

[14] a) Z.-X. Wang, Y. Tu, M. Frohn, J.-R. Zhang, Y. Shi, *J. Am. Chem. Soc.* **1997**, *119*, 11224–11235; b) A. Armstrong, T. Tsuchiya, *Tetrahedron* **2006**, *62*, 257–263.

[15] U. Sundermeier, C. Döbler, M. Beller, in: *Modern Oxidation Methods* (Ed.: J. E. Bäckvall), Wiley-VCH, Weinheim, Germany, **2004**, p. 1.

[16] a) M. Tokunaga, J. F. Larrow, F. Kakuichi, E. N. Jacobsen, *Science* **1997**, *277*, 936–938; b) A. Gayet, S. Bertilsson, P. G. Anderson, *Org. Lett.* **2002**, *4*, 3777–3779.

[17] A. Ozanne-Beaudenon, S. Quideau, *Tetrahedron Lett.* **2006**, *47*, 5869–5873.

[18] F. G. Gelalcha, G. Anilkumar, M. K. Tse, A. Brückner, M. Beller, *Chem. Eur. J.* **2008**, *14*, 7687–7698.

Neutral and Anionic Antimony(III) Species Supported by a Bicyclic Guanidinate

Benjamin M. Day,[a] Martyn P. Coles,*[b] and Peter B. Hitchcock[a]

Bicyclic guanidine 1,3,4,6,7,8-hexahydro-2H-pyrimido[1,2-a]pyrimidine (hppH) was investigated as a source of anionic or neutral ligand at antimony. Reaction of the in situ generated lithium guanidinate with $SbCl_3$ in a 1:1 or 2:1 ratio forms the expected metathesis products $Sb(hpp)_nCl_{3-n}$ (**1**, $n = 1$; **2**, $n = 2$). The molecular structures of **1** and **2** were determined by X-ray diffraction, which shows chelating guanidinates and suggests the presence of a stereochemically active lone

pair of electrons. The reaction of two equivalents of the neutral guanidine hppH with $SbCl_3$ proceeds via proton transfer between the hpp fragments, affording the ion pair $[hppH_2][Sb(hpp)Cl_3]$ (**3**), where $[Sb(hpp)Cl_3]^-$ is an unusual example of a monometallic antimonate(III) anion. The molecular structure of **3** shows hydrogen bonding between two of the chlorides and the N*H* functionalities of the guanidinium cation.

Introduction

We have a long-standing interest in the application of bicyclic guanidines as neutral[1] and anionic[2] ligands at main group and transition metal centres. Much of our work has focussed on the {6:6}-fused system, hppH (1,3,4,6,7,8-hexahydro-2H-pyrimido[1,2-a]pyrimidine), during which time we have noted a diverse range of coordination modes (Figure 1). In addition to the bidentate coordination **A**, typical for acyclic guanidinate derivatives,[3] constraining the nitrogen substituents of the amidine component into the six-membered heterocycles promotes a number of bridging modes **B**–**G** incorporating two,[4] three[4h,4i,5] or four[4h,4i,6]

Figure 1. Reported bonding modes for the bicyclic guanidinate derived from 1,3,4,6,7,8-hexahydro-2H-pyrimido[1,2-a]pyrimidine (hppH).

[a] Department of Chemistry, University of Sussex,
Falmer, Brighton BN1 9QJ, UK
[b] School of Chemical and Physical Sciences, Victoria University of Wellington,
P. O. Box 600, Wellington, New Zealand
Fax: +64-4-4635237
E-mail: martyn.coles@vuw.ac.nz

metals. The propensity for bridging has been explained in terms of a wide (parallel) projection of the nitrogen donor orbitals in [hpp]−. This contrasts with the situation in acyclic anions in which steric interactions between the nitrogen substituents force these orbitals to point towards the "mouth" of the ligand (Figure 2).

Figure 2. Schematic representation of the orbital projection in [hpp]− and a generic acyclic guanidinate anion, $[R_2NC\{NR'\}_2]^-$.

Within groups 13 and 14, the chemistry of the [hpp]− anion has focussed mainly on the lighter elements boron[7] and silicon.[8] The corresponding coordination chemistry of aluminium,[4a] gallium[4k] and tin[4d] has shown a tendency for the ligand to adopt a bridging **B**-type coordination (Figure 1), although both **A** and **B** coordination have been noted for Sn^{II}.[4d] We were curious to see whether coordinating the [hpp]− anion to a larger metal ion would favour chelation (**A**-type bonding) and targeted antimony(III) compounds to determine whether this would be the case [effective ionic radii: Al^{3+} 0.535 Å, Ga^{3+} 0.62 Å, Sb^{3+} 0.76 Å].[9]

Earlier publications describing amidinate complexes of antimony in the +3[10] and +5 oxidation states[11] were mainly restricted to structural reports. More recently attention has focussed on the coordination chemistry of antimony(III) (Figure 3),[12] with interest primarily derived from the ability of such ligands to support low-oxidation-state metals.[12b] We report herein our preliminary studies

into the application of [hpp]⁻ as a ligand at Sb^III, including the crystal structure of an unanticipated ionic species consisting of a guanidinium cation and an antimonate(III) anion.

Figure 3. Examples of structurally characterized Sb^III–amidinate and –guanidinate compounds (Ar = 2,6-iPr$_2$C$_6$H$_3$).

Scheme 1. Synthesis of Sb(hpp)$_n$Cl$_{3-n}$ (**1**, n = 1; **2** n = 2) and [hppH$_2$][Sb(hpp)Cl$_3$] (**3**).

spectra are consistent with a symmetrical environment for the guanidinate ligand in each compound.

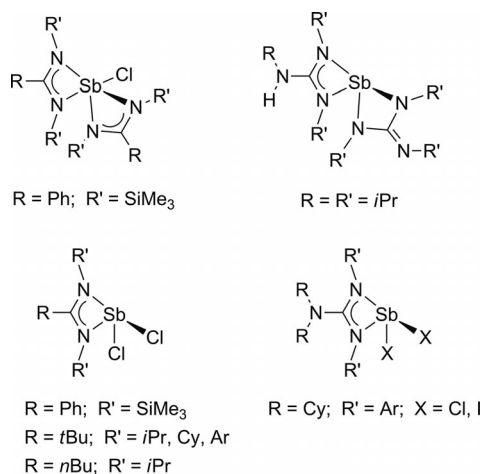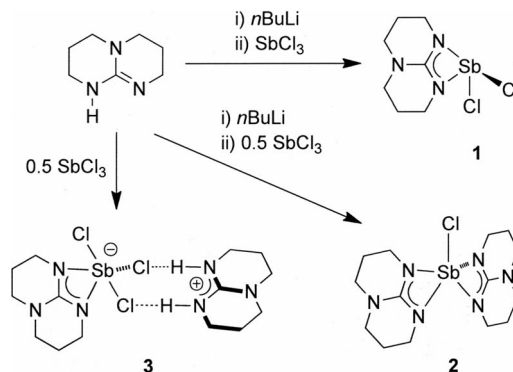The X-ray crystal structure of compound **1** (Tables 1 and 2) confirmed the formulation as the monomeric dichloride Sb(hpp)Cl$_2$ (Figure 4a). The geometry at the metal may be described as highly distorted trigonal bipyramidal, the axial positions defined by Cl1 and N2 and a stereochemically

Results and Discussion

The 1:1 reaction of in situ generated Li[hpp][4h] with one equivalent of SbCl$_3$ gave colourless crystals of Sb(hpp)Cl$_2$ (**1**) upon work-up (Scheme 1). The analogous procedure with 0.5 equiv. of anitimony(III) chloride afforded the bis(guanidinate) complex Sb(hpp)$_2$Cl (**2**). Three resonances for the annular methylene groups in the ¹H and ¹³C NMR

Table 2. Selected bond lengths [Å] and angles [°] for **1**.

Sb–N1	2.060(6)	Sb–N2	2.244(7)
Sb–Cl1	2.587(2)	Sb–Cl2	2.414(2)
C1–N1	1.332(9)	C1–N2	1.341(9)
C1–N3	1.345(10)		
N1–Sb–N2	61.3(2)	N1–Sb–Cl1	85.79(17)
N1–Sb–Cl2	96.3(2)	N2–Sb–Cl1	146.90(16)
N2–Sb–Cl2	89.77(19)	Cl1–Sb–Cl2	90.57(7)

Table 1. Crystal structure and refinement data for Sb(hpp)Cl$_2$ (**1**), Sb(hpp)$_2$Cl (**2**) and [hppH$_2$][Sb(hpp)Cl$_3$] (**3**).

	1	2	3
Empirical formula	C$_7$H$_{12}$Cl$_2$N$_3$Sb	C$_{14}$H$_{24}$ClN$_6$Sb	C$_{14}$H$_{26}$Cl$_3$N$_6$Sb
M_r	330.85	433.59	506.51
T [K]	173(2)	173(2)	173(2)
Crystal size [mm]	0.10 × 0.05 × 0.01	0.24 × 0.14 × 0.08	0.15 × 0.10 × 0.10
Crystal system	monoclinic	monoclinic	triclinic
Space group	$P2_1/n$ (alternative No.14)	$P2_1/c$ (No. 14)	$P\bar{1}$ (No. 2)
a [Å]	9.3783(8)	12.0687(5)	7.8127(2)
b [Å]	8.1401(8)	8.3115(3)	8.5487(2)
c [Å]	13.8748(10)	16.9864(8)	14.8964(4)
$α$ [°]	90	90	100.132(2)
$β$ [°]	99.636(5)	100.511(2)	91.754(1)
$γ$ [°]	90	90	97.835(2)
V [Å³]	1044.26(16)	1675.30(12)	968.73(4)
Z	4	4	2
$d_{calcd.}$ [Mg m⁻³]	2.10	1.72	1.74
Absorption coefficient [mm⁻¹]	3.11	1.81	1.85
$θ$ range [°]	3.50 to 26.02	1.72 to 27.48	3.49 to 25.99
Reflections collected	8878	10016	13137
Independent reflections	2049 [R_{int} = 0.101]	3797 [R_{int} = 0.049]	3797 [R_{int} = 0.030]
Reflections with $I > 2σ(I)$	1617	3176	3513
Data/restraints/parameters	2049/0/118	3797/0/199	3797/0/225
Final R indices [$I > 2σ(I)$]	R_1 = 0.060, wR_2 = 0.146	R_1 = 0.030, wR_2 = 0.083	R_1 = 0.021, wR_2 = 0.047
Final R indices (all data)	R_1 = 0.077, wR_2 = 0.158	R_1 = 0.044, wR_2 = 0.112	R_1 = 0.024, wR_2 = 0.048
GooF on F^2	1.098	1.195	1.090
Largest diff. peak/hole [e Å⁻³]	2.43 and –1.72[a]	1.34 and –1.84	0.40 and –0.46

[a] Near Sb.

active lone pair of electrons occupying an equatorial position (Figure 5a). The Sb–N and Sb–Cl distances support this with shorter bonds to the proposed equatorial atoms and longer bonds to the corresponding axial atoms [Sb–N1$_{(eq)}$ 2.060(6) Å vs. Sb–N2$_{(ax)}$ 2.244(7) Å; Sb–Cl2$_{(eq)}$ 2.414(2) Å vs. Sb–Cl1$_{(ax)}$ 2.587(2) Å]. The repulsive influence of the lone pair and acute bite angle of the guanidinate [N1–Sb–N2 61.3(2)°] cause a large reduction of the N2–Sb–Cl1 angle from its ideal linear arrangement to 146.90(16)°. Within the CN$_3$ core of the guanidinate, the C–N distances

are identical (within experimental uncertainty), suggesting efficient delocalization.

The degree of aggregation of antimony compounds incorporating amidinate and guanidinate anions varies considerably with the steric profile of the ligand and the solvent from which the compound is crystallized (i.e., whether solvate molecules are included in the crystal lattice). For example, the bulky amidinate and guanidinate compounds Sb(RC{NR′}$_2$)Cl$_2$ (R′ = Ar; R = tBu,[12c] Cy$_2$N[12b]), the former of which crystallizes as the bis(chloroform) solvate, are monomeric in the solid state. In contrast, when R = tBu and R′ = iPr or Cy,[12c] or R = Ph and R′ = SiMe$_3$,[10a] the molecules are linked by a single intermolecular Sb···Cl contact to generate corner-bridged polymeric structures. Compound **1** has two symmetry-related Sb···Cl contacts [Sb···Cl 3.240 Å] that generate an edge-shared dimer (Figure 4b), as noted in Sb(nBuC{NiPr}$_2$)Cl$_2$.[12c] These intermolecular contacts may contribute to the elongation in the Sb–Cl1 bond length described above.

The crystal structure of **2** (Figure 6, Tables 1 and 3) shows a monomeric, five-coordinate antimony centre with chelating [hpp]$^-$ ligands and a terminal chloride ligand. The angles at the metal range from the small bite of the guanidinates [57.32(10)° and 60.47(11)° for C1 and C8 ligands, respectively] to 141.64(8)° for Cl–Sb–N5. The latter value is close to that proposed for the *trans*-equatorial substituents distorted by lone-pair repulsions and chelation in **1**. A similar metal geometry was observed for the bis(amidinate) compound Sb(PhC{NSiMe$_3$}$_2$)$_2$Cl,[10b] in which the metal
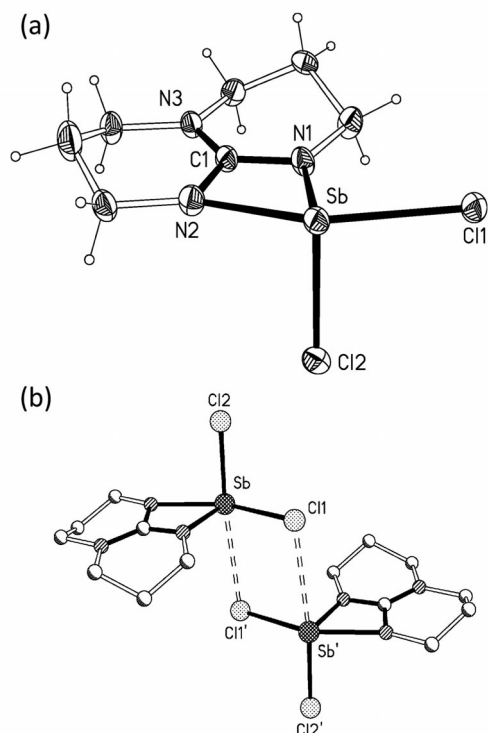
Figure 4. (a) Thermal ellipsoid plot (30% probability) of **1**; (b) schematic diagram showing the association of **1** into edge-shared dimers.

Figure 6. Thermal ellipsoid plot (30% probability) for **2**.

Figure 5. Top: geometries at antimony for (a) compound **1** and (b, c) alternatives for compound **2**. Bottom: localized and delocalization descriptions of bonding in the Sb(hpp) fragment.

Table 3. Selected bond lengths [Å] and angles [°] for **2**.

Sb–N1	2.057(3)	Sb–N2	2.526(3)
Sb–N4	2.151(3)	Sb–N5	2.209(3)
Sb–Cl	2.6831(9)	C1–N1	1.353(5)
C1–N2	1.322(5)	C1–N3	1.355(5)
C8–N4	1.340(4)	C8–N5	1.328(4)
C8–N6	1.345(4)		
N1–Sb–N2	57.32(10)	N1–Sb–N4	95.33(11)
N1–Sb–N5	91.01(11)	N1–Sb–Cl	83.38(9)
N2–Sb–N4	131.44(11)	N2–Sb–N5	79.17(10)
N2–Sb–Cl	126.39(7)	N4–Sb–N5	60.47(11)
N4–Sb–Cl	82.20(8)	N5–Sb–Cl	141.61(8)

B. M. Day, M. P. Coles, P. B. Hitchcock

was described as having distorted octahedral geometry with a "stereochemically strongly effective lone electron pair"; this description may be applied to the geometry of **2** (**2**-Oh, Figure 5b).

An alternative description for the geometry of **2** is a distorted trigonal bipyramidal geometry (**2**-tbp, Figure 5c) in which N2 is only loosely coordinated to the antimony centre. Evidence for this comes from a very long Sb–N2 bond [2.526(3) Å] compared to the remaining Sb–N distances in **2** [2.057(3)–2.209(3) Å] and those in **1**. We also note localization of π-electron density in the N1–C1–N2 component of the [hpp]⁻ ligand, indicated by long C1–N1 and short C1–N2 bonds [1.353(5) and 1.322(5) Å, respectively]. This is consistent with a large contribution from localized bonding of the **I/I′** type previously noted for amidinates in five-coordinate aluminium systems.[13] The π-bonding in the other guanidinate ligand shows a similar, although less pronounced, trend.

In addition to using the [hpp]⁻ anion as a ligand in coordination chemistry, the neutral guanidine, hppH, also serves as an effective N-donor ligand.[4h,5a,14] The typical bonding mode is by lone-pair donation from the imine nitrogen to an available orbital on the metal centre. For metal halide compounds, this interaction may be strengthened by intramolecular hydrogen bonding to the halide atom (Figure 7). Many bis(N-donor ligand) adducts of antimony(III) chloride are known, including, for example, those of 1,4-diazabutadiene,[15] bipy,[16] 1,2-bis(aryl-imino)acenaphthene,[17] 4-phenylpyridine[18] and 2,6-dimethylaniline.[19] We therefore investigated the use of hppH as a neutral N-donor ligand with antimony(III) chloride as the metal reagent.
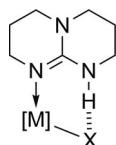
Figure 7. Coordination of a neutral hppH guanidine at a generic metal halide fragment showing stabilization by intramolecular hydrogen bonding.

The reaction between two equivalents of hppH and SbCl₃ afforded colourless crystals of **3** after the appropriate work-up (Scheme 1). The crystals were insoluble in common NMR spectroscopic solvents but dissolved in [D₃]-acetonitrile, enabling spectroscopic analysis. Key features include a broad resonance at 7.57 ppm with a relative integral of 2H in the ¹H NMR spectrum, as well as two resonances at 159.2 and 152.5 ppm (corresponding to the CN_3 carbon atom) in the ¹³C{¹H} NMR spectrum. These data indicate two different ligand environments and suggest that one may be associated with a guanidinium component as the low-field resonance in the proton NMR spectrum is typical for the N*H* atoms of the [hppH₂]⁺ cation.[20]

X-ray diffraction analysis (Figure 8, Tables 1 and 4) showed that **3** consists of the hydrogen-bonded ion pair [hppH₂][Sb(hpp)Cl₃]. This salt may be considered as the net result of a proton transfer between hppH molecules to af-

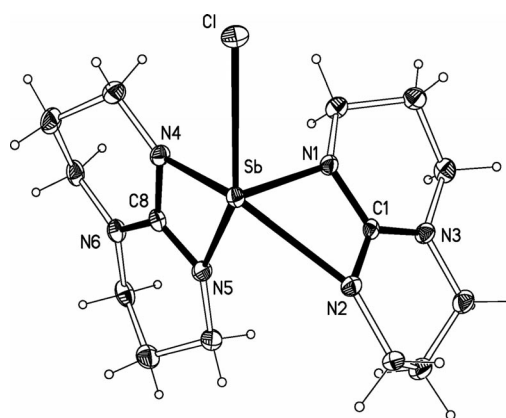ford the cation [hppH₂]⁺ and the anion [hpp]⁻, the latter of which coordinates to SbCl₃. Mechanistic details of this reaction are not known.
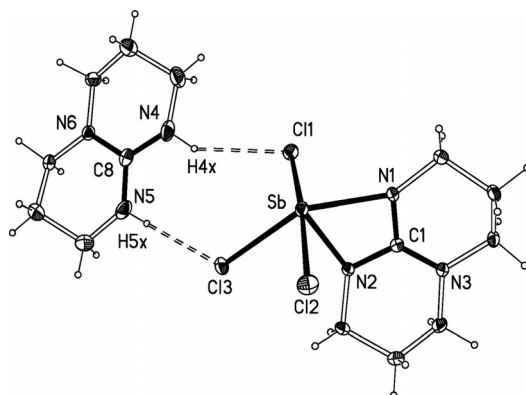
Figure 8. Thermal ellipsoid plot (30% probability) of **3**.

Table 4. Selected bond lengths [Å] and angles [°] for **3**.

Sb–N1	2.2602(17)	Sb–N2	2.0756(17)
Sb–Cl1	2.5932(6)	Sb–Cl2	2.6570(6)
Sb–Cl3	2.5906(6)	C1–N1	1.320(3)
C1–N2	1.357(3)	C1–N3	1.337(3)
C8–N4	1.337(3)	C8–N5	1.338(3)
C8–N6	1.331(3)		
N1–Sb–N2	61.00(6)	N1–Sb–Cl1	87.00(5)
N1–Sb–Cl2	96.72(5)	N1–Sb–Cl3	144.33(5)
N2–Sb–Cl1	93.50(5)	N2–Sb–Cl2	84.51(5)
N2–Sb–Cl3	84.82(5)	Cl1–Sb–Cl2	174.225(19)
Cl1–Sb–Cl3	85.108(19)	Cl2–Sb–Cl3	89.31(2)

The [Sb(hpp)Cl₃]⁻ anion is an unusual example of a monometallic antimonate(III) anion. The propensity for halides to bridge in anionic antimonate systems has strong grounding in the literature. Although [SbCl₄]⁻ was structurally described as early as 1970,[21] close contacts (less than 4.0 Å, the sum of the van der Waals radii) to additional chloride ions are frequently encountered in the solid state. The most common description of this unit is an octahedrally coordinated antimony within a polymeric chain bridged by chloride ions.[22] Both the bromide and the iodide systems are known as isolated octahalodiantimonate(III) ions, [X₃Sb(μ-X)₂SbX₃]²⁻ (X = Br,[23] I[24]). Substitution by phenyl groups in the anions form the [Cl₂(Ph)Sb(μ-Cl)₂Sb(Ph)Cl₂]²⁻ dimer for the monophenyl anion, and the monomer is only formed for the diphenyl derivative [SbCl₂Ph₂]⁻.[25] This system is further complicated by reports of [Cl₃(Ph)Sb(μ-Cl)Sb(Ph)Cl₃]³⁻ as a bimetallic trianion, which retains a single chloride bridge.[26] It appears that the formation of two strong hydrogen bonds to the [hppH₂]⁺ cation is sufficient to prevent the anion from dimerizing through the chlorides in **3**.

Considering a lone pair lying in the plane between N1 and Cl3, the geometry of Sb is best considered as distorted octahedral, with Cl1 and Cl2 *trans* to one another [Cl1–Sb–Cl2 174.225(19)°] and a typically small bite angle for the [hpp]⁻ anion [N1–Sb–N2 61.00(6)°]. The difference in Sb–N bond length [Sb–N1 2.2602(17) Å, Sb–N2 2.0756(17) Å]

is reflected in a shorter C1–N1 [1.320(3) Å] relative to C1–N2 [1.357(3) Å] and is consistent with a large contribution from the localized form of π-bonding (**I/I′**, Figure 5).[13]

The [hppH$_2$]$^+$ cation forms hydrogen bonds to Cl1 and Cl3, with intermolecular Cl···HN distances of 2.51 and 2.52 Å, respectively. The C–N bond lengths within the core are equivalent (within 3σ), indicating effective delocalization of the positive charge. Similar hydrogen bonding between [hppH$_2$]$^+$ and metal halide anions have been recorded for [CuCl$_4$]$^{2–}$[27] and [TaCl$_6$]$^–$.[28]

Conclusions

In summary, we have demonstrated that the large size of the Sb^{3+} ion enables the [hpp]$^–$ anion to bond through both available nitrogen atoms as a chelating ligand. The structure of both **1** and **2** indicate the presence of a stereochemically active lone pair, which, in addition to the narrow bite angle of the chelating guanidinate anion(s), generates highly distorted metal geometries. We have also shown that simple adduct formation with neutral hppH does not readily occur, the preferred mode of reactivity involving salt formation to afford a rare monometallic five-coordinate antimonate(III) anion.

Experimental Section

General Procedures: All manipulations were carried out under dry nitrogen with standard Schlenk line and cannula techniques or in a conventional nitrogen-filled glovebox. Solvents were dried with appropriate drying agents and degassed prior to use. NMR spectra were recorded by using a Bruker Avance DPX 300 MHz spectrometer at 300.1 (^{1}H) and 75.4 (^{13}C{^{1}H}) MHz or a Varian VNMRS 500 MHz spectrometer at 500.1 (^{1}H), 125.4 (^{13}C{^{1}H}) MHz. Proton and carbon chemical shifts were referenced internally to residual solvent resonances. Elemental analyses were performed by S. Boyer at London Metropolitan University. Compounds hppH and SbCl$_3$ were purchased from Sigma–Aldrich and used as received.

Sb(hpp)Cl$_2$ (1): nBuLi in hexanes (1.8 mmol, 0.7 mL, 2.6 M) was added dropwise to solution of hppH (0.252 g, 1.8 mmol) in THF at –78 °C. The resultant mixture was warmed to ambient temperature and stirred for 1 h, after which time full conversion to the lithium salt was assumed. The "hppLi" solution was added to SbCl$_3$ (0.413 g, 1.8 mmol) in THF (ca. 20 mL) at –78 °C to obtain a colourless solution. The solution was warmed to ambient temperature for 1 h, after which time a dark grey precipitate had formed. The volatiles were removed under vacuum, and the product was extracted with CH$_2$Cl$_2$. Yield 0.13 g, 22.3%. X-ray crystallographic quality crystals were obtained by slowly cooling a hot (ca. 70 °C) toluene solution to room temperature. C$_7$H$_{12}$Cl$_2$N$_3$Sb (330.85): calcd. C 25.41, H 3.66, N 12.70; found C 25.49, H 3.53, N 12.86. ^{1}H NMR (500 MHz, CDCl$_3$, 303 K): δ = 3.43, 3.23, 2.03 (m, 8 H, hpp-CH_2) ppm. ^{13}C{^{1}H} NMR (125 MHz, CDCl$_3$, 300 K): δ = *, 46.0, 39.9, 23.6 (hpp-CH$_2$) ppm; * resonance for CN$_3$ not observed.

Sb(hpp)$_2$Cl (2): Compound **2** was made by using the same synthetic procedure as that described for **1**, with hppH (0.648 g, 4.9 mmol), a solution of nBuLi in hexanes (5.0 mmol, 2.0 mL, 2.5 M) and SbCl$_3$ (0.560 g, 2.5 mmol). The product was isolated as a white powder

that was purified by crystallization from THF at –20 °C. Yield 0.40 g, 37%. C$_{14}$H$_{24}$ClN$_6$Sb (433.59): calcd. C 38.78, H 5.58, N 19.38; found C 38.67, H 5.61, N 19.30. ^{1}H NMR (500 MHz, CDCl$_3$, 303 K): δ = 3.33 (m, 8 H, hpp-CH_2), 3.11 (m, 8 H, hpp-CH_2), 1.91 (m, 8 H, hpp-CH_2). ^{13}C{^{1}H} NMR (125 MHz, CDCl$_3$, 300 K): δ = *, 46.3, 40.6, 23.8 (hpp-CH$_2$) ppm; * resonance for CN$_3$ not observed.

[hppH$_2$][Sb(hpp)Cl$_3$] (3): A solution of hppH (0.50 g, 3.6 mmol) in THF (ca. 30 mL) was added dropwise to a solution of SbCl$_3$ (0.41 g, 1.8 mmol) in THF (ca. 25 mL). A cloudy white precipitate formed, which coagulated to a gummy solid over a period of 1 h. Warming this mixture to approximately 60 °C and filtering afforded a colourless filtrate that was allowed to cool slowly to room temperature, affording colourless crystals **3**. Yield 0.19 g, 21%. C$_{14}$H$_{26}$Cl$_3$N$_6$Sb (506.51): calcd. C 33.19, H 5.17, N 16.59; found C 33.25, H 5.08, N 16.48. ^{1}H NMR (300 MHz, CD$_3$CN, 300 K): δ = 7.57 (br. s, 2 H, hppH_2), 3.22 (m, 16 H, hpp-CH_2), 1.92 (m, 8 H, hpp-CH_2) ppm. ^{13}C{^{1}H} NMR (75 MHz, CD$_3$CN, 300 K): δ = 159.2, 152.5 (CN$_3$), 47.1 (br), 40.7, 38.7, 24.1, 21.3 (hpp-CH$_2$) ppm.

Crystallographic Data Collection and Refinement Procedures: Details of the crystal data, intensity collection and refinement for complexes **1**, **2** and **3** are presented in Table 1. Crystals were covered in an inert oil, and suitable single crystals were selected under a microscope and mounted on a Kappa CCD diffractometer. Data was collected at 173(2) K with Mo-K_α radiation at 0.71073 Å. The structures were refined with SHELXL-97.[29]

CCDC-848242 (for **1**), -848243 (for **2**) and -848244 (for **3**) contain the supplementary crystallographic data for this paper. These data can be obtained free of charge from The Cambridge Crystallographic Data Centre via www.ccdc.cam.ac.uk/data_request/cif.

[1] M. P. Coles, *Dalton Trans.* **2006**, 985–1001.
[2] M. P. Coles, *Chem. Commun.* **2009**, 3659–3676.
[3] P. J. Bailey, S. Pace, *Coord. Chem. Rev.* **2001**, *214*, 91–141.
[4] a) S. L. Aeilts, M. P. Coles, D. C. Swenson, R. F. Jordan, V. G. Young Jr., *Organometallics* **1998**, *17*, 3265–3270; b) F. A. Cotton, X. Feng, D. J. Timmons, *Inorg. Chem.* **1998**, *37*, 4066–4069; c) M. P. Coles, P. B. Hitchcock, *J. Chem. Soc., Dalton Trans.* **2001**, 1169–1171; d) S. R. Foley, G. P. A. Yap, D. S. Richeson, *Polyhedron* **2002**, *21*, 619–627; e) M. P. Coles, P. B. Hitchcock, *Organometallics* **2003**, *22*, 5201–5211; f) M. D. Irwin, H. E. Abdou, A. A. Mohamed, J. P. Fackler Jr., *Chem. Commun.* **2003**, 2882–2883; g) M. P. Coles, P. B. Hitchcock, *Inorg. Chim. Acta* **2004**, *357*, 4330–4334; h) M. P. Coles, P. B. Hitchcock, *Chem. Commun.* **2005**, 3165–3167; i) C. Brinkmann, F. García, J. V. Morey, M. McPartlin, S. Singh, A. E. H. Wheatley, D. S. Wright, *Dalton Trans.* **2007**, 1570–1572; j) A. A. Mohamed, A. P. Mayer, H. E. Abdou, M. D. Irwin, L. M. Pérez, J. P. Fackler Jr., *Inorg. Chem.* **2007**, *46*, 11165–11172; k) G. Robinson, C. Y. Tang, R. Köppe, A. R. Cowley, H.-J. Himmel, *Chem. Eur. J.* **2007**, *13*, 2648–2654; l) A. A. Mohamed, H. E. Abdou, A. Mayer, J. P. Fackler Jr., *J. Cluster Sci.* **2008**, *19*, 551–559.
[5] a) F. A. Cotton, C. A. Murillo, D. J. Timmons, *Polyhedron* **1999**, *18*, 423–428; b) S. J. Birch, S. R. Boss, S. C. Cole, M. P. Coles, R. Haigh, P. B. Hitchcock, A. E. H. Wheatley, *Dalton Trans.* **2004**, 3568–3574; c) M. P. Coles, P. B. Hitchcock, *Eur. J. Inorg. Chem.* **2004**, 2662–2672.

[6] a) S. R. Boss, M. P. Coles, R. Haigh, P. B. Hitchcock, R. Snaith, A. E. H. Wheatley, *Angew. Chem.* **2003**, *115*, 5751; *Angew. Chem. Int. Ed.* **2003**, *42*, 5593–5596; b) S. R. Boss, M. P. Coles, V. Eyre-Brook, F. García, R. Haigh, P. B. Hitchcock, M. McPartlin, J. V. Morey, N. Hiroshi, P. R. Raithby, H. A. Sparkes, C. W. Tate, A. E. H. Wheatley, *Dalton Trans.* **2006**, 5574–5582.

[7] a) O. Ciobanu, P. Roquette, S. Leingang, H. Wadepohl, J. Mautz, H.-J. Himmel, *Eur. J. Inorg. Chem.* **2007**, 4530–4534; b) R. Dinda, O. Ciobanu, H. Wadepohl, O. Hübner, R. Acharyya, H.-J. Himmel, *Angew. Chem.* **2007**, *119*, 9270; *Angew. Chem. Int. Ed.* **2007**, *46*, 9110–9113; c) O. Ciobanu, F. Allouti, P. Roquette, S. Leingang, M. Enders, H. Wadepohl, H.-J. Himmel, *Eur. J. Inorg. Chem.* **2008**, 5482–5493; d) O. Ciobanu, D. Emeljanenko, E. Kaifer, J. Mautz, H.-J. Himmel, *Inorg. Chem.* **2008**, *47*, 4774–4778; e) O. Ciobanu, E. Kaifer, M. Enders, H.-J. Himmel, *Angew. Chem.* **2009**, *121*, 5646; *Angew. Chem. Int. Ed.* **2009**, *48*, 5538–5541.

[8] a) D. Kummer, S. H. A. Halim, W. Kuhs, G. Mattern, *J. Organomet. Chem.* **1993**, *446*, 51–65; b) S. H. Oakley, M. P. Coles, P. B. Hitchcock, *Dalton Trans.* **2004**, 1113–1114; c) S. H. Oakley, M. P. Coles, P. B. Hitchcock, *Inorg. Chem.* **2004**, *43*, 5168–5172; d) J. Maaranen, O. S. Andell, T. Vanne, I. Mutikainen, *J. Organomet. Chem.* **2006**, *691*, 240–246; e) M. P. Coles, S. E. Sözerli, J. D. Smith, P. B. Hitchcock, *Organometallics* **2007**, *26*, 6691–6693; f) M. P. Coles, S. M. El-Hamruni, J. D. Smith, P. B. Hitchcock, *Angew. Chem.* **2008**, *120*, 10301; *Angew. Chem. Int. Ed.* **2008**, *47*, 10147–10150; g) M. P. Coles, S. E. Sözerli, J. D. Smith, P. B. Hitchcock, I. J. Day, *Organometallics* **2009**, *28*, 1579–1581; h) R. S. Ghadwal, K. Pröpper, B. Dittrich, P. G. Jones, H. W. Roesky, *Inorg. Chem.* **2011**, *50*, 358–364.

[9] R. D. Shannon, *Acta Crystallogr., Sect. A* **1976**, *32*, 751–767.

[10] a) C. Ergezinger, F. Weller, K. Dehnicke, *Z. Naturforsch. Teil B* **1988**, *43*, 1119–1124; b) U. Patt-Seibel, U. Müller, C. Ergezinger, B. Borgsen, K. Dehnicke, D. Fenske, G. Baum, *Z. Anorg. Allg. Chem.* **1990**, *582*, 30–36.

[11] a) F. Weller, J. Pebler, K. Dehnicke, K. Hartke, H.-M. Wolff, *Z. Anorg. Allg. Chem.* **1982**, *486*, 61–69; b) W. Höneise, W. Schwarz, G. Heckmann, A. Schmidt, *Z. Anorg. Allg. Chem.* **1986**, *533*, 55–64.

[12] a) P. J. Bailey, R. O. Gould, C. N. Harmer, S. Pace, A. Steiner, D. S. Wright, *Chem. Commun.* **1997**, 1161–1162; b) S. P. Green, C. Jones, G. Jin, A. Stasch, *Inorg. Chem.* **2007**, *46*, 8–10; c) B. Lyhs, S. Schulz, U. Westphal, D. Bläser, R. Boese, M. Bolte, *Eur. J. Inorg. Chem.* **2009**, 2247–2253.

[13] M. P. Coles, D. C. Swenson, R. F. Jordan, V. G. Young Jr., *Organometallics* **1997**, *16*, 5183–5194.

[14] a) M. P. Coles, P. B. Hitchcock, *Polyhedron* **2001**, *20*, 3027–3032; b) S. H. Oakley, M. P. Coles, P. B. Hitchcock, *Inorg. Chem.* **2003**, *42*, 3154–3156; c) S. H. Oakley, M. P. Coles, P. B. Hitchcock, *Inorg. Chem.* **2004**, *43*, 7564–7566; d) S. H. Oakley, D. B. Soria, M. P. Coles, P. B. Hitchcock, *Dalton Trans.* **2004**, 537–546; e) J. F. Berry, F. A. Cotton, P. Huang, C. A. Murillo, X. Wang, *Dalton Trans.* **2005**, 3713–3715; f) S. H. Oakley, D. B. Soria, M. P. Coles, P. B. Hitchcock, *Polyhedron* **2006**, *25*, 1247–1255; g) F. A. Cotton, J. P. Donahue, N. E. Gruhn, D. L. Lichtenberger, C. A. Murillo, D. J. Timmons, L. O. Van Dorn, D. Villagrán, X. Wang, *Inorg. Chem.* **2006**, *45*, 201–213; h) A. Peters, U. Wild, O. Hübner, E. Kaifer, H.-J. Himmel, *Chem. Eur. J.* **2008**, *14*, 7813–7821; i) U. Wild, P. Roquette, E. Kaifer, J. Mautz, O. Hübner, H. Wadepohl, H.-J. Himmel, *Eur. J. Inorg. Chem.* **2008**, 1248–1257; j) G. M. Chiarella, D. Y. Melgarejo, A. Rozanski, P. Hempte, L. M. Perez, C. Reber, J. P. Fackler Jr., *Chem. Commun.* **2010**, *46*, 136–138.

[15] D. Gudat, T. Gans-Eichler, M. Nieger, *Chem. Commun.* **2004**, 2434–2435.

[16] A. Lipka, H. Wunderlich, *Z. Naturforsch. Teil B* **1980**, *35*, 1548–1551.

[17] N. J. Hill, G. Reeske, J. A. Moore, A. H. Cowley, *Dalton Trans.* **2006**, 4838–4844.

[18] A. Lipka, *Z. Naturforsch. Teil B* **1983**, *38*, 341–346.

[19] N. Burford, E. Edelstein, J. C. Landry, M. J. Ferguson, R. McDonald, *Chem. Commun.* **2005**, 5074–5076.

[20] M. S. Khalaf, S. H. Oakley, M. P. Coles, P. B. Hitchcock, *CrystEngComm* **2008**, *10*, 1653–1661.

[21] S. K. Porter, R. A. Jaconson, *J. Chem. Soc. A* **1970**, 1356–1359.

[22] M. G. B. Drew, P. P. K. Claire, G. R. Willey, *J. Chem. Soc., Dalton Trans.* **1988**, 215–218.

[23] A. T. Mohammed, U. Muller, *Z. Naturforsch. Teil B* **1985**, *40*, 562–564.

[24] S. Pohl, W. Saak, D. Haase, *Angew. Chem.* **1987**, *99*, 462; *Angew. Chem. Int. Ed. Engl.* **1987**, *26*, 467–468.

[25] M. Hall, D. B. Sowerby, *J. Organomet. Chem.* **1988**, *347*, 59–70.

[26] W. S. Shedrick, C. Martin, *Z. Naturforsch. Teil B* **1992**, *47*, 919–924.

[27] I. Díaz, V. Fernández, J. L. Martínez, L. Beyer, A. Pilz, U. Müller, *Z. Naturforsch. Teil B* **1998**, *53*, 933–938.

[28] D. B. Soria, J. Grundy, M. P. Coles, P. B. Hitchcock, *Polyhedron* **2003**, *22*, 2731–2737.

[29] G. M. Sheldrick, *SHELXL-97, Program for the Refinement of Crystal Structures*, Göttingen, **1997**.

Synthesis, Molecular Structures, and Reactivity of Dianionic Guanidinate Lanthanide/Lithium Derivatives

Xingmin Zhang,[a] Cunwei Qian,[a] Chuanyong Wang,[a] Yong Zhang,[a] Yaorong Wang,[a] Yingming Yao,[a] and Qi Shen*[a,b]

Anhydrous $LnCl_3$ was treated with [LiiPrNC(HNiPr)N-($C_6H_4$$p$-Cl)] and nBuLi at a molar ratio of 1:2:2 in THF to afford heterometallic Ln–Li chlorides stabilized by two dianionic guanidinate ligands [{[(iPrN)$_2$C[NLi(THF)$_3$($C_6H_4$$p$-Cl)]}$_2$Ln($\mu$-Cl$_2$)Li(THF)$_2$]·$n$THF [Ln = La (**1**), Nd (**2**) n = 2; Sm (**3**), Yb (**4**), Y (**5**) n = 3] in good yields. Treatment of the chlorides with NaOiPr and KOtBu yielded the corresponding isopropoxides [{[(iPrN)$_2$CN($C_6H_4$$p$-Cl)]$_2$(DME)(LiCl)Ln-(O$i$Pr)$_2$}$_2$]$^{2-}$[{Li(DME)$_3$}$^+$]$_2$·3$C_6H_{14}$ [Ln = Nd (**6**), Sm (**7**), Yb (**8**), Y (**9**); DME = 1,2-dimethoxyethane] and $tert$-butoxides [{(iPrN)$_2$C(NC$_6H_4$$p$-Cl)Li(DME)(LiCl)}$_2$Ln(O$t$Bu)$_2$]$^-$[Li(DME)$_3$]$^+$·0.5$C_6H_{14}$ [Ln = Nd (**10**), Yb (**11**)]. Attempts to

synthesize the corresponding amide and guanidinate complexes by treating **2** with LiNHC$_6H_5$ and [LiiPrNC(HNiPr)-N(C_6H_5)] led to the isolation of guanidinate lithium, [LiiPrNC(HNiPr)N($C_6H_4$$p$-Cl)(THF)]$_2$ (**12**). Addition of diisopropylcarbodiimide (iPrN=C=NiPr) into the reaction system of trisguanidinate lanthanide complex [{iPrNHC(NiPr)-(NC$_6H_4$$p$-Cl)}$_3$Yb(THF)] and nBuLi led to the preparation of the first heterometallic Yb–Li complex with a novel biguanidinate ligand [{iPrNHC(NiPr)N($C_6H_4$$p$-Cl)}$_2$Yb{($i$PrNC(N$i$Pr)$_2$)-N($C_6H_4$$p$-Cl)C($i$PrN)}Li(THF)]·THF (**13**). The molecular structures of **1**–**3** and **6**–**13** were determined by X-ray crystal structural analysis.

Introduction

Monoanionic guanidinato ligands are one of the most attractive non-cyclopentadienyl (Cp) ancillary ligands in coordination and organometallic chemistry of lanthanide metals[1] as they have the advantages of being easy to access and flexibile in electronic and steric demands by variation of substituents on the nitrogen atoms. Various lanthanide complexes that contain Ln–H,[2] Ln–C,[3] Ln–N,[4] and Ln–O[5] bonds were stabilized by guanidinate ligands and proven to be efficient precatalysts in a series of homogeneous catalyses.[2–5] Among these guanidinate ligands, N,N',N''-trialkyl guanidinate ligands should be particularly interesting, as the presence of a second N–H function in these species provides the capability of producing dianionic guanidinate ligands by deprotonation of the N–H bond. The introduction of a dianionic guanidinate ligand into a metal coordination sphere may make the complex take on a unique conjugated π system by means of delocalization

of the lone pairs on the sp^2-hybridized nitrogen centers, which may lead to different binding modes. Moreover, the application of a dianionic guanidinato ligand may also provide a convenient route to homo- and heteromultimetallic complexes. A series of main- and transition-metal complexes including homo- and heteromultimetallic complexes have been stabilized by dianionic guanidinate ligands.[6] In contrast, the application of these dianionic guanidinate ligands in organolanthanide chemistry has been limited to date. The first lanthanocene dianionic guanidinate complexes were reported by Zhou's group in 2007.[7] Later, they reported the synthesis of heterobimetallic lanthanide–lithium complexes with the formula [Cp$_2$Ln{(CyN)$_2$CNPh}-Li(THF)$_3$] and the reactivities of Li–N bonds in these complexes toward various electrophiles.[8] In the same year, we reported the synthesis and molecular structures of heteromultimetallic lanthanide and lithium complexes that bore three dianionic guanidinate ligands, [{Li(THF)-(DME)}$_3$Ln{μ-$\eta^2\eta^1$(iPrN)$_2$C(NC$_6H_4$$p$-Cl)}$_3$] (DME = 1,2-dimethoxyethane), by the reaction of trisguanidinate lanthanide [{iPrNHC(NiPr)(NC$_6H_4$$p$-Cl)}$_3$Ln] with nBuLi, and their catalytic activity in the amidation reaction of aldehydes with amines under mild conditions, in which they served as excellent precatalysts.[9a] The activity of these heterometallic dianionic guanidinate complexes is much higher than that of the corresponding monoguanidinate lanthanide complexes.[9b]

It is well known that the guanidinate chlorides of lanthanides are important precursors to a series of corresponding

[a] College of Chemistry, Chemical Engineering and Materials Science,
Soochow University,
Suzhou 215123, People's Republic of China
Fax: +86-512-65880305
E-mail: qshen@suda.edu.cn
[b] State Key Laboratory of Organometallic Chemistry, Shanghai Institute of Organic Chemistry,
Chinese Academy of Sciences,
Shanghai 200032, People's Republic of China
Supporting information for this article is available on the WWW under http://dx.doi.org/10.1002/ejic.201100901.

derivatives that contain Ln-active groups.[2–5] However, no dianionic guanidinate chlorides of lanthanides have been reported up to now. Thus, we tried to synthesize hetero-metallic dianionic guanidinate chlorides of lanthanides and lithium to address whether the chlorides could be stabilized. Fortunately, the chlorides with the formula [{(*i*PrN)$_2$C-[NLi(THF)$_3$(C$_6$H$_4$*p*-Cl)]}$_2$Ln(µ-Cl)$_2$Li(THF)$_2$]·*n*THF [Ln = La (**1**), Nd (**2**) *n* = 2; Sm (**3**), Yb (**4**), Y (**5**) *n* = 3] could be prepared in high yields by the metathesis reaction of LnCl$_3$ with lithium guanidinate and *n*BuLi in a 1:2:2 molar ratio, and these chlorides could be used as precursors for the syn-thesis of the corresponding isopropoxide [{[(*i*PrN)$_2$-CN(C$_6$H$_4$*p*-Cl)Li]$_2$(DME)(LiCl)Ln(O*i*Pr)$_2$}$_2$]$^{2-}$-[{Li-(DME)$_3$}$^+$]$_2$·3C$_6$H$_{14}$ [Ln = Nd (**6**), Sm (**7**), Yb (**8**), Y (**9**)] and *tert*-butoxide [{(*i*PrN)$_2$C(NC$_6$H$_4$*p*-Cl)Li(DME)-(LiCl)}$_2$Ln(O*t*Bu)$_2$]$^-$[Li(DME)$_3$]$^+$·0.5C$_6$H$_{14}$ [Ln = Nd (**10**), Yb (**11**)] complexes. However, attempts to synthesize the corresponding amide complex [(NHC$_6$H$_5$)Nd{µ-η^2,η^1(N*i*Pr)$_2$CNLi(C$_6$H$_4$*p*-Cl)}$_2$] and guanidinate complex [{(NH*i*Pr)*i*PrNCN(C$_6$H$_4$*p*-Cl)}Nd{µ-η^2,η^1(N*i*Pr)$_2$CNLi-(C$_6$H$_4$*p*-Cl)}$_2$] by the reaction of **2** with LiNHC$_6$H$_5$ and [Li-*i*PrNC(HN*i*Pr)N(C$_6$H$_5$)], respectively, were not successful, and the same guanidinate lithium [Li*i*PrNC(HN*i*Pr)-N(C$_6$H$_4$*p*-Cl)] (**12**) was isolated for both reactions. An ad-dition of diisopropylcarbodiimide (*i*PrN=C=N*i*Pr) into the reaction system of trisguanidinate lanthanide complex [Yb{*i*PrNC(HN*i*Pr)N(C$_6$H$_4$*p*-Cl)}$_3$] and *n*BuLi led to the preparation of a heterometallic Yb–Li complex with a novel biguanidinate ligand [{*i*PrNHC(N*i*Pr)N(C$_6$H$_4$*p*-Cl)}$_2$Ln-{(*i*PrNC(N*i*Pr)$_2$)N(C$_6$H$_4$*p*-Cl)C(*i*PrN)}Li(THF)]·THF (**13**) and prevented the formation of **12**. Herein we report the results.

Results and Discussion

Synthesis and Molecular Structure of [{(*i*PrN)$_2$C[NLi-(THF)$_3$(C$_6$H$_4$*p*-Cl)]}$_2$Ln(µ-Cl)$_2$Li(THF)$_2$]·*n*THF [Ln = La (1), Nd (2) *n* = 2; Sm (3), Yb (4), Y (5) *n* = 3]

The synthesis of the heterometallic dianionic guanidinate chloride of lanthanide and lithium complexes was at-tempted by use of [(NC$_6$H$_4$*p*-Cl)C(N*i*Pr)$_2$]$^{2-}$ as a dianionic guanidinate ligand, due to the fact that complexes with this ligand showed higher activity than those with phenyl guani-diante.[9a] Treatment of anhydrous LaCl$_3$ with two equiva-lents of [Li$_2$(NC$_6$H$_4$*p*-Cl)C(N*i*Pr)$_2$], which was formed in situ by treatment of [LiHN(C$_6$H$_4$*p*-Cl)] with diisopropylcar-bodiimide (*i*PrN=C=N*i*Pr) in THF, and *n*BuLi at a 1:1:1 molar ratio afforded a clear colorless solution. Removal of the THF solvent, washing the residues with cold hexane, and crystallization from a mixture of THF and hexane solu-tions at 0 °C gave the product as colorless crystals in 85 % yield. Full characterization of the crystals including an X-ray crystallography analysis indicated that the crystals were anionic heterometallic chlorides [{(*i*PrN)$_2$C[NLi(THF)$_3$-(C$_6$H$_4$*p*-Cl)]}$_2$La(µ-Cl)$_2$Li(THF)$_2$]·2THF (**1**) (Scheme 1). The formation of **1** indicates that both the La–Cl and the Li–N active species in **1** coexist and no further metathesis reaction between them could occur. By this procedure, the analogous complexes with other lanthanide metals [{(*i*PrN)$_2$-C[NLi(THF)$_3$(C$_6$H$_4$*p*-Cl)]}$_2$Ln(µ-Cl)$_2$Li(THF)$_2$] [Ln = Nd (**2**), Sm (**3**), Yb (**4**), Y(**5**)] were also synthesized in good yields (Scheme 1). However, an attempt to synthesize either neutral or anionic bis(chloride) complexes [(*i*PrN)$_2$CNLi-(THF)$_3$(C$_6$H$_4$*p*-Cl)LnCl$_2$] and/or [(*i*PrN)$_2$CNLi(THF)$_3$-
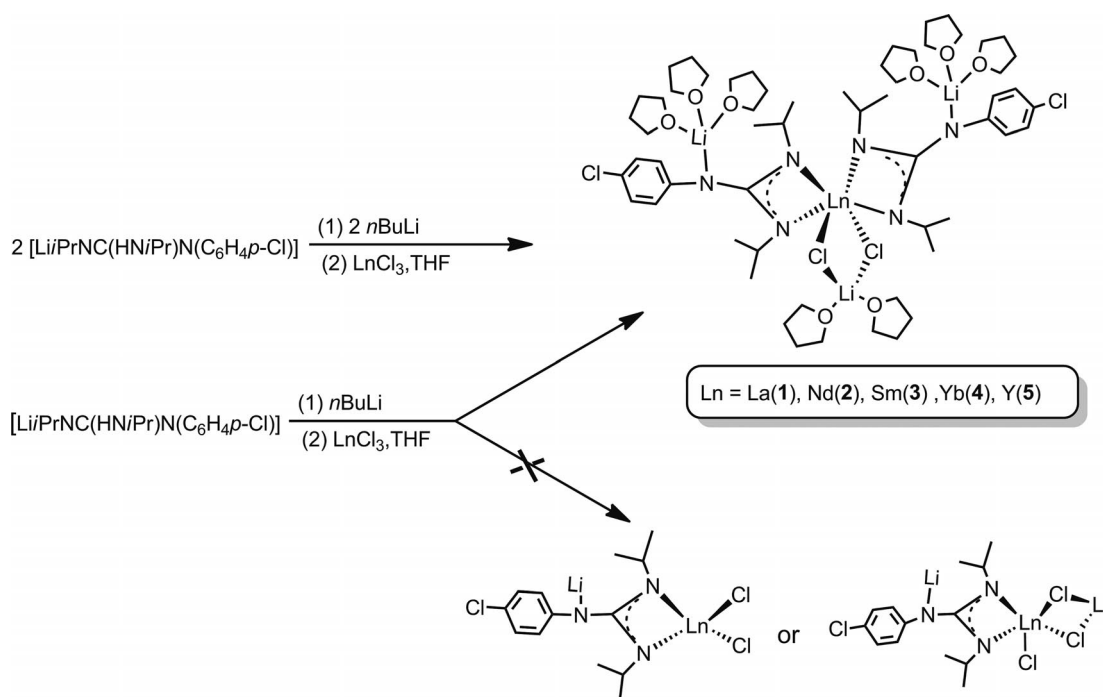
Scheme 1. Synthesis of complexes **1**–**5**.

$(C_6H_4p\text{-}Cl)LnCl_2(LiCl)(THF)_2]$ by changing the molar ratio of the reactants failed; only the anionic monochloride complexes were isolated in a rather low yield (Scheme 1).

The empirical formula of **1–5** was confirmed by elemental analysis, infrared (IR) spectroscopy, and NMR spectroscopy for **1** and **5**. The N=C=N stretch of the parent carbodiimide (2117 cm^{-1}) disappeared, whereas a C=N stretch at approximately 1630 cm^{-1} is observed in the IR spectra of each complex, thereby suggesting that the π electrons within the double bonds of the N–C–N linkage are delocalized. The ^{1}H and ^{13}C NMR spectra of the diamagnetic complexes **1** and **5** in C_4D_8O at 25 °C showed the expected sets of resonances of the dianionic guanidinate moiety. X-ray structural determination of **1–3** demonstrated that they are the "ate" complexes [{(iPrN)$_2$C[NLi(THF)$_3$-(C_6H_4p-Cl)]}$_2$Ln(μ-Cl$_2$)Li(THF)$_2$].

Complexes **1** and **2** crystallize in the monoclinic space group $P2_1c$ with four molecules in the unit cell, whereas complex **3** crystallizes in the orthorhombic space group $Pba2$ with two molecules in the unit cell. The molecular structures of **1–3** are shown in Figure 1; they are quite similar. The selected bond lengths and angles are listed in Table 1. As shown in Figure 1, **1** and **2** have a monomeric structure and possess two asymmetrical chlorido bridges. There are two THF molecules in the unit cell of **1** and **2**, whereas there are three THF molecules in that of **3**. The coordination sphere around each central metal is composed of four nitrogen atoms from the two dianionic guanidinate ligands and two bridged chloro atoms to form a distorted octahedron. The {(iPrN)$_2$C[NLi(THF)$_3$(C_6H_4p-Cl)]}$_2$Ln moiety is bonded through two chlorido bridges to a lithium cation (Li3), which in turn is bonded to two oxygen atoms of two THF molecules. The third nitrogen atom of each guanidinate (N3, N6) lies outside of the coordination sphere of the lanthanide metal and bonds to one lithium

ion (Li1, Li2). The coordination geometry around each Li ion (Li1 and Li2) is a tetrahedon by one nitrogen atom and the additional three oxygen atoms from the three THF molecules. The coordinated dianionic guanidinate groups and the lanthanide atoms form essentially four-membered planes with the sum of the angles 359.9(8)° for Nd [N1–Nd1–N2, 54.8(3)°; C1–N1–Nd1, 97.2(3)°; C1–N2–Nd1, 95.9(7)°; N1–C1–N2, 111.9(5)°], 359.8(6)° for La [N1–La1–N2, 53.6(1)°; C1–N1–La1, 97.3(9)°; C1–N2–La1, 95.5(8)°; N1–C1–N2, 113.2(8)°], and 359.9(4)° for Sm [N1–Sm1–N2,

Table 1. Selected bond lengths [Å] and angles [°] for complexes **1**–**3**.

|	**1**	**2**	**3**
Bond lengths			
Ln1–Cl3	2.871(2)	2.818(3)	2.770(3)
Ln1–Cl4	2.883(2)	2.833(4)	2.770(3)
Ln1–N1	2.466(4)	2.402(8)	2.408(7)
Ln1–N2	2.500(4)	2.441(7)	2.353(7)
Ln1–N4	2.453(4)	2.390(7)	2.408(7)
Ln1–N5	2.514(4)	2.438(8)	2.353(7)
N1–C1	1.336(6)	1.354(1)	1.339(1)
N2–C1	1.346(6)	1.335(1)	1.348(9)
N3–C1	1.406(6)	1.395(1)	1.391(1)
N6–C26	1.393(6)	1.393(1)	1.391(1)
N3–Li1	1.983(1)	2.00(2)	1.990(1)
N6–Li2	1.993(9)	2.00(2)	1.990(1)
Bond angles			
Cl3–Ln1–Cl4	78.73(6)	79.8(1)	81.1(9)
N1–Ln1–N2	53.6(1)	54.8(3)	55.8(2)
N4–Ln1–N5	53.9(1)	54.8(3)	55.8(2)
N4–Ln1–N1	103.1(1)	103.2(3)	106.0(2)
N1–Ln1–N5	104.1(1)	105.0(3)	106.0(2)
C1–Ln1–C26	119.8(1)	120.6(3)	120.7(2)
Cl3–Li3–Cl4	102.1(9)	101.7(1)	100.1(1)
N2–C1–N1	113.3(4)	112.0(8)	112.0(7)
N4–C26–N5	113.0(4)	110.9(8)	112.0(7)
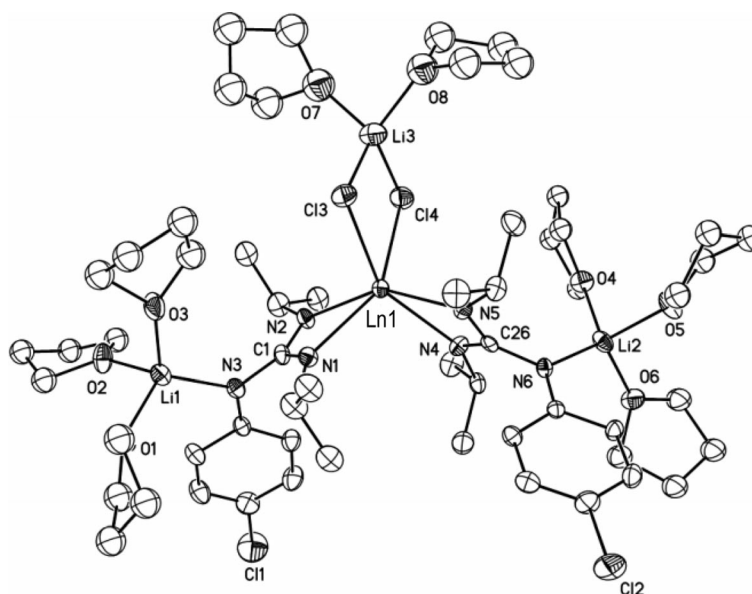
Figure 1. ORTEP diagram of the molecular structures of complexes **1–3** [Ln = La (**1**), Nd (**2**), Sm (**3**)]. Thermal ellipsoids are drawn at the 30% probability level and hydrogen atoms are omitted for clarity.

55.7(6)°; C1–N1–Sm1, 94.9(3)°; C1–N2–Sm1, 97.1(8)°; N1–C1–N2, 112.0(7)°]. The bond angles of N1–Ln1–N2 and N4–Ln1–N5 are equal to 54.8(4)° for Nd, 53.7(0)° for La, and 55.7(6)° for Sm, which are similar to those found in the monoanionic guanidinate complexes reported.[10] The average distances of Li–N in **1**–**3** [1.987(5) Å for **1**, 2.000(2) Å for **2**, and 1.990(1) Å for **3**] are consistent with those found in lithium amides[11] but somewhat shorter than those in lithium guanidinate.[12] The average bond lengths of Ln–Cl are 2.877(2) Å for **1**, 2.825(8) Å for **2**, and 2.770(4) Å for **3**, which are comparable to those in [{(SiMe$_3$)$_2$NC(NiPr)$_2$}$_2$Ln(μ-Cl)$_2$Li(THF)$_2$] (Ln = Yb [2.619(1) Å] and Nd [2.840(7) Å] when the different ionic radii were considered.[2a,3d,13,14]

Synthesis and Molecular Structure of [{[(iPrN)$_2$CN-(C$_6$H$_4$$p$-Cl)Li]$_2$(DME)(LiCl)Ln(O$i$Pr)$_2$}$_2$]$^{2-}$[{Li(DME)$_3$}$^+$]$_2$· 3C$_6H_{14}$ [Ln = Nd (6), Sm (7), Yb (8), Y (9)]

To see whether this kind of chloride could be used as the precursors as the monoanionic guanidinate lanthanide chlorides,[2,3,13] the reaction of **2** with NaOiPr (1 equiv.) was tried. The reaction went smoothly, after workup, to afford the product as light blue crystals in a rather low yield (23%). Elemental analysis, IR spectra, and an X-ray single-crystal structure analysis demonstrated the crystals to be an ion-pair complex [{[(iPrN)$_2$CN(C$_6$H$_4$$p$-Cl)Li]$_2$(DME)-(LiCl)Nd(O$i$Pr)$_2$}$_2$]$^{2-}$[{Li(DME)$_3$}$^+$]$_2$·3C$_6H_{14}$ (**6**). The existence of the cations Li, not the cations Na, should be attributed to the substitution of the Na$^+$ by the Li$^+$, which is often observed in the preparation of anionic organolanthanide complexes.[16] The yield of complex **6** can be improved to 58% by increasing the amount of NaOiPr (to

2 equiv.) and an addition of LiCl (2 equiv.). The analogous complexes **7**–**9** could also be prepared as crystals by the reactions of the corresponding complexes **3**–**5** with NaOiPr [Scheme 2, Equation (1)].

Complexes **6**–**9** were characterized by elemental analysis, IR spectroscopy, and ^{1}H and ^{13}C NMR spectroscopy for **9**. The ^{1}H and ^{13}C NMR spectra of **9** in C$_6$D$_6$ at 25 °C show the expected sets of resonances for the dianioinc guanidinate ligands and the isopropoxide groups. Complexes **7**–**9** crystallized as three hexane-solvated crystals, which was further confirmed by X-ray single-crystal structural determinations.

Complexes **6**–**9** are sensitive to air and moisture and soluble in THF, DME, and slightly soluble in n-hexane. The molecular structures of **6**–**9** are shown in Figure 2; they are isostructural. Selected bond lengths and angles are given in Table 2.

As shown in Figure 2, each of them is composed of a discrete dianion [{[(iPrN)$_2$CN(C$_6$H$_4$$p$-Cl)Li]$_2$(DME)(LiCl)-Ln(O$i$Pr)$_2$}$_2$]$^{2-}$ and two cations [Li(DME)$_3$$^+$]$_2$. In the anion, two units of {[(iPrN)$_2$CN(C$_6$H$_4$$p$-Cl)Li]$_2$(DME)(LiCl)-Ln(O$i$Pr)$_2$} are connected by two bridged OiPr groups and two bridged nitrogen atoms from one of the dianionic guanidinate groups of each unit. There are three hexane molecules in the unit cell. The anion can be roughly viewed as a tricyclic structure.

Each central Ln atom in the dianion coordinates to four nitrogen atoms from the two dianionic guandinate ligands and two oxygen atoms from OiPr groups to adopt a distorted octahedral geometry. Each four-membered ring Ln–N–C–N is almost a plane. The Ln–N bond lengths vary from 2.420(7) to 2.589(8) Å for **6**, 2.398(5) to 2.529(5) Å for **7**, 2.305(5) to 2.424(6) Å for **8**, and 2.350(5) to 2.467(5) Å
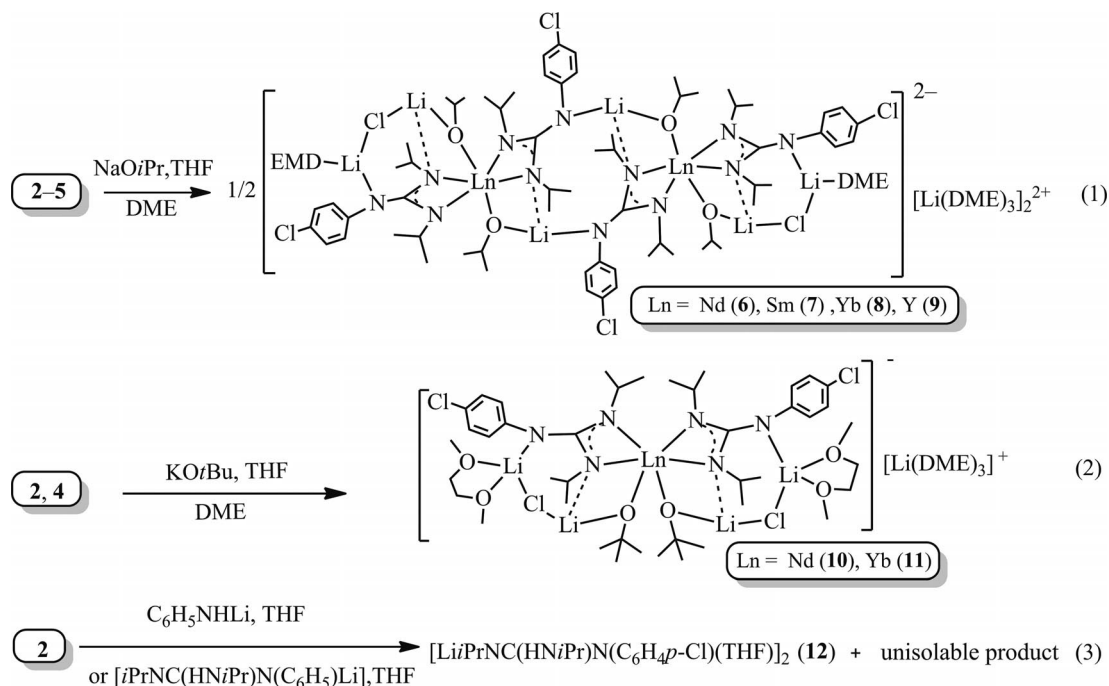
Scheme 2. Synthesis of complexes **6**–**12**.

Figure 2. ORTEP diagram of the structures of the anionic part in complexes **6–9** [Ln = Nd (**6**), Sm (**7**), Yb (**8**), Y (**9**)]. Thermal ellipsoids are drawn at the 30% probability level and hydrogen atoms are omitted for clarity.

Table 2. Selected bond lengths [Å] and angles [°] for complexes **6–9**.

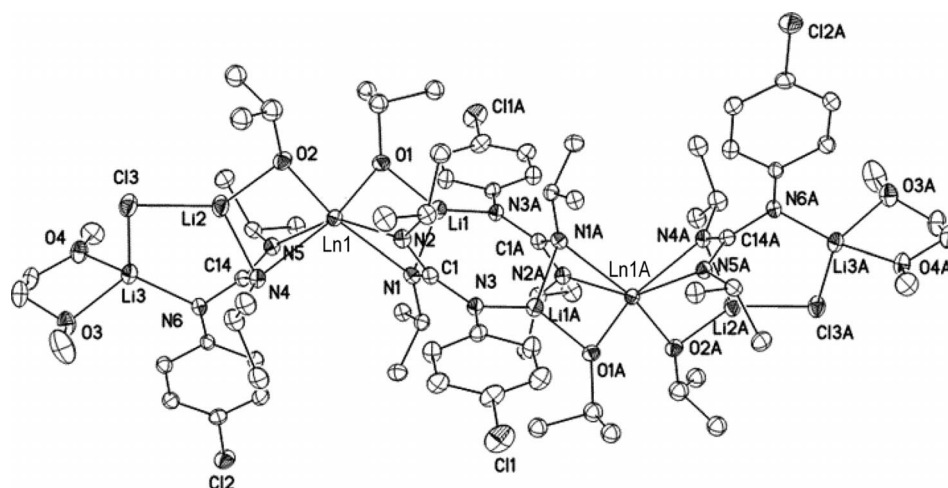|	**6**	**7**	**8**	**9**
Bond lengths				
Ln1–O1	2.256(7)	2.226(4)	2.163(5)	2.163(5)
Ln1–O2	2.255(6)	2.237(5)	2.144(6)	2.178(5)
Ln1–N1	2.589(8)	2.529(5)	2.415(6)	2.457(6)
Ln1–N2	2.420(7)	2.398(5)	2.305(5)	2.350(5)
Ln1–N4	2.564(6)	2.523(5)	2.424(6)	2.467(5)
Ln1–N5	2.489(6)	2.451(5)	2.348(6)	2.389(6)
N1–C1	1.375(1)	1.381(7)	1.364(8)	1.359(8)
N2–C1	1.363(1)	1.360(9)	1.361(7)	1.368(9)
N3–C1	1.391(1)	1.374(7)	1.379(8)	1.382(8)
N6–C14	1.364(1)	1.378(7)	1.389(9)	1.394(8)
N1–Li1	2.084(1)	2.085(1)	2.091(1)	2.085(1)
N4–Li2	2.040(2)	2.050(1)	2.061(1)	2.044(1)
N6–Li3	1.991(2)	1.987(1)	1.987(1)	1.986(1)
Bond angles				
O1–Ln1–O2	106.3(3)	105.2(2)	99.6(2)	100.3(2)
O1–Ln1–N2	96.0(2)	95.6(2)	97.2(2)	96.8(2)
O2–Ln1–N2	102.4(3)	102.2(2)	101.2(2)	101.4(2)
O1–Ln1–N5	100.2(2)	100.8(2)	101.1(2)	101.4(2)
N2–Ln1–N5	150.3(3)	150.8(2)	150.5(2)	150.0(2)
O1–Ln1–N1	79.0(2)	79.4(1)	81.8(2)	81.4(2)
O2–Ln1–N1	156.4(2)	156.9(2)	158.1(2)	157.3(2)
N2–Ln1–N1	54.0(2)	54.8(1)	57.0(2)	56.1(2)
N5–Ln1–N1	105.0(2)	104.7(2)	102.9(2)	103.6(2)
O1–Ln1–N4	153.0(2)	154.2 (2)	156.9(2)	156.2(2)
O2–Ln1–N4	78.3(2)	78.4(2)	81.0(2)	80.5(2)
N2–Ln1–N4	109.2(2)	108.7(1)	105.4(2)	106.4(2)
N5–Ln1–N4	52.9(2)	53.6(1)	105.4(2)	54.8(2)
N1–Ln1–N4	107.7(2)	107.5(2)	106.2(2)	107.1(2)
N1–C1–N2	112.7(7)	111.8(5)	117.7(6)	112.1(5)
N5–C14–N4	113.1(6)	112.6(5)	112.9(7)	112.9(6)

for **9**, and the average distances [2.5161(7) Å for **6**, 2.475(7) Å for **7**, 2.373(5) Å for **8** and 2.416(3) Å for **9**] are almost consistent when the differences in ion radii among them are considered.[14] The values can also be compared with those reported for analogues.[10] The C–N bond lengths in the dianionic guanidinate ligands differ only slightly from each other [1.363(1)–1.381(7) Å for **6**,

1.360(9)–1.389(9) Å for **7**, 1.361(7)–1.389(9) Å for **8**, and 1.359(8)–1.394(8) Å for **9**], thereby reflecting electron delocalization within the NCN units. The average Ln–O bond length for each complex is longer than those found for the terminal Ln–O distances.[5a,5b]

Primary results demonstrated that **6–9** can serve as efficient initiators for the ring-opening polymerization of ε-caprolactone (ε-CL) at 20 °C with the active sequence of **9** < **8** < **7** < **6**, which is often observed in various lanthanide initiator systems. All the systems gave the polymers with a monomodal molecular-weight distribution and the rather narrow molecular-weight distribution index. Taking **7** as an example, the polymerization of ε-CL at a molar ratio of ε-CL/**7** of 3000 in toluene at 20 °C gave the polymer in a quantitative yield after 2 h. The M_n and M_w/M_n (molecular-weight distribution index) of the resulting polymer are 22.71×10^4 and 1.59, respectively.

Synthesis and Molecular Structures of [{(*i*PrN)$_2$C(NC$_6$H$_4$*p*-Cl)Li(DME)(LiCl)}$_2$Ln(O*t*Bu)$_2$]⁻[Li(DME)$_3$]⁺·0.5C$_6$H$_{14}$ [Ln = Nd (10) and Yb (11)]

The success in the synthesis of the isopropoxide complexes encouraged us to expand to the synthesis of *tert*-butoxide complexes. Treatment of complex **2** with KO*t*Bu (1 equiv.) in THF at 25 °C led to a blue solution from which light blue crystals were isolated in 17% yield by crystallization from a mixture of DME and hexane. The crystals were characterized by an X-ray crystal structure analysis to be an ion-pair *tert*-butoxide complex of Nd/Li supported by dianionic guanidinate ligands [{(*i*PrN)$_2$C(NC$_6$H$_4$*p*-Cl)-Li(DME)(LiCl)}$_2$Nd(O*t*Bu)$_2$]⁻[Li(DME)$_3$]⁺·0.5C$_6$H$_{14}$ (**10**). Clearly the shortage of KO*t*Bu and LiCl led to the low yield. Indeed, increasing the amount of KO*t*Bu to two equivalents and an addition of LiCl (2 equiv.) resulted in an increase of the yield to 48%. The lower yield than that of complex **6** may be attributed to the better solubility of **10** than that of **6**. The analogous Yb complex **11** was also pre-

pared by the reaction of **4** with KO*t*Bu (2 equiv.) and LiCl (2 equiv.) in THF at 25 °C [Scheme 2, Equation (2)]. Attempts to synthesize a neutral heterometallic *tert*-butoxide of Ln/Li have not been successful. This may be because of the existence of oxophilic Li metals in these molecules.

Complexes **10** and **11** are soluble in THF and DME, and sparingly soluble in *n*-hexane. Complexes **10** and **11** are isostructural and their molecular structures are shown in Figure 3. Selected bond lengths and angles are given in Table 3. Both of them are composed of a discrete anion [{(*i*PrN)$_2$-C(NC$_6$H$_4$*p*-Cl)Li(DME)(LiCl)}$_2$Ln(O*t*Bu)$_2$]$^-$ and a cation [Li(DME)$_3$]$^+$. There are 0.5 hexane molecules in the unit cell. The anion can be roughly viewed as a bicyclic structure (Ln1, N1, N3, Li2, Cl2, Li1, O1; and Ln1, N4, N6, Li4, Cl4, Li3, O2 rings).

The coordination sphere around each Ln center is completed by four nitrogen atoms from the two dianionic guanidinate ligands and two oxygen atoms of the O*t*Bu group to form a distorted octahedron. The O2 from the O*t*Bu group and N1 from one of the dianionic guanidinate ligands occupy the axial positions. The O2–Ln–N1 angles are 161.5(2)° for **10** and 161.8(4)° for **11**, which deviate greatly from linearity. The N2, N4, N5, O1, and Ln occupy the equatorial sites. The sum of the angles around the Ln atoms deviates slightly from the idealized 360° (about 3° for **10** and 2° for **11**). The average bond lengths of Ln–O in **10** [2.257(6) Å] and **11** [2.137(5) Å] are approximately consistent when the difference in ionic radii between Nd and Yb was considered.[14] All the C–N distances within the chelating dianioinc guanidinate ligands are approximately equal
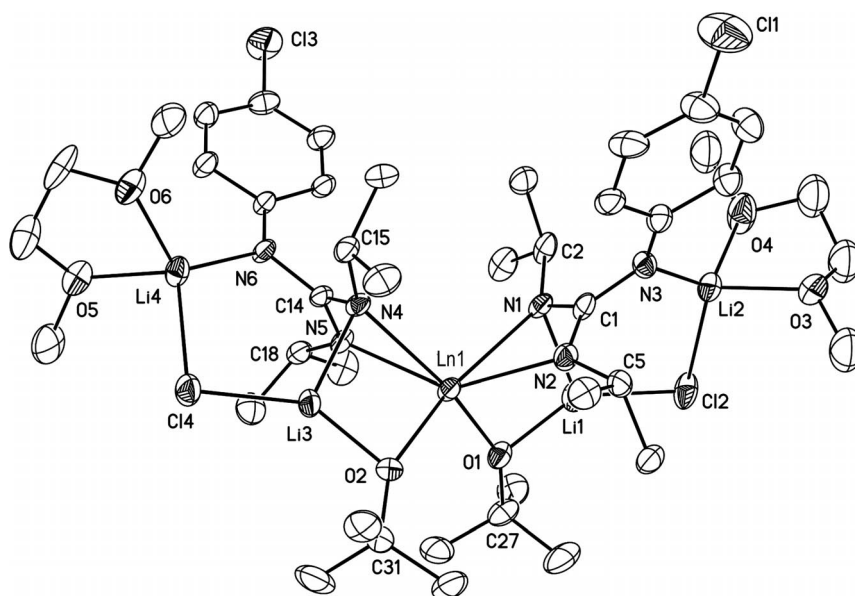
Figure 3. ORTEP diagram of the structures of anionic part of complexes **10** and **11** [Ln = Nd (**10**), Yb (**11**)]. Thermal ellipsoids are drawn at the 30% probability level and hydrogen atoms are omitted for clarity.

Table 3. Selected bond lengths [Å] and angles [°] for complexes **10** and **11**.

	10	**11**		**10**	**11**
Bond lengths			Bond angles		
Ln1–O1	2.264(6)	2.136(8)	O1–Ln1–O2	104.7(2)	101.8(3)
Ln1–O2	2.251(7)	2.126(7)	O1–Ln1–N2	93.6(3)	96.7(3)
Ln1–N1	2.555(8)	2.399(1)	O2–Ln1–N2	108.4(2)	105.4(4)
Ln1–N2	2.481(8)	2.337(1)	O2–Ln1–N5	93.9(3)	96.7(3)
Ln1–N4	2.559(6)	2.400(1)	O1–Ln1–N5	107.9(2)	105.3(3)
Ln1–N5	2.478(7)	2.365(1)	N2–Ln1–N5	144.0(3)	144.7(3)
N1–C1	1.372(1)	1.367(2)	O2–Ln1–N1	161.5(2)	161.8(4)
N2–C1	1.338(1)	1.354(2)	O1–Ln1–N1	79.5(2)	82.1(3)
N3–C1	1.378(1)	1.391(1)	N2–Ln1–N1	53.1(3)	56.3(4)
N6–C14	1.388(1)	1.426(1)	N5–Ln1–N1	102.0(3)	99.4(3)
N1–Li1	2.08(2)	2.070(3)	O2–Ln1–N4	79.2(2)	81.1(3)
N3–Li2	1.964(2)	1.931(3)	O1–Ln1–N4	160.9(2)	161.7(3)
N4–Li3	2.047(2)	1.98(2)	N2–Ln1–N4	103.0(3)	99.9(3)
N6–Li4	2.020(2)	2.02(2)	N5–Ln1–N4	53.0(2)	56.4(4)
			N1–Ln1–N4	102.9(2)	100.8(3)
			C1–N1–C2	118.2(9)	116.7(1)
			N4–C14–N5	112.2(7)	112.3(1)

and shorter than a C–N single bond length, thereby indicating that the π electrons are delocalized within the N–C–N fragment. The dihedral angles of two dianionic guandinate Ln(NCN) planes [77.9(1)°] in **10** are comparable to the corresponding value in **11**. These values can also be compared to those in complexes **6–9**.

Complexes **10** and **11** are also efficient initiators for polymerization of ε-CL. The catalytic behavior of them is similar to that of **6–9**.

Reactions of 2 with LiNHC$_6$H$_5$ and [LiiPrNC(HNiPr)-N(C$_6$H$_5$)] to Monoanionic Guanidinate Lithium [LiiPrNC(HNiPr)N(C$_6$H$_4$p-Cl)(THF)]$_2$ (12)

To synthesize the corresponding lanthanide amide complexes, the reaction of **2** with LiNHC$_6$H$_5$ was conducted in THF at 60 °C for 2 d. The blue of the reaction solution changed immediately to dark brown when a solution of LiNHC$_6$H$_5$ in THF was added into the solution of **2**. Removing the solvent by vacuum and extracting with hot toluene to remove the LiCl by centrifugation led to a dark brown solution. It was unexpected that monoanionic guanidinate lithium [LiiPrNC(HNiPr)N(C$_6$H$_4$p-Cl)(THF)]$_2$ (**12**), not the expected amide complex [(NHC$_6$H$_5$)Nd{μ-η^2,η^1(NiPr)$_2$CNLi(p-ClC$_6$H$_4$)}$_2$], was isolated in almost quantitative yield on the basis of the LiNHC$_6$H$_5$ used. Complex **12** was fully characterized including an X-ray crystal structure analysis. Isolation of the other product from the residue was not successful [Scheme 2, Equation (3)].

Similarly, the reaction of **2** with N,N′,N″-trisubstituted guanidinate lithium [LiiPrNC(HNiPr)N(C$_6$H$_5$)] did not afford the corresponding guanidinate complex [{iPrNHC-

(NiPr)(NC$_6$H$_5$)}Nd{μ-η^2,η^1(NiPr)$_2$CNLi(p-ClC$_6$H$_4$)}$_2$] either, but **12** was obtained in addition to a product that could not be isolated [Scheme 2, Equation (3)].

The formation of LiCl from both reaction systems indicates that both metathesis reactions do occur. The isolation of **12** for both cases demonstrates that the complexes with the Ln-active species that contain a hydrogen group might not be stabilized by the dianionic guanidinate ligand, and **12** may by formed either by de-guanidinated Li from the dianionic guanidinate species or by a simple ligand-substitution reaction.

Synthesis and Molecular Structure of Heterometallic Yb–Li Biguanidinate Complex [{iPrNHC(NiPr)N(C$_6$H$_4$p-Cl)}$_2$Yb{(iPrNC(NiPr)$_2$)N(C$_6$H$_4$p-Cl)C(iPrN)}Li(THF)]·THF (13)

The reaction of [{iPrNHC(NiPr)(NC$_6$H$_4$p-Cl)}$_3$Yb-(THF)], which was formed in situ by treatment of YbCl$_3$ with **12** (3 equiv.), and nBuLi (1 equiv.) was conducted to see whether the target complex [{iPrNHC(NiPr)N(C$_6$H$_4$p-Cl)}$_2$Yb{μ-η^2,η^1(NiPr)$_2$CNLi(C$_6$H$_4$p-Cl)}] (**A**) could also not be stabilized like the cases mentioned in Scheme 2, Equation (3). Indeed, **12** was prepared as the only isolable product; no target complex was obtained from the reaction solution. However, the addition of iPrN=C=NiPr into the above reaction solution led to a novel complex with a newly formed biguanidinate ligand [{iPrNHC(NiPr)N(C$_6$H$_4$p-Cl)}$_2$Yb{(iPrNC(NiPr)$_2$)N(C$_6$H$_4$p-Cl)C(iPrN)}Li(THF)]·THF (**13**) in 80% yield. Obviously, **13** could be prepared either by treatment of iPrN=C=NiPr with the dianionic guanidinate species of **A**, or by the reaction of bis(guanidinate) chloride complex [{iPrNHC(NiPr)N(C$_6$H$_4$p-
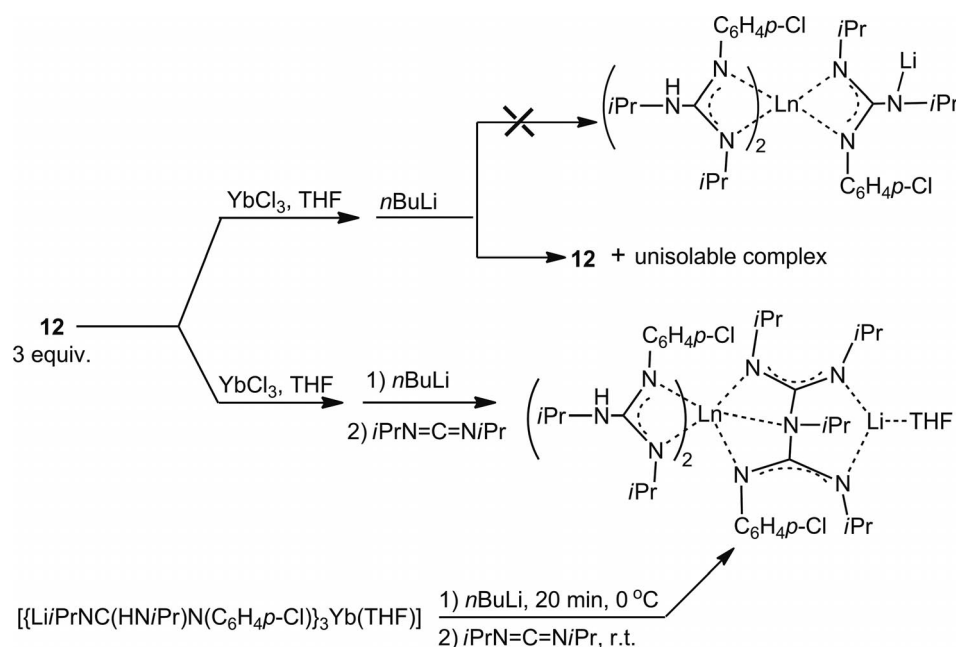
Scheme 3.
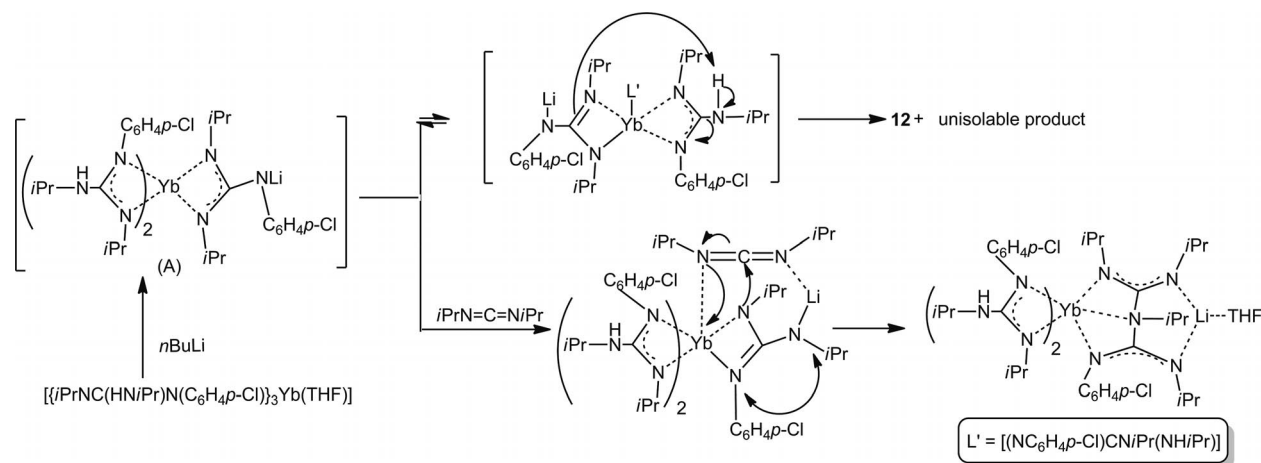
Scheme 4.

Cl)}$_2$Yb(μ-Cl)$_2$Li(THF)$_2$], which was formed in situ by treating YbCl$_3$ with **12** (2 equiv.), with biguanidinate lithium formed in situ by the reaction of **12** with *n*BuLi and *i*PrN=C=N*i*Pr, if the above reaction of YbCl$_3$ with **12** (3 equiv.) did not proceed completely and the undesired [{*i*PrNHC(N*i*Pr)N(C$_6$H$_4$*p*-Cl)}$_2$Yb(μ-Cl)$_2$Li(THF)$_2$] was formed. To further confirm the mechanism for the formation of **13**, the reaction with purified trisguanidinate Yb complex [{*i*PrNHC(N*i*Pr)(NC$_6$H$_4$*p*-Cl)}$_3$Yb(THF)],[9] instead of the one formed in situ, was conducted again. After workup, the same complex **13** was isolated in almost same yield (86%) (Scheme 3).

Thus, complex **13** was prepared unequivocally by the addition of *i*PrN=C=N*i*Pr to the dianionic guanidinate species of **A** through a cooperation of both Yb and Li metals, followed by the inversion of the guanidinate group owing to steric demand (Scheme 4). The formation of **12** might be attributable to the instability of the mono(dianionic guanidinate) lanthanide complex as shown in Scheme 4.

The molecular structure of **12**, which is quite similar to published guanidinate lithium complexes,[12] is shown in Figure 4 with the main bond parameters.

Single crystals of complex **13** were grown from a toluene solution at 0 °C. The molecular structure of **13** is shown in Figure 5. The selective bond lengths and angles are listed in Table 4. As shown in Figure 5, the Yb ion is seven-coordinate by four nitrogen atoms from two guanidinate ligands (N6, N7, N9, and N10) and three nitrogen atoms of the biguanidinate ligand (N1, N2, and N4). The coordination polyhedron around the Yb ion can be described as a distorted trigonal bipyramid with each chelating bidentate monoguanidinate ligand occupying one coordination vertex, in which the C25, N4, and N1 atoms lie at the equatorial positions, whereas the C38 and N2 sites are at the axial positions. The C38–Yb1–N2 angle deviates greatly from the idealized 180° to 151.34(7)°. The coordination geometry around the Li ion is trigonal by the two N atoms of the biguanidinate ligand and one O atom from a THF molecule. The sum of the angles around the Li ion is 359.20(4)°,
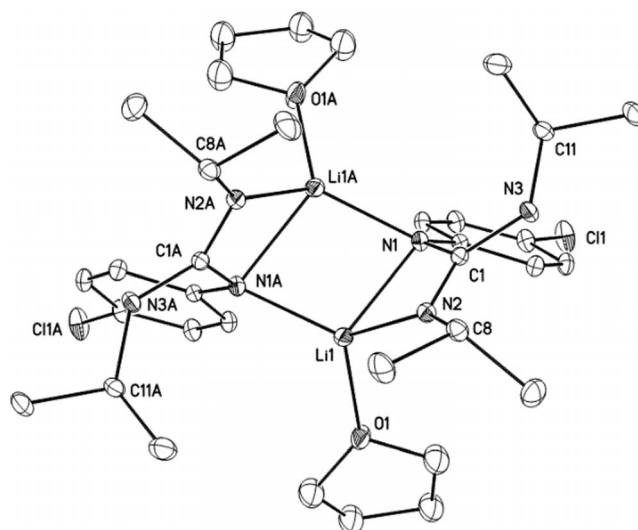
Figure 4. ORTEP diagram of the molecular structure of complex [Li(*i*PrNC(HN*i*Pr)N(C$_6$H$_4$*p*-Cl)(THF)]$_2$ (**12**). Thermal ellipsoids are drawn at the 30% probability level and hydrogen atoms are omitted for clarity. Selected bond lengths [Å] and angles [°] for complex **12**: O1–Li1 1.943(6), N1–Li1 2.147(7), N2–Li1 2.031(7), C1–Li1 2.466(7), N1–C1 1.393(4), N1–C2 1.378(4), N3–C1 1.375(4); C2–N1–C1 119.9(3), C2–N1–C1 119.9(3), C2–N1–Li1 121.2(3), C1–N1–Li1 85.5(2).

as the distance between Li1 and N2 atoms [2.807(1) Å] is far from the length of a donating bond.

The most striking feature of the molecular structure of **13** is that the biguanidinate ligand binds to both metals of Yb and Li to form a bicyclic unit that is formed by two six-membered rings of Yb1, N1, C1, N2, C14, N4 (ring 1) and Li1, N3, C1, N2, C14, N5 (ring 2). Both of the six-membered rings adopt a boat conformation; the two atoms of Yb1 and N2 for ring 1 and Li1 and N2 for ring 2 are situated in the two top positions. The four atoms at the bottom positions of each boat (N1, C1, C14, and N4; N3, C1, C14, and N5) are nearly coplanar with the sum of the angles being 358.1(8) and 357.0(5)°, respectively. The dihedral an-

Figure 5. ORTEP diagram of the molecular structure of complex **13**. Hydrogen atoms are omitted for clarity, and thermal ellipsoids are drawn at the 30% probability level.

Table 4. Selected bond lengths [Å] and angles [°] for complexes **13**.

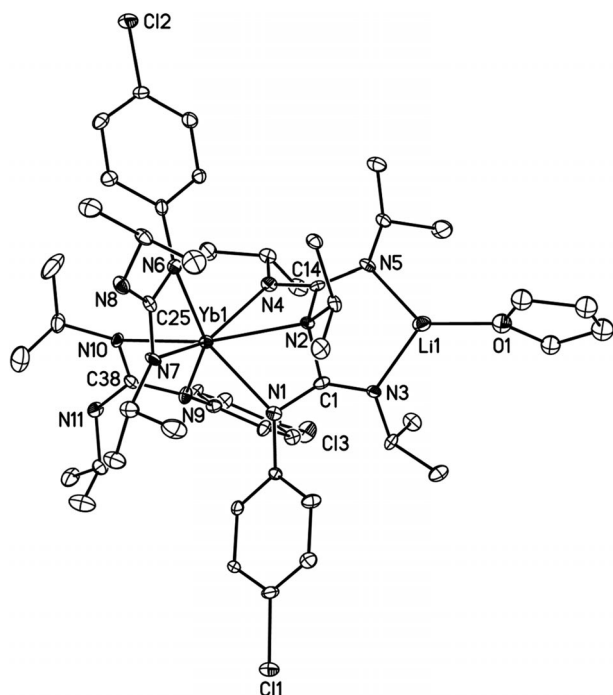|			
Yb1–N4	2.322(9)	N2–C1	1.492(11)
Yb1–N7	2.352(9)	N3–C1	1.296(13)
Yb1–N1	2.365(9)	N3–Li1	1.97(2)
Yb1–N9	2.370(9)	N4–C14	1.335(13)
Yb1–N6	2.400(8)	N5–C14	1.302(13)
Yb1–N10	2.432(8)	N5–Li1	1.95(2)
Yb1–N2	2.530(8)	N6–C25	1.365(13)
Yb1–C38	2.816(11)	N7–C25	1.322(13)
Yb1–C25	2.844(11)	N8–C25	1.377(13)
Yb1–C1	2.919(10)	C1–Li1	2.79(3)
Yb1–C14	2.997(11)	C14–Li1	2.67(2)
N1–C1	1.334(13)	N9–C38	1.371(14)
O1–Li1	1.94(3)	N10–C38	1.305(14)
N2–C14	1.469(13)	N11–C38	1.394(13)
N4–Yb1–N1	94.4(3)	C1–Yb1–C14	48.8(3)
N7–Yb1–N6	56.0(3)	N3–C1–N1	136.7(9)
N1–Yb1–N2	55.7(3)	N3–C1–N2	115.1(10)
C1–N1–Yb1	100.5(6)	N1–C1–N2	108.1(8)
C14–N2–Yb1	93.3(6)	N10–C38–N9	115.0(10)

gle between the two boat bottom planes is 22.2(4)°. The dihedral angle between the bottom plane (N1, C1, C14, and N4) and the plane N1, Yb1, and N4 [27.1(1)°] is larger than that between the bottom plane (N3, C1, C14, and N5) and the plane of N3, Li1, and N5 [8.8(3)°].

The bond lengths of C1–N2 and C14–N2 are 1.492(1) and 1.469(1) Å, respectively, which indicate a C–N single bond. The C–N bond lengths of C1–N1 and C1–N3, and C14–N4 and C14–N5 are 1.334(2) and 1.296(2) Å, and 1.335(1) and 1.302(1) Å, respectively, thereby indicating the delocalized structure of the π electrons within each NCN group in the biguanidinate group. A similar situation was found in a biamidinate titanium complex.[15]

The average bond length of Yb–N in the two monoguanidiante ligands [2.389(3) Å] is comparable to Yb–N1 [2.364(11) Å] and Yb–N4 (2.323 Å) in the novel biguanidinate ligand, whereas the distance of Yb–N2 (2.530 Å) indicates that ytterbium ions are coordinated with the N4 atom. It is interesting that the bond lengths of Li1–N5 [1.970(2) Å] and Li1–N3 [1.950(2) Å] are consistent with each other, and the average length of 1.960(2) Å is shorter than 2.104(2) Å found in [Li(*i*PrNC(HN*i*Pr)N(C$_6$H$_4$*p*-Cl)(THF)]$_2$ (**12**) (Figure 4). The bond parameters for the two monoguanidiante ligand units are normal and can be comparable to those for the corresponding guanidinate lanthanide derivatives.[2–5]

Conclusion

The dianionic guanidinate group can be used as a "normal" ancillary ligand to stabilize heterometallic Ln–Li chlorides [{(*i*PrN)$_2$C[NLi(THF)$_3$(C$_6$H$_4$*p*-Cl)]}$_2$Ln(µ-Cl$_2$)-Li(THF)$_2$]·*n*THF [Ln = La (**1**), Nd (**2**) *n* = 2; Sm (**3**), Yb (**4**), Y (**5**), *n* = 3] and the corresponding isopropoxides [{[(*i*PrN)$_2$CN(C$_6$H$_4$*p*-Cl)Li]$_2$(DME)(LiCl)Ln(O*i*Pr)$_2$}$_2$]²⁻-[{Li(DME)$_3$}⁺]$_2$·3C$_6$H$_{14}$ [Ln = Nd (**6**), Sm (**7**), Yb (**8**), Y (**9**)] and *tert*-butoxides [{(*i*PrN)$_2$C(NC$_6$H$_4$*p*-Cl)Li-(DME)(LiCl)}$_2$Ln(O*t*Bu)$_2$]⁻[Li(DME)$_3$]⁺·0.5C$_6$H$_{14}$ [Ln = Nd (**10**), Yb (**11**)]. However, the corresponding amide complex [(NHC$_6$H$_5$)Nd{µ-η², η¹(N*i*Pr)$_2$CNLi(*p*-ClC$_6$H$_4$)}$_2$] and N,N′,N′′-trisubstituted guanidinate complex [{*i*PrNHC-(N*i*Pr)(NC$_6$H$_5$)}Nd{µ-η², η¹(N*i*Pr)$_2$CNLi(*p*-ClC$_6$H$_4$)}$_2$] could not be prepared by metathesis reactions, although guanidinate lithium was attained for both cases. A novel complex with a bisguanidinate ligand [{*i*PrNHC(N*i*Pr)N(C$_6$H$_4$*p*-Cl)}$_2$Yb{(*i*PrNC(N*i*Pr)$_2$)N(C$_6$H$_4$*p*-Cl)C(*i*PrN)}Li(THF)]·THF (**13**) was synthesized by means of an addition of *i*PrN=C=N*i*Pr to a dianionic guanidinate species, which represents the first example of a heterometallic Ln–Li biguanidinate complex by the insertion of a carbodiimide into the guanidinate–metal bond. The high reactivity of dianionic guanidinate species toward small molecules presented here indicates that the heterometallic dianionic guanidinate complexes may have a wide reaction chemistry. Work on the reactivity of heterometallic Ln–alkali-metal dianionic guanidinate derivatives toward organic molecules continues.

Experimental Section

Materials and Methods: Standard Schlenk techniques and a Vacuum Atmospheres N$_2$-filled glovebox were used throughout the isolation and handling of all metal complexes. Tetrahydrofuran, toluene, DME, and *n*-hexane were dried and distilled from sodium/benzophenone ketyl under argon prior to use. The other reagents were purchased from Acros Chemical and used as received without further purification. [{*i*PrNHC(N*i*Pr)(NC$_6$H$_4$*p*-Cl)}$_3$Yb(THF)] was prepared according to the literature method.[9] ¹H and ¹³C NMR spectra were recorded with a 300 or 400 MHz instrument and processed with MestReNova software. Elemental analyses were performed by direct combustion with a Carlo–Erba EA 1110 instru-

ment. The IR spectra were recorded with a Magna-IR 550 spectrometer as KBr pellets. Molecular weight and molecular-weight distributions were determined against a polystyrene standard by gel-permeation chromatography (GPC) with a Waters 1515 apparatus and three HR columns (HR-1, HR-2, and HR-4); THF was used as an eluent at 30 °C.

[{(*i*PrN)$_2$C[NLi(THF)$_3$(C$_6$H$_4$*p*-Cl)]}$_2$La(μ-Cl$_2$)Li(THF)$_2$]·2THF (1): A Schlenk flask was charged with *p*-ClC$_6$H$_4$NH$_2$ (1.037 g, 8.13 mmol), THF (20 mL), and a stir bar. The solution was cooled to 0 °C, and *n*BuLi (3.4 mL, 8.13 mmol, 2.40 M in hexane) was added. The solution was then slowly warmed to room temperature and stirred for 2 h. *N*,*N*′-Diisopropylcarbodiimide (1.3 mL, 8.13 mmol) was added to this solution at 0 °C, stirred for 2 h, and another equivalent of *n*BuLi (3.4 mL, 8.13 mmol, 2.40 M in hexane) was added dropwise. The resulting solution was slowly warmed to room temperature, stirred for 1 h, and then added slowly to a pale gray slurry of LaCl$_3$ (1.00 g, 4.06 mmol) in THF (20 mL). The color of the solution changed to yellow. The resulting solution was then stirred for another 24 h. Removing the THF solvent, washing the residues with cold hexane, and crystallization from a mixture of THF and hexane at 0 °C gave the product **1** as colorless crystals (5.03 g, 85%). C$_{66}$H$_{116}$Cl$_4$LaLi$_3$N$_6$O$_{10}$ (1455.18): calcd. C 54.47, H 8.03, N 5.78, La 9.55; found C 53.44, H 7.69, N 6.05, La 10.03. ^{1}H NMR (300 MHz, C$_4$D$_8$O): δ = 1.04 (br. m, 24 H, CH_3), 3.57 [m, 4 H, –HC(N)(CH$_3$)$_2$], 6.20–6.89 (m, 8 H, H–Ph) ppm. ^{13}C NMR (75 MHz, C$_4$D$_8$O): δ = 26.2, 27.2, 27.5, 27.9, 46.3, 68.1, 111.0, 115.5, 122.4, 128.1, 156.2, 177.4 ppm. IR (KBr): ṽ = 3304 (s), 2974 (s), 2869 (m), 1635 (s), 1499 (s), 1461 (s), 1365 (m), 1236 (m), 1100 (m), 1069 (m), 947 (w), 807 (w), 762 (w) cm^{-1}.

[{(*i*PrN)$_2$C[NLi(THF)$_3$(C$_6$H$_4$*p*-Cl)]}$_2$Nd(μ-Cl$_2$)Li(THF)$_2$]·2THF (2): Complex **2** was synthesized by following the standard procedure described for **1** from *p*-ClC$_6$H$_4$NH$_2$ (1.19 g, 9.3 mmol), *n*BuLi (3.9 mL, 9.3 mmol, 2.40 M in hexane), *N*,*N*′-diisopropylcarbodiimide (1.5 mL, 9.3 mmol), *n*BuLi (3.9 mL, 9.3 mmol, 2.40 M in hexane), and NdCl$_3$ (1.16 g, 4.65 mmol) in THF (30 mL). Complex **2** was isolated as a light blue crystalline solid (4.96 g, 73%). C$_{66}$H$_{116}$Cl$_4$Li$_3$N$_6$NdO$_{10}$ (1460.51): calcd. C 54.28, H 8.01, N 5.75, Nd 9.88; found C 52.99, H 7.89, N 6.01, Nd 10.03. ^{1}H NMR (400 MHz, C$_4$D$_8$O): δ = –9.74 (s), –2.94 (br.), 8.12 (m), 13.87 (m), 27.86 (br) ppm. IR (KBr): ṽ = 3321 (s), 2973 (s), 2869 (m), 1634 (s), 1584 (s), 1497 (s), 1365 (m), 1266 (m), 1125 (m), 1007 (s), 947 (w), 897 (w), 764 (w) cm^{-1}.

[{(*i*PrN)$_2$C[NLi(THF)$_3$(C$_6$H$_4$*p*-Cl)]}$_2$Sm(μ-Cl$_2$)Li(THF)$_2$]·3THF (3): Complex **3** was synthesized following the standard procedure described for **1** from *p*-ClC$_6$H$_4$NH$_2$ (1.61 g, 12.6 mmol), *n*BuLi (5.3 mL, 12.6 mmol, 2.40 M in hexane), *N*,*N*′-diisopropylcarbodiimide (1.97 mL, 12.6 mmol), *n*BuLi (5.3 mL, 12.6 mmol, 2.40 M in hexane), and SmCl$_3$ (1.62 g, 6.3 mmol) in THF (30 mL). Complex **3** was isolated as a light yellow crystalline solid (6.31 g, 65%). C$_{70}$H$_{124}$Cl$_4$Li$_3$N$_6$O$_{11}$Sm (1538.72): calcd. C 54.64, H 8.12, N 5.46, Sm 9.77; found C 53.42, H 7.85, N 5.91, Sm 10.08. ^{1}H NMR (400 MHz, C$_4$D$_8$O): δ = –1.48 (m), 0.86 (br.), 0.06 (s), 1.92 (m), 2.93 (m), 4.48 (m), 5.58 (m), 6.81–7.02 (m) ppm. IR (KBr): ṽ = 3314 (s), 2971 (s), 2870 (m), 1634 (s), 1580 (s), 1496 (s), 1365 (m), 1264 (m), 1127 (m), 1048 (s), 897 (w), 858 (w), 810 (w) cm^{-1}.

[{(*i*PrN)$_2$C[NLi(THF)$_3$(C$_6$H$_4$*p*-Cl)]}$_2$Yb(μ-Cl$_2$)Li(THF)$_2$]·3THF (4): Complex **4** was synthesized by following the standard procedure described for **1** from *p*-ClC$_6$H$_4$NH$_2$ (1.21 g, 9.4 mmol), *n*BuLi (3.9 mL, 9.4 mmol, 2.40 M in hexane), *N*,*N*′-diisopropylcarbodiimide (1.48 mL, 9.4 mmol), *n*BuLi (3.9 mL, 9.4 mmol, 2.40 M in hexane), and YbCl$_3$ (1.31 g, 4.7 mmol) in THF (30 mL). Complex **4** was isolated as a yellow crystalline solid (5.14 g, 70%).

C$_{70}$H$_{124}$Cl$_4$Li$_3$N$_6$O$_{11}$Yb (1561.36): calcd. C 53.84, H 8.00, N 5.38, Yb 11.08; found C 52.87, H 7.79, N 5.83, Yb 11.38. IR (KBr): ṽ = 3318 (s), 2971 (s), 2872 (m), 1628 (s), 1580 (s), 1495 (s), 1388 (m), 1252 (m), 1161 (m), 1050 (s), 907 (w), 859 (w), 714 (w) cm^{-1}.

[{(*i*PrN)$_2$C[NLi(THF)$_3$(C$_6$H$_4$*p*-Cl)]}$_2$Y(μ-Cl$_2$)Li(THF)$_2$]·3THF (5): Complex **5** was synthesized by following the standard procedure described for **1** from *p*-ClC$_6$H$_4$NH$_2$ (1.81 g, 14.2 mmol), *n*BuLi (5.96 mL, 14.2 mmol, 2.40 M in hexane), *N*,*N*′-diisopropylcarbodiimide (2.21 mL, 14.2 mmol), *n*BuLi (5.96 mL, 14.2 mmol, 2.40 M in hexane), and YCl$_3$ (1.39 g, 7.1 mmol) in THF (30 mL). Complex **5** was isolated as a colorless crystalline solid (8.08 g, 77%). C$_{70}$H$_{124}$Cl$_4$Li$_3$N$_6$O$_{11}$Y (1477.23): calcd. C 56.91, H 8.46, N 5.69, Y 6.02; found C 56.89, H 8.18, N 6.21, Y 6.65. ^{1}H NMR (300 MHz, C$_4$D$_8$O): δ = 0.85–1.20 (m, 24 H, CH_3), 3.35–4.21 (m, 4 H, –HC(N)(CH$_3$)$_2$), 5.95–6.94 (m, 8 H, H–Ph) ppm. ^{13}C NMR (75 MHz, C$_4$D$_8$O): δ = 23.7, 26.0, 26.5, 27.7, 45.2, 45.4, 46.1, 46.4, 68.4, 117.1, 122.8, 123.2, 128.5, 128.7, 128.9, 151.7, 156.2, 165.5 ppm. IR (KBr): ṽ = 3304 (s), 2970 (s), 2873 (m), 1627 (s), 1579 (s), 1492 (s), 1388 (m), 1253 (m), 1162 (m), 1048 (m), 907 (w), 859 (w), 811 (w) cm^{-1}.

[{[(*i*PrN)$_2$CN(C$_6$H$_4$*p*-Cl)Li]$_2$(DME)(LiCl)Nd(O*i*Pr)$_2$}$_2$]$^{2-}$[{Li(DME)$_3$}$^+$]$_2$·3C$_6$H$_{14}$ (6): A solution of NaO*i*Pr (0.31 g, 3.76 mmol) and LiCl (0.08 g, 1.88 mmol) in THF (10 mL) was added to a solution of **2** (2.75 g, 1.88 mmol) in THF (20 mL) at 20 °C, and the reaction mixture was stirred for 24 h. The solution was filtered and the solvent was evaporated under vacuum. The solid residue was recrystallized from a mixture of DME and hexane to afford light blue crystals of **6** (1.38 g, 56%). C$_{114}$H$_{222}$Cl$_6$Li$_8$N$_{12}$Nd$_2$O$_{20}$ (2637.74): calcd. C 51.91, H 8.48, N 6.37, Nd 10.94; found C 50.84, H 8.31, N 6.71, Nd 11.21. IR (KBr): ṽ = 3447 (s), 2973 (s), 2869 (m), 1635 (s), 1584 (s), 1499 (s), 1365 (m), 1266 (m), 1164 (m), 1091 (m), 951 (s), 858 (w), 765 (w), 596 (w) cm^{-1}.

[{[(*i*PrN)$_2$CN(C$_6$H$_4$*p*-Cl)Li]$_2$(DME)(LiCl)Sm(O*i*Pr)$_2$}$_2$]$^{2-}$[{Li(DME)$_3$}$^+$]$_2$·3C$_6$H$_{14}$ (7): This compound was prepared by following the procedure described above for **6** starting from **3** (1.38 g, 1 mmol) in THF (20 mL), NaO*i*Pr (0.164 g, 2 mmol), and LiCl (0.042 g, 1 mmol) in THF (10 mL). Compound **7** was isolated as colorless crystals (0.73 g, 55%). C$_{114}$H$_{222}$Cl$_6$Li$_8$N$_{12}$O$_{20}$Sm$_2$ (2649.96): calcd. C 51.67, H 8.44, N 6.34, Sm 11.34; found C 51.03, H 8.13, N 6.88, Sm 11.91. IR (KBr): ṽ = 3345 (s), 2978 (s), 2868 (m), 1631 (s), 1579 (s), 1498 (s), 1368 (m), 1264 (m), 1165 (m), 1078 (m), 947 (s), 847 (w), 764 (w), 587 (w) cm^{-1}.

[{[(*i*PrN)$_2$CN(C$_6$H$_4$*p*-Cl)Li]$_2$(DME)(LiCl)Yb(O*i*Pr)$_2$}$_2$]$^{2-}$[{Li(DME)$_3$}$^+$]$_2$·3C$_6$H$_{14}$ (8): This compound was prepared by following the procedure described above for **6** starting from **4** (2.34 g, 1.67 mmol) in THF (20 mL), NaO*i*Pr (0.273 g, 3.34 mmol), and LiCl (0.07 g, 1.67 mmol) in THF (10 mL). Compound **8** was isolated as colorless crystals (1.15 g, 51%). C$_{114}$H$_{222}$Cl$_6$Li$_8$N$_{12}$O$_{20}$Yb$_2$ (2695.34): calcd. C 50.80, H 8.30, N 6.24, Yb 12.84; found C 50.16, H 7.84, N 6.31, Yb 13.07. IR (KBr): ṽ = 3322 (s), 2966 (s), 2869 (m), 1625 (s), 1578 (s), 1496 (s), 1364 (m), 1259 (m), 1164 (m), 1093 (m), 956 (m), 861 (m), 745 (w), 575 (m) cm^{-1}.

[{[(*i*PrN)$_2$CN(C$_6$H$_4$*p*-Cl)Li]$_2$(DME)(LiCl)Y(O*i*Pr)$_2$}$_2$]$^{2-}$[{Li(DME)$_3$}$^+$]$_2$·3C$_6$H$_{14}$ (9): This compound was prepared following the procedure described above for **6** starting from **5** (2.61 g, 1.99 mmol) in THF (20 mL), NaO*i*Pr (0.326 g, 3.98 mmol), and LiCl (0.084 g, 1.99 mmol) in THF (10 mL). Compound **9** was isolated as colorless crystals (1.15 g, 46%). C$_{114}$H$_{222}$Cl$_6$Li$_8$N$_{12}$O$_{20}$Y$_2$ (2527.08): calcd. C 54.18, H 8.85, N 6.65, Y 7.03; found C 53.78, H 8.67, N 6.94, Y 7.21. ^{1}H NMR (400 MHz, C$_4$D$_8$O and C$_6$D$_6$): δ = 0.83–1.29 [m, 36 H, CH_3 (–*i*Pr and –O*i*Pr),] 3.12 (s, 12 H, CH_3/DME), 3.31 (s, 8 H, CH_2/DME) 3.21–4.31 [m, 6 H, CH (–*i*Pr and

–O*i*Pr)], 6.62–7.91 (m, 8 H, *H*–Ph) ppm. ^{13}C NMR (100 MHz, C$_4$D$_8$O & C$_6$D$_6$): δ = 23.7, 24.3, 24.6, 24.8, 25.0, 25.2, 25.7, 44.0, 44.6, 45.6, 45.8, 58.7, 65.2, 72.2, 116.6, 118.1, 121.6, 123.1, 123.2, 127.8, 128.1, 128.3, 152.1, 156.2, 163.7 ppm. IR (KBr): ṽ = 3305 (s), 2968 (s), 2867 (m), 1629 (s), 1579 (s), 1496 (s), 1366 (m), 1257 (m), 1160 (m), 1091 (m), 978 (m), 858 (m), 765 (w), 505 (m) cm^{-1}.

[{(*i*PrN)$_2$C(NC$_6$H$_4$*p*-Cl)Li(DME)(LiCl)}$_2$Nd(O*t*Bu)$_2$]$^-$·[Li(DME)$_3$]$^+$· 0.5C$_6$H$_{14}$ (10): A solution of KO*t*Bu (0.39 g, 3.5 mmol) and LiCl (0.15 g, 3.5 mmol) in THF (10 mL) was added to a solution of **2** (2.45 g, 1.75 mmol) in THF (20 mL) at 20 °C, and the reaction mixture was stirred for 24 h. The solution was filtered and the solvent was evaporated under vacuum. The solid residue was recrystallized from a mixture of DME and hexane to afford light blue crystals of **10** (1.17 g, 48%). C$_{57}$H$_{111}$Cl$_4$Li$_5$N$_6$NdO$_{12}$ (1393.26): calcd. C 49.14, H 8.03, N 6.03, Nd 10.35; found C 48.31, H 8.16, N 6.45, Nd 10.78. IR (KBr): ṽ = 3321 (s), 2973 (s), 2869 (m), 1634 (s), 1584 (s), 1498 (s), 1462 (m), 1365 (m), 1190 (m), 1165 (m), 1091 (m), 953 (w), 858 (m), 761 (w), 596 (w) cm^{-1}.

[{(*i*PrN)$_2$C(NC$_6$H$_4$*p*-Cl)Li(DME)(LiCl)}$_2$Yb(O*t*Bu)$_2$]$^-$·[Li(DME)$_3$]$^+$· 0.5C$_6$H$_{14}$ (11): This compound was prepared by following the procedure described above for **10** starting from **4** (1.76 g, 1.26 mmol) in THF (20 mL), KO*t*Bu (0.282 g, 2.52 mmol), and LiCl (0.107 g, 2.52 mmol) in THF (10 mL). Compound **11** was isolated as colorless crystals (0.896 g, 50%). C$_{57}$H$_{111}$Cl$_4$Li$_5$N$_6$O$_{12}$Yb (1422.06): calcd. C 48.14, H 7.87, N 5.97, Yb 12.17; found C 47.89, H 7.53, N 6.18, Yb 12.34. IR (KBr): ṽ = 3341 (s), 2971 (s), 2867 (m), 1629 (s), 1579 (s), 1496 (s), 1460 (m), 1363 (m), 1192 (m), 1162 (m), 1090 (m), 954 (w), 857 (m), 757 (w), 594 (w) cm^{-1}.

Reaction of 2 with LiNHC$_6$H$_5$: A solution of LiNHC$_6$H$_5$ in THF (2.9 mmol) treated with PhNH$_2$ (0.26 mL, 2.9 mmol) and *n*BuLi (1.2 mL, 2.9 mmol, 2.40 M in hexane) at 0 °C was added to a solution of **2** (4.24 g, 2.9 mmol) in THF (40 mL), and the reaction mixture was stirred for 48 h at 60 °C. Removing the solvent by vacuum and extraction with hot toluene to remove the LiCl by centrifugation led to a dark brown solution. The resulting solution was slowly concentrated to a quarter of its volume and was then cooled to –30 °C. The colorless crystals **12** were washed with cold hexane and dried under vacuum (1.67 g, 80%). C$_{34}$H$_{54}$Cl$_2$Li$_2$N$_6$O$_2$ (663.61): calcd. C 61.53, H 8.21, N 12.66; found C 61.03, H 8.02, N 12.98. IR (KBr): ṽ = 3312 (s), 2925 (s), 2870 (s), 1632 (s), 1580 (s), 1520 (s), 1426 (s), 1365 (s), 1327 (s), 1162 (m), 1123 (m), 1034 (m), 939 (m) cm^{-1}.

Reaction of 2 with [Li*i*PrNC(HN*i*Pr)N(C$_6$H$_5$)]: The fresh guanidinate lithium Li[*i*PrNC(HN*i*Pr)N(C$_6$H$_5$)] (2.4 mmol), which was generated by PhNH$_2$ (0.22 mL, 2.4 mmol), *n*BuLi (1.0 mL, 2.4 mmol, 2.40 M in hexane), and *N,N*′-diisopropylcarbodiimide (0.37 mL, 2.4 mmol), was added to a solution of **2** (3.51 g, 2.4 mmol) in THF (40 mL), and the reaction mixture was stirred for 48 h at 60 °C. Removing the solvent by vacuum, extraction with hot toluene, and removing the LiCl by centrifugation led to a brown solution. The resulting solution was slowly concentrated at room temperature to a quarter of its volume and was then cooled to –30 °C. The colorless crystals **12** were washed with cold hexane and dried under vacuum (1.28 g, 81%).

Reaction of YbCl$_3$ with 12 and *n*BuLi: A solution of **12** (6 mmol) in THF, which was generated by reaction of *p*-ClPhNH$_2$ (0.765 g, 6 mmol) with *n*BuLi (2.5 mL, 6 mmol, 2.40 M in hexane) and *N,N*′-diisopropylcarbodiimide (0.93 mL, 6 mmol) at room temperature, was added to a solution of YbCl$_3$ (0.558 g, 2 mmol) in THF (20 mL),. After stirring for 6 h, the reaction solution was cooled to 0 °C. A solution of *n*BuLi (0.83 mL, 2 mmol, 2.40 M) in hexane was added to the solution at the same temperature, then stirred for 2 h.

The solution was then slowly warmed to room temperature and stirred overnight. Removing the solvent by vacuum and extraction with hot toluene to remove the LiCl by centrifugation led to a brown yellow solution. The solution was concentrated to a quarter of its volume at room temperature and then cooled to –30 °C. The colorless crystals **12** were washed with cold hexane and dried under vacuum (1.13 g, 85%, based on the second amount of *n*BuLi used).

Reaction of YbCl$_3$ with 12, *n*BuLi, and Diisopropylcarbodiimide: Synthesis of [{*i*PrNHC(N*i*Pr)N(C$_6$H$_4$*p*-Cl)}$_2$Yb{(*i*PrNC(N*i*Pr)$_2$) N(C$_6$H$_4$*p*-Cl)C(*i*PrN)}Li(THF)]·THF (13): A solution of **12** (9 mmol) in THF, which was generated by the reaction of *p*-ClPhNH$_2$ (1.15 g, 9 mmol) with *n*BuLi (3.75 mL, 9 mmol, 2.40 M in hexane) and *N,N*′-diisopropylcarbodiimide (1.4 mL, 9 mmol) at room temperature, was added to a solution of YbCl$_3$ (0.838 g, 3 mmol) in THF (20 mL). After stirring for 6 h, the reaction solution was cooled to 0 °C. A solution of *n*BuLi (1.25 mL, 3 mmol, 2.40 M) in hexane was added to the solution at the same temperature, then stirred for 20 min. *N,N*′-diisopropylcarbodiimide (0.47 mL, 3 mmol) was added. The solution was then slowly warmed to room temperature and stirred overnight. Removing the solvent by vacuum and extraction with hot toluene to remove the LiCl by centrifugation led to a brown yellow solution. The resulting solution was slowly concentrated and cooled to 0 °C. The yellow crystals **13** were washed with cold hexane and dried under vacuum (2.89 g, 80%). C$_{54}$H$_{86}$Cl$_3$LiN$_{11}$O$_2$Yb (1207.67): calcd. C 53.70, H 7.18, N 12.76, Yb 14.33; found C 53.43, H 7.01, N 12.88, Yb 14.25. ^{1}H NMR (400 MHz, C$_6$D$_6$): δ = –10.73 (m), –2.85 (m), 0.67–1.13 (m), 2.12 (m), 3.13 (s), 3.66 (s), 6.82–7.16 (m) ppm. IR (KBr): ṽ = 3401 (s), 3060 (s), 2982 (s), 2913 (s), 2856 (s), 1640 (s), 1615 (s), 1570 (s), 1533 (s), 1501 (s), 1470 (s), 1354 (m), 1178 (m), 1059 (m), 1031 (m), 948 (m), 850 (m) cm^{-1}.

Reaction of [{*i*PrNHC(N*i*Pr)(NC$_6$H$_4$*p*-Cl)}$_3$Yb(THF)] with *n*BuLi and *i*PrN=C=N*i*Pr: Synthesis of [{*i*PrNHC(N*i*Pr)N(C$_6$H$_4$*p*-Cl)}$_2$Yb{(*i*PrNC(N*i*Pr)$_2$)N(C$_6$H$_4$*p*-Cl)C(*i*PrN)}Li(THF)]·THF (13): A solution of [{*i*PrNHC(N*i*Pr)(NC$_6$H$_4$*p*-Cl)}$_3$Yb(THF)] (2.509 g, 2.5 mmol) in toluene (30 mL) was cooled to 0 °C, then *n*BuLi (1.04 mL, 2.5 mmol, 2.40 M in hexane) was added dropwise, and it was stirred for 20 min. *i*PrN=C=N*i*Pr (0.39 mL, 2.5 mmol) was added to this solution at 0 °C. The resulting solution was slowly warmed to room temperature and stirred overnight. The solution was concentrated at room temperature to a quarter of its volume and then cooled to 0 °C. The yellow crystals **13** were washed with cold hexane and then dried under vacuum (2.59 g, 86%).

Typical Procedure for the Polymerization Reactions: A 50 mL Schlenk flask equipped with a magnetic stir bar was charged with ε-caprolactone (0.6 mL) and toluene (5.8 mL). Initiator **7** (10.0 mM in toluene, 0.18 mL) was added to this solution with a syringe. The contents of the flask were then stirred vigorously at 20 °C for 2 h, during which time the mixture became very viscous, which disrupted the stirring. The polymerization was quenched by adding a 5% solution of HCl in methanol. The polymer precipitated from methanol and was dried under vacuum.

X-ray Crystallography: Crystals suitable for X-ray diffraction of complexes **1–3** and **6–14** were sealed in a thin-walled glass capillary filled with argon for structural analysis. Diffraction data were collected with a Rigaku Mercury CCD area detector in the ω scan mode using Mo-*K$_α$* radiation (λ = 0.71073 and 0.71075 Å). The diffracted intensities were corrected for Lorentz polarization effects and empirical absorption corrections. Details of the intensity data collection and crystal data are given in Tables 1, 2, and 3. The structures were solved by direct methods and refined by full-matrix least-squares procedures based on |*F*|^2. All of the non-hydrogen

Q. Shen et al.

atoms were refined anisotropically. The hydrogen atoms in these complexes were all generated geometrically, assigned appropriate isotropic thermal parameters, and allowed to ride on their parent carbon atoms. All of the hydrogen atoms were held stationary and included in the structure factor calculations in the final stage of full-matrix least-squares refinement. The structures were refined using SHELEXL-97 programs.

CCDC-839061 (for **1**), -839062 (for **2**) -839063 for (for **3**) -839064 (for **6**) -839065 (for **7**) -839066 (for **8**) -839067 (for **9**) -839068 (for **10**) -839069 (for **11**) -839070 (for **12**), and -839071 (for **13**) contain the supplementary crystallographic data for this paper. These data can be obtained free of charge from The Cambridge Crystallographic Data Centre via www.ccdc.cam.ac.uk/data_request/cif.

Supporting Information (see footnote on the first page of this article): Crystallographic data for compounds **1**–**3** and **6**–**13**, and NMR spectra.

Acknowledgments

[1] a) P. J. Bailey, S. Pace, *Coord. Chem. Rev.* **2001**, *214*, 91–141; b) M. P. Coles, *Dalton Trans.* **2006**, 985–1001; c) F. T. Edelmann, *Chem. Soc. Rev.* **2009**, *38*, 2253–2268; d) F. T. Edelmann, *Adv. Organomet. Chem.* **2008**, *57*, 183–352.

[2] a) A. A. Trifonov, E. A. Fedorova, G. K. Fukin, M. N. Bochkarev, *Eur. J. Inorg. Chem.* **2004**, 4396–4401; b) A. A. Trifonov, G. G. Skvortsov, D. M. Lyubov, N. A. Skorodumova, G. K. Fukin, E. V. Baranov, V. N. Glushakova, *Chem. Eur. J.* **2006**, *12*, 5320–5327; c) D. M. Lyubov, G. K. Fukin, A. A. Trifonov, *Inorg. Chem.* **2007**, *46*, 11450–11456.

[3] a) Y. Zhou, G. P. A. Yap, D. S. Richeson, *Organometallics* **1998**, *17*, 4387–4391; b) Z. Lu, G. P. A. Yapp, D. S. Richeson, *Organometallics* **2001**, *20*, 706–712; c) Y. J. Luo, Y. M. Yao, Q. Shen, *Macromolecules* **2002**, *35*, 8670–8671; d) A. A. Trifonov, D. M. Lyubov, E. A. Fedorova, G. K. Fukin, H. Schumann, S. Mühle, M. Hummert, M. N. Bochkarev, *Eur. J. Inorg. Chem.* **2006**, 747–756; e) S. Z. Ge, A. Meetsma, B. Hessen, *Organometallics* **2008**, *27*, 3131–3135.

[4] a) Y. Yao, Y. Luo, J. Chen, Z. Zhang, Y. Zhang, Q. Shen, *J. Organomet. Chem.* **2003**, *679*, 229–237; b) A. Milanov, R. Bhakta, A. Baunemann, *Inorg. Chem.* **2006**, *45*, 11008–11018.

[5] a) G. R. Giesbrecht, G. D. Whitener, J. Arnold, *J. Chem. Soc., Dalton Trans.* **2001**, 923–927; b) N. Ajellal, D. M. Lyubov, M. A. Sinenkov, G. K. Fukin, A. V. Cherkasov, C. M. Thomas, J.-F. Carpentier, A. A. Trifonov, *Chem. Eur. J.* **2008**, *14*, 5440–5448.

[6] a) N. J. Bremer, Ab Cutcliff, M. F. Farona, W. G. Kofron, *J. Chem. Soc. A* **1971**, 3264–3266; b) P. J. Bailey, A. J. Blake, M. Kryszczuk, S. Parsons, D. Reed, *J. Chem. Soc., Chem. Commun.* **1995**, 1647–1648; c) M. B. Dinger, W. Henderson, *Chem. Commun.* **1996**, 211–212; d) T. Chivers, M. Parvez, G. Schatte, *J. Organomet. Chem.* **1998**, *550*, 213–220; e) P. J. Bailey, R. O. Gould, C. N. Harmer, S. Pace, A. Steiner, D. S. Wright, *Chem. Commun.* **1997**, 1161–1162; f) S. R. Foley, G. P. A. Yap, D. S. Richeson, *Inorg. Chem.* **2002**, *41*, 4149–4157; g) P. J. Bailey, S. Pace, *Coord. Chem. Rev.* **2001**, *214*, 91–141; h) M. K. T. Tin, G. P. A. Yap, D. S. Richeson, *Inorg. Chem.* **1998**, *37*, 6728–6730; i) N. Thirupathi, G. P. A. Yap, D. S. Richeson, *Organometallics* **2000**, *19*, 2573–2579; j) T.-G. Ong, G. P. A. Yap, D. S. Richeson, *J. Am. Chem. Soc.* **2003**, *125*, 8100–8101; k) N. Thirupathi, G. P. A. Yap, D. S. Richeson, *Chem. Commun.* **1999**, 2483–2484; l) T.-G. Ong, G. P. A. Yap, D. S. Richeson, *Chem. Commun.* **2003**, 2612–2613; m) M. K. T. Tin, N. Thirupathi, G. P. A. Yap, D. S. Richeson, *J. Chem. Soc., Dalton Trans.* **1999**, 2947–2951.

[7] a) C. Pi, Z. Zhang, Z. Pang, J. Zhang, J. Luo, Z. Chen, L. Weng, X. Zhou, *Organometallics* **2007**, *26*, 1934–1946; b) C. Pi, R. Liu, P. Zheng, Z. Chen, X. Zhou, *Inorg. Chem.* **2007**, *46*, 5252–5259.

[8] P. Zheng, J. Hong, R. Liu, Z. Zhang, Z. Pang, L. Weng, X. Zhou, *Organometallics* **2010**, *29*, 1284–1289.

[9] a) C. Qian, X. Zhang, J. Li, F. Xu, Q. Shen, *J. Organomet. Chem.* **2010**, *695*, 747–752; b) C. Qian, X. Zhang, J. Li, F. Xu, Y. Zhang, Q. Shen, *Organometallics* **2009**, *28*, 3856–3862.

[10] L. Zhou, Y. Yao, Y. Zhang, M. Xue, J. Chen, Q. Shen, *Eur. J. Inorg. Chem.* **2004**, 2167–2172.

[11] a) R. D. Rogers, J. L. Atwood, R. Gruning, *J. Organomet. Chem.* **1978**, *157*, 229–237; b) M. Lappert, M. Slade, A. Singh, J. Atwood, R. Rogers, *J. Am. Chem. Soc.* **1983**, *105*, 302–303.

[12] T.-G. Ong, J. S. O'Brien, I. Korobkov, D. S. Richeson, *Organometallics* **2006**, *25*, 4728–4730.

[13] Y. Luo, Y. Yao, Q. Shen, K. Yu, *Eur. J. Inorg. Chem.* **2003**, 318–323.

[14] R. D. Shannon, *Acta Crystallogr., Sect. A* **1976**, *32*, 751–767.

[15] Y. Ohashi, K. Yanagi, Y. Mitsuhashi, K. Nagata, Y. Kaizu, Y. Sasada, H. Kobayashi, *J. Am. Chem. Soc.* **1979**, *101*, 4740–4742.

[16] M. Shibasaki, H. Sasai, T. Arai, *Angew. Chem.* **1997**, *109*, 1290; *Angew. Chem. Int. Ed. Engl.* **1997**, *36*, 1236–1256.

Diverse Coordination Behaviour of Phosphorus(V)-Functionalised 6-Chloroaminobenzothiazole Anions at Various Metal Centres

Simon J. Coles,[a] Sophie H. Dale,[b] Mark R. J. Elsegood,[b] Kirsty G. Gaw,[b] Thomas Gelbrich,[a] Michael B. Hursthouse,[a] Mark E. Light,[a] Thomas A. Noble,[b] and Martin B. Smith*[b]

Aminobenzothiazole-functionalised phosphane **1** and its corresponding phosphorus(V) analogues **2–4** were synthesised in high yields. New 1D polymeric salts K[ClC$_6$H$_3$NC(S)NP-(E)Ph$_2$]$_\infty$ (E = O **5**; E = S **6**) were shown, by using single-crystal X-ray diffraction, to exhibit unique potassium metal ion coordination through either κ^3-N$_2$O tridentate (E = O) or κ^2-N$_2$ bridging (E = S) modes. In contrast, κ^2-NE chelation (E = S, Se) was observed upon complexation to a range of metal

fragments including {Ir(η^5-Cp*)Cl} (E = S **8**; E = Se **9**), {Rh(η^5-Cp*)Cl} (E = S **10**; E = Se **11**), {Ru(η^6-p-MeC$_6$H$_4$iPr)Cl} (E = S **12**), {Ru(η^6-C$_6$Me$_6$)Cl} (E = S **13**) and {Pt(PMe$_2$Ph)Cl} (E = S **14**). All new compounds were characterised by a combination of multinuclear NMR, FTIR and microanalysis. Seven compounds were structurally characterised by using single-crystal X-ray crystallography.

Introduction

Chelating anionic ligands, such as the ubiquitous acac anion (acac = acetylacetonato), have attracted considerable interest over the years for their importance in many diverse aspects of coordination chemistry. Aside from acac, many other bidentate anionic ligands bearing group 15 or 16 donor atoms have been widely documented. Scheme 1 illustrates a selection of popular recent examples including: amidinate (**I**),[1] guanidinate (**II**),[2] β-diketiminate (nacnac$^-$) (**III**),[3] bis(phosphinimino)methanide (**IV**)[4] and imidodiphosphinate (**V**)[5] ligands (R and R′ denote various alkyl/silyl/aryl groups; E = O, S, Se, Te). In these examples, the principal bonding motifs observed are either κ^2-NN- or κ^2-EE-chelation. Considerable recent interest in sulfur and selenium analogues of **V** strides from observations that these complexes are suitable single-source precursors for binary metal sulfide[5c] or selenide[5d] thin semiconducting films.

As part of continuing studies in our group investigating neutral and singly/doubly deprotonated functionalised tertiary phosphanes,[6] we report here the facile synthesis and structural characterisation of two unusual potassium salts of an anionic, benzothiazole-modified amino(phosphane) oxide and sulfide.[7] We show, depending on the group 16
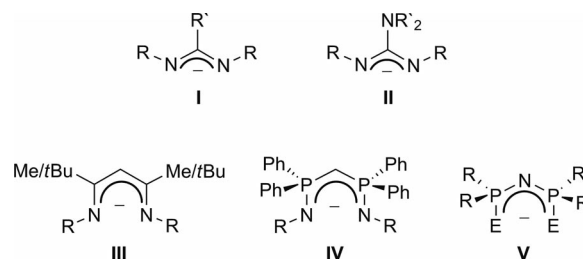
Scheme 1.

donor atom (O or S), two distinct coordination modes utilising a combination of both nitrogen and/or O donor centres. Furthermore, classical κ^2-NE-chelation (E = S, Se) was achieved upon facile complexation to a range of late transition metal fragments including {M(η^5-Cp*)Cl} (M = Ir, Rh; Cp* = pentamethylcyclopentadienyl), {Ru(η^6-p-Me-C$_6$H$_4$iPr)Cl}, {Ru(η^6-C$_6$Me$_6$)Cl} and {Pt(PMe$_2$Ph)Cl}. All new compounds reported here were characterised by a combination of spectroscopic and crystallographic techniques.

Results and Discussion

Reaction of commercially available 6-chloroaminobenzothiazole with Ph$_2$PCl and NEt$_3$, in diethyl ether, gave, after work-up, amino(phosphane) **1** in excellent (95%) yield.[8] Under standard conditions,[7b] oxidation with either aqueous H$_2$O$_2$ (30% w/w), elemental S$_8$ or grey Se afforded the corresponding phosphorus(V) compounds **2–4** in approximately 90% yield. The molecular structure of phosphane oxide **2** was determined (Figure 1) and shows a tautomeric

[a] EPSRC National Crystallography Service, School of Chemistry, University of Southampton, Highfield, Southampton SO17 1BJ, U.K.
[b] Department of Chemistry, Loughborough University, Loughborough, Leics LE11 3TU, U.K.
Fax: +44-1509-223925
E-mail: m.b.smith@lboro.ac.uk

WILEY ONLINE LIBRARY

arrangement with the NH hydrogen on the endocyclic N(2) atom. The P(1)–N(1) [1.636(2) Å], N(1)–C(1) [1.293(3) Å] and C(1)–N(2) [1.353(3) Å] bond lengths provide evidence of delocalisation in the P(1)–N(1)–C(1)–N(2) backbone.[7b] Intermolecular N–H···O H-bonding links molecules of **2** into a 1D polymeric chain [N(2)···O(1A) 2.696(3) Å; N(2)–H(2)···O(1A) 153(3)°].
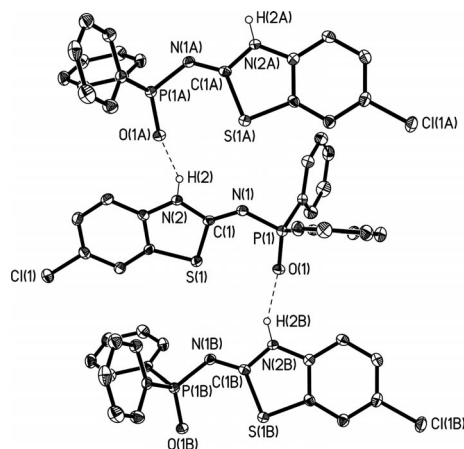

Figure 1. Ellipsoid plot of **2**. Thermal ellipsoids are drawn at the 50% probability level. All hydrogen atoms except those on N(2), N(2A) and N(2B) are omitted for clarity. Selected bond lengths [Å] and angles [°]: P(1)–O(1) 1.4935(18), P(1)–N(1) 1.636(2), N(1)–C(1) 1.293(3), C(1)–N(2) 1.353(3), C(1)–S(1) 1.790(2); O(1)–P(1)–N(1) 117.09(10), P(1)–N(1)–C(1) 125.01(18), N(1)–C(1)–N(2) 122.6(2), N(1)–C(1)–S(1) 128.10(19). Symmetry operator: A = x + 1/2, –y + 1/2, –z + 1.

Metallation of **2**–**4** was smoothly achieved, at ambient temperature, with *t*BuOK in MeOH to generate potassium salts **5**–**7**. Cleavage of the chloride bridge[9] of [MCl(μ-Cl)(η⁵-Cp*)]₂ (M = Ir, Rh), [RuCl(μ-Cl)(η⁶-*p*-MeC₆H₄-*i*Pr)]₂, [RuCl(μ-Cl)(η⁶-C₆Me₆)]₂ or [PtCl(μ-Cl)(PMe₂Ph)]₂ with 2 equiv. of **6** or **7** (preformed or generated directly from **3** or **4**/*t*BuOK) gave the neutral mononuclear metal complexes Ir(η⁵-Cp*)Cl(**6/7**) (E = S **8**; E = Se **9**), Rh(η⁵-Cp*)Cl(**6/7**) (E = S **10**; E = Se **11**), Ru(η⁶-*p*-MeC₆H₄*i*Pr)-Cl(**6**) (**12**), Ru(η⁶-C₆Me₆)Cl(**6**) (**13**) and Pt(PMe₂Ph)Cl(**6**) (**14**) in good yields (Scheme 2).

The molecular structures of potassium salts **5** and **6** were successfully determined by using X-ray crystallography (Figures 2 and 3). For oxide **5**, the asymmetric unit comprises two potassium cations, two anionic ligands and half a chloroform molecule of crystallisation, the latter disordered over an inversion centre. The unsaturated nitrogen and oxygen atoms of the anionic ligand bridge two potassium centres, which leads to a centrosymmetric dimer comprising two K₂N₂O₂ units. In contrast, the second N atom bridges[7b] to an adjacent potassium ion within a second dinuclear unit. The K(1)–N(2′A)/K(1)–N(2′) bond lengths are 3.057(3)/3.103(3) Å with K(1)–O(1′A)/K(1)–O(1′) bond lengths of 2.623(2)/2.871(2) Å; both are in the normal expected range. Within the 6-chloroaminobenzothiazole anion, the P(1)–O(1), P(1)–N(1), N(1)–C(1), C(1)–N(2), C(1)–S(1) bond lengths are 1.494(2), 1.621(2), 1.341(4), 1.310(4), 1.782(3) Å, respectively, and a more pronounced
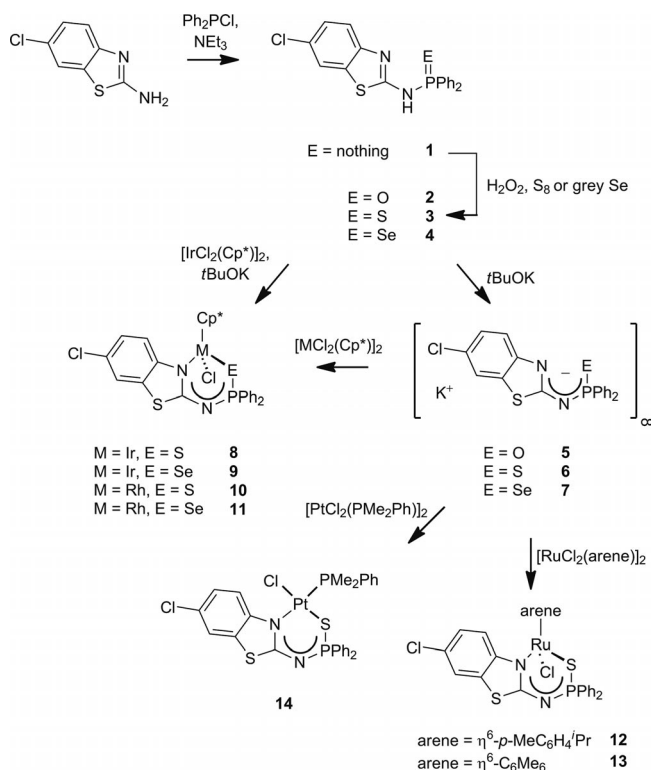
Scheme 2. Synthesis of compounds **1**–**14**.

N(1)–C(1)–N(2) bond angle of 129.9(3)° (with respect to sulfide **6**, vide infra) was observed.[10] These metric parameters suggest some degree of delocalisation within the O(1)–P(1)–N(1)–C(1)–N(2) skeletal backbone. The coordination environment around K(1) is completed by a further K(1)–N(1) bond [2.820(2) Å] from an adjacent dimeric unit and additional K···π contacts [K(1)···C(14) 3.447(3) Å; K(1)···C(19′) 3.274(4) Å; K(1)···C(19) 3.339(3) Å]. Further intermolecular contacts are present within the second unique dimeric unit and comprise K···C [3.392(4) Å] and K···S [3.6260(11) Å]. These are significantly shorter than the van der Waals radii for K/C (ca. 4.5 Å) and K/S (ca. 4.5 Å) atoms.[11]

In contrast to **5**, different structural ligating features are clearly evident for the solvated sulfide analogue **6**. Each potassium is sevenfold coordinated by four nitrogen atoms of the deprotonated 6-chloroaminobenzothiazole ligands and three MeOH molecules. Moreover, the unsaturated/terminal amido N atoms of both anionic ligands bridge between two symmetry-equivalent K metal ions. The resulting dimer is centrosymmetric and has a K₂N₄ unit at its centre. Imposed by symmetry, each four-membered K₂N₂ ring is exactly planar. The rings exhibit K–N bond lengths of 2.865(2) and 2.920(2) Å, with additional longer K–N distances of 3.138(2) and 3.054(2) Å.[12] The two K₂N₂ rings form a dihedral angle of 58.83(5)°. Within the anionic ligand the N(1)–C(7) and N(2)–C(7) bond lengths are 1.322(3) and 1.334(3) Å, respectively, indicative of delocalisation within the N–C–N backbone. The P(1)–N(2), P(1)–S(2) and S(1)–C(7) distances are 1.627(2), 1.9847(9) and 1.799(2) Å,
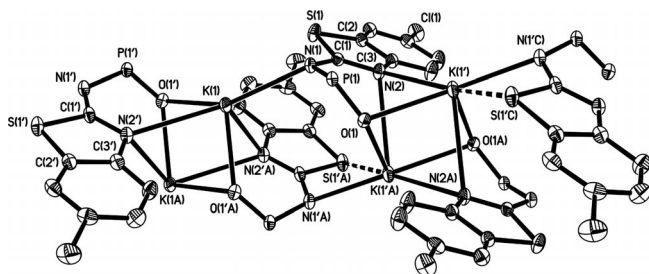
Figure 2. Ellipsoid plot of **5** showing the coordination environment around each potassium metal centre. Thermal ellipsoids are drawn at the 30% probability level. All C–*H* hydrogen atoms and phenyl groups on phosphorus are omitted for clarity. Selected bond lengths [Å] and angles [°]: K(1)–N(1) 2.820(2), K(1)–N(2′A) 3.057(3), K(1)–N(2′) 3.103(3), K(1)–O(1′A) 2.623(2), K(1)–O(1′) 2.871(2), P(1)–O(1) 1.494(2), P(1)–N(1) 1.621(2), N(1)–C(1) 1.341(4), C(1)–N(2) 1.310(4), C(1)–S(1) 1.782(3); O(1)–P(1)–N(1) 120.34(13), P(1)–N(1)–C(1) 119.6(2), N(1)–C(1)–N(2) 129.9(3). Symmetry operators: –x + 2, –y, –z + 1; –x + 2, –y, –z + 2; x, y, z + 1.
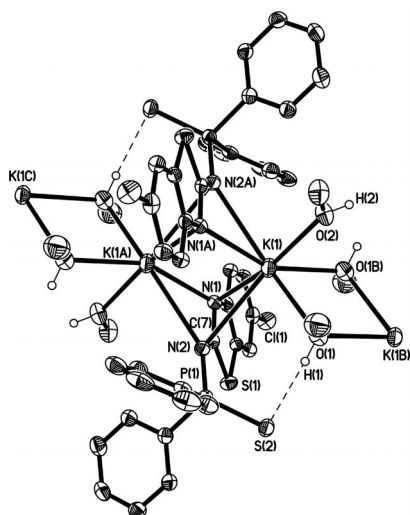

Figure 3. Ellipsoid plot of **6** showing part of the 1D chain and the coordination environment around K(1). Thermal ellipsoids are drawn at the 50% probability level. All C–H hydrogen atoms except those on O(1), O(1A) and O(2) are omitted for clarity. Selected bond lengths [Å] and angles [°]: K(1)–N(1) 2.920(2), K(1)–N(2) 3.138(2), K(1)–N(1A) 2.865(2), K(1)–N(2A) 3.054(2), K(1)–O(1) 2.829(2), K(1)–O(2) 2.6882(19), K(1)–O(1A) 2.779(2), N(1)–C(7) 1.322(3), N(2)–C(7) 1.334(3), S(1)–C(7) 1.799(2), N(2)–P(1) 1.627(2), P(1)–S(2) 1.9851(9); N(1)–K(1)–N(2) 44.93(5), K(1)–N(2)–C(7) 81.41(13), N(1)–C(7)–N(2) 122.1(2), C(7)–N(1)–K(1) 90.68(14), P(1)–N(2)–C(7) 123.61(18), K(1)–N(2)–P(1) 125.08(10), N(2)–P(1)–S(2) 117.84(7). Symmetry operators: –x, –y, –z – 1; –x + 1, –y, –z – 1; 1 + x, y, z.

respectively.[10,13] The potassium ion is additionally coordinated by two bridging [K–O 2.779(2) and 2.829(2) Å] and one nonbridging MeOH [K–O 2.6882(19) Å] solvent molecules.[14] As a result, the dimeric units are connected through K₂O₂ rings to give 1D chains that extend parallel to the crystallographic *a* axis. The plane of the K₂O₂ core forms dihedral angles of 59.70(8) and 68.26(8)° with adjacent K₂N₂ rings. Furthermore, the K···K separations are 3.6938(10) and 4.2659(11) Å within the K₂N₂ and K₂O₂

units, respectively. The coordination polyhedron about potassium is a capped trigonal prism in which the four nitrogen substituents are exactly planar. There are also two intermolecular O–H···S hydrogen bonds, which presumably assist in stabilisation of the unusual 1D chain [O(1)···S(2) 3.247(2) Å; O(1)–H(1)···S(2) 169(3)° and O(2)···S(2) 3.263(2) Å; O(2)–H(2)···S(2) 154(2)°; see Figure 3 and Supporting Information].

The molecular structures of **8** (Supporting Information), **9** and **11** (Figures 4 and 5) are isostructural (Tables 1 and 2) and each reveals a classic piano-stool arrangement comprising an η⁵-Cp*, a chelating κ²-N/Se-[ClC₆H₃NC(S)-NP(E)Ph₂]⁻ (E = S, Se) anion and a chloride ligand around

Figure 4. Ellipsoid plot of **9**. Thermal ellipsoids are drawn at the 50% probability level. All hydrogen atoms are removed for clarity. Selected bond lengths [Å] and angles [°]: Ir(1)–Se(1) 2.5102(4), Ir(1)–N(1) 2.128(3), Ir(1)–Cl(2) 2.4161(9), Ir(1)–C$_{av}$ 2.166(4), Se(1)–P(1) 2.1591(10), P(1)–N(2) 1.610(3), N(2)–C(17) 1.324(4), N(1)–C(17) 1.335(4); Cl(2)–Ir(1)–N(1) 91.24(8), Cl(2)–Ir(1)–Se(1) 82.14(2), N(1)–Ir(1)–Se(1) 88.93(7), Ir(1)–Se(1)–P(1) 97.57(3), Se(1)–P(1)–N(2) 117.07(12), P(1)–N(2)–C(17) 125.9(3), N(1)–C(17)–N(2) 130.9(3), Ir(1)–N(1)–C(17) 122.6(2).

Figure 5. Ellipsoid plot of **11**. Thermal ellipsoids are drawn at the 50% probability level. All hydrogen atoms are removed for clarity. Selected bond lengths [Å] and angles [°]: Rh(1)–Se(1) 2.5110(7), Rh(1)–N(1) 2.132(5), Rh(1)–Cl(1) 2.4217(16), Rh(1)–C$_{av}$ 2.167(6), Se(1)–P(1) 2.1584(17), P(1)–N(2) 1.606(5), N(2)–C(17) 1.332(8), N(1)–C(17) 1.338(7); Cl(1)–Rh(1)–N(1) 93.40(13), Cl(1)–Rh(1)–Se(1) 83.26(4), N(1)–Rh(1)–Se(1) 89.69(12), Rh(1)–Se(1)–P(1) 97.30(5), Se(1)–P(1)–N(2) 117.9(2), P(1)–N(2)–C(17) 126.1(4), N(1)–C(17)–N(2) 129.8(5), Rh(1)–N(1)–C(17) 123.4(4).

the metal centre. Extensive delocalisation within the M(1)–E(1)–P(1)–N(2)–C(17)–N(1) (M = Ir, Rh) six-membered ring is evident, as indicated by the appropriate differences in bond lengths. Hence the P–Se bond lengths [2.1591(10) Å for **9**; 2.1584(17) Å for **11**] are intermediate between those expected for P–Se single and P=Se double bonds, which is supportive of regular charge delocalisation across the SePCN$_2$ framework.[15] The six-membered metallacyclic ring in **8**, **9** and **11** adopts an asymmetric boat conformation in which atoms N(1), C(17), P(1) and E(1) are essen-

tially coplanar to within approximately ±0.04 Å and N(2) and Ir(1) lie in the range 0.244–0.256 and 1.121–1.250 Å, respectively, to the same side of this plane.

The molecular structure of **14** (Figure 6) confirms the κ^2-N/S-bidentate behaviour of the [ClC$_6$H$_3$NC(S)NP(S)Ph$_2$]$^-$ anion around the square-planar Pt^{II} centre with PMe$_2$Ph/Cl$^-$ present as auxiliary ligands. Of the two possible geometric isomers that could be anticipated, the X-ray structure of **14** reveals that the N(1) donor centre is *trans* to P(2). The Pt(1)–P(2), Pt(1)–S(1), Pt(1)–N(1) and Pt(1)–Cl(1) bond

Table 1. Crystallographic data for **2**, **5**, **6** and **8**.

Compound	2	5	6	8
Empirical formula	C$_{19}$H$_{14}$ClN$_2$OPS	2(C$_{38}$H$_{26}$Cl$_2$K$_2$N$_4$O$_2$P$_2$S$_2$)·CHCl$_3$	C$_{21}$H$_{21}$ClKN$_2$O$_2$PS$_2$	C$_{29}$H$_{28}$Cl$_2$IrN$_2$PS$_2$
Formula weight	384.80	1810.98	503.04	762.72
Crystal system	orthorhombic	triclinic	triclinic	monoclinic
Space group	$P2_12_12_1$	$P\bar{1}$	$P\bar{1}$	$P2_1/n$
a [Å]	10.6308(2)	13.1740(2)	7.7261(2)	7.9797(16)
b [Å]	12.0146(4)	13.2239(2)	12.8359(3)	16.183(3)
c [Å]	13.7050(4)	13.6498(2)	13.0946(4)	21.534(4)
α [°]		107.8897(10)	68.9510(10)	
β [°]		113.0629(8)	80.0470(10)	90.41(3)
γ [°]		91.7783(8)	77.472(2)	
Volume [Å^3]	1750.47(8)	2050.76(5)	1176.66(5)	2780.7(9)
Z	4	1	2	4
T [K]	120(2)	150(2)	150(2)	150(2)
Density (calcd.) [Mg/m^3]	1.460	1.466	1.420	1.822
Absorption coeff. [mm^{-1}]	0.438	0.679	0.605	5.224
Crystal habit, colour	block, colourless	plate, colourless	block, colourless	needle, yellow
Crystal size [mm^3]	0.18 × 0.10 × 0.08	0.17 × 0.17 × 0.10	0.10 × 0.07 × 0.05	0.32 × 0.04 × 0.04
θ Range [°]	3.39–27.54	3.10–25.25	2.95–25.25	2.99–27.49
Independent reflections	4013	7398	4250	6368
R_{int}	0.0767	0.0433	0.0479	0.0523
Final R, Rw[a]	0.0406, 0.0845	0.0491, 0.1372	0.0394, 0.0978	0.0303, 0.0650

[a] $R = \Sigma||F_o| - |F_c||/\Sigma|F_o|$ for "observed" reflections having $F2 > 2\sigma$ ($F2$). $Rw = [\Sigma w(F_o^2 - F_c^2)^2/\Sigma w(F_o^2)^2]^{1/2}$ for all data.

Table 2. Crystallographic data for **9**, **11** and **14**.

Compound	9	11	14
Empirical formula	C$_{29}$H$_{28}$Cl$_2$IrN$_2$PSSe	C$_{29}$H$_{28}$Cl$_2$N$_2$PRhSSe	C$_{27}$H$_{24}$Cl$_2$N$_2$P$_2$PtS$_2$·0.91OEt$_2$·0.09CH$_2$Cl$_2$
Formula weight	809.62	720.33	843.62
Crystal system	monoclinic	monoclinic	monoclinic
Space group	$P2_1/n$	$P2_1/n$	$P2_1/n$
a [Å]	8.00540(10)	7.9701(3)	9.7390(19)
b [Å]	16.2441(3)	16.3122(8)	15.142(3)
c [Å]	21.5752(5)	21.5858(13)	23.176(5)
α [°]			
β [°]	90.4909(7)	90.811(2)	97.93(3)
γ [°]			
Volume [Å^3]	2805.55(9)	2806.1(2)	3385.0(12)
Z	4	4	4
T [K]	150(2)	120(2)	150(2)
Density (calcd.) [Mg/m^3]	1.917	1.705	1.655
Absorption coeff. [mm^{-1}]	6.401	2.251	4.561
Crystal habit, colour	block, orange	plate, orange	block, colourless
Crystal size [mm^3]	0.15 × 0.10 × 0.08	0.12 × 0.08 × 0.01	0.15 × 0.15 × 0.10
θ Range [°]	3.00–26.00	2.99–25.33	2.98–27.46
Independent reflections	5498	5083	7582
R_{int}	0.0398	0.129	0.0471
Final R, Rw[a]	0.0263, 0.0554	0.0530, 0.1067	0.0360, 0.0826

[a] $R = \Sigma||F_o| - |F_c||/\Sigma|F_o|$ for "observed" reflections having $F2 > 2\sigma$ ($F2$). $Rw = [\Sigma w(F_o^2 - F_c^2)^2/\Sigma w(F_o^2)^2]^{1/2}$ for all data.

lengths are broadly as anticipated, and the S(1)–P(1)–N(2)–C(1)–N(1) distances are similar to those found in **8** (Supporting Information).
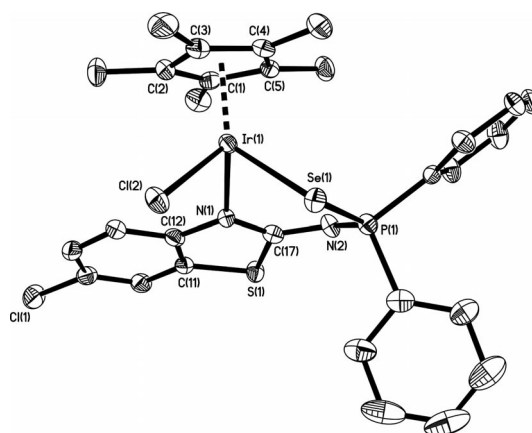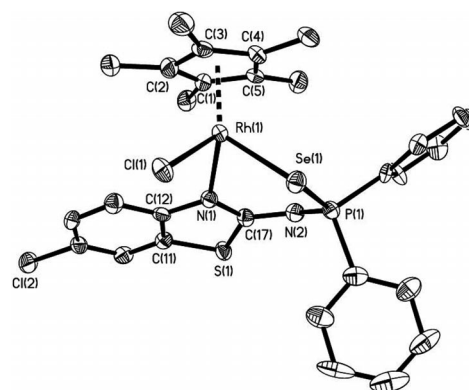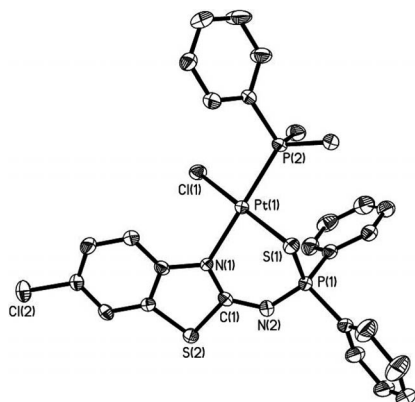

Figure 6. Ellipsoid plot of **14**. Thermal ellipsoids are drawn at the 50% probability level. All hydrogen atoms are removed for clarity. Selected bond lengths [Å] and angles [°]: Pt(1)–S(1) 2.3177(11), Pt(1)–N(1) 2.107(3), Pt(1)–Cl(1) 2.3076(11), Pt(1)–P(2) 2.2336(11), S(1)–P(1) 2.0251(17), P(1)–N(2) 1.599(4), N(2)–C(1) 1.335(5), C(1)–N(1) 1.338(5); Cl(1)–Pt(1)–N(1) 90.07(9), Cl(1)–Pt(1)–S(1) 177.78(4), N(1)–Pt(1)–S(1) 89.82(9), Pt(1)–S(1)–P(1) 89.84(5), S(1)–P(1)–N(2) 116.94(15), P(1)–N(2)–C(1) 125.3(3), N(2)–C(1)–N(1) 129.1(4), Pt(1)–N(1)–C(1) 121.6(3).

Conclusions

We observed three distinct ligating modes for a derivatised benzothiazole anion at a potassium or late transition metal centre based on Ir^{III}, Rh^{III}, Ru^{II} or Pt^{II}. Further studies are underway and will be reported in due course.

Experimental Section

Materials: The syntheses of compounds **1**–**4** were conducted under a nitrogen atmosphere whilst all other reactions were carried out under aerobic conditions. Dichloromethane was previously distilled from CaH$_2$, diethyl ether from sodium/benzophenone, thf and hexanes from sodium. The chlorido-bridged dimers [IrCl(μ-Cl)(η^5-Cp*)]$_2$,[16] [RhCl(μ-Cl)(η^5-Cp*)]$_2$,[16] [RuCl(μ-Cl)(η^6-p-Me-C$_6$H$_4$$i$Pr)]$_2$,[17] [RuCl(μ-Cl)(η^6-C$_6Me_6$)]$_2$[18] and [PtCl(μ-Cl)(PMe$_2$Ph)]$_2$[19] were synthesised according to published methods. All other solvents and chemicals were obtained from commercial suppliers. With the exception of Ph$_2$PCl, which was distilled under high vacuum prior to use, all other solvents and chemicals were used without any further purification.

Instrumentation: Fourier transform infrared (FTIR) spectra were recorded within pressed KBr pellets by using either a Perkin–Elmer system 2000 (over the range 4000–400 cm^{-1}) or Spectrum 100S (over the range 4000–250 cm^{-1}) Fourier-transform spectrometer. ^{1}H NMR and ^{31}P{^{1}H} NMR spectra were recorded with a JEOL FX90Q, Bruker AC250 FT, Bruker FX 400 or Bruker DPX-400 FT spectrometer with chemical shifts (δ) reported relative to either external tetramethylsilane (TMS) or 85% H$_3$PO$_4$. Coupling constants (J) were recorded in Hertz. All NMR spectra were recorded in CDCl$_3$ unless otherwise stated. Elemental analyses (Perkin–Elmer 2400 or Exeter Analytical Inc. CE-440 CHN Elemental Ana-

lysers) were performed by the Loughborough University Analytical Services within the Department of Chemistry. The mass spectra for **1**, **2**, **4** and **12**–**14** were analysed (JEOL SX102 instrument) by fast atom bombardment (FAB) in a positive ionisation mode by using a 3-nitrobenzyl alcohol (NOBA) matrix. Compounds **3**, **5**, **6**, **8** and **9** were analysed (Thermofisher LTQ Orbitrap XL) by nano-electrospray (nano-ESI) in a positive ionisation mode with CH$_2$Cl$_2$/CH$_3$OH as solvent and NH$_4$[OAc].

Compound 1: To a stirred solution of 6-chloroaminobenzothiazole (4.181 g, 22.64 mmol) and NEt$_3$ (2.507 g, 24.78 mmol) in diethyl ether (50 mL) at 0 °C was added dropwise a solution of Ph$_2$PCl (4.948 g, 22.43 mmol) over 30 min. The resulting white suspension was stirred for 18 h and concentrated to dryness, and degassed distilled water (50 mL) was added. Solid **1** was collected by suction filtration, washed with distilled water (50 mL), n-hexane (50 mL), absolute ethanol (2 × 30 mL) and dried in vacuo. Yield: 7.986 g (95%). ^{31}P{^{1}H} NMR (CDCl$_3$): δ = 42.5 ppm. ^{1}H NMR: δ = 7.50 (s, arom. H), 7.41–7.29 (m, arom. H), 7.20 (s, arom. H), 7.08 (s, arom. H) ppm. FTIR: ṽ = 3113 (NH), 1594 (CN), 924 (PN) cm^{-1}. FAB-MS: m/z = 369 [M]$^+$. C$_{19}$H$_{14}$ClN$_2$PS (368.8): calcd. C 61.88, H 3.83, N 7.60; found C 61.52, H 3.80, N 7.54.

Compound 2: To a stirred solution of **1** (0.192 g, 0.517 mmol) in thf (10 mL) was added aqueous H$_2$O$_2$ (30% w/w, 0.1 mL, 0.88 mmol). The solution was stirred for approximately 1 h, the volume was reduced to approximately 5 mL, and diethyl ether (30 mL) was added. The solid was collected by suction filtration, washed with diethyl ether (5 mL) and dried in vacuo. Yield: 0.193 g (97%). ^{31}P{^{1}H} NMR (CDCl$_3$): δ = 26.5 ppm. ^{1}H NMR: δ = 7.82–7.77 (m, arom. H), 7.47–7.30 (arom. H), 7.14 (dd, J = 8.6, J = 2 Hz, arom. H), 7.04 (d, J = 8.6 Hz, arom. H) ppm. FTIR: ṽ = 3076 (NH), 1631 (CN), 1163 (PO), 957 (PN) cm^{-1}. FAB-MS: m/z = 385 [M]$^+$. C$_{19}$H$_{14}$ClN$_2$OPS (384.8): calcd. C 59.30, H 3.67, N 7.28; found C 59.25, H 3.63, N 7.12.

Compound 3: The solids **1** (1.000 g, 2.696 mmol) and S$_8$ (0.086 g, 2.682 mmol) were stirred in thf (20 mL) for 4 h. The solvent was concentrated in vacuo to approximately 1–2 mL, and addition of diethyl ether (30 mL) resulted in a pale yellow solid **3**. The product was collected by suction filtration, washed with diethyl ether (5 mL) and dried in vacuo. Yield: 1.028 g (95%). ^{31}P{^{1}H} NMR (CDCl$_3$): δ = 49.5 ppm. ^{1}H NMR: δ = 8.01–7.87 (m, arom. H), 7.41–7.33 (arom. H), 7.17 (dd, J = 8.6, J = 2 Hz, arom. H), 7.01 (d, J = 8.6 Hz, arom. H) ppm. FTIR: ṽ = 3181 (NH), 1624 (CN), 948 (PN), 626 (PS) cm^{-1}. FAB-MS: m/z = 401 [M]$^+$. C$_{19}$H$_{14}$ClN$_2$PS$_2$ (400.9): calcd. C 56.93, H 3.52, N 6.99; found C 56.92, H 3.61, N 6.84.

Compound 4: The solids **1** (0.165 g, 0.445 mmol) and grey Se (0.036 g, 0.456 mmol) were stirred in thf (20 mL) for 4 h. Unreacted Se was removed by filtration through a Celite pad. The solvent was concentrated in vacuo to approximately 1–2 mL, and addition of diethyl ether (30 mL) resulted in a colourless solid **4**. The product was collected by suction filtration, washed with diethyl ether (5 mL) and dried in vacuo. Yield: 0.175 g (88%). ^{31}P{^{1}H} NMR [CDCl$_3$/(CD$_3$)$_2$SO]: δ = 43.9 ($^1J_{PSe}$ = 726 Hz) ppm. ^{1}H NMR: δ = 7.92–7.87 (m, arom. H), 7.37–7.35 (arom. H), 7.18 (dd, J = 8.5, J = 2 Hz, arom. H), 7.02 (d, J = 8.5 Hz, arom. H) ppm. FTIR: ṽ = 3070 (NH), 1619 (CN), 948 (PN), 586 (PSe) cm^{-1}. FAB-MS: m/z = 449 [M]$^+$. C$_{19}$H$_{14}$ClN$_2$PSSe (447.8): calcd. C 50.96, H 3.15, N 6.26; found C 51.11, H 2.94, N, 6.12.

Potassium Salts 5–7: An illustrative example is given here for the synthesis of compound **5**. To a suspension of **2** (0.100 g, 0.260 mmol) in MeOH (10 mL) was added tBuOK (0.029 g, 0.258 mmol). The solution was stirred for 18 h and concentrated to

dryness to afford the moisture-sensitive solid **5**. Yield: 0.087 g (65%). Selected data for **5**: ^{31}P{^{1}H} NMR (CD$_3$OD): δ = 23.8 ppm. ^{1}H NMR (CD$_3$OD): δ = 7.91–7.07 (arom. H) ppm. FTIR: $\tilde{\nu}$ = 1220 (PO), 965 (PN) cm^{-1}. FAB-MS: m/z = 385 [M – K + 2H]$^+$. C$_{19}$H$_{13}$ClKN$_2$OPS·0.5CHCl$_3$ (482.6): calcd. C 48.53, H 2.83, N 5.81; found C 49.17, H 2.70, N 5.47. The sulfide analogue **6** was prepared in 67% yield. Selected data for **6**: ^{31}P{^{1}H} NMR (CD$_3$OD): δ = 47.4 ppm. ^{1}H NMR: δ = 8.05–7.02 (arom. H) ppm. FTIR: $\tilde{\nu}$ = 962 (PN), 610 (PS) cm^{-1}. FAB-MS: m/z = 401 [M – K(CH$_3$OH)$_2$]$^+$. C$_{19}$H$_{13}$ClKN$_2$PS$_2$·2H$_2$O (475.0): calcd. C 48.04, H 3.61, N 5.90; found C 47.49, H 3.50, N 5.48. The selenide analogue **7** was similarly prepared in quantitative yield from **4**. Selected data for **7**: ^{31}P{^{1}H} NMR [(CD$_3$)$_2$SO]: δ = 33.3 ($^1J_{PSe}$ = 697 Hz) ppm. ^{1}H NMR: δ = 7.95–7.05 (arom. H) ppm. C$_{19}$H$_{13}$ClKN$_2$PSSe·4H$_2$O (557.9): calcd. C 40.90, H 3.80, N 5.02; found C 40.61, H 2.39, N 4.57.

Complexes 8–14: An illustrative example is given here for the synthesis of compound **9**. To an orange suspension of [IrCl(μ-Cl)(η^5-Cp*)]$_2$ (0.058 g, 0.073 mmol) in thf (10 mL) were added **4** (0.065 g, 0.145 mmol) and *t*BuOK (0.017 g, 0.151 mmol). The orange solution was stirred at room temp. for approximately 3 h and concentrated to dryness under reduced pressure. The residue was extracted into CH$_2$Cl$_2$ (10 mL), filtered through a Celite plug and concentrated to approximately 1 mL. Addition of diethyl ether (20 mL) afforded a yellow solid, which was collected by suction filtration and dried in vacuo. Yield: 0.098 g (80%). Selected data for **9**: ^{31}P{^{1}H} NMR (CDCl$_3$): δ = 11.9 ($^1J_{PSe}$ = 554 Hz) ppm. ^{1}H NMR: δ = 8.22 (d, J = 8.8 Hz, arom. H), 8.10 (m, arom. H), 7.66 (m, arom. H), 7.45 (m, arom. H), 7.29 (d, J = 2.4 Hz, arom. H), 7.23 (m, arom. H), 7.13 (dd, J = 8.8, J = 2.1 Hz, arom. H), 1.30 (Cp*) ppm. FTIR: $\tilde{\nu}$ = 1492 (CN), 577 (PSe) cm^{-1}. FAB-MS: m/z = 775 [M – Cl]$^+$. C$_{29}$H$_{28}$Cl$_2$IrN$_2$PSSe (810.4): calcd. C 42.98, H 3.49, N 3.46; found C 42.72, H 3.47, N 3.41. In a similar manner, complex **8** was prepared in 78% yield. Selected data for **8**: ^{31}P{^{1}H} NMR (CDCl$_3$): δ = 23.1 ppm. ^{1}H NMR: δ = 8.13–8.08 (m, arom. H), 7.72 (m, arom. H), 7.46 (m, arom. H), 7.29–7.21 (m, arom. H), 7.12 (dd, J = 8.8, J = 2.4 Hz, arom. H), 1.30 (Cp*) ppm. FTIR: $\tilde{\nu}$ = 1493 (CN), 601 (PS) cm^{-1}. FAB-MS: m/z = 726 [M – Cl]$^+$. C$_{29}$H$_{28}$Cl$_2$IrN$_2$PS$_2$ (763.5): calcd. C 45.62, H 3.70, N 3.67; found C 45.45, H 3.47, N 3.45. Complexes **10–14** were prepared from the isolated potassium salts **6** or **7** and the appropriate chlorido-bridged dimer (isolated yields given in parentheses): **10** (77%), **11** (56%), **12** (84%), **13** (75%), **14** (60%). Selected data for **10**: ^{31}P{^{1}H} NMR (CDCl$_3$): δ = 27.8 ppm. ^{1}H NMR: δ = 8.31 (d, J = 8.8 Hz, arom. H), 8.12 (m, arom. H), 7.71 (m, arom. H), 7.45 (m, arom. H), 7.30 (d, J = 2.2 Hz, arom. H), 7.14 (dd, J = 8.8, J = 2.2 Hz, arom. H), 1.31 (Cp*) ppm. FTIR: $\tilde{\nu}$ = 1494 (CN), 601 (PS) cm^{-1}. C$_{29}$H$_{28}$Cl$_2$N$_2$PRhS$_2$ (673.5): calcd. C 51.71, H 4.20, N 4.16; found C 51.43, H 4.17, N 3.94. Selected data for **11**: ^{31}P{^{1}H} NMR (CDCl$_3$): δ = 16.7 ($^1J_{PSe}$ 564 Hz, $^2J_{PRh}$ 3.8 Hz) ppm. ^{1}H NMR: δ = 8.44 (d, J = 8.9 Hz, arom. H), 8.14 (m, arom. H), 7.65 (m, arom. H), 7.46 (m, arom. H), 7.32 (d, J = 2.2 Hz, arom. H), 7.16 (dd, J = 8.9, J = 2.2 Hz, arom. H), 1.32 (Cp*) ppm. FTIR: $\tilde{\nu}$ = 1487 (CN), 576 (PSe) cm^{-1}. C$_{29}$H$_{28}$Cl$_2$N$_2$PRhSSe (720.26): calcd. C 48.36, H 3.93, N 3.89; found C 48.10, H 3.76, N 3.86. Selected data for **12**: ^{31}P{^{1}H} NMR (CDCl$_3$): δ = 31.7 ppm. ^{1}H NMR: δ = 8.34 (d, J = 8.9 Hz, arom. H), 8.28–7.21 (m, arom. H), 7.15 (dd, J = 8.9, J = 2.2 Hz, arom. H), 5.54 (d, J = 5.4 Hz, cym), 5.24 (d, J = 6.1 Hz, cym), 5.13 (d, J = 5.4 Hz, cym), 4.44 (d, J = 5.8 Hz, cym), 2.77 (sept, CH), 2.10 (s, CH$_3$), 1.50 (Cp*), 1.13 (virtual t, CH$_3$) ppm. FTIR: $\tilde{\nu}$ = 1493 (CN), 606 (PS) cm^{-1}. FAB-MS: m/z = 670 [M]$^+$. C$_{29}$H$_{27}$Cl$_2$N$_2$PRuS$_2$ (670.7): calcd. C 51.93, H 4.07, N 4.18; found C 52.11, H 4.25, N 3.76. Selected data for **13**: ^{31}P{^{1}H} NMR

(CDCl$_3$): δ = 27.3 ppm. ^{1}H NMR: δ = 8.29 (d, J = 8.8 Hz, arom. H), 8.11 (m, arom. H), 7.63 (m, arom. H), 7.44 (m, arom. H), 7.29 (d, J = 2.3 Hz, arom. H), 7.14 (m, arom. H), 1.76 (s, CH$_3$) ppm. FTIR: $\tilde{\nu}$ = 1486 (CN), 602 (PS) cm^{-1}. FAB-MS: m/z = 698 [M]$^+$. C$_{31}$H$_{31}$Cl$_2$N$_2$PRuS$_2$ (698.7): calcd. C 53.29, H 4.48, N 4.01; found C 53.17, H 4.33, N 3.83. Selected data for **14**: ^{31}P{^{1}H} NMR (CDCl$_3$): δ = –20.3 ($^1J_{PPt}$ = 3385 Hz), 27.1 ($^2J_{PPt}$ = 138 Hz) ppm. ^{1}H NMR: δ = 7.94 (d, J = 8.8 Hz, arom. H), 7.83 (m, arom. H), 7.49–7.27 (m, arom. H), 7.14 (dd, J = 8.8, J = 2.2 Hz, arom. H), 1.49 (br. s, CH$_3$) ppm. FTIR: $\tilde{\nu}$ = 1496 (CN), 597 (PS) cm^{-1}. FAB-MS: m/z = 767 [M]$^+$. C$_{27}$H$_{24}$Cl$_2$N$_2$P$_2$PtS$_2$ (768.6): calcd. C 42.19, H 3.15, N 3.65; found C 42.58, H 3.57, N 3.40.

Single-Crystal X-ray Structure Determinations: Slow diffusion of hexanes into a CDCl$_3$ solution of **2** gave suitable crystals. Vapour diffusion of Et$_2$O into a CDCl$_3$/MeCN solution of **5** gave suitable crystals. Slow concentration of a MeOH solution of **6** gave suitable crystals. X-ray quality crystals of **8**, **9** and **11** were obtained upon slow diffusion of petroleum ether (b.p. 60–80 °C) into a CDCl$_3$ solution. Vapour diffusion of Et$_2$O into a CDCl$_3$ solution of **14** gave suitable crystals. Measurements for **2**, **5**, **6**, **8**, **9**, **11** and **14** were obtained with a Nonius κ CCD area-detector diffractometer mounted at the window of a rotating molybdenum anode, and Ω scans were employed such that 95% of the unique data were recorded at least once. Data collection and processing were carried out with the programs COLLECT[20] and DENZO,[21] and an empirical absorption correction was applied with SORTAV.[22] The structures were solved by direct methods or Patterson synthesis[23,24] and refined by full-matrix least-squares[24] on F^2. Non-hydrogen atoms were refined anisotropically, and hydrogen atoms were treated by using a riding model, except for O*H* in **6**, for which coordinates were freely refined. Disordered CH$_2$Cl$_2$ (9%) in **14** was isotropically modelled. CCDC-223295 (for **14**), -838885 (for **5**), -838886 (for **6**), -838887 (for **9**), -852752 (for **2**), -852753 (for **8**) and -852754 (for **11**) contain the supplementary crystallographic data for this paper. These data can be obtained free of charge from The Cambridge Crystallographic Data Centre via www.ccdc.cam. ac.uk/data_request/cif.

Supporting Information (see footnote on the first page of this article): Additional X-ray figures for **5**, **6** and **8**.

Acknowledgments

[1] For recent examples of amidinate chemistry, see: a) S. Collins, *Coord. Chem. Rev.* **2011**, *255*, 118–138; b) E. F. Trunkely, A. Epshteyn, P. Y. Zavalij, L. R. Sita, *Organometallics* **2010**, *29*, 6587–6593; c) J. R. Walensky, R. L. Martin, J. W. Ziller, W. J. Evans, *Inorg. Chem.* **2010**, *49*, 10007–10012.

[2] For recent examples of guanidinate chemistry, see: a) C. Jones, C. Schulten, L. Fohlmeister, A. Stasch, K. S. Murray, B. Moubaraki, S. Kohl, M. Z. Ertem, L. Gagliardi, C. J. Cramer, *Chem. Eur. J.* **2011**, *17*, 1294–1303; b) J.-U. Rohde, W.-T. Lee, *J. Am. Chem. Soc.* **2009**, *131*, 9162–9163.

[3] For recent examples of β-diketiminate (nacnac$^-$) chemistry, see: a) M. M. Khusniyarov, E. Bill, T. Weyhermüller, E. Bothe, K. Wieghardt, *Angew. Chem. Int. Ed.* **2011**, *50*, 1652–1655; b) M. L. Scheuermann, U. Fekl, W. Kaminsky, K. I. Goldberg, *Organometallics* **2010**, *29*, 4749–4751; c) V. T. Annibale, L. M. Lund, D. Song, *Chem. Commun.* **2010**, *46*, 8261–8263.

[4] For recent examples of bis(phosphinimino)methanide chemistry, see: a) G. Ma, M. J. Ferguson, R. G. Cavell, *Chem. Commun.* **2010**, *46*, 5370–5372; b) A. Buchard, R. H. Platel, A. Auffrant, X. F. Le Goff, P. Le Floch, C. K. Williams, *Organometallics* **2010**, *29*, 2892–2900; c) S. Schulz, S. Gondzik, D. Schuchmann, U. Westphal, L. Dobrzycki, R. Boese, S. Harder, *Chem. Commun.* **2010**, *46*, 7757–7759.

[5] For recent examples of imidodiphosphinate chemistry, see: a) E. Ferentinos, D. Maganas, C. P. Raptopoulou, A. Terzis, V. Psycharis, N. Robertson, P. Kyritsis, *Dalton Trans.* **2011**, *40*, 169–180; b) T. Chivers, J. S. Ritch, S. D. Robertson, J. Konu, H. M. Tuononen, *Acc. Chem. Res.* **2010**, *43*, 1053–1062; c) D. Oyetunde, M. Afzaal, M. A. Vincent, I. H. Hillier, P. O'Brien, *Inorg. Chem.* **2011**, *50*, 2052–2054; d) S. D. Robertson, T. Chivers, J. Akhtar, M. Afzaal, P. O'Brien, *Dalton Trans.* **2008**, 7004–7011.

[6] a) S. E. Durran, M. R. J. Elsegood, S. R. Hammond, M. B. Smith, *Dalton Trans.* **2010**, *39*, 7136–7146; b) S. E. Durran, M. R. J. Elsegood, S. R. Hammond, M. B. Smith, *Inorg. Chem.* **2007**, *46*, 2755–2766; c) M. R. J. Elsegood, M. B. Smith, P. M. Staniland, *Inorg. Chem.* **2006**, *45*, 6761–6770.

[7] a) P. C. Kunz, C. Wetzel, M. Bongartz, A. L. Noffke, B. Spingler, *J. Organomet. Chem.* **2010**, *695*, 1891–1897; b) Z. García-Hernández, A. Flores-Parra, J. M. Grevy, A. Ramos-Organillo, R. Contreras, *Polyhedron* **2006**, *25*, 1662–1672; c) H. L. Milton, M. V. Wheatley, A. M. Z. Slawin, J. D. Woollins, *Inorg. Chim. Acta* **2005**, *358*, 1393–1400.

[8] a) S. Zhang, R. Pattacini, P. Braunstein, *Organometallics* **2010**, *29*, 6660–6667; b) W. Lackner-Warton, S. Tanaka, C. M. Standfest-Hauser, O. Öztopcu, J.-C. Hsieh, K. Mereiter, K. Kirchner, *Polyhedron* **2010**, *29*, 3097–3012; c) G. Margraf, R. Pattacini, A. Messaoudi, P. Braunstein, *Chem. Commun.* **2006**, 3098–3100.

[9] P. Bhattacharryya, A. M. Z. Slawin, M. B. Smith, *J. Chem. Soc., Dalton Trans.* **1998**, 2467–2475.

[10] V. V. Sushev, N. V. Belina, G. K. Fukin, Y. A. Kurskiy, A. N. Kornev, G. A. Abakumov, *Inorg. Chem.* **2008**, *47*, 2608–2612.

[11] A. Bondi, *J. Phys. Chem.* **1964**, *68*, 441–451.

[12] P. Gantzel, P. J. Walsh, *Inorg. Chem.* **1998**, *37*, 3450–3451.

[13] A. M. Z. Slawin, J. Ward, D. J. Williams, J. D. Woollins, *J. Chem. Soc., Chem. Commun.* **1994**, 421–422.

[14] a) Y.-L. Hsu, L.-C. Liang, *Organometallics* **2010**, *29*, 6201–6208; b) K. Izod, J. Young, W. Clegg, R. W. Harrington, *Dalton Trans.* **2005**, 1658–1663.

[15] a) M. Risto, J. Konu, T. Chivers, *Inorg. Chem.* **2011**, *50*, 406–408; b) J. D. Woollins, *J. Chem. Soc., Dalton Trans.* **1996**, 2893–2901.

[16] C. White, A. Yates, P. M. Maitlis, *Inorg. Synth.* **1992**, *29*, 228–234.

[17] M. A. Bennet, T. N. Huang, T. W. Matheson, A. R. Smith, *Inorg. Synth.* **1982**, *21*, 74–78.

[18] M. A. Bennet, A. K. Smith, *J. Chem. Soc., Dalton Trans.* **1974**, 233–241.

[19] W. Baratta, P. S. Pregosin, *Inorg. Chim. Acta* **1993**, *209*, 85–87.

[20] COLLECT Data Collection Software, R. Hooft, Nonius B. V. **1998**.

[21] DENZO: Z. Otwinowski, W. Minor, in *Methods in Enzymology, Macromolecular Crystallography, Part A, Vol. 276* (Eds.: C. W. Carter Jr., R. M. Sweet), Academic Press, **1997**, p. 307.

[22] SORTAV: R. H. Blessing, *Acta Crystallogr., Sect. A* **1995**, *51*, 33–38.

[23] a) R. H. Blessing, *J. Appl. Crystallogr.* **1997**, *30*, 421–426; b) DIRDIF-96: A Computer Program System for Crystal Structure Determination by Patterson Methods and Direct Methods Applied to Difference Structure Factors, P. T. Beurskens, G. Beurskens, W. P. Bosman, R. De Gelda, S. Garcia-Granda, R. O. Gould, R. Isräel, J. M. M. Smits, Crystallography Laboratory, University of Nijmegen, The Netherlands, **1996**.

[24] G. M. Sheldrick, *Acta Crystallogr., Sect. A* **2008**, *64*, 112–120.

FULL PAPER

Energetic Salts of Symmetrical Dimethylhydrazine (SDMH)

Carles Miró Sabaté*[a] and Henri Delalu[a]

N,*N*′-Dimethylhydrazine and several of its salts with energetic anions were synthesized and fully characterized by elemental analysis, DSC, mass spectrometry, multinuclear NMR (^{1}H, ^{13}C, and ^{15}N) spectroscopy, and vibrational (Raman, IR) spectroscopy. According to the DSC measurements, the compounds exhibit good thermal stabilities, and the nitrate (**2**) and dicyanamide (**4**) salts belong to the ionic-liquid type (i.e., $T_m < 100$ °C). Additionally, the solid-state crystal structure of the nitrate [**2**: triclinic, $P\bar{1}$, $a = 5.360(2)$ Å, $b = 5.806(2)$ Å, $c = 6.866(2)$ Å, $\alpha = 113.73(2)°$, $\beta = 92.44(2)°$, $\gamma = 90.08(2)°$, $V = 195.4(1)$ Å^3], perchlorate [**3**: orthorhombic, *Pbca*, $a = 11.774(2)$ Å, $b = 11.072(3)$ Å, $c = 14.050(3)$ Å, $V = 1831.6(7)$ Å^3], sulfate [**5**: monoclinic, $P2_1/n$, $a = 5.913(1)$ Å, $b = 9.509(1)$ Å, $c = 10.351(1)$ Å, $\beta = 90.29(1)°$, $V = 582.0(1)$ Å^3],

monopicrate [**6b**: monoclinic, $P2_1/c$, $a = 10.910(1)$ Å, $b = 6.7436(1)$ Å, $c = 16.442(2)$ Å, $\beta = 103.40(1)°$, $V = 1176.7(2)$ Å^3], and dipicrate dihydrate [**6**·2H$_2$O: monoclinic, $P2_1/n$, $a = 8.230(1)$ Å, $b = 13.024(1)$ Å, $c = 10.642(1)$ Å, $\beta = 104.43(1)°$, $V = 1104.7(2)$ Å^3] salts were determined. Furthermore, a natural bond orbital (NBO) analysis of the structure of the [MeNH$_2$–NH$_2$Me]$^{2+}$ cation was performed. Standard tests were used to examine the sensitivity of the compounds towards impact, friction, and electrostatic discharge. Lastly, the heats of formation of the compounds were calculated by means of quantum chemical calculations and used to determine the detonation parameters and specific impulses of the compounds and those of mixtures with an oxidizer.

Introduction

Hydrazine (H$_2$N–NH$_2$) and methylated hydrazines such as MeNH–NH$_2$ (MMH = monomethylhydrazine) or Me$_2$N–NH$_2$ (UDMH = unsymmetrical dimethylhydrazine) (Figure 1) are widely used as hypergolic bipropellants in combination with oxidizers such as N$_2$O$_4$ (NTO = nitrogen tetroxide), RFNA (red fuming nitric acid), or LOX (liquid oxygen). However, many concerns have been raised in the recent past about the explosive nature of high-purity liquid hydrazines in the presence of an oxidizer and, in particular, the relationship with the high toxicity and carcinogenic character of these compounds.[1]

On the other hand, commonly used high explosives such as TNT (2,4,6-trinitrotoluene) or RDX (1,3,5-trinitroperhydro-1,3,5-triazine) generally suffer from high sensitivities, low performances, detrimental decomposition gases, high production costs, and incompatibility issues. In comparison to neutral compounds, salt-based materials are often advantageous due to their lower vapor pressures and higher densities.[2] Additionally, salt-based energetic materials tend to form extensive hydrogen-bonded networks, which results in lower sensitivities and higher thermal and chemical stabilities than commonly used high explosives.

Figure 1. Formula drawings of (a) hydrazine, (b) monomethylhydrazine (MMH), (c) unsymmetrical dimethylhydrazine (UDMH), (d) symmetrical dimethylhydrazine (SDMH), (e) 2,4,6-trinitrotoluene (TNT), and (f) 1,3,5-trinitroperhydro-1,3,5-triazine (RDX).

In this context, the synthesis of salt-based compounds has been the focus of much attention in the last few years.[3] The anion can be of inorganic nature (e.g., nitrate, perchlorate, and azide)[4] as well as organic (e.g., picrate,[5] 5,5′-azotetrazolate,[6] and 3-nitrotriazolate).[7] Although many salt-based energetic derivatives of hydrazine,[8] MeNH–NH$_2$,[9] and Me$_2$N–NH$_2$[10] are known, energetic salts of the less readily available MeNH–NHMe (SDMH = symmetrical dimethylhydrazine) have only been poorly studied if at all. To the best of our knowledge, the only examples of salts of MeNH–NHMe reported in the international literature

[a] Laboratoire Hydrazines et Composés Ènergétiques Polyazotés, Université Claude Bernard Lyon 1, Bâtiment Berthollet, 3è étage,
22, avenue Gaston Berger, 69622 Villeurbanne, France
Fax: +33-4-72431291
E-mail: carlos.miro-sabate@univ-lyon1.fr

are the 5,5′-azotetrazolate[11] and azide[12] salts of the [MeNH$_2$–NHMe]$^+$ cation and the sulfate (synthesis in the gas phase)[13] and chloride[14] salts that contain the [MeNH$_2$–NH$_2$Me]$^{2+}$ cation. Therefore, in view of their possible interest for energetic applications, we decided to undertake the synthesis, full characterization, and study of the energetic properties of salts of MeNH–NHMe with energetic anions that have previously been considered for the synthesis of energetic salts.

Results and Discussion

Syntheses

The metathesis reaction of the chloride salt {[MeNH$_2$–NH$_2$Me]Cl$_2$ (**1**)} with a suitable silver salt in water or alcohol led, upon filtration of the insoluble silver chloride, to the isolation of the nitrate {[MeNH$_2$–NH$_2$Me][NO$_3$]$_2$ (**2**)}, perchlorate {[MeNH$_2$–NH$_2$Me][ClO$_4$]$_2$ (**3**)}, dicyanamide {[MeNH$_2$–NH$_2$Me][N(CN)$_2$]$_2$ (**4**)}, and sulfate {[MeNH$_2$–NH$_2$Me][SO$_4$] (**5**)} salts. Subsequent treatment of the sulfate salt (**5**) with barium picrate hexahydrate led to the formation of insoluble barium sulfate and the isolation of the corresponding picrate salt {[MeNH$_2$–NH$_2$Me]-[(NO$_2$)$_3$Ph–O] (**6**)} (see Scheme 1). Alternatively, **6** could be conveniently prepared by the deprotonation of **1** with sodium hydroxide to form the MeNH–NHMe free base, which was added to a suspension of picric acid in ether, thereby leading to the precipitation of **6** in high purity and quantitative yield. Lastly, two methods for the synthesis of the 5-aminotetrazolate salt (**7**) in analogy to those used for the picrate salt **6** were used. However, in both cases, 5-amino-1H-tetrazole monohydrate was recovered (see the Experimental Section).

Compounds **1**–**6** are readily soluble in DMSO, water, and alcohols such as methanol, ethanol, or iPrOH, and insoluble in apolar or less-polar solvents such as ether or cyclohexane.
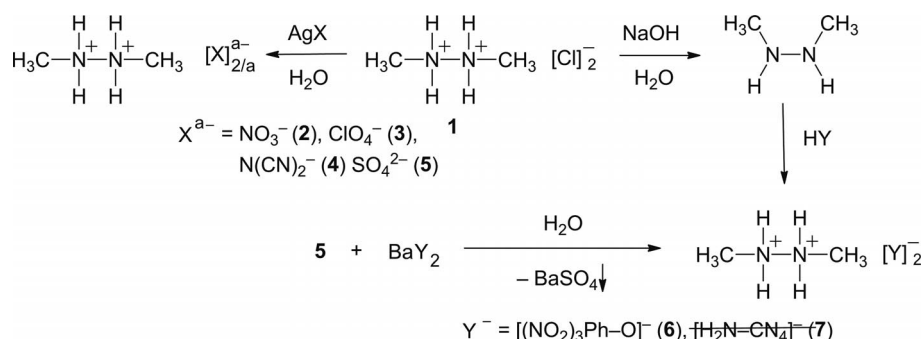
Vibrational and NMR Spectroscopy

Computational Details

The (gas-phase) geometry of the [MeNH$_2$–NH$_2$Me]$^{2+}$ cation was fully optimized using DFT calculations

(B3LYP)[15,16] at the 6-311+G(d,p) level of theory. The optimized geometry was a minimum on the potential-energy surface and no imaginary frequencies were found. The optimized structure was used to calculate the vibrational frequencies with the corresponding infrared (IR) intensities and Raman activities (Gaussian 03W package).[17] The obtained raw frequencies were scaled (by a factor of 0.9613 for the B3LYP method) as suggested by Scott et al.[18]

Table S1 in the Supporting Information contains the results of the frequency calculations (i.e., scaled frequencies with IR intensities and Raman activities) together with averaged values found experimentally for the salts of the [MeNH$_2$–NH$_2$Me]$^{2+}$ cation in this work and assignment of the vibration modes. As expected, the calculated frequencies tend to systematically overestimate the experimental values.[19] However, there is little difference in the frequencies obtained from the IR and Raman measurements of all compounds, thus indicating important similarities in the solid-state structure of the [MeNH$_2$–NH$_2$Me]$^{2+}$ cation in the different salts, as confirmed by X-ray diffraction analysis (see discussion below). The most intense band in the Raman spectra of the salts of the synthesized [MeNH$_2$–NH$_2$Me]$^{2+}$ cation corresponds to the vibration modes of the different anions, observed at 1050 cm^{-1} [nitrate, ν(NO$_3$)],[20] 931 and 459 cm^{-1} [perchlorate, ν(ClO$_4$) and δ(ClO$_4$)],[21] 2177 cm^{-1} [dicyanamide, ν(CN)],[22] 971 cm^{-1} [sulfate, ν(SO$_4$)],[23] and 1344 and 1296 cm^{-1} [picrate, ν(NO$_2$)].[24] As for the [MeNH$_2$–NH$_2$Me]$^{2+}$ cation, the most intense band in the Raman spectra corresponds to a combined C–H torsion and N–H rocking vibration observed at $\tilde{\nu} \approx 1070$ cm^{-1}. On the other hand, the IR spectra are dominated by bands of medium intensity that obscure the vibrations of the anion and the most intense vibration corresponds to the out-of-plane bending of the N–H and C–H bonds ($\tilde{\nu} \approx 1290$ cm^{-1}). The remainder of the vibrations are of lower intensity and can be assigned as follows (ν = stretching, δ = in-plane bending, γ = out-of-plane bending, ω = in-plane rocking, τ = torsion, s = symmetric, as = antisymmetric): 2950–3005 [ν_s(N–H) and ν_{as}(N–H)], 2750–2860 [ν_s(C–H) and ν_{as}(C–H)], 1550–1760 [δ_s(N–H) and δ_{as}(N–H)], 1270–1490 [γ(N–H)], 1450–1500 [δ_s(C–H) and δ_{as}(C–H)], 1435 [τ(C–H) and τ(N–H)], 920–1400 [γ(C–H)], 1030–1120 [τ(C–H) and τ(N–H)], <820 [ω(N–H) and ω(C–H)], and 730–860 cm^{-1} [ν(C–N) + ν(N–N)].[25] Note that the free base MeNH–NHMe

Scheme 1. Reaction scheme for the synthesis of salts of the [MeNH$_2$–NH$_2$Me]$^{2+}$ cation.

Table 1. ^1H, ^{13}C, and ^{15}N NMR spectroscopic chemical shifts [ppm] for the $[MeNH_2–NH_2Me]^{2+}$ cation in compounds **1–6**.[a]

| | ^1H NMR | | ^{13}C NMR | ^{15}N NMR[b] |
	N–CH₃	NH	N–CH₃	N–CH₃
MeNH–NHMe	2.36	4.07	36.9	+97.5
[MeNH₂–NH₂Me]Cl₂ (**1**)	2.57	9.26	34.6	
[MeNH₂–NH₂Me][NO₃]₂ (**2**)	2.55	10.15	35.1	+75.2 (–22.3)[c]
[MeNH₂–NH₂Me][ClO₄]₂ (**3**)	2.58	10.21	35.1	
[MeNH₂–NH₂Me][N(CN)₂]₂ (**4**)	2.57	7.89	35.2	
[MeNH₂–NH₂Me][SO₄] (**5**)	2.58	7.76	35.0	
[MeNH₂–NH₂Me][(NO₂)₃Ph–O] (**6**)	2.60	8.46	34.8	

[a] In [D₆]DMSO. [b] NH₃ was used as an external standard. [c] PIS [ppm].

shows similar IR frequencies (see the Experimental Section); however, it suffers from Raman fluorescence.

Multinuclear NMR spectroscopic studies (^1H, ^{13}C, and ^{15}N) were used to obtain information about the $[MeNH_2–NH_2Me]^{2+}$ cation in solution. These results are summarized in Table 1 together with the corresponding shifts for MeNH–NHMe. In the ^1H NMR spectra of salts **1–6** in [D₆]DMSO, two resonances are observed. The –CH₃ groups resonate at approximately $\delta = 2.60$ ppm, whereas the –NH groups have broad resonances in the range between approximately 7.70 and 10.20 ppm. Both these signals are shifted to low field in comparison to the analogous signals in MeNH–NHMe [$\delta = 2.36$ (–CH₃) and 4.07 ppm (N–H)]. In the ^{13}C NMR spectra, the –CH₃ groups of compounds **1–6** have very consistent resonances at approximately 35.0 ppm, which are shifted to high field relative to the free base ($\delta = 36.9$ ppm). Additionally, the ^{15}N NMR spectrum of the nitrate salt (**2**) was measured (see Figure 2) as a representative example of a salt that contained the $[MeNH_2–NH_2Me]^{2+}$ cation. In comparison to MeNH–NHMe, the nitrogen atoms in **2** show a proton-induced shift (PIS)[26] of $\delta = –22.3$ ppm.
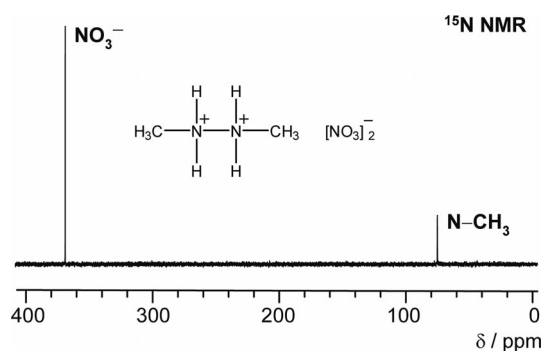
Figure 2. ^{15}N NMR spectrum of $[MeNH_2–NH_2Me][NO_3]_2$ (**2**) in [D₆]DMSO.

Crystal Structures

Low-temperature X-ray diffraction analysis was used to determine the solid-state structure of the salts of MeNH–NHMe, **2**, **3**, **5**, **6b**, and **6·2H₂O**. X-ray-quality single crystals were grown as described below (see the Experimental Section). An Oxford Diffraction Xcalibur 3 diffractometer equipped with a CCD detector using the CrysAlis CCD software was used for the measurements,[27] and the CrysAlis RED software was used to reduce the data.[28] All data were collected using graphite-monochromated Mo-K_α radiation ($\lambda = 0.71073$ Å). The structures were solved by direct methods and refined by means of full-matrix least-squares procedures using WinGX and the available software in the package.[29–32] Finally, the structures were checked using PLATON.[33] The absorption corrections were performed using a SCALE3 ABSPACK multiscan method.[34] All non-hydrogen atoms were refined anisotropically, whereas the hydrogen atoms were located from difference Fourier electron density maps and refined isotropically.

The crystal-structure solution and refinement data of salts **2**, **3**, **5**, **6b**, and **6·2H₂O** are summarized in Table 2. A record of the C–N and N–N bond lengths and angles of the $[MeNH_2–NH_2Me]^{2+}$ cation ($[MeNH_2–NHMe]^+$ cation for **6b**) has been collected in Table 3 together with the DFT-optimized parameters using a B3LYP/6-311+G(d,p) basis set. Additionally, the geometry of medium to strong hydrogen bonds found in the structure of the compounds as well as the results of the graph-set analysis can be found in the Supporting Information (see Tables S2, S3, S4, S5, S6, and S7, respectively). Lastly, the CIF files of the compounds have been deposited at the Cambridge Crystallographic Data Centre.[35]

To the best of our knowledge, the only salt of MeNH–NHMe that has been structurally characterized is its monoazide $[MeNH_2–NHMe][N_3]$.[12] No crystallographic reports that describe compounds based on $[RNH_2–NH_2R']^{2+}$ (with R and R' = alkyl, aryl, acyl, and so on) can be found among the CCDC data, and in addition to the azide report mentioned above, only four matches can be found for salts based on a $[RNH_2–NHR']^+$ cation.[36] For example, the solid-state structure of pyrazolidinium azide was reported by Klapötke et al.[36d]

Apart from compounds **2** and **3**, which have a triclinic and an orthorhombic cell of the space groups $P\bar{1}$ and $Pbca$, respectively (see Table 2), the remainder of the compounds crystallize in monoclinic cells of the space group $P2_1/n$ (**5** and **6·2H₂O**) and $P2_1/c$ (**6b**).

To obtain a better understanding of the structure of the $[MeNH_2–NH_2Me]^{2+}$ cation, its gas-phase structure was optimized by using B3LYP functional analyses with a 6-311+G(d,p) basis set.[37] As can be expected from the lack of molecular packing in the gas phase, the computed bond lengths and angles for the $[MeNH_2–NH_2Me]^{2+}$ cation over-

Table 2. Crystal-structure solution and refinement of salts of MeNH–HMe.[a]

	2	3	5	6b	6·2H₂O
Formula	$C_2H_{10}N_4O_6$	$C_2H_{10}N_2Cl_2O_8$	$C_2H_{10}N_2O_4S$	$C_8H_{11}N_5O_7$	$C_{14}H_{18}N_8O_{16}$
M_r	186.14	261.02	158.18	289.20	554.34
T [K]	293(2)	293(2)	110(2)	110(2)	110(2)
Crystal shape	needles	block	plate	needles	plate
Color	colorless	colorless	colorless	yellow	yellow
Crystal size	$0.052\times0.167\times0.550$	$0.073\times0.118\times0.216$	$0.496\times0.407\times0.089$	$0.403\times0.148\times0.104$	$0.483\times0.233\times0.157$
Crystal system	triclinic	orthorhombic	monoclinic	monoclinic	monoclinic
Space group	$P\bar{1}$	$Pbca$	$P2_1/n$	$P2_1/c$	$P2_1/n$
a [Å]	5.360(2)	11.774(2)	5.913(1)	10.910(1)	8.230(1)
b [Å]	5.806(2)	11.072(3)	9.509(1)	6.743(1)	13.024(1)
c [Å]	6.866(2)	14.050(3)	10.351(1)	16.442(2)	10.642(1)
α [°]	113.73(2)	90	90	90	90
β [°]	92.44(2)	90	90.29(1)	103.40(1)	104.43(1)
γ [°]	90.08(2)	90	90	90	90
V [Å³]	195.4(1)	1831.6(7)	582.0(1)	1176.7(2)	1104.7(2)
Z	1	8	4	4	2
$D_{calcd.}$ [g cm⁻³]	1.582	1.893	1.805	1.632	1.666
μ [cm⁻¹]	1.383	6.746	0.502	1.264	1.361
$F(000)$	98	1072	336	600	572
θ range [°]	7.05–66.29	6.30–66.71	3.93–29.46	4.16–66.68	5.47–66.47
hkl range	$-6\leq h\leq6$	$-13\leq h\leq12$	$-8\leq h\leq7$	$-12\leq h\leq12$	$-9\leq h\leq8$
	$-6\leq k\leq6$	$-13\leq k\leq8$	$-13\leq k\leq13$	$-8\leq k\leq7$	$-15\leq k\leq15$
	$-8\leq l\leq8$	$-16\leq l\leq16$	$-14\leq l\leq14$	$-18\leq l\leq19$	$-12\leq l\leq12$
Reflns. measd.	2096	4974	8603	8336	7477
Unique reflns.	684	1582	1505	2059	1923
R_{int}	0.045	0.073	0.064	0.063	0.052
Data/restr./param.	684/0/55	1582/0/127	1505/0/83	2059/0/182	1923/0/173
$R(F)/wR(F^2)$[a] (all data)	0.056/0.152	0.061/0.160	0.057/0.159	0.048/0.118	0.045/0.124
GoF (F^2)	1.006	1.011	1.047	0.930	1.033
$\Delta\rho_{fin}$ [e Å⁻³]	−0.41/0.41	−1.18/0.70	−0.75/0.62	−0.33/0.32	−0.35/0.31

[a] Symmetry codes: $R1 = \Sigma||F_o| - |F_c||/\Sigma|F_o|$; $R_w = [\Sigma(F_o^2 - F_c^2)/\Sigma w(F_o)2]1/2$; $w = [\sigma_c^2(F_o^2) + (xP)2 + yP]^{-1}$, $P = (F_o^2 - 2F_c^2)/3$.

Table 3. Experimental (X-ray) selected bond lengths [Å] and angles [°] in the crystal structure of salts of the [MeNH₂–NH₂Me]²⁺ cation and computed values for the optimized structure using DFT calculations [B3LYP/6-311+G(d,p)].

	2[a]	3	5A[b]	5B[b]	6b[c]	6·2H₂O[d]	B3LYP
C1–N2	1.485(3)	1.490(5)	1.482(4)	1.488(4)	1.472(2)	1.485(2)	1.501
N2–N3	1.447(3)	1.445(5)	1.438(5)	1.447(5)	1.458(2)	1.452(2)	1.452
N3–C4	1.485(3)	1.492(6)	1.482(4)	1.488(4)	1.476(2)	1.485(2)	1.501
N3–N2–C1	111.5(2)	111.6(3)	111.7(2)	111.4(2)	109.9(1)	111.3(1)	114.6
N2–N3–C4	111.5(2)	112.4(3)	111.7(2)	111.4(2)	110.3(1)	111.3(1)	114.6

[a] For **2**: N3 = N2^i and C4 = C1^i; symmetry code (**2**): (i) $2-x$, $2-y$, $1-z$. [b] For **5A**: N3 = N2^i and C4 = C1^i; for **5B**: C1 = C2, N2 = N3, N3 = N3^{ii}, and C4 = C2^{ii}; symmetry codes [**5A** and **5B**]: (i) $1-x$, $1-y$, $1-z$; (ii) $1-x$, $1-y$, $-z$. [c] Compound **6b** is a salt of the [MeNH₂–NHMe]⁺ cation. [d] For **6·2H₂O**: N3 = N2^i and C4 = C1^i; symmetry code (**6·2H₂O**): (i) $1-x$, $-y$, $-z$.

estimate the (X-ray) experimental results. In any case, the optimized geometry of the gas-phase structure of the [MeNH₂–NH₂Me]²⁺ cation is in good agreement with the (solid-state) X-ray diffraction results. The average N2–N3 bond length (ca. 1.445 Å) is very close to the expected N–N single bond length (1.450 Å)[38] and in agreement with the analogous distance in Me₂N–NH₂[39] and N,N'-dimethylhydrazinium diazide[12] (see Figure 3 and Table 3).

A natural bond orbital (NBO) analysis (Gaussian 03W)[17] was performed on the optimized structure of the [MeNH₂–NH₂Me]²⁺ cation. The results have been summarized in Figure 4. Due to the symmetry of the molecule, the NBO analysis predicts identical charges for the two nitro-
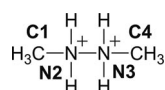
Figure 3. X-ray labeling scheme for the [MeNH₂–NH₂Me]²⁺ cation (see Table 3).
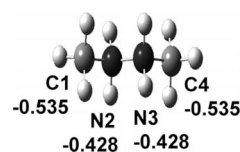
Figure 4. Optimized geometry and charge distribution in the [MeNH₂–NH₂Me]²⁺ cation as found with NBO analysis [B3LYP/6-31+G(d,p)].

C. M. Sabaté, H. Delalu

gen atoms (N2 and N3 = –0.428 e) and for the two carbon atoms (C1 and C4 = –0.535 e). These results suggest the possibility of extensive hydrogen bonding in the gas phase, which is in keeping with the (solid-state) X-ray diffraction results (see Table S2 in the Supporting Information).

[MeNH$_2$–NH$_2$Me][NO$_3$]$_2$ (**2**) crystallizes and forms non-planar layers with the two methyl groups of the [MeNH$_2$–NH$_2$Me]$^{2+}$ cation pointing upwards and downwards from the plane of the layers, respectively. Apart from covalent forces with the methyl groups, there exists no significant interaction between layers. Figure 5 shows a view of one of the nonplanar layers with the hydrogen-bonding and labeling scheme. As represented in Figure 6, the packing in the structure of the compound is characterized by extensive hydrogen bonding between cations and anions. In total, seven hydrogen bonds are formed (see Table S2 in the Supporting Information): five are between anions and cations, and the remaining two hydrogen bonds are nonclassical hydrogen bonds, which are formed between the methyl groups of the cation and the oxygen atoms of the nitrate anion. The extensive hydrogen bonding found in the crystal structure of the compound accounts for the relatively high density of the nitrate salt ($D_{calcd.}$ = 1.582 g cm^{-3}) relative to the analogous azide salt ($D_{calcd.}$ = 1.227 g cm^{-3}).[12]
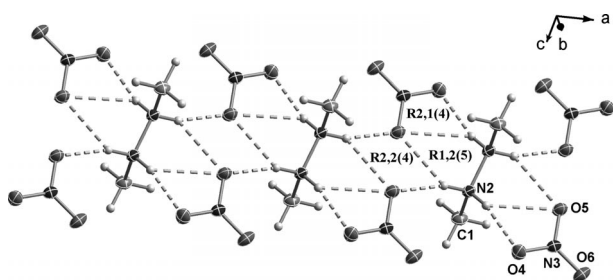
Figure 5. View of a nonplanar layer in the crystal structure of [MeNH$_2$–NH$_2$Me][NO$_3$]$_2$ (**2**) with hydrogen bonding (dotted lines) and the labeling scheme. Diamond ellipsoids are represented at 50% probability.

The formalism of graph-set analysis[40] is useful to describe the complex hydrogen-bonding networks found in the structure of the compounds in this work. For salt **2**, the computer program RPLUTO identified the five (classical) hydrogen bonds in Table S2 in the Supporting Information as forming dimeric chains so that the unitary hydrogen-bonding network is described by N_1 = 5*D1,1(2)[D2,2(6)] (see Table S3 in the Supporting Information). At the secondary level, these finite chain interactions combine to form infinite chains with the labels C1,2(X) (X = 4, 5) and C2,2(X) (X = 5, 6) in addition to ring networks with the descriptors R1,2(5), R2,1(X) (X = 3, 4), R2,2(X) (X = 4, 6), R2,4(X) (X = 8, 10), and R4,4(X) (X = 7, 10, 12, 14). Some of these ring graph sets are represented in Figure 5, for example, the R2,1(4) graph sets are formed by two hydrogen bonds between one cation and one anion [N2···O4 = 2.783(3) Å and N2···O5 = 2.893(3) Å]; two cations and two anions interact to form R2,2(4) graph sets [N2···O5 = 2.923(3) Å and N2···O5^{iii} = 2.699(3) Å; symmetry code: (iii) 1 + x, y, z].
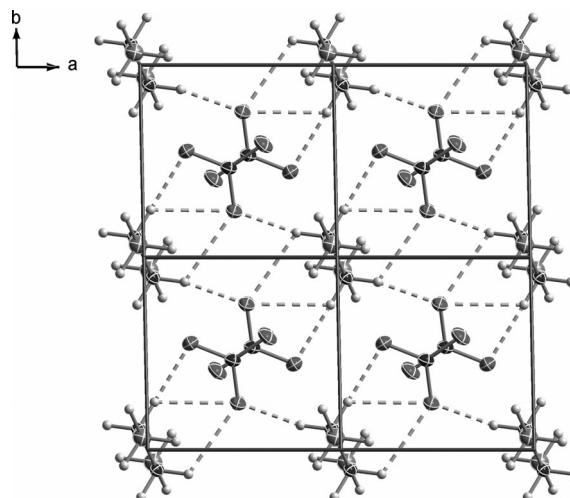
Figure 6. Packing in the 2×2×2 [–1 – +1] supercell of [MeNH$_2$–NH$_2$Me][NO$_3$]$_2$ (**2**, view along the *c* axis) with extensive hydrogen bonding (dotted lines).

[MeNH$_2$–NH$_2$Me][ClO$_4$]$_2$ (**3**) crystallizes with the highest calculated density of all compounds in this work ($D_{calcd.}$ = 1.893 g cm^{-3}). Figure 7 shows the asymmetric unit (ASU) of the compound with the labeling scheme. The ASU is made up of one cation and two crystallographically independent perchlorate anions. Similar to the nitrate salt, the compound is involved in the formation of extensive hydrogen bonding (see Table S2 in the Supporting Information). Compound **3** participates in the formation of up to nine hydrogen bonds: two nonclassical hydrogen bonds between methyl groups and anions, and seven classical hydrogen bonds between cations and anions.
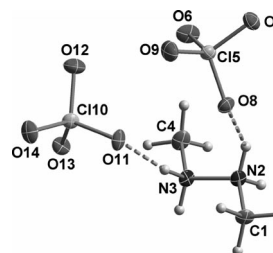
Figure 7. Asymetric unit of [MeNH$_2$–NH$_2$Me][ClO$_4$]$_2$ (**3**) and labeling scheme. Diamond ellipsoids are represented at the 50% probability.

The complex hydrogen-bonding patterns found in the structure of the compound are represented in Figure 8. The unitary network is described exclusively by dimeric interactions [N_1 = 7*D1,1(2)], which combine at the secondary level to form other dimeric interactions of the type D2,1(3) and D2,2(X) (X = 5, 6), C2,2(X) infinite chains, and one R2,1(4) ring motif (Table S4 in the Supporting Information). The latter graph set, formed by interaction of the –NH$_2^+$ moieties of the cation with two oxygen atoms of the same anion [N3···O13^i = 2.811(6) Å and N3···O14^i = 2.988(6) Å; symmetry code: (i) x, 0.5 – y, 0.5 + z] is analo-

gous to that found in the nitrate salt (see discussion above) and common for salts with anions that contain an $-XO_2$ (X = N, Cl) unit.[4c,5c]
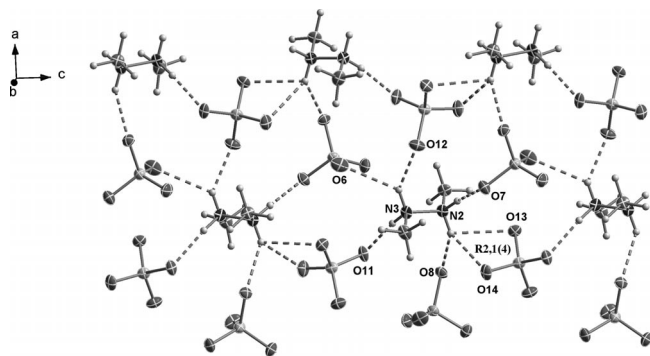
Figure 8. Packing in the crystal structure of [MeNH$_2$–NH$_2$Me]-[ClO$_4$]$_2$ (3). The dashed lines represent hydrogen bonding.

[MeNH$_2$–NH$_2$Me][SO$_4$] (5) crystallizes with a high calculated density ($D_{calcd.}$ = 1.805 cm^{-3}). The asymmetric unit is made up of one SO$_4^{2-}$ anion and 2.5 [MeNH$_2$–NH$_2$Me]$^{2+}$ cations so that the global charge is zero. The 2.5 cations lay on a symmetry plane so that the other half of the cation can be generated by symmetry [symmetry codes: (i) 1 − x, 1 − y, 1 − z; (ii) 1 − x, 1 − y, −z]. In analogy to the nitrate and perchlorate salts, a total of seven classical hydrogen bonds between cations and anions are formed (see Table S2 in the Supporting Information). The extensive hydrogen-bonding networks found in the structure of the compound can be described as N_1 = 7*D1,1(2) [D2,2(6)] at the primary level. At the secondary level, in addition to dimeric patterns with the descriptors D1,2(3) and D2,2(5), there exist also infinite chains of the type C2,1(4) and C2,2(X) (X = 6, 7), and R1,2(X) (X = 4, 5), R2,2(7), R2,4(8), and R4,4(X) (X = 12, 14) ring graph sets (see Table S5 in the Supporting Information). Figure 9 shows the two types of R2,2(7) ring graph sets found in the structure of the compound, which are formed between the hydrogen bonds labeled A and C [N2···O9 = 3.040(3) Å and N2···O7^{iv} = 2.683(3) Å; sym-

metry code: (iv) 1 − x, 1 − y, 1 − z] and between D and G [N3···O9^v = 2.974(3) Å and N3···O8 = 2.658(3) Å; symmetry code: (v) 1 − x, 1 − y, −z]. In addition, R3,4(6) networks are also formed at the quaternary level (i.e., they involve the combination of four hydrogen bonds, namely, A, B, D, and E). These latter motifs (not included in Table S5) are also depicted in Figure 9.

After recrystallization from ethanol of the dipicrate salt [MeNH$_2$–NH$_2$Me][(NO$_2$)$_3$Ph–O]$_2$ (6), single crystals of the monopicrate [MeNH$_2$–NHMe][(NO$_2$)$_3$Ph–O] (6b) were obtained. Figure 10 shows the asymmetric unit of the compound with the labeling scheme and the hydrogen bonding between cations and anions. Similar to what is found in the crystal structure of 6·2H$_2$O (see discussion below), the p-NO$_2$ group of the picrate anion is almost coplanar to the benzene ring [C8–C9–N15–O16 = 3.7(2)°], whereas the o-NO$_2$ groups are considerably deviated [C10–C11–N18–O19 = 36.2(2)° and C6–C7–N12–O13 = 34.2(2)°].
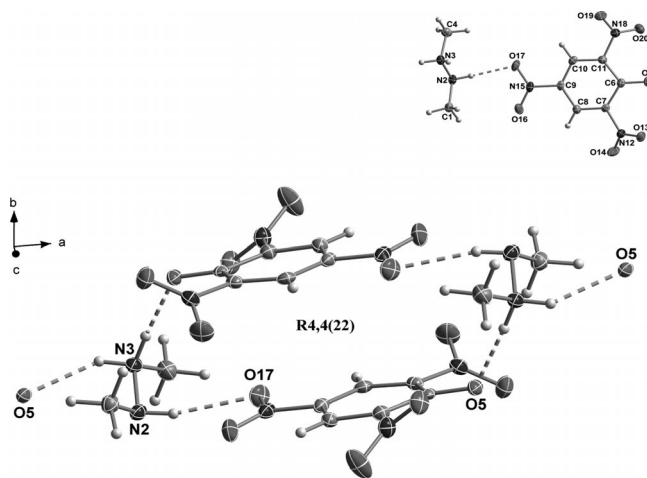
Figure 10. Labeling scheme in the crystal structure of [MeNH$_2$–NHMe][(NO$_2$)$_3$Ph–O] (6b) and hydrogen bonding (dotted lines). Diamond ellipsoids are represented at 50% probability.

Figure 9. Packing in the unit cell of [MeNH–NHMe][SO$_4$] (5) with the labeling scheme view along the a axis. The dashed lines represent hydrogen bonding. Diamond ellipsoids are represented at 50% probability.

In the unit cell (Figure 11), the picrate anions form non-planar layers, which are connected by hydrogen bonding with the formally negatively charged oxygen atom O5 [N3···O5^{ii} = 2.797(3) Å, symmetry code: (ii) x, 1 + y, z]. The lack of water of crystallization in the structure of the compound accounts for two fewer hydrogen bonds, namely, three, in comparison with the hydrated dipicrate salt 6·2H$_2$O (Table S2 in the Supporting Information). The primary hydrogen-bonding network is described by N_1 = 3*D1,1(2) (Table S6 in the Supporting Information). At the secondary level, there exist two infinite chain graph sets of the type C1,2(4) and C2,2(11) and one ring network with the label R4,4(22). This last hydrogen-bonding motif is represented in Figure 10 and is formed by the hydrogen bond between layers mentioned above (N3···O5^{ii}) and the hydrogen bond formed by the p-NO$_2$ group [N2···O17^{iv} = 3.054(3) Å; symmetry code: (iv) 2 − x, 1 − y, 1 − z]. In addition, one of the C–H groups in the anion is involved in

nonclassical hydrogen bonding with the o-NO$_2$ groups [C10···O14^i = 3.421(3) Å; symmetry code: (i) x, 0.5 – y, 0.5 + z].
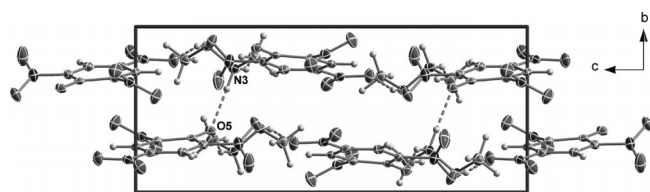
Figure 11. View of the unit cell of [MeNH$_2$–NHMe][(NO$_2$)$_3$Ph–O] (**6b**) along the a axis with the hydrogen bonding between nonplanar layers (dotted lines).

After recrystallization from water of the dipicrate salt [MeNH$_2$–NH$_2$Me][(NO$_2$)$_3$Ph–O]$_2$ (**6**), single crystals of the dihydrated species [MeNH$_2$–NH$_2$Me][(NO$_2$)$_3$Ph–O]$_2$·2H$_2$O (**6·2H$_2$O**) were obtained. Figure 12 shows the molecular formula of the compound in the solid state. Half of the molecule can be generated by symmetry [symmetry code: (i) 1 – x, –y, –z]. Whereas the p-NO$_2$ group of the picrate anion is almost coplanar with the benzene ring [C6–C7–N13–O15 = 8.2(2)°], the o-NO$_2$ groups are considerably deviated [C6–C5–N10–O12 = 33.8(2)° and C8–C9–N16–O17 = 34.9(2)°]. As pointed out above, this situation is analogous to that found in the monopicrate salt **6b**; however, it is in contrast to a report on the crystal structure of azolium salts[5c] in which two nitro groups are approximately coplanar with the benzene ring and one of the o-NO$_2$ groups is more significantly tilted. These differences might be related to packing effects.

Figure 12. View of the molecular formula of [MeNH$_2$–NH$_2$Me][(NO$_2$)$_3$Ph–O]$_2$·2H$_2$O (**6·2H$_2$O**) with hydrogen bonding (dotted lines) and the labeling scheme. Diamond ellipsoids are represented at 50% probability.

In analogy to the nitrate and perchlorate salts described above, all four N–H hydrogen atoms in the cation are involved in hydrogen bonding to form three out of the six important interactions found in the structure of the compound (see Table S2 in the Supporting Information). In addition, a nonclassical hydrogen bond is formed between one of the C–H groups in the anion and one of the o-NO$_2$ groups [C6···O17^i = 3.383(2) Å; symmetry code: (i) 1 + x, y, z], whereas the two molecules of water are involved in two hydrogen bonds, which link the picrate anions along the c direction to form wavy layers (Figure 13). Two consecutive layers are connected by hydrogen bonding over the [MeNH$_2$–NH$_2$Me]$^{2+}$ cations and the water molecules,

whereas the aromatic rings interact through π stacking [$d_{C3–C7}$ = 3.834(2) Å]. The primary hydrogen-bonding network is described by N_1 = 5*D1,1(2) (Table S7 in the Supporting Information). At the secondary level, there exist many dimer interactions of the type D2,2(X) (X = 4–7, 9), chain graph sets with the label C2,2(10), and ring networks with the descriptor R2,1(6). The latter are formed by the interaction of one cation and one anion [N2···O3 = 2.598(2) Å and N2···O11 = 2.846(2) Å] and are represented in Figure 12. Lastly, the density of the picrate salt ($D_{calcd.}$ = 1.666 gcm^{-3}) is similar to that of recently reported picrate salts with azolium cations.[5c]

Figure 13. Nonplanar layers formed by the picrate anions in the crystal structure of [MeNH$_2$–NH$_2$Me][(NO$_2$)$_3$Ph–O]$_2$·2H$_2$O (**6·2H$_2$O**, view along the a axis) with the hydrogen bonding (dotted lines).

DSC Analysis, Sensitivity Tests, and Predicted Performance

MP2 Calculations

The Møller–Plesset perturbation theory truncated at the second order (MP2)[41] with a correlation-consistent polarized valence double-ζ basis set (cc-pVDZ)[42,43] was used to calculate the electronic energies of the [MeNH$_2$–NH$_2$Me]$^{2+}$ cation and the different anions in this study. An approximation of the lattice enthalpy was used for the calculations, as described previously by Jenkins and co-workers.[44] These values were used unscaled as provided by the Gaussian 03W program.[17]

Differential scanning calorimetry (DSC) was used to assess the thermal stability of the salts of MeNH–NHMe in this work (see Table 4). At a heating rate of β = 5 °C min^{-1}, compound **3** does not show a defined melting point, whereas the remainder of the materials melt at defined temperatures far below the decomposition points. Compound **4** exhibits the largest liquid range (i.e., the largest difference between melting and decomposition temperatures) at 143 °C and, together with the nitrate salt **2**, they belong to the ionic liquid class (i.e., T_m < 100 °C). As expected, the picrate salt **6** shows the highest thermal stability and decomposes at temperatures above 225 °C. In addition to DSC analysis, the compounds were loaded on a metal spatula and submitted to a thermal shock in the flame of a Bunsen burner. Under these conditions all of the compounds failed to explode; however, salts **2** and **3**, based on an oxidizing anion, namely, nitrate and perchlorate, showed a significantly more vigorous reaction with an easy burning-to-deflagration transition.
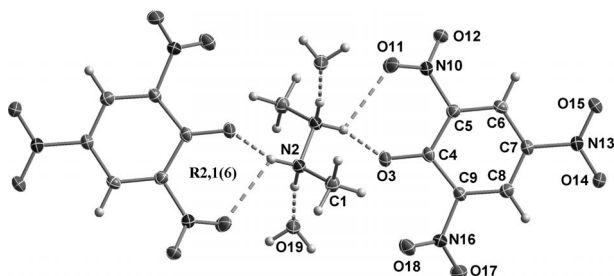
Table 4. Physical and chemical properties of energetic salts of the $[MeNH_2–NH_2Me]^{2+}$ cation (**2**, **3**, **4**, and **6**) and of the $[MeNH_2–NHMe]^+$ cation (**6b**).

	2	**3**	**4**	**6**	**6b**
Formula	$C_2H_{10}N_4O_6$	$C_2H_{10}N_2O_8Cl_2$	$C_6H_{10}N_8$	$C_{14}H_{14}N_8O_{14}$	$C_8H_{11}N_5O_7$
M_r [g mol^{-1}]	186.12	261.01	194.19	518.31	289.20
T_m/T_g [°C][a]	98	–	37	112	123
T_d [°C][b]	220	175	180	225	211
Ω [%][c]	−26	0	−140	−65	−69
$\rho_{calcd.}$ [g cm^{-3}][d]	1.582	1.893	1.420	1.666	1.632
ΔH_L [kJ mol^{-1}][e]	1590	1528	1531	1236	461
ΔU_f° [kJ kg^{-1}][f]	1162	3205	2957	−258	268
ΔH_f° [kJ kg^{-1}][g]	1029	3120	2842	−345	171

[a] Phase-transition temperature. [b] Decomposition point (from DSC onsets) with measurements at β = 5 °C min^{-1}. [c] Oxygen balance. [d] Density from pycnometer (**4**) or X-ray (**2**, **3**, **6**, and **6b**) measurements (the X-ray density of **6** was approximated to that of **6**·2H$_2$O). [e] Lattice enthalpy. [f] Computed (MP2) energy of formation. [g] Computed (MP2) enthalpy of formation.

Standardized Bundesanstalt für Materialforschung und -prüfung (BAM)[45–48] procedures were also used to assess the sensitivity of the salts of MeNH–NHMe towards impact, friction, and electrostatic discharge. These results have been summarized in Table 5 together with relevant performance data for the same compounds. In the BAM drop hammer and friction tests, compounds **2**, **3**, **4**, **6**, and **6b** all showed decreased sensitivity towards impact and friction. The perchlorate salt **3** showed particularly high explosive power and shattered the ceramic plate used for the friction test (see Figure S1 in the Supporting Information). Compounds **4**, **6**, and **6b**, which are based on a less oxidizing anion, did not show any sign of decomposition at the maximum loading of these tests (i.e., $i > 40$ J and $f > 360$ N); however, salts **2** and **3**, based both on typically oxidizing anions, decomposed explosively at lower loadings, in particular, the better oxygen-balanced salt **3** (i = 20 J and f = 150 N). The electrostatic sensitivity test was conducted by placing the compounds on a metallic plate and applying the electrostatic discharge of a Tesla coil. No explosion was observed for any of the compounds tested.

With the exception of perchlorate salt **3**, the low sensitivity of the salts of MeNH–NHMe in this work provides a clear advantage over commonly used explosives such as TNT (2,4,6-trinitrotoluene), which is significantly more sensitive towards impact (i = 15 J); for salts **4**, **6**, and **6b**, it is also more friction-sensitive (f = 355 N).[49] Furthermore, the compounds in this study also present lower sensitivities than recently reported hydrazinium salts with nitrogen- or oxygen-rich anions.[50–52]
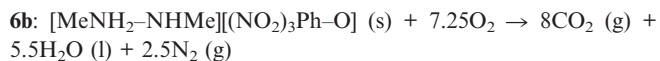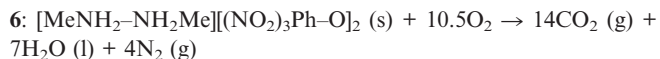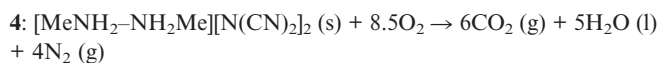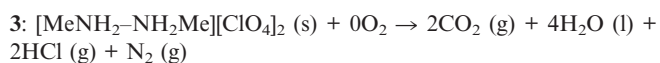
The (MP2)-calculated electronic energies of the $[MeNH_2–NH_2Me]^{2+}$ cation {$[MeNH_2–NHMe]^+$ cation for salt **6b**} and the different anions used were combined to obtain the energies of combustion of the compounds in this work. Subsequently, the energies of formation were calculated on the basis of the combustion equations of salts **2**, **3**, **4**, **6**, and **6b** (see below) by using Hess' law and the known standard heats of formation for dioxygen, carbon dioxide, water, dinitrogen, and hydrogen chloride.[53] Except for salt **6** (ΔH_f° = −345 kJ kg^{-1}), all compounds in this work including **6b** are predicted to have positive heats of formation, which vary between 171 (for **6b**) and 3120 kJ kg^{-1} (for **3**). These values are comparable to those of previously reported energetic salts based on picrate,[5c] nitrate, perchlorate,[4b,54] and dicyanamide anions.[22] Note the higher (positive) heat of formation of the monopicrate salt **6b** than the dipicrate salt **6**, which is as expected, since the enthalpy of formation is inversely proportional to the lattice enthalpy and salt **6**, based on a divalent cation, has a significantly higher predicted lattice enthalpy than compound **6b**, which is based on a monovalent cation (ΔH_L = 1236 and 461 kJ mol^{-1}, respectively).

Table 5. Relevant performance parameters (calculated using EXPLO5) and results of the sensitivity tests of salts of the $[MeNH_2–NH_2Me]^{2+}$ cation (**2**, **3**, **4**, and **6**) and of the $[MeNH_2–NHMe]^+$ cation (**6b**).

	$T_{expl.}$ [K][a]	V_0 [L kg^{-1}][b]	$P_{det.}$ [kbar][c]	D [m s^{-1}][d]	$I_{sp.}$ [s][e]	Impact [J][f]	Friction [N][f]	ESD (+/−)[g]	Thermal shock[h]
2	4745	893	241	8117	225	>30	>360	−	burns fast
3	6755	756	387	8624	249	<2	<42	−	deflagrates
4	2375	671	159	6885	199	>40	>360	−	burns slowly
6	3691	627	237	7576	211	>40	>360	−	burns slowly
6b	3579	681	237	7769	216	>40	>360	−	burns slowly

[a] Temperature of the explosion gases. [b] Volume of the explosion gases. [c] Pressure. [d] Velocity of detonation (detonation run, 1% TFNA = trifluorotrinitroazahexane was added for perchlorate salt **3**). [e] Specific impulse (isobaric combustion for the pure compound at a chamber pressure = 60.0 bar). [f] Impact and friction sensitivity values (according to BAM methods). The nitrate salt **2** decomposed without explosion at this friction load. [g] Rough sensitivity to electrostatic discharge using a Tesla coil (ca. 20 kV), + sensitive, − insensitive. [h] Response to fast heating in the flame test.

2: $[MeNH_2–NH_2Me][NO_3]_2$ (s) + $1.5O_2 \rightarrow 2CO_2$ (g) + $5H_2O$ (l) + $2N_2$ (g)

3: $[MeNH_2–NH_2Me][ClO_4]_2$ (s) + $0O_2 \rightarrow 2CO_2$ (g) + $4H_2O$ (l) + $2HCl$ (g) + N_2 (g)

4: $[MeNH_2–NH_2Me][N(CN)_2]_2$ (s) + $8.5O_2 \rightarrow 6CO_2$ (g) + $5H_2O$ (l) + $4N_2$ (g)

6: $[MeNH_2–NH_2Me][(NO_2)_3Ph–O]_2$ (s) + $10.5O_2 \rightarrow 14CO_2$ (g) + $7H_2O$ (l) + $4N_2$ (g)

6b: $[MeNH_2–NHMe][(NO_2)_3Ph–O]$ (s) + $7.25O_2 \rightarrow 8CO_2$ (g) + $5.5H_2O$ (l) + $2.5N_2$ (g)
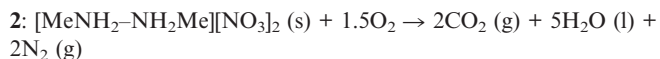
The computer program EXPLO5[55] was used to estimate the detonation parameters and specific impulses of the salts of the $[MeNH_2–NH_2Me]^{2+}$ cation. The following values for the Becker–Kistiakowsky–Wilson[56] equation of state were used: $\alpha = 0.5$, $\beta = 0.176$, $\kappa = 14.71$, and $\theta = 6620$. The detonation parameters (i.e., detonation pressure and velocity) of compounds **2**, **3**, **4**, **6**, and **6b** vary between $P_{det.} = 159$ (**4**) and 387 kbar (**3**) and $D = 6885$ (**4**) and 8624 m s^{-1} (**3**), respectively. Note that the detonation parameters, calculated from the energies of formation obtained from MP2-calculated electronic energies of the cation and anion, tend to overestimate the real values.[57] In any case, the predicted detonation parameters are comparable to those of commonly used explosives such as TNT ($P_{det.} = 205$ kbar and $D = 7171$ m s^{-1}) and RDX ($P_{det.} = 340$ kbar and $D = 8885$ m s^{-1}).[44] On the other hand, the specific impulses vary between 199 (**4**) and 249 s (**3**), which are comparable or superior to those of recently reported salts that contain a 1,1-dimethylhydrazinium cation.[22]

The performance of an energetic compound is basically a function of the density, the heat of formation, and the oxygen balance.[58] The densities of the salts of MeNH–NHMe vary between moderate (1.420 g cm^{-3} for compound **4**) and high (1.893 cm^{-3} for compound **3**) and are significantly higher than that of the azide salt.[12] However, the oxygen balances are neutral in the case of the perchlorate salt **3** and negative for the remainder of the materials. Therefore, it can be anticipated that improving the oxygen balance of the compounds in this work should result in better performances. Along these lines, we calculated the performances of mixtures of the compounds with a negative oxygen balance (i.e., **2**, **4**, and **6**) with two commonly used oxidizers, namely, AN = ammonium nitrate and ADN = ammonium dinitramide. The mixtures were chosen such that the oxygen balance of the mixture was as close to neutral as possible. The results of these calculations have been collected in the Supporting Information (Tables S8 and S9). Formulations of compounds **2**, **3**, **4**, **6**, and **6b** with AN or ADN are predicted to have higher detonation parameters and specific impulses than the values reported in Table 5 for the stand-alone materials. Mixtures of **2**, **3**, **4**, **6**, and **6b** with AN are predicted to perform in the range $P_{det.} = 266$ (**4** + AN) to 317 kbar (**2** + AN), $D = 8171$ (**4** + AN) to 8767 m s^{-1} (**2** + AN), and $I_{sp.} = 227$ (**4** + AN) to 256 s (**2** + AN). On the other hand, formulations with ADN are anticipated to have better performances that vary between $P_{det.} = 337$ (**6** + ADN) to 363 kbar (**2** + ADN), $D = 8743$

(**6** + ADN) to 9159 m s^{-1} (**2** + ADN), and $I_{sp.} = 247$ (**6** + ADN) to 268 s (**2** + ADN). Note the more significant increase in performance for the formulations of the a priori lower-performing dicyanamide salt **4**.

Conclusion

High-yield and straightforward syntheses of salts of MeNH–NHMe with energetic anions including nitrate, perchlorate, dicyanamide, and picrate, are presented, which allowed us to obtain the materials in high purities. All compounds were characterized by analytical (mass spectrometry and elemental analysis) and spectroscopic (NMR, IR and Raman) methods, including ^{15}N NMR spectroscopic measurements (compound **2**). The structure of the $[MeNH_2–NH_2Me]^{2+}/[MeNH_2–NHMe]^+$ cation in the solid state of salts **2**, **3**, **5**, **6b**, and **6**·2H$_2$O was solved by low-temperature single-crystal X-ray experiments. Description of the extensive hydrogen-bonded networks found in the crystal structure of the salts was facilitated by graph-set analysis. In addition, differential scanning calorimetry measurements show a good thermal stability of the $[MeNH_2–NH_2Me]^{2+}/[MeNH_2–NHMe]^+$ cation up to 225 °C (**6**), and salts **2** and **4** classify as ionic liquids (i.e., $T_m < 100$ °C). According to standard BAM tests and with the exception of perchlorate salt **3**, the compounds exhibit low or no sensitivity against impact, friction, and electrostatics, which are clear advantages over commonly used energetic compounds such as TNT or RDX. Furthermore, the MP2 method was used as a starting point to calculate the detonation parameters and specific impulses of the materials using the EXPLO5 computer software. These calculations showed moderate to high predicted performances, which were expected to improve for oxygen-balanced mixtures with an oxidizer (i.e., ammonium nitrate or dinitramide). Current work focuses on the study of the vapor pressures of the ionic compounds in this work with an eye toward possible energetic applications. This will be the focus of a future communication from our group.

Experimental Section

Caution! Although the compounds described in this work exhibit low friction and impact sensitivities, they are nevertheless (except for salt **6**) endothermic materials and should be regarded as potentially explosive. We recommend the synthesis and handling of this type of compounds to be carried out only by expert personnel with the best safety practices.

General Procedure: All chemicals used in this work were obtained either from Acros Organics or from Sigma–Aldrich Fine Chemicals Inc. and were used without further purification. Barium picrate hexahydrate[59] and MeNH–NHMe[60] were prepared according to modified literature procedures as described in the Supporting Information. The syntheses of silver dicyanamide and of the sulfate salt **5** are also presented in the Supporting Information. The ^1H, ^{13}C, ^{35}Cl, and ^{15}N NMR spectra were recorded with a Bruker instrument at or near 25 °C. The chemical shifts are given relative to tetramethylsilane (^1H, $^{13}C\{^1H\}$), sodium chloride (^{35}Cl), and ammonia (^{15}N) as external standards. Infrared (IR) spectra of all com-

pounds were recorded with a Perkin–Elmer Spectrum 100 FTIR spectrometer equipped with a universal ATR sampling accessory at or near 25 °C. The IR intensities are described in parentheses as w = weak, m = medium, and s = strong. Raman spectra were recorded with a KAISER RXN1 (Nd:YAG laser at 785 nm) instrument equipped with an optic fiber of silicon and a sapphire probe. Raman activities are reported relative to the most intense peak and given in parentheses. For all solid substances, melting and/or decomposition points were determined by differential scanning calorimetry with a DSC 131 Setaram instrument (calibrated with standard pure indium and zinc). Measurements were performed in closed aluminum sample pans with a 1 μm hole in the top for gas release with a nitrogen flow of 20 mL min^{-1}. An empty identical aluminum sample pan was used as the reference.

Synthesis of [MeNH$_2$–NH$_2$Me][NO$_3$]$_2$ (2): N,N'-Dimethylhydrazinium dichloride (2.000 g, 15.04 mmol) was dissolved in distilled water (20 mL) and treated at room temperature with a solution of silver nitrate (5.108 g, 30.07 mmol) in distilled water (20 mL). Immediate precipitation of white silver chloride was observed, and the reaction mixture was stirred for around 2 h under the exclusion of light. After this time, the insoluble material was filtered under gravity and washed with a little water. The solvents were then removed under reduced pressure with a rotary evaporator and the powder thus obtained was dried under high vacuum to give a colorless compound. No further purification was necessary (2.724 g, 97%). Single crystals suitable for X-ray analysis were grown by slow evaporation of a solution of the compound in methanol. $\rho_{calcd.}$ (X-ray) = 1.582 g cm^{-3}. C$_2$H$_{10}$N$_4$O$_6$ (186.12): calcd. C 12.91, H 5.41, N 30.10; found C 12.96, H 5.51, N 30.28. DSC (5 °C min^{-1}): 98 °C (m.p.), 220 °C (decomp. with explosion). MS (ESI$^+$): m/z: 192.9 (10), 183.9 (4) [2Cat$^+$ + A$^-$], 174.9 (3), 124.0 (2) [Cat^{2+} + A$^-$], 120.9 (6), 108.0 (12), 102.1 (3), 62.0 (4), 61.0 (100) [Cat^{2+} − H$^+$]. MS (ESI$^-$): m/z: 487.0 (45) [6A$^-$ + 5Na$^+$], 480.7 (45), 474.7 (31), 450.7 (15), 401.8 (23) [5A$^-$ + 4Na$^+$], 396.0 (22), 389.8 (24), 317.0 (9) [4A$^-$ + 3Na$^+$], 310.8 (11), 231.8 (34), [3A$^-$ + 2Na$^+$], 226.1 (100), 147.1 (29) [2A$^-$ + Na$^+$], 62.0 (8) [A$^-$]. ^{1}H NMR ([D$_6$]DMSO, 400.18 MHz, TMS): δ = 2.55 (s, 6 H, –CH$_3$), 10.15 (s, 4 H, $^+$NH$_2$) ppm. ^{13}C NMR ([D$_6$]DMSO, 100.52 MHz, TMS): δ = 35.1 (2 C, N–CH$_3$) ppm. ^{15}N NMR ([D$_6$]DMSO, 40.51 MHz, NH$_3$): δ = +369.0 (s, 2 N, NO$_3$$^-$), +75.2 (s, 2 N, N–CH$_3$) ppm. IR (Raman) (rel. int.): $\tilde{\nu}$ = 2950 (23), 2863 (3), 2823 (2), 2117 (18), 1683 (4), 1621 (4), 1526 (5), 1491 (7), 1436 (10), 1383 (5), 1345 (4), 1310 (3), 1275 (3), 1229 (4), 1118 (2), 1066 (28), 1050 (100), 1023 (3), 991 (2), 735 (11), 719 (9), 670 (39), 614 (9), 374 (7), 332 (5) cm^{-1}. IR: $\tilde{\nu}$ = (golden gate, rel. int.): 3038 (w), 2664 (w), 2419 (w), 1745 (w), 1584 (w), 1398 (s), 1287 (s), 1095 (m), 1034 (m), 976 (m), 920 (m), 813 (m), 732 (m), 706 (w) cm^{-1}.

Synthesis of [MeNH$_2$–NH$_2$Me][ClO$_4$]$_2$ (3): N,N'-Dimethylhydrazinium dichloride (1.000 g, 7.52 mmol) was dissolved in distilled water (10 mL) and treated at room temperature with a solution of 97% anhydrous silver perchlorate (3.214 g, 15.04 mmol) in distilled water (10 mL). Immediate precipitation of white silver chloride was observed and the reaction mixture was stirred for around 30 min under the exclusion of light. After this time, the insoluble material was filtered under gravity and washed with a little water. The solvents were then carefully removed under high vacuum at 50 °C and a colorless polycrystalline solid was obtained. No further purification was necessary (1.887 g, 96%). Single crystals of the compound suitable for X-ray analysis were grown when **3** was dissolved in methanol and the solvent was left to slowly evaporate under the nitrogen atmosphere of a glovebox. $\rho_{calcd.}$ (X-ray) = 1.893 g cm^{-3}. C$_2$H$_{10}$Cl$_2$N$_2$O$_8$ (261.01): calcd. C 8.09, H 4.75, N 9.43; found C 8.07, H 4.66, N 9.34. DSC (5 °C min^{-1}): 175 °C (decomp. with ex-

plosion). MS ($^+$c ESI): m/z: 220.9 (100), 222.9 (25) [2C − 2H + A$^-$]$^+$, 380.7 (20), 382.7 (11) [3C − 3H + 2A$^-$]$^+$, 540.6 (82), 542.6 (62) [4C − 4H + 3A$^-$]$^+$, 662.7 (25), 664.6 (27), 700.5 (46), 702.6 (62) [5C − 5H + 4A$^-$]$^+$. MS ($^-$c ESI): m/z: 99.0 (99) [A]$^-$, 101.0 (32), 221.0 (28), 219.0 (20), 258.9 (51) [2C^{2+} + 2A$^-$ − H]$^-$, 260.9 (20), 418.6 (35) [2C^{2+} + 3A$^-$ − 2H]$^-$, 420.7 (32), 578.6 (10) [3C^{2+} + 4A$^-$ − 3H]$^-$, 580.6 (14), 738.5 (45), [4C^{2+} + 5A$^-$ − 4H]$^-$, 740.4 (100). ^{1}H NMR ([D$_6$]DMSO, 400.18 MHz, TMS): δ = 2.58 (s, 6 H, –CH$_3$), 10.21 (s, 4 H, $^+$NH$_2$) ppm. ^{13}C NMR ([D$_6$]DMSO, 100.52 MHz, TMS): δ = 35.1 (2 C, N–CH$_3$) ppm. ^{35}Cl NMR ([D$_6$]DMSO, 49.03 MHz, NaCl): δ = 1011 (ClO$_4$$^-$) ppm. ^{35}Cl NMR ([D$_6$]DMSO, 39.21 MHz, NaCl): δ = 1012 ([ClO$_4$]$^-$) ppm. IR (Raman) (rel. int.): $\tilde{\nu}$ = 3056 (2), 2979 (7), 2935 (4), 1760 (5), 1603 (11), 1459 (7), 931 (100), 625 (9), 459 (12), 238 (8). IR: $\tilde{\nu}$ = (golden gate, rel. int.): 3061 (m), 2773 (m), 2410 (w), 2050 (w), 1629 (w), 1542 (m), 1465 (m), 1413 (m), 1030 (vs), 954 (m), 930 (m), 859 (m), 615 (s) cm^{-1}.

Synthesis of [MeNH$_2$–NH$_2$Me][N(CN)$_2$]$_2$ (4): After the reaction mixture that contained silver dicyanamide [prepared as described above from 96% sodium dicyanoamide (1.000 g, 10.78 mmol) and silver nitrate (1.830 g, 10.78 mmol)] had been stirred for 30 min, the precipitate was washed with distilled water (20 mL) two times and taken up into distilled water (15 mL) before it was treated with a solution of N,N'-dimethylhydrazinium dichloride (0.623 g, 4.68 mmol) in distilled water (10 mL). The reaction mixture was then stirred overnight under the exclusion of light, the insolubles were filtered and discarded, and the solvent was stripped under low pressure to give the crude product as a sticky mass. This compound was washed with acetone (5 mL three times) with subsequent drying under high vacuum to give the pure product as a colorless powder (0.723 g, 73%). $\rho_{calcd.}$ (17.6 °C) = 1.420 g cm^{-3}. C$_6$H$_{10}$N$_8$ (194.19): calcd. C 37.11, H 5.19, N 57.70; found C 37.26, H 5.21, N 57.38. DSC (5 °C min^{-1}): 37 °C (m.p.), 180 °C (decomp.). MS ($^+$c ESI): m/z: 128.1 (100) [C^{2+} + A$^-$]$^+$. MS ($^-$c ESI): m/z: 108.0 (62), 147.1 (100), 151.0 (99), 175.1 (40), 210.1 (95), 213.9 (65), 236.0 (41), 242.1 (27), 260.0 (20) [C^{2+} + 3A$^-$]$^-$, 303.0 (38). ^{1}H NMR ([D$_6$]-DMSO, 400.18 MHz, TMS): δ = 2.57 (s, 6 H, –CH$_3$), 7.89 (s, 4 H, $^+$NH$_2$) ppm. ^{13}C NMR ([D$_6$]DMSO, 100.52 MHz, TMS): δ = 35.2 (2 C, N–CH$_3$), 119.23 (2 C, –CN) ppm. ^{14}N NMR ([D$_6$]DMSO, 40.51 MHz, NH$_3$): δ = 334.6 (s, 2 N, –CN) ppm. IR (Raman) (rel. int.): $\tilde{\nu}$ = 2950 (16), 2863 (5), 2823 (3), 2177 (12), 1683 (5), 1621 (6), 1526 (8), 1491 (10), 1435 (11), 1383 (6), 1345 (5), 1310 (4), 1275 (3), 1229 (4), 1118 (1), 1066 (25), 1050 (100), 1023 (2), 991 (1), 735 (8), 719 (5), 670 (45), 614 (6), 375 (5), 332 (3). IR (golden gate, rel. int.): $\tilde{\nu}$ = 3415 (w), 3382 (w), 3281 (w), 3120 (m), 2255 (w), 2154 (m), 1979 (w), 1696 (m), 1656 (m), 1618 (m), 1576 (m), 1538 (m), 1488 (m), 1437 (m), 1341 (s), 1226 (m), 1177 (m), 1108 (m), 1087 (m), 1025 (w), 981 (w), 915 (w), 823 (w), 786 (w), 750 (w), 736 (w), 695 (m), 671 (w) cm^{-1}.

[MeNH$_2$–NH$_2$Me][(NO$_2$)$_3$Ph-O]$_2$ (6): Method 1: Barium picrate hexahydrate (0.700 g, 1.00 mmol) and **5** (0.158 g, 1.00 mmol) were dissolved and stirred in distilled water (10 mL). After approximately 3 h, the insoluble barium sulfate that formed was filtered through a plug of Celite. The Celite was washed thoroughly with fresh solvent, and the combined filtrates were stripped under reduced pressure. Recrystallization of the crude product from ethanol/ether yielded the pure compound as a crystalline yellow powder (0.411 g, 79%). Method 2: Alternatively, N,N'-dimethylhydrazine (0.120 g, 2.00 mmol) was dissolved in diethyl ether (5 mL) and treated with neat picric acid (0.804 g, 3.51 mmol). Immediate precipitation of a yellow powder was observed, and the reaction mixture was stirred for 20 min at room temperature. After this time, the insoluble solid was filtered from the bright yellow solution, washed with cold ether, and dried under vacuum to yield the pure

title compound (0.789 g, 87%). Single crystals of the dihydrate (**6**·2H$_2$O) suitable for X-ray analysis were grown by recrystallization of the compound from hot water, whereas recrystallization from hot ethanol rendered X-ray-quality single crystals of *N,N′*-dimethylhydrazinium monopicrate (**6b**). $\rho_{calcd.}$ (dihydrate, X-ray) = 1.666 g cm^{-3}. C$_{14}$H$_{14}$N$_8$O$_{14}$ (518.31): calcd. C 32.44, H 2.72, N 21.62; found C 32.41, H 2.57, N 21.52. DSC (5 °C min^{-1}): 112 °C (m.p.), >225 °C (decomp.). MS (ESI$^+$): *m/z*: 61.0 (100) [Cat$^+$]. MS (ESI$^-$): *m/z*: 228.2 (100) [A$^-$], 478.9 (54) [2A$^-$ + Na$^+$]. ^{1}H NMR ([D$_6$]DMSO, 400.18 MHz, TMS): δ = 2.60 (s, 6 H, –CH$_3$), 8.46 (br. s, 4 H, N–H), 8.60 (s, 4 H, Ar–H) ppm. ^{13}C NMR ([D$_6$]DMSO, 100.52 MHz, TMS): δ = 160.6 (1 C, C1), 141.8 (2 C, C2), 125.1 (2 C, C3), 124.4 (1 C, C4), 34.8 (4 C, CH$_3$) ppm. IR (Raman) (rel. int.): $\tilde{\nu}$ = 3281 (3), 3113 (1), 3064 (1), 3020 (1), 2974 (2), 1633 (4), 1614 (3),1547 (15), 1490 (4), 1344 (96), 1296 (100), 1168 (14), 1086 (7), 1009 (1), 942 (9), 916 (3), 822 (21), 747 (4), 701 (4), 527 (2), 474 (3), 400 (3), 330 (9), 201 (8). IR (golden gate, rel. int.): $\tilde{\nu}$ = 3277 (w), 3056 (w), 2972 (w), 2856 (w), 2827 (w), 2796 (w), 2766 (w), 2482 (w), 2256 (w), 2108 (w), 1885 (w), 1831 (w), 1628 (w), 1605 (m), 1566 (m), 1539 (m), 1515 (m), 1481 (m), 1464 (m), 1455 (m), 1432 (m), 1417 (w), 1403 (w), 1364 (m), 1341 (s), 1320 (s), 1282 (s), 1270 (s), 1166 (s), 1102 (w), 1085 (m), 1061 (w), 1005 (m), 961 (m), 941 (m), 911 (s), 838 (m), 828 (s), 792 (s), 747 (m), 739 (m), 709 (s), 700 (s) cm^{-1}.

Attempted Synthesis of [MeNH$_2$–NH$_2$Me][H$_2$N-CN$_4$]$_2$ (7): Method 1: 98% Barium hydroxide octahydrate (0.731 g, 2.27 mmol) and 97% 5-amino-1*H*-tetrazole monohydrate (0.482 g, 4.54 mmol) were dissolved in distilled water (15 mL) and the mixture was boiled overnight. After this time, the insoluble barium carbonate was filtered and neat **5** (0.360 g, 2.27 mmol) was added to the filtrate at room temperature. The reaction mixture was stirred for 2.5 h and the insoluble barium sulfate was filtered through a plug of Celite. The solvent was then stripped under reduced pressure to leave behind a white powder (0.429 g). The IR of this product was almost identical to that of a pure sample of 97% 5-amino-1*H*-tetrazole monohydrate. Method 2: Alternatively, *N,N′*-dimethylhydrazine (0.105 g, 1.75 mmol) and 97% 5-amino-1*H*-tetrazole monohydrate (0.369 g, 3.47 mmol) were suspended in ethanol (10 mL), and the reaction mixture was boiled for 2.5 h. After this time, the volatiles were eliminated under reduced pressure to give a white solid, which was dried under high vacuum (0.347 g). IR analysis and X-ray measurements of crystals grown by slow evaporation of an ethanolic solution showed the compound isolated to be 5-amino-1*H*-tetrazole monohydrate. IR (golden gate, rel. int.): $\tilde{\nu}$ = 3469 (w), 3335 (m), 3270 (m), 3188 (m), 2933 (w), 2769 (w), 2643 (w), 2454 (w), 2164 (w), 2144 (w), 2026 (w), 1979 (w), 1941 (w), 1778 (w), 1637 (s), 1520 (m), 1448 (m), 1297 (m), 1248 (w), 1222 (w), 1157 (m), 1108 (w), 1054 (m), 1013 (m), 993 (m), 907 (m), 755 (m), 740 (m), 689 (w), 677 (w) cm^{-1}. X-ray (Mo-K_α): *a* = 6.40 Å, *b* = 7.27 Å, *c* = 9.86 Å, β = 90.2°, *V* = 458.8 Å^3.

Supporting Information (see footnote on the first page of this article): Tables that contain calculated frequencies for the [MeNH$_2$–NH$_2$Me]$^{2+}$ cation, hydrogen-bonding geometry, the results of the graph-set analysis, performance data for the formulations with AN and ADN, pictures of the friction test, and synthesis of the starting materials.

Acknowledgments

[1] *International Conference on Green Propellant for Space Propulsion*, Noordwijk, The Netherlands, June 20–22, **2001**. http://esamultimedia.esa.int/conferences/01a05/index.html.

[2] H. Gao, R. Wang, B. Twamley, M. A. Hiskey, J. M. Shreeve, *Chem. Commun.* **2006**, 4007–4009.

[3] a) R. P. Singh, R. D. Verma, D. T. Meshri, J. M. Shreeve, *Angew. Chem.* **2006**, *118*, 3664; *Angew. Chem. Int. Ed.* **2006**, *45*, 3584–3601; b) G. Steinhauser, T. M. Klapoetke, *Angew. Chem.* **2008**, *120*, 3376; *Angew. Chem. Int. Ed.* **2008**, *47*, 3330–3347.

[4] a) H. Xue, Y. Gao, B. Twamley, J. M. Shreeve, *Chem. Mater.* **2005**, *17*, 191–198; b) K. Karaghiosoff, T. M. Klapötke, P. Mayer, C. Miró Sabaté, A. Penger, J. M. Welch, *Inorg. Chem.* **2008**, *47*, 1007–1019; c) C. Darwich, T. M. Klapötke, C. Miró Sabaté, *Chem. Eur. J.* **2008**, *14*, 5756–5771.

[5] a) C. M. Jin, C. Ye, C. Piekarski, B. Twamley, J. M. Shreeve, *Eur. J. Inorg. Chem.* **2005**, 3760–3767; b) T. M. Klapötke, C. Miró Sabaté, *Z. Anorg. Allg. Chem.* **2008**, *634*, 1017–1024; c) T. M. Klapötke, C. Miró Sabaté, *Eur. J. Inorg. Chem.* **2008**, *34*, 5350–5366.

[6] a) A. Hammerl, M. A. Hiskey, G. Holl, T. M. Klapoetke, K. Polborn, J. Stierstorfer, J. J. Weigand, *Chem. Mater.* **2005**, *17*, 3784–3793; b) T. M. Klapötke, C. Miró Sabaté, *Chem. Mater.* **2008**, *20*, 1750–1763.

[7] H. Xue, Y. Gao, B. Twamley, J. M. Shreeve, *Inorg. Chem.* **2005**, *44*, 5068–5072.

[8] a) J. E. Paustian (Thiokol Chemical Corp.), US 3,769,389, **1973**; b) K. C. Patil, R. Soundararajan, V. R. P. Verneker, *Proc. - Indian Acad. Sci.* **1978**, *87A*, 281–284; c) F. W. M. Zee, J. M. Mul, A. C. Hordijk (Aerospace Propulsion Products B. V. Neth) WO 9,410,104, **1994**; d) A. C. Hordijk, J-M. Mul, J. J. Meulenbrugge, P. A. O. G. Korting, P. L. Lit, A. J. Schnorhk, H. F. R. Schoyer, *International Annual Conference of ICT*, Rijswijk, Netherlands, **1994**, *69*, 1–11; e) M. Göbel, T. M. Klapötke, *Z. Anorg. Allg. Chem.* **2007**, *633*, 1006–1017; f) T. M. Klapötke, P. Mayer, C. Miró Sabaté, J. M. Welch, N. Wiegand, *Inorg. Chem.* **2008**, *47*, 6014–6027; g) T. M. Klapötke, J. Stierstorfer, A. U. Wallek, *Chem. Mater.* **2008**, *20*, 4519–4530.

[9] a) L. S. Korablina, V. D. Krylov, L. M. Kharchevnikova, V. V. Yastrebov, *Izvestiya Vysshikh Uchebnykh Zavedenii, Khimiya i Khimicheskaya Tekhnologiya* **1966**, *9*, 351–354; b) E. A. Lawton, C. M. Moran, *J. Chem. Eng. Data* **1984**, *29*, 357–358; c) H. S. Jadhav, M. B. Talawar, D. D. Dhavale, S. N. Asthana, V. N. Krishnamurthy, *Ind. J. Chem. Technol.* **2005**, *12*, 187–192.

[10] a) J. R. Thornton (Atlas Chemical Industries Inc.), US 3,297,747, **1967**; b) M. Stammler (Aerojet-General Corp.), US 3,316,301, **1967**; c) S. P. Singh, R. K. Prasad, *J. Indian Chem. Soc.* **1983**, *60*, 170–175.

[11] A. Hammerl, G. Holl, M. Kaiser, T. M. Klapoetke, P. Mayer, H. Piotrowski, M. Vogt, *Z. Naturforsch., Teil B* **2001**, *56*, 847–856.

[12] A. Hammerl, G. Holl, K. Huebler, M. Kaiser, T. M. Klapoetke, P. Mayer, *Eur. J. Inorg. Chem.* **2001**, 755–760.

[13] H. J. Abendroth (Farbenfabriken Bayer A.-G.), DE 1,127,907, **1962**.

[14] a) H. H. Hatt, *Org. Synth.* **1936**, *16*, 18–21; b) K. S. Kumar, F. D. Cazer, D. T. Witiak, *J. Labelled Compd. Radiopharm.* **1982**, *19*, 763–767.

[15] A. D. Becke, *J. Chem. Phys.* **1993**, *98*, 5648.

[16] C. Lee, W. Yang, R. G. Parr, *Phys. Rev. B* **1988**, *37*, 785.

[17] E. D. Glendening, A. E. Reed, J. E. Carpenter, F. Weinhold, *NBO Version 3.1* from *Gaussian 03*, Revision, D.01, Gaussian, Inc., Wallingford, CT, **2004**.

[18] A. P. Scott, L. Radom, *J. Phys. Chem.* **1996**, *100*, 16502.

[19] P. Mani, H. Umamaheswari, B. D. Joshua, N. Sundaraganesan, *THEOCHEM* **2008**, *863*, 44–49.

[20] a) K. Williamson, P. Li, J. P. Devlin, *J. Chem. Phys.* **1968**, *48*, 3891–3896; b) J. R. Fernandes, S. Ganguly, C. N. R. Rao, *Spectrochim. Acta Part A* **1979**, *35*, 1013–1019.

[21] a) H. Cohn, *J. Chem. Soc.* **1952**, 4282–4284; b) P. Redlich, J. Holt, T. Biegeleisen, *J. Am. Chem. Soc.* **1944**, *66*, 13–16; c) H. Grothe, H. Willner, *Angew. Chem.* **1996**, *108*, 816–818; *Angew. Chem. Int. Ed. Engl.* **1996**, *35*, 768–769.

[22] Y. Zhang, H. Gao, Y. Guo, Y. H. Joo, J. M. Shreeve, *Chem. Eur. J.* **2010**, *16*, 3114–3120.

[23] T. M. Klapötke, P. Mayer, J. Stierstorfer, *Phosphorus Sulfur Silicon Relat. Elem.* **2009**, *184*, 2393–2407.

[24] T. M. Klapötke, C. Miró Sabaté, *Z. Anorg. Allg. Chem.* **2008**, *634*, 1017–1024.

[25] N. B. Colthup, L. H. Daly, S. E. Wiberley, *Introduction to Infrared, Raman Spectroscopy*, Academic Press, Boston, USA, **1990**.

[26] J. C. Gálvez-Ruiz, H. Holl, K. Karaghiosoff, T. M. Klapötke, K. Löhnwitz, P. Mayer, H. Nöth, K. Polborn, C. Rohbogner, M. Suter, J. J. Weigand, *Inorg. Chem.* **2005**, *44*, 4237–4253.

[27] *CrysAlis CCD*, version 1.171.27p5 beta, Oxford Diffraction Ltd.

[28] *CrysAlis RED*, version 1.171.27p5 beta, Oxford Diffraction Ltd.

[29] A. Altomare, G. Cascarano, C. Giacovazzo, A. Guagliardi, *J. Appl. Crystallogr.* **1993**, *26*, 343.

[30] G. M. Sheldrick, *SHELXS-97, Program for Crystal Structure Solution*, Institut für Anorganische Chemie der Universität Göttingen, Germany, **1997**.

[31] G. M. Sheldrick, *SHELXL-97, Program for the Refinement of Crystal Structures*, Institut für Anorganische Chemie der Universität Göttingen, Germany, **1997**.

[32] L. J. Farrugia, *J. Appl. Crystallogr.* **1999**, *32*, 837.

[33] A. L. Spek, *PLATON, A Multipurpose Crystallographic Tool*, Utrecht, The Netherlands, **1999**.

[34] *SCALE3 ABSPACK - An Oxford Diffraction Program*, Oxford Diffraction, **2005**.

[35] CCDC-812949 (for **2**), -812950 (for **3**), -812951 (for **5**), -812952 (for **6b**), and -812953 (for **6**·2H$_2$O) contain the supplementary crystallographic data for this paper. These data can be obtained free of charge from The Cambridge Crystallographic Data Centre via www.ccdc.cam.ac.uk/data_request/cif..

[36] a) P. C. Chieh, G. J. Palenik, *J. Chem. Soc.* **1971**, 576; b) N. Okabe, H. Fukuda, T. Nakamura, *Acta Crystallogr., Sect. C* **1993**, *49*, 1677; c) Q. C. Ton, M. Bolte, *Acta Crystallogr., Sect. E* **2004**, *60*, o1129; d) A. Hammerl, G. Holl, M. Kaiser, T. M. Klapotke, R. Kranzle, M. Vogt, *Z. Anorg. Allg. Chem.* **2002**, *628*, 322.

[37] R. G. Parr, W. Yang, *Density Functional Theory of Atoms, Molecules*, Oxford University Press, New York, USA, **1989**.

[38] *International Tables for X-ray Crystallography*, vol. III, Kynoch Press, Birmingham, **1962**, p. 270.

[39] W. H. Beamer, *J. Am. Chem. Soc.* **1948**, *70*, 2979.

[40] a) M. C. Etter, J. C. MacDonald, *Acta Crystallogr., Sect. B* **1990**, *46*, 256–262; b) J. Bernstein, R. E. Davis, L. Shimoni, N. L. Chang, *Angew. Chem.* **1995**, *107*, 1689–1708; *Angew. Chem. Int. Ed. Engl.* **1995**, *34*, 1555–1573; c) http://www.ccdc.cam.ac.uk/suport/documentation/rpluto/TOC.html.

[41] J. A. Pople, R. Seeger, R. Krishnan, *Int. J. Quantum Chem. Symp.* **1977**, *11*, 149.

[42] A. K. Rick, T. H. Dunning, J. H. Robert, *J. Chem. Phys.* **1992**, *96*, 6796.

[43] A. P. Kirk, E. W. David, T. H. Dunning, *J. Chem. Phys.* **1994**, *100*, 7410.

[44] a) H. D. B. Jenkins, D. Tudela, L. Glasser, *Inorg. Chem.* **2002**, *41*, 2364–2367; b) H. D. B. Jenkins, H. K. Roobottom, J. Passmore, L. Glasser, *Inorg. Chem.* **1999**, *38*, 3609–3620.

[45] http://www.bam.de; http://www.reichel-partner.de.

[46] a) NATO standardization agreement (STANAG) on explosives, impact sensitivity tests, no. 4489, Ed. 1, Sept. 17, **1999**; b) NATO standardization agreement (STANAG) on explosive, friction sensitivity tests, no. 4487, Ed. 1, Aug. 22, **2002**.

[47] WIWEB-Standardarbeitsanweisung 4–5.1.03, *Ermittlung der Explosionsgefährlich or der Reibeempfindlichkeit mit dem Reibeapparat*, Nov. 8, **2002**.

[48] Impact: insensitive ($i > 40$ J), less sensitive ($i \geq 35$ J), sensitive ($i \geq 4$ J), very sensitive ($i \leq 3$ J). Friction: insensitive ($f > 360$ N), less sensitive ($f = 360$ N), sensitive (360 N $> f > 80$ N), very sensitive ($f \leq 80$ N), extremely sensitive ($f \leq 10$ N). According to the UN Recommendations on the Transport of Dangerous Goods (+) indicates not safe for transport.

[49] J. Köhler, R. Meyer, *Explosivstoffe*, 9th ed., Wiley-VCH, Weinheim, Germany, **1998**.

[50] A. Hammerl, T. M. Klapötke, H. Nöth, M. Warchhold, *Inorg. Chem.* **2001**, *40*, 3570–3575.

[51] M. Göbel, T. M. Klapötke, *Z. Anorg. Allg. Chem.* **2007**, *633*, 1006–1017.

[52] T. M. Klapötke, P. Mayer, C. Miró Sabaté, J. M. Welch, N. Wiegand, *Inorg. Chem.* **2008**, *47*, 6014–6027.

[53] NIST Chemistry WebBook, NIST Standard Reference Database Number 69, **2005**; http://webbook.nist.gov.

[54] T. M. Klapötke, C. Miró Sabaté, A. Penger, M. Rusan, J. M. Welch, *Eur. J. Inorg. Chem.* **2009**, 880–896.

[55] a) M. Sućeska, *Propellants Explos. Pyrotech.* **1991**, *16*, 197; b) M. Sućeska, *Propellants Explos. Pyrotech.* **1999**, *24*, 280.

[56] J. Akhavan, *The Chemistry of Explosives*, 2nd ed., RSC Paperbacks, Cambridge, UK, **2004**.

[57] H. Gao, C. Ye, C. M. Piekarski, J. M. Shreeve, *J. Phys. Chem.* **2007**, *C111*, 10718.

[58] A. K. Sikder, N. Sikder, *J. Hazard. Mater.* **2004**, *A112*, 1.

[59] Y. Inoue, M. Ouchi, T. Hakushi, *Bull. Chem. Soc. Jpn.* **1985**, *58*, 525–530.

[60] a) U. Wannagat, M. Schlingmann, *Z. Anorg. Allg. Chem.* **1974**, *406*, 7; b) A. Hammerl, Master Thesis, Ludwig-Maximilians University of Munich, Germany, **1998**.

FULL PAPER

A New Silver-Based Precursor as Ink for Soft Printing Techniques

Julia Fritsch,[a] Benjamin Schumm,[a] Ralf Biedermann,[a] Julia Grothe,*[a] and Stefan Kaskel[a]

A new, easily obtainable silver–pyrrolidone complex that is suitable for printing applications was synthesized by the reaction of silver nitrate and 2-pyrrolidone (Pyl) at room temperature. According to single-crystal X-ray crystallographic studies, the product $[Ag(Pyl)_2]NO_3$ crystallizes in the monoclinic space group $C2/c$ (no. 15) [a = 5.358(1) Å, b = 15.217(3) Å, c = 14.986(3) Å, β = 99.296(6)°]. Highly concentrated solutions of the complex can be obtained in an ethanol/water mixture, thereby allowing for the manufacture of thin films by means of dip coating. Subsequent UV irradiation and moderate-temperature treatment yielded compact films of elemental silver with thicknesses of about 100 nm and sheet resistances down to 6.5 Ω Furthermore, microcontact printing (μcp) and embossing of $[Ag(Pyl)_2]NO_3$ were performed, also followed by UV treatment. By means of the photoreduction of the complex and subsequent moderate-thermal treatment, defined structures of elemental silver lines were obtained.

Introduction

Transparent conductive films play a key role in several optoelectronic applications such as flat-panel displays, organic light-emitting diodes (OLEDs), and photovoltaics (PV).[1–4] With increasing demand for structured transparent electrodes, printings of functional materials like transparent conductive oxides,[5,6] conductive polymers,[7] carbon-based materials,[8,9] or metals[10,11] have attracted much attention in recent years.[12,13]

In particular, silver-based materials have been studied due to their advantages like very low resistivity, stability, and flexibility compared to transparent conductive oxides or polymers and carbon-based materials. However, the challenge in using silver is the fabrication of transparent materials. Due to that fact, several methods for the preparation of ultrathin films such as chemical vapor deposition or vacuum-thermal evaporation techniques have been investigated.[14–16] Also, different printing techniques of metallic materials to obtain structured patterns with higher transparency have been reported recently. One way is to use simple metal solutions such as silver nitrate, which can be converted into silver at high temperatures (above 400 °C).[17] A second way is to use metallo-organic precursors or stabilized metal solutions, which can be converted into metals at lower temperatures.[18–20] Another well-known method is the generation of silver-nanoparticle suspensions stabilized with polymers such as poly(N-vinyl-2-pyrrolidone) (PVP) or others.[21,22] In addition to their stabilizing effect, PVP or pyrrolidone derivatives support the photoreduction of silver ions to elemental silver.[23] Based on these conditions, we created an easily obtainable complex of silver nitrate and 2-pyrrolidone. Both silver nitrate and 2-pyrrolidone are highly soluble in water or water/ethanol mixtures. Similar to PVP, the organic 2-pyrrolidone ligand should have a stabilizing effect and support photoreduction. Due to these facts, the generated complex can be used as an ink for direct soft printing methods such as microcontact printing (μcp) or embossing processes that offer a way to fabricate conductive transparent substrates.

In the following we describe the structure of the new, easily obtainable silver complex synthesized by mixing silver nitrate and 2-pyrrolidone (Pyl) in water. In addition, we demonstrate its suitability as an ink by using dip coating for compact silver films and soft print methods for structured coatings.

Results and Discussion

Synthesis and Structural Characterization of $[Ag(Pyl)_2]NO_3$

The reaction between aqueous solutions of silver nitrate and 2-pyrrolidone at room temperature under exclusion of light led to the formation of colorless crystals of $[Ag(Pyl)_2]$-NO_3 (Scheme 1).
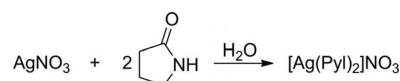
Scheme 1. Synthesis of the $[Ag(Pyl)_2]NO_3$.

[a] Department of Inorganic Chemistry, Dresden University of Technology
Bergstrasse 66, 01069 Dresden, Germany
Fax: +49-351-46337287
E-mail: Julia.Grothe@chemie.tu-dresden.de

The linear 1D polymeric silver complex poly-[Ag(Pyl)$_2$]-NO$_3$ crystallizes in the monoclinic space group C2/c (no. 15) with four formula units per unit cell. The formula unit contains the 2-pyrrolidone molecules, one silver atom, and one nitrate anion. The silver atom and the nitrate anion occupy special positions on twofold axes. The Ag atom exhibits an irregular AgO$_6$ coordination geometry, which consists of two oxygen atoms from monodentate-coordinated 2-pyrrolidone molecules and four oxygen atoms from two bidentate-coordinated nitrate anions. The Ag–O distances are in the range of 2.358(2)–2.683(4) Å. The nitrate anions have a linker function and connect the structure into 1D polymeric chains, which are located along the [100] direction (Figure 1). The silver atoms are connected to a linear polymeric chain by μ$_2$-O bridging oxygen atoms O4 with a significantly longer Ag1–O4 distance [2.683(1) Å] than Ag1–O2 [2.536(4) Å]. In the crystal structure, the 1D polymeric chains are connected into the 2D network by intermolecular N–H···O hydrogen bonds (Figure 2) [N2–H3N···O1^i: D···A 2.952(4) Å, D–H···A 163°; i: 0.5 – x, 0.5 – y, –z].
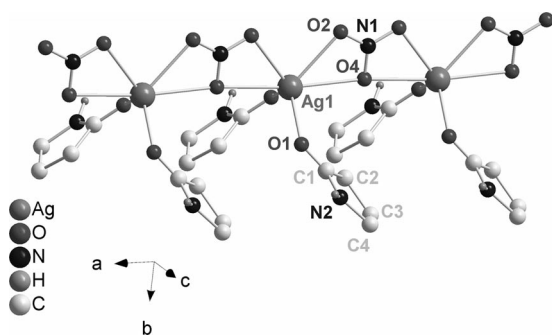

Figure 1. Linker function of the nitrate ion connecting the structure into 1D polymeric chains.
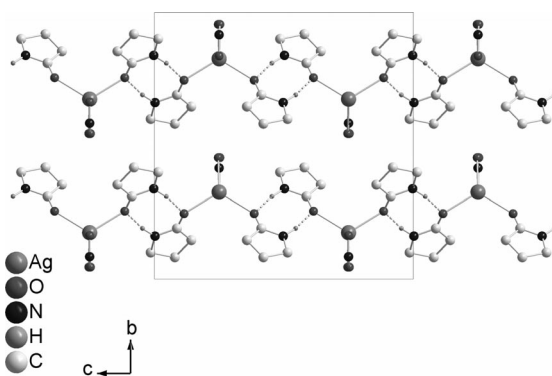

Figure 2. Two-dimensional network of –[Ag(Pyl)$_2$]NO$_3$, which is connected through intermolecular N–H···O hydrogen bonds in the 1D polymeric chains.

As shown in Figure 3, the powder X-ray pattern of the silver complex conforms to the calculated one from the solved structure. The differences in intensity between several peaks are due to the preferred orientation of the acicular crystallites in the powdered sample. According to thermogravimetric analysis (see the Supporting Information),

the silver complex decomposes in two steps (see the Supporting Information, Figure a), whereas the major organic part (>60%) evaporates up to a temperature of 220 °C. This mass loss can be attributed to the 2-pyrrolidone ligand and parts of the nitrate. The second step at about 400–440 °C results in the volatilization of the residual nitrate. The final residue could be identified as elemental silver by using powder X-ray diffraction (PXRD) and supports the results from the elemental analysis (see the Supporting Information, Figures b and d).
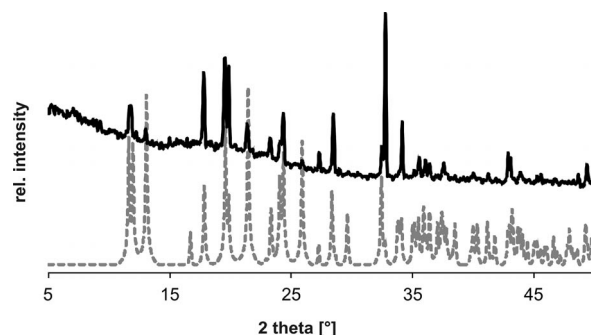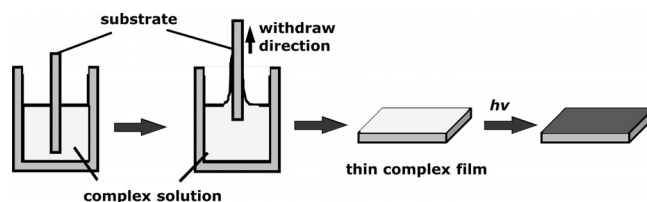

Figure 3. PXRD pattern of the silver complex (black) compared to the pattern that was calculated from the solved structure (dashed line).

Preparation of Compact, Thin Silver Films

The suitability of [Ag(Pyl)$_2$]NO$_3$ as an ink for the fabrication of thin, conductive silver films through soft printing techniques was tested by the preparation of thin, compact silver films. For this purpose, glass substrates were coated with an aqueous/ethanolic solution of the silver complex by means of dip coating (Scheme 2). Subsequently, the substrates were irradiated with UV light to obtain compact silver films. To achieve an optimal adhesion of the complex solution, the microscope slides were pretreated with a piranha solution. With this pretreatment, it was possible to obtain thin, homogeneously coated substrates.

Scheme 2. Schematic description of the dip-coating process to fabricate thin, compact silver coatings.

The photoreduction of the silver complex was examined by recording XRD patterns and SEM pictures after different periods of UV irradiation. As shown in the XRD of

Figure 4 (light gray line) and the respective photo, there is no complete conversion into elemental silver without UV irradiation. Additionally, the films are not homogeneous (Figure 5a). After 10 min of UV irradiation, elemental silver resulted (Figure 4, gray line), but as shown in the SEM image (Figure 5b), the layer is not homogeneous. An optimal silver coating was obtained after 20 min of irradiation (black line in the XRD of Figure 4, SEM image in Figure 5c). The broad signal in the thin-film XRDs from $2\theta \approx$ 20 to 30° results from the glass substrate. Additionally, a thermogravimetric analysis of the UV-reduced sample was carried out (see the Supporting Information, Figure c). In contrast to the complex that was not irradiated, the decomposition took place in only one step at 220 °C, and no further decomposition was observed at about 400–440 °C, thus indicating the decomposition of the nitrate during the UV reduction. The residual mass fits the content of silver in a "nitrate-free" complex. Since the thermogravimetric analysis of the UV-reduced sample shows complete decomposition at 220 °C, the coated substrates were additionally treated at a temperature of 220 °C after UV irradiation. The necessity of this additional temperature treatment is demonstrated, for example, in a thicker layer with an UV-irradiation period of 20 min. As shown in Figure 6, the untreated layer (gray line) shows a slight crystallinity compared to the

Figure 4. XRD patterns of the reduced complex with the following irradiation times: 0 min (light gray), 10 min (gray), 20 min (black); dashed lines: reference of silver [4-783]; photos of the substrates without UV irradiation (bottom) and after 20 min irradiation (top). Additionally, all coated substrates were treated at 220 °C for 60 min.

Figure 5. SEM images of the reduced complex with the following irradiation times: (a) 0, (b) 10, and (c) 20 min. All samples were treated after reduction at 220 °C.

sample treated at 220 °C (black line). Furthermore, without the temperature treatment, the dip-coated layers did not show good values in sheet resistance due to the presence of the organic ligand. To avoid an abrupt vaporization of any volatile components after UV irradiation, the samples were heated slowly to 220 °C at a rate of 5 K min^{-1}.
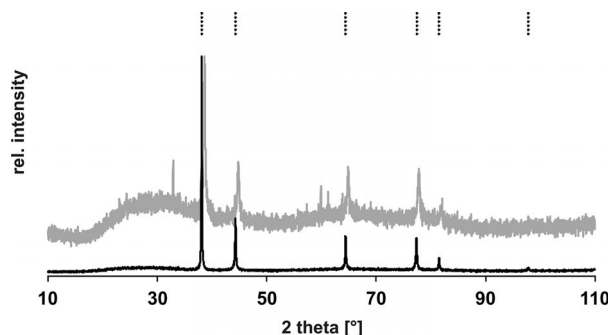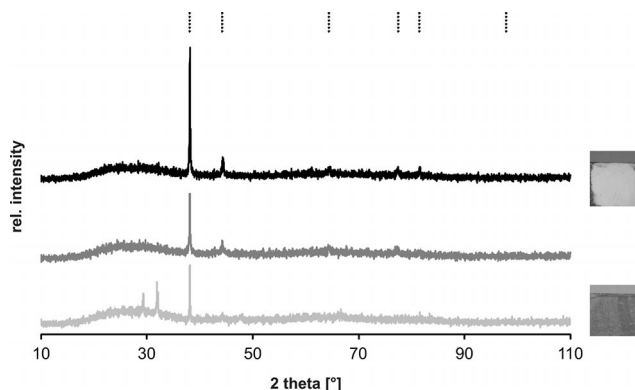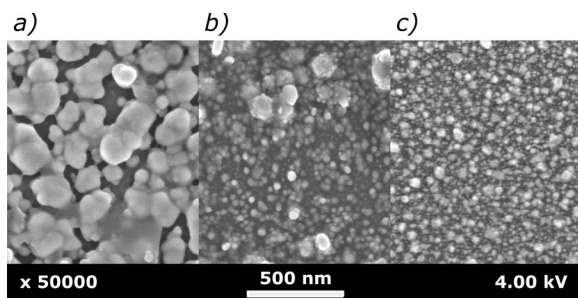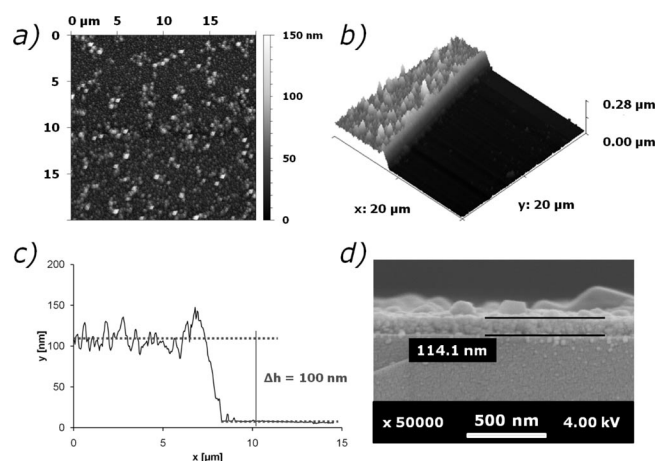

Figure 6. XRD pattern of the reduced complex without thermal treatment (gray) compared to that with thermal treatment (black); dashed lines: reference of silver ICSD [4-783].

To examine the thickness and surface morphology of the compact silver films, atomic force microscopy (AFM) and SEM measurements were used. In Figure 7a, an AFM image of a produced silver coating with optimized reduction conditions is shown. As seen in the picture, the surface of the film shows roughness. Surface roughness values were calculated with R_a = 12.6 nm/R_{ms} = 17.3 nm. Due to that, the values of sheet resistance were measured by means of a four-point method spread between 6.5 and 20 Ω in one sample. However, for the calculation of the specific electrical resistance, we determined the thickness of the silver layers by means of AFM. In Figure 7b and c, the measurement of a scratch made with a scalpel with a resulting film thick-

Figure 7. (a) AFM image of a compact dip-coated silver film that was UV-irradiated for 20 min and treated at 220 °C; (b) and (c) height profile of an AFM micrograph of the compact film scratched with a scalpel. The AFM cross section (c) shows the scratched zero level on the substrate and the silver film. To calculate the height, average values of both levels were estimated (dashed lines). (d) An SEM image of the edge of the silver film on the glass substrate with a determined film thickness of 114.1 nm.

ness of about 100 nm is shown. For the evaluation of the thickness, the values for both areas (the silver layer and the scratched area) were averaged (dashed lines) and the difference in height was estimated. By considering an average film thickness of about 100 nm, specific electrical resistances of $6.5 \times 10^{-7}\ \Omega\,m$ ($6.5 \times 10^{-5}\ \Omega\,cm$) to $2 \times 10^{-6}\ \Omega\,m$ ($2 \times 10^{-4}\ \Omega\,cm$, relative to the sheet resistances between 6.5 and 20 Ω) could be estimated. Compared to the resistance of the bulk material ($1.587 \times 10^{-8}\ \Omega\,m$),[24] the films show a reduced performance that could be due to the roughness of the film surface but also grain boundaries in the nanoparticulate film with a mean particle size of about 40 nm [calculated from the single peak widths in the powder pattern of Figure 4 (black) and the SEM picture of Figure 5c]. To verify these results, SEM images at a cut edge of the silver film were recorded. As shown in the picture of Figure 7d, a film thickness of about 114 nm was examined, which is similar to the results of the AFM measurements. Slight differences are due to the surface roughness or the error limit of both methods.

Printed Silver Films

With the new silver complex, an ink for printing applications was synthesized. To prove this suitability, we tested the ink in soft printing techniques. We obtained patterned silver films with two different processes. In Scheme 3i, the microcontact printing (μcp) process is shown. The precursor solution was adjusted (A) with a polydimethylsiloxane (PDMS) stamp. Afterwards, the inked stamp was pressed onto the substrate (B) and the ink had to be transferred to the substrate (C). With a subsequent precursor–metal transformation, the silver-coated substrate could be obtained. By using a procedure similar to an embossing process (Scheme 3ii),[13] the substrate could be coated with a compact precursor solution (A). Subsequently, the PDMS stamp was pressed into the compact film (B), and after removing a structured coating, the silver complex was obtained (C). Finally, a precursor–metal transformation resulted in the structured silver film.
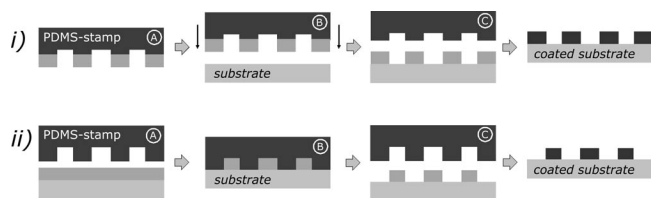
Scheme 3. Schematical description of (i) the microcontact printing and (ii) the embossing process.

With both these soft printing processes, we were able to obtain structured silver coatings. To avoid crystallization of the complex during the printing process, a small amount (10 wt.-%) of an alkyl derivative of the ligand, 1-*tert*-butyl-pyrrolidin-2-one, was added to the reaction mixture. Figure 8a shows an optical microscope picture of silver lines with a line width of 20 μm and a distance of 20 μm between

the lines, which was printed by using the embossing technique. SEM measurements (Figure 8b) provide evidence of the compactness of elemental silver in the line that is comparable to the compact silver films (Figure 5c). The structuring can also be followed in an energy-dispersive X-ray (EDX) mapping (Figure 8c). For comparison, the mapping was made for silver and oxygen. As seen in the picture, silver is present only at the lines, and oxygen (from the glass substrate) is only visible between the lines. There are only minor amounts of silver between the lines due to an incomplete takeup of the ink in the printing process.
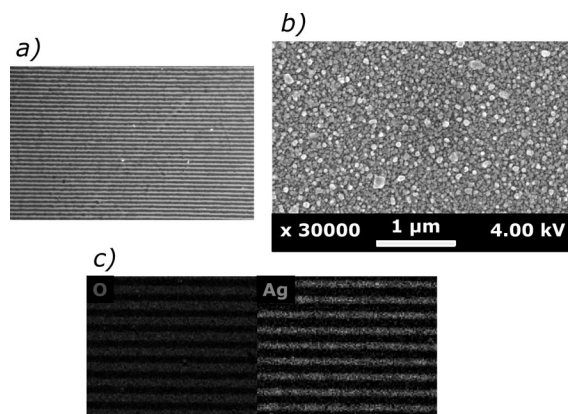

Figure 8. (a) Photo of the silver lines made by using an optical microscope. (b) SEM image measured in the line to show the compactness of silver in the lines. (c) EDX mapping of silver and oxygen on the structured substrate to show silver only in the printed area.

By using the μcp technique, it was also possible to obtain structured silver lines (Figure 9). On the left, an optical microscope picture of the obtained silver lines is shown. As seen in the picture, the line width is slightly enlarged relative to the distances between the lines, which could be due to smearing of the ink. That was previously observed in the embossing process but to a lesser extent. The structuring of silver was again verified by means of EDX mapping.
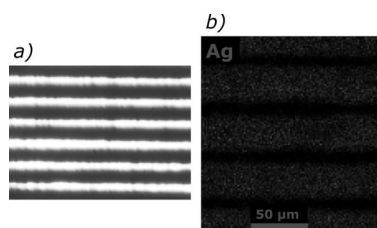

Figure 9. (a) Photo of the silver lines made by using an optical microscope. (b) EDX mapping on the structured substrate to show silver only in the printed area.

To conclude, patterned silver films could be obtained with both methods. With the embossing process, we were able to obtain homogeneous structuring. The compactness in the silver lines was included by using SEM analysis. EDX mapping shows silver only in the printed area. Minor amounts of silver between the lines could be due to an incomplete displacement or takeup of the ink. When using

the µcp technique, there is no silver between the lines but, as shown in Figure 9, the smearing of the ink is enlarged relative to the embossing process. With regards to the fabrication of transparent electrodes, the printing process has to be optimized in terms of the nano dimension of the line width.

Conclusion

A simple reaction was used for the synthesis of a silver–pyrrolidone complex. The preparation of colorless crystals of [Ag(Pyl)$_2$]NO$_3$ was possible, and the corresponding crystal structure was solved and refined. Photoreduction by using UV irradiation and a subsequent thermal treatment at moderate temperatures allowed for the formation of elemental silver. This precursor–metal transformation was used in the preparation of thin compact films as well as structured silver films. For the compact silver coatings, we measured sheet resistances down to 6.5 Ω on films irradiated with UV light for 20 min and treated at 220 °C for 60 min. These values correspond to specific electrical resistances of down to 6.5×10^{-5} Ω cm by a calculated film thickness of about 100 nm. Structured silver coatings were obtained by using soft printing techniques.

Experimental Section

General Remarks: Triethylamine for the synthesis of *tert*-butylpyrrolidone was dried with CaH$_2$. THF was dried with an M. Braun MB SPS-800 instrument. All other reagents and solvents were used as received without further purification. PXRD data were collected in transmission geometry with a Stoe Stadi-P powder diffractometer and Cu-$K_{\alpha 1}$ radiation. XRD patterns of thin films were recorded in Bragg–Brentano geometry with a Panalytical X'Pert Pro diffractometer, also with Cu-$K_{\alpha 1}$ radiation [λ = 0.154(05) nm]. For crystallite size determinations, the single-line size/strain analysis (WinXPow, Stoe) was used. For correction of the instrumental broadening, a LaB$_6$ standard sample was used. The sheet resistance of compact silver coatings was measured by means of a four-point method with a Keithley 2400 source meter coupled with a four-point probe cascade by Cascade Microtech. For scanning electron microscopy (SEM) and energy-dispersive X-ray spectroscopy, a ZEISS DSM-982 Gemini was used. EDX evaluations of the films were performed by applying an acceleration voltage of 12 kV at a magnification of 1000×. The surface morphology and thickness of the silver films were evaluated with a Dimension 3100 atomic force microscope controlled by a Nanoscope IV SPM controller from Veeco Digital Instruments. The measurements were performed in tapping mode with a Veeco Nanoprobe RTESP7 tip. NMR spectra were recorded with a Bruker DRX 500 P (^{1}H: 500 MHz). Elemental analysis for the elements C, H, and N was performed with a CHNS 932 analyzer from Leco. The respective metal content was determined with an ICP-OES Vista RL apparatus from Varian Inc.

X-ray Crystallography: Single-crystal X-ray diffraction data for [Ag(Pyl)$_2$]NO$_3$ were recorded with a Bruker APEX-II CCD and Mo-$K_{\alpha 1}$ radiation. The structure was solved and refined with the help of SHELX-97 software.[25] Further details of the structural analysis are summarized in Table 1. CCDC-842454 ([Ag(Pyl)$_2$]-

NO$_3$) contains the supplementary crystallographic data for this paper. These data can be obtained free of charge from The Cambridge Crystallographic Data Centre via www.ccdc.cam.ac.uk/data_request/cif.

Table 1. Crystallographic data for [Ag(Pyl)$_2$]NO$_3$.

	[Ag(Pyl)$_2$]NO$_3$
Empirical formula	Ag$_1$C$_8$H$_{14}$N$_3$O$_5$
M_r	340.09
Space group (no.)	$C2/c$ (15)
a [Å]	5.3583(10)
b [Å]	15.217(3)
c [Å]	14.986(3)
α [°]	90
β [°]	99.296(6)
γ [°]	90
V [Å^3]	1205.9(4)
Z	4
Reflections collected/independent	5080/1364
$\theta_{max.}$	27.50
GoF on F^2	1.098
R_{int}	0.0207
R_1, wR_2	0.0299, 0.0854
Max., min. peaks [e Å^{-3}]	0.727, –0.471

Preparation of [Ag(Pyl)$_2$]NO$_3$: Silver nitrate (0.34 g, 2 mmol, 99.5%, Sigma Aldrich) was dissolved in water (1 mL). 2-Pyrrolidone (0.34 g, 4 mmol, 99.0%, Sigma Aldrich) was added to the solution, and the mixture was stored under exclusion of light. The product was crystallized by slowly evaporating the solvent after a few days at room temperature.

Reduction of [Ag(Pyl)$_2$]NO$_3$ and Preparation of Thin Films: To reduce the silver complex, solutions of [Ag(Pyl)$_2$]NO$_3$ in ethanol/water (4:1) were prepared. Photoreduction was carried out by UV irradiation for 20 min. Subsequent treatment at T = 220 °C yielded highly crystalline elemental silver. Compact films of silver were prepared by means of dip coating complex solutions (0.8 M) on pretreated glass substrates and subsequent reduction.

Synthesis of 1-*tert*-Butylpyrrolidin-2-one:[26] THF (20 mL), triethylamine (3.5 g, 34.5 mmol, Acros Organics), and *tert*-butylamine (2.52 g, 34.5 mmol, 99.5%, Sigma Aldrich) were mixed in an argon-flushed flask and cooled to 0 °C. 4-Chlorobutyryl chloride (4.85 g, 34.5 mmol, 99.0%, Sigma Aldrich) was added very slowly under vigorous stirring, and the mixture was stirred at 0 °C for 2 h. Afterwards, deposited triethylamine hydrochloride was filtered off, washed two times with THF (10 mL), and the filtrate was concentrated under reduced pressure. The raw product was mixed with ethyl acetate (90 mL), transferred into a separating funnel, and washed with HCl (1 M, 10 mL) and two times with brine (10 mL). The organic layer was dried with MgSO$_4$, and the solvent was removed under reduced pressure.

The obtained *tert*-butyl-4-chlorobutanamide (6 g, 33.8 mmol) dissolved in THF (10 mL) was added to a solution of potassium *tert*-butoxide (3.9 g, 35 mmol, 99.99% sublimated grade, Sigma Aldrich) in THF (25 mL) with vigorous stirring very slowly at 0 °C (Ar). After 2 h of stirring in an ice bath, the mixture was transferred into a separating funnel, mixed with ethyl acetate (50 mL), and washed two times with brine (20 mL). The organic layer was dried with MgSO$_4$, and the solvent was removed under reduced pressure. After distillation under reduced pressure (14 mbar) at 75 °C, the product was obtained as a colorless liquid (yield: 60%). ^{1}H NMR spectroscopic analysis provided evidence of the purity of the product compared to the data in the literature.[26]

Nanoimprint Lithography (NIL) and Microcontact Printing (μcp): Printed structures were fabricated with a GeSiM μ-contact printer 3.0. As stamp material, a Sylgard 184 PDMS cross-linked by standard procedure (1 h at 80 °C) was used. The silicon masters were manufactured by standard e-beam lithography techniques. To prepare defined structures, the solutions of the silver complex were printed on pretreated glass substrates by using μcp and NIL techniques. Afterwards, the printed substrates were reduced analogously to the compact films.

Pretreatment of the Glass Substrates: To obtain an optimal adhesion for homogeneous thin films on the glass substrates, it was necessary to pretreat them. First, the glass slides were cleaned by sonication in ethanol for 15 min. Then they were placed in a piranha solution (1 part 30% H_2O_2, 3 parts concd. H_2SO_4) for 30 min. Finally, the slides were washed with MilliQ water and carefully dried under a slight nitrogen flow.

Supporting Information (see footnote on the first page of this article): TG analysis of the silver complex and the UV reduced sample, the elemental analysis of the silver complex, and a PXRD pattern of silver after the TG analysis.

Acknowledgments

[1] K. L. Chopra, S. Major, D. K. Pandya, *Thin Solid Films* **1983**, *102*, 1–46.

[2] S. Calnan, A. N. Tiwari, *Thin Solid Films* **2010**, *518*, 1839–1849.

[3] H. Liu, V. Avrutin, N. Izyumskaya, Ü. Özgür, H. Morkoç, *Superlattices Microstruct.* **2010**, *48*, 458–484.

[4] C. G. Granqvist, *Sol. Energy Mater. Sol. Cells* **2007**, *91*, 1529–1598.

[5] B. Schumm, P. Wollmann, J. Fritsch, J. Grothe, S. Kaskel, *J. Mater. Chem.* **2011**, *21*, 10697.

[6] H. Stiebig, N. Senoussaoui, C. Zahren, C. Haase, J. Müller, *Prog. Photovolt. Res. Appl.* **2006**, *14*, 13–24.

[7] C. Liu, C. Huang, S. Wu, J. Han, K. Hsieh, *Polym. Int.* **2010**, *59*, 517–522.

[8] Q. Cao, J. A. Rogers, *Adv. Mater.* **2009**, *21*, 29–53.

[9] M. Bansal, R. Srivastava, C. Lal, M. N. Kamalasanan, L. S. Tanwar, *Nanoscale* **2009**, *1*, 317.

[10] M.-G. Kang, L. J. Guo, *Adv. Mater.* **2007**, *19*, 1391–1396.

[11] J.-T. Wu, S. L.-C. Hsu, M.-H. Tsai, W.-S. Hwang, *Thin Solid Films* **2009**, *517*, 5913–5917.

[12] Y. Xia, G. M. Whitesides, *Annu. Rev. Mater. Sci.* **1998**, *28*, 153–184.

[13] E. Menard, M. A. Meitl, Y. Sun, J.-U. Park, D. J.-L. Shir, Y.-S. Nam, S. Jeon, J. A. Rogers, *Chem. Rev.* **2007**, *107*, 1117–1160.

[14] T. Struppert, A. Jakob, A. Heft, B. Grünler, H. Lang, *Thin Solid Films* **2010**, *518*, 5741–5744.

[15] R. B. Pode, C. J. Lee, D. G. Moon, J. I. Han, *Appl. Phys. Lett.* **2004**, *84*, 4614.

[16] A. Jakob, T. Rüffer, H. Schmidt, P. Djiele, K. Körbitz, P. Ecorchard, T. Haase, K. Kohse-Höinghaus, S. Frühauf, T. Wächtler, S. Schulz, T. Gessner, H. Lang, *Eur. J. Inorg. Chem.* **2010**, 2975–2986.

[17] Z. Liu, Y. Su, K. Varahramyan, *Thin Solid Films* **2005**, *478*, 275–279.

[18] A. L. Dearden, P. J. Smith, D.-Y. Shin, N. Reis, B. Derby, P. O'Brien, *Macromol. Rapid Commun.* **2005**, *26*, 315–318.

[19] J. J. P. Valeton, K. Hermans, C. W. M. Bastiaansen, D. J. Broer, J. Perelaer, U. S. Schubert, G. P. Crawford, P. J. Smith, *J. Mater. Chem.* **2010**, *20*, 543.

[20] J.-T. Wu, S. L.-C. Hsu, M.-H. Tsai, W.-S. Hwang, *J. Phys. Chem. C* **2010**, *114*, 4659–4662.

[21] S. L.-C. Hsu, R.-T. Wu, *Mater. Lett.* **2007**, *61*, 3719–3722.

[22] M. Layani, M. Gruchko, O. Milo, I. Balberg, D. Azulay, S. Magdassi, *ACS Nano* **2009**, *3*, 3537–3542.

[23] W.-F. Lee, K.-T. Tsao, *J. Mater. Sci.* **2009**, *45*, 89–97.

[24] D. R. Lide, *CRC Handbook of Chemistry and Physics*, CRC Press, Taylor & Francis, Boca Raton, Florida, **2009**.

[25] *SHELXS-97: Programs for Crystal Structure Solution*: G. M. Sheldrick, *Acta Crystallogr., Sect. A* **2008**, *64*, 112–122.

[26] K. Takao, K. Noda, Y. Morita, K. Nishimura, Y. Ikeda, *Cryst. Growth Des.* **2008**, *8*, 2364–2376.